Stockholm
University

Developments for the FPGA-Based Digitiser in the PANDA Electromagnetic Calorimeters

Markus Preston

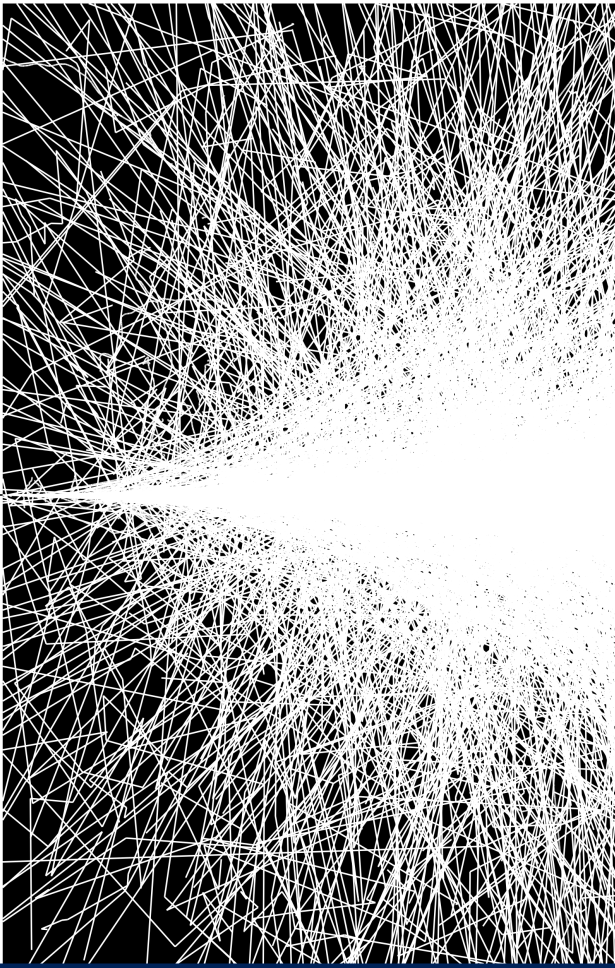

Doctoral Thesis in Physics at Stockholm University, Sweden 2020

Developments for the FPGA-Based Digitiser in the PANDA Electromagnetic Calorimeters

Markus Preston

Academic dissertation for the Degree of Doctor of Philosophy in Physics at Stockholm University to be publicly defended on Friday 17 April 2020 at 09.00 in sal FB55, AlbaNova universitetscentrum, Roslagstullsbacken 21.

Abstract

The strong interaction between quarks and gluons is one of the fundamental interactions described by the standard model of particle physics. Systems of quarks bound together by the strong interaction are known as hadrons, of which the proton and the neutron are the most common examples. The theoretical framework of quantum chromodynamics (QCD) is used to describe the strong interaction, but becomes increasingly difficult to use as the distance between the interacting particles increases. On the length scales relevant for hadrons, for instance, non-perturbative approaches to QCD have to be used. Experimental data are needed to verify these approaches. PANDA is one of the four experimental pillars of the upcoming FAIR facility in Darmstadt, Germany. In PANDA, an antiproton beam with a momentum between 1.5 and 15 GeV/c will interact in a hydrogen or nuclear target, allowing studies of various aspects of non-perturbative QCD. Motivated by the high interaction rates and the diverse physics goals of the experiment, a triggerless readout approach will be employed. In this approach, each detector subsystem will be equipped with intelligent front-end electronics that independently identify signals of interest in real time. In the electromagnetic calorimeter, FPGA-based digitiser modules will be used for this task. The high-radiation environment in PANDA will pose a challenge to these modules, due to both potential radiation damage and high signal rates from the calorimeter. In this thesis, these issues are addressed. First, the results from experimental measurements and Monte Carlo modelling of radiation-induced single event upsets in the FPGA are described. These studies have allowed predictions of the rate of single event upsets during operation of PANDA. Secondly, a newly developed algorithm for real-time processing of calorimeter signals in an FPGA at high pile-up rates is described. This algorithm provides a significant improvement in the time resolution of the calorimeter and allows reconstruction of the pulse height and timing of piled-up detector signals.

Keywords: *PANDA, calorimeter, FPGA, single event upset, Geant4, Monte Carlo, pile-up, feature extraction.*

Stockholm 2020
http://urn.kb.se/resolve?urn=urn:nbn:se:su:diva-179733

ISBN 978-91-7911-036-9
ISBN 978-91-7911-037-6

Stockholm University

Department of Physics

Stockholm University, 106 91 Stockholm

DEVELOPMENTS FOR THE FPGA-BASED DIGITISER IN THE PANDA ELECTROMAGNETIC CALORIMETERS

Markus Preston

Stockholm
University

Developments for the FPGA-Based Digitiser in the PANDA Electromagnetic Calorimeters

Markus Preston

©Markus Preston, Stockholm University 2020

ISBN print 978-91-7911-036-9
ISBN PDF 978-91-7911-037-6

Cover art shows the interactions of 1 GeV photons in silicon, as obtained from a Geant4 (http://geant4.web.cern.ch/) Monte Carlo simulation.

Printed in Sweden by Universitetsservice US-AB, Stockholm 2020

This Thesis

This thesis summarises the work that I have done during my PhD studies as a member of the PANDA collaboration. It consists of a rather extensive three-part description of developments for the front-end electronics used in the PANDA detector, along with two papers that have come out of this work. As an overview of the contents of the different parts in this thesis is also given in Ch. 1, I will here give details about my contribution.

My Contribution

Part I of the thesis covers background material relevant for understanding Parts II, III and the papers. Part II presents studies of radiation-induced single event upsets in the FPGA used in the PANDA front-end electronics. These errors were first studied through irradiations of the FPGA, and together with colleagues from Stockholm, Uppsala and Groningen I took part in the planning and execution of four such experiments at different accelerator and neutron-source facilities. This included configuring and setting up the FPGAs for irradiation, data taking and data analysis. I took full responsibility for the data analysis and initiated the low-energy neutron irradiations which were performed at Stockholm University. The results of the experiments are presented in Ch. 6. In parallel with the experimental studies, I initiated the development of a Monte Carlo model of single event upsets in an FPGA. This model was developed solely by me, and was developed for execution on a high-performance cluster. I took responsibility for all stages of model development, testing and validation. The initial results on my work on this topic are presented in Paper I. Ch. 7 of the thesis describes how the model evolved through my work, ending with the model which is also described in Paper II. For Ch. 8, I performed additional simulations of the expected radiation field in PANDA to predict the resulting rate of single event upsets.

Part III of the thesis describes work that was performed during the last year of my PhD studies, where I turned towards studying signal-processing algorithms that could be implemented in the FPGA used in PANDA. Here, the focus was on the shashlyk calorimeter, and I obtained experimental data from tests with a prototype detector performed earlier by colleagues from Gießen and Protvino. In Ch. 9 of the thesis, potential pulse-processing methods are introduced. Ch. 10 describes a Monte Carlo model of the shashlyk calorimeter which I concieved and developed, with the aim of describing the time structure of the detector signals realistically. As in Part II of the thesis, I performed all model development, testing and validation tasks. In Ch. 11, I conceived and developed the entire VHDL algorithm, and performed extensive optimisations using logic simulation. Finally, in Ch. 12 I performed all simulation studies, including the simulation of the expected rate in PANDA. We aim to publish the work presented in Part III of the thesis.

I have written both Papers I and II myself, implementing comments and suggestions from the co-authors. Throughout my PhD studies, I have regularly presented the results from my research on these topics at international conferences, workshops and collaboration meetings.

The following papers, referred to in the text by their Roman numerals, are included in this thesis.

PAPER I: **Measurements and Simulations of Single-Event Upsets in a 28-nm FPGA**
Markus Preston, Per-Erik Tegnér, Hans Calén, Tord Johansson, Karoly Makónyi, Pawel Marciniewski, Myroslav Kavatsyuk, and Peter Schakel, *Topical Workshop on Electronics for Particle Physics*, Santa Cruz, CA, USA (2017).
DOI: https://doi.org/10.22323/1.313.0096
Reprinted as allowed under the Creative Commons "BY-NC-ND 4.0" licence (https://creativecommons.org/licenses/by-nc-nd/4.0/).

PAPER II: **Proton and Neutron Induced Single Event Upsets in FPGAs for the PANDA Experiment**
Markus Preston, Hans Calén, Tord Johansson, Myroslav Kavatsyuk, Karoly Makónyi, Pawel Marciniewski, Peter Schakel, and Per-Erik Tegnér, *Submitted for publication in IEEE Transactions on Nuclear Science* (2020).
©2020 IEEE. Reprinted, with permission (author-submitted version).

Where applicable, permission to reuse figures have been obtained from the respective copyright holders. Some of the material in Parts I and II of this thesis has been adapted, with some modifications, from my licentiate thesis:

1. **Chapter 2**. The majority of the chapter. The discussion on the theory of the strong interaction was extended somewhat.

2. **Chapter 3**. The majority of the chapter, except for Sec. 3.3, which has been added.
3. **Chapter 4**. The majority of the chapter. Since this thesis contains work on the shashlyk calorimeter, a more detailed description of this calorimeter has been added, as well as more details on the physics in electromagnetic calorimeters.
4. **Chapter 5**. The majority of the chapter, with some small modifications.
5. **Chapter 6**. The majority of the chapter, with some detail on the recalculated neutron-source intensities added.
6. **Chapter 7**. The majority of the chapter has been adapted from the licentiate thesis, but has now been extended to include the newly developed model which was not described earlier.
7. **Chapter 8**. The majority of the chapter, which has now been adapted to show the results of the final model.

Contents

List of Figures xv

List of Tables xix

Abbreviations xxi

Acknowledgements xxv

I Motivation

1 Aim of this Thesis 3

2 Physics Introduction 5
2.1 The Standard Model of Particle Physics 5
2.2 Physics of the Strong Interaction 7
2.3 The PANDA Physics Case 12

3 The PANDA Experiment 15
3.1 Facility for Antiproton and Ion Research 15
3.2 The PANDA Detector System 17
3.3 Data Acquisition 26

4 The PANDA Electromagnetic Calorimeters 31
4.1 Radiation Interaction with Matter 31
4.2 Requirements for the PANDA Calorimeters 39
4.3 Target-Spectrometer Electromagnetic Calorimeter 42
4.4 Forward-Spectrometer Electromagnetic Calorimeter 44
4.5 Front-End Digitiser 45

II Single Event Upsets in the Front-End Digitiser FPGA

5 Single Event Upsets 51

5.1 Semiconductor Devices 51
5.2 The CMOS Inverter 54
5.3 The 6-Transistor SRAM Cell 56
5.4 The Kintex-7 Configuration Memory 57
5.5 Radiation Damage in a CMOS Device 57
5.6 SEU Bit Multiplicity 63
5.7 The SEU Cross Section 64

6 Experiments 65
6.1 Experimental Setup 65
6.2 Data Analysis 70

7 Theoretical Modelling 77
7.1 Modelling Single Event Upsets 77
7.2 Geant4 Setup 80
7.3 Model 1 82
7.4 Model 2 87
7.5 Fit to Data 92
7.6 Comparison with Experimental Data 96
7.7 Discussion 97

8 Results and Discussion 101
8.1 Monoenergetic Protons and Neutrons 101
8.2 Neutron-Induced SEUs in PANDA 102
8.3 Discussion 103

III Feature Extraction for the Shashlyk Calorimeter

9 Feature Extraction 107
9.1 Energy and Timing Measurements 108
9.2 Constant-Fraction Discriminator 113
9.3 Optimal Filter 114

10 Detector Modelling 121
10.1 Prototype Tests 121
10.2 Geant4 Simulation 123
10.3 Calorimeter Response Function 126
10.4 Model Calibration 130
10.5 Signal Generation 137
10.6 Model Validation 138

11 Algorithm Development 143

11.1 Pulse-Shape Template 143
11.2 Binary-Search Constant Fraction Discriminator 144
11.3 Optimising the Filter Length 147
11.4 Pile-Up Reconstruction 148
11.5 VHDL Implementation 151
11.6 Method Validation 155
11.7 Discussion 158

12 Results and Discussion 165
12.1 Monoenergetic Photons 165
12.2 Pile-Up Reconstruction 169
12.3 Feature Extraction Under PANDA Conditions 174
12.4 Discussion 180

Sammanfattning på svenska 183

References 187

List of Figures

2.1 Feynman diagrams of quark-antiquark and three-gluon interactions 10
2.2 Coupling strength of the strong force as a function of Q 11
2.3 The charmonium spectrum 13

3.1 Overview of the FAIR facility 15
3.2 Schematic drawing of the high energy storage ring at FAIR 17
3.3 Overview of the full PANDA experiment 18
3.4 Schematic view of the PANDA data acquisition system 28

4.1 Stopping power of electrons in three different materials 34
4.2 Cross sections for different types of photon-matter interaction . . . 35
4.3 Kinetic energy of the recoil nucleus after elastic p-^{28}Si scattering . . 37
4.4 The distribution of an electromagnetic shower in lead 40
4.5 Schematic drawing of PANDA, highlighting the calorimeters . . . 42
4.6 Photograph of two PWO-II crystals 43
4.7 The forward-endcap EMC digitiser module 46
4.8 Schematic diagram of the readout chain in the forward-endcap EMC 47

5.1 The p–n junction 52
5.2 Potential difference in a p–n junction under different bias conditions 52
5.3 The two types of MOS transistors — the nMOS and the pMOS . . 54
5.4 Schematic drawing of a CMOS inverter 55
5.5 Schematic overview of a 6T SRAM cell 56
5.6 Layout of the Kintex-7 FPGA 58
5.7 Cross sections for various proton-silicon nuclear reactions 59
5.8 Charge collection by an n$^+$ node in a transistor 60
5.9 Struck drain voltage as a function of time for three LET values . . 63

6.1 Experimental setup during irradiations 66
6.2 Neutron energy spectrum at the location of the digitiser at TSL . . 68
6.3 Neutron-energy spectra for RaBe and AmBe neutron sources . . . 69
6.4 PDF corresponding to the 100-MeV proton SEU cross section . . . 74

6.5 Measured cross sections for proton-induced SEUs 75
6.6 Measured cross sections for neutron-induced SEUs 75

7.1 The RPP model 79
7.2 Geometry of the memory cell in model 1 83
7.3 A Geant4 step intersecting one of the model-1 SVs 84
7.4 Histograms of the deposited energy in one of the four model-1 SVs 85
7.5 Cross section predicted by model 1 as a function of E_{crit} and d_{SV} . . 87
7.6 Geometry of the memory cell in model 2 89
7.7 A Geant4 step intersecting one of the model-2 SVs 90
7.8 Histograms of the collected charge in one of the four model-2 SVs . 91
7.9 Cross section predicted by model 2 as a function of Q_{crit} and d_{SV} . 92
7.10 Likelihood values as a function of the model parameters 95
7.11 Posterior probability distribution of the model parameters 98
7.12 Model-determined cross sections for proton-induced SEUs 99
7.13 Model-determined cross sections for neutron-induced SEUs 99

8.1 Model-predicted energy dependence of the SEU cross sections . . . 102

9.1 Purpose of pulse-height algorithms 109
9.2 Purpose of timing algorithms 110
9.3 Purpose of pile-up recovery algorithms 112
9.4 Principle of the constant fraction discriminator 114
9.5 Principle of a finite impulse response filter 115
9.6 Principle of the feature-extraction algorithm proposed in this work 119

10.1 The 4 × 4 shashlyk prototype used during the 2014 tests 122
10.2 Examples of waveforms acquired during the 2014 tests 123
10.3 Schematic side view of a single shashlyk-calorimeter cell 124
10.4 Schematic drawing of a single shashlyk-calorimeter layer 125
10.5 Spectra of simulated energy depositions in a single cell 125
10.6 Flowchart of the calorimeter components affecting the pulse shape 126
10.7 Simulated shower shape in a cell at three incident-photon energies . 131
10.8 Fraction between energy deposition in scintillators and in whole cell 133
10.9 Simulated total energy deposition in all scintillator layers 134
10.10 Fit to one of the experimentally obtained waveforms 135
10.11 The overall scaling factor G as a function of energy deposition . . . 136
10.12 Example of a simulated event 138
10.13 Pulse-height distribution of measured and modelled signals 139
10.14 Relative energy resolution as a function of incident-photon energy 140
10.15 Time resolution as a function of energy deposition per cell 141

11.1 Fit of the lognormal function to model-generated data 144
11.2 Working principle of the binary-search CFD method 146
11.3 Time resolution as a function of the chosen OF coefficients 149
11.4 Example of a generated waveform and the chosen OF “fit range” . . 150
11.5 A generated waveform, the fitted pulse shape and the residuals . . . 151
11.6 Flowchart of the VHDL implementation 152
11.7 Relative energy resolution determined from experimental data . . 156
11.8 Relative energy resolution determined from model data 157
11.9 Time resolution determined from experimental data 158
11.10 Time resolution determined from model data 159
11.11 Time resolution determined from model data using $\sigma(T_1 - T_0)$ . . 160
11.12 Comparison between $\sigma(\Delta T)/\sqrt{2}$ and $\sigma(T_1 - T_0)$ 161
11.13 Pulse timings in two adjacent cells relative to T_0 162
11.14 Linear-CFD estimated T_1 and T_2 functions of the T_0 phase 163
11.15 Linear CFD timing as a function of the T_0 phase 164
11.16 OF timing as a function of the T_0 phase 164

12.1 Comparison of relative energy resolutions obtained by two methods 166
12.2 Comparison of time resolutions obtained by two methods 167
12.3 Detection efficiency as a function of incident-photon energy 168
12.4 Example of an event where the maximum ADC value is reached . . 169
12.5 Modelled pile-up events at different time differences 170
12.6 Pulse-height distributions for reconstructed pile-up signals 171
12.7 Timing distributions for reconstructed pile-up signals 172
12.8 Pulse height/timing when a nuisance signal arrives at Δt 173
12.9 Detection efficiency when a nuisance signal arrives at Δt 174
12.10 Expected distributions of the energy deposition per cell 175
12.11 Pulse height/timing when a PANDA nuisance signal arrives at Δt . 177
12.12 Detection efficiency when a PANDA nuisance signal arrives at Δt . 178
12.13 Pulse height/timing as a function of the average hit rate 179
12.14 Detection efficiency as a function of the average hit rate 180

List of Tables

2.1 The elementary fermions in the standard model of particle physics 6
2.2 The elementary bosons in the standard model of particle physics . 7
2.3 The six non-exotic J^{PC} quantum numbers of an $\mathrm{f}\bar{\mathrm{f}}$ system 9

3.1 Phase 1 and 2 of the PANDA target-spectrometer detectors 21
3.2 Phase 1 and 2 of the PANDA forward-spectrometer detectors . . . 24

4.1 Requirements on the EMC detectors in PANDA 41

5.1 Truth table for the CMOS inverter 55

6.1 Beam properties and number of observed errors of each type . . . 71
6.2 Probabilities for different bit multiplicities 72
6.3 Summary of the PDFs used for determining the SEU cross sections 73
6.4 Results of the experiments 74

7.1 The two possible initial-state situations in the model 86
7.2 The fitted parameters of model 1 96
7.3 The fitted parameters of model 2 96

8.1 The predicted rate of neutron induced SEUs in the forward endcap 103

11.1 Difference between the B-CFD time and the lognormal T_{L} parameter 147

12.1 Rate of hits giving an energy deposition of at least 1 MeV in one cell 175

Abbreviations

6T	6-transistor
ADC	Analogue-to-digital converter
AmBe	Americium-beryllium
APD	Avalanche photodiode
B-CFD	Binary-search constant fraction discriminator
CFD	Constant fraction discriminator
CMOS	Complementary metal-oxide semiconductor
DAQ	Data acquisition
DCFD	Digital constant-fraction discriminator
DIRC	Detection of internally reflected Čerenkov light
DPM	Dual parton model
DSP	Digital signal processing
EFT	Effective field theory
EMC	Electromagnetic calorimeter
FAIR	Facility for Antiproton and Ion Research
FEE	Front-end electronics
FIR	Finite impulse response
FPGA	Field-programmable gate array
FS	Forward spectrometer
Geant4	Geometry and Tracking 4
GEM	Gas electron multiplier
HESR	High Energy Storage Ring
HL	High luminosity

HPGe	High-purity germanium
HR	High resolution
IC	Integrated circuit
IP	Interaction point
KVI-CART	Kernfysisch Versneller Instituut — Center for Advanced Radiation Technology
LED	Leading edge discriminator
LET	Linear energy transfer
LQCD	Lattice quantum chromodynamics
MAMI	Mainzer Mikrotron
MBU	Multi-bit upset
MDT	Mini drift tube
MOS	Metal-oxide-semiconductor
MTBU	Mean time between upsets
MVD	Micro vertex detector
nMOS	n-type MOS
OF	Optimal filter
PANDA	Antiproton Annihilation at Darmstadt
PDF	Probability density function
pMOS	p-type MOS
PMT	Photomultiplier tube
PROM	Programmable read-only memory
pTP	Para-terphenyl
PWA	Partial wave analysis
PWO	Lead tungstate
QCD	Quantum chromodynamics
RaBe	Radium-beryllium
RPP	Rectangular parallelepiped
SBU	Single-bit upset
SEM	Soft Error Mitigation

SEU	Single event upset
SM	Standard model
SNR	Signal-to-noise ratio
SRAM	Static random-access memory
STT	Straw tube tracker
SV	Sensitive volume
TOF	Time of flight
TS	Target spectrometer
TSL	The Svedberg Laboratory
TTS	Transit-time spread
VPTT	Vacuum phototetrode
WLS	Wavelength-shifting

Acknowledgements

This thesis describes several years of research, and when summarising these years in written form some essence of the work is inevitably lost — neither the "heureka" moments nor the moments of frustration are given a fair representation. In a similar way, giving a fair representation of my appreciation to all the people who in different ways have been a part of this journey is not easy.

I would like to start by thanking Per-Erik Tegnér, my main supervisor. Thank you for the constant support and enlightening discussions throughout my PhD studies, and for allowing me to discover and pursue my particular research interests under your supervision. I would also like to thank my co-supervisors; Sam Silverstein and Pawel Marciniewski. Thank you, Sam, for introducing me to VHDL programming and the methods ultimately forming the basis of Part III of the thesis. Thank you, Pawel, for explaining how the PANDA front-end digitiser and the FPGA firmware works, for all the help during the preparation and execution of the irradiation tests and for the initial idea of using a tail-subtraction method for the pile-up reconstruction.

I want to thank the rest of my colleagues at the Instrumentation Physics division at Stockholm University. Special thanks go to Dirk Wölbing, Károly Makónyi, Christian Bohm and Maria Doncel Monasterio. Dirk, my office mate and fellow PANDA PhD student over the past years — sharing an office with someone very much in the same situation as myself has been very valuable. Károly, for introducing me to the calorimeter prototype in Stockholm, to Geant4 and for patient assistance during the TSL irradiations. Christian, for valuable input as my mentor and for suggestions regarding the feature-extraction algorithm. Maria, for carefully proofreading this thesis. Thanks to all others at Instrumentation Physics — Rebecca, Stefan, Katie, Anders, Fredrik, Lennart, Anders, Suhyun, Lucilio, Ansgar and Eduardo — for creating the friendly work environment I have known over the past years.

There are many others who in different ways have contributed to the work presented here. Hans Calén (Uppsala), Myroslav Kavatsyuk and Peter Schakel (Groningen) were all instrumental to the irradiations at TSL and KVI-CART. Thank you for answering my questions about the facilities and for helpful assistance during the experiments. I would also like to acknowledge the skillful accelerator staff at both facilities. For my work on the shashlyk calorimeter, I would like to acknowledge

Pavel Semenov (Protvino) and Stefan Diehl (Gießen) for providing me with data from the 2014 testbeam measurements.

Even though the work related to this thesis has occupied a great deal of my mind over the past years, there are several people outside of work who have contributed to keeping me sane. First of all, my family. Thank you for all the support even though I have probably been bad at explaining what I am *actually* doing — hopefully this thesis will provide some answers to all those questions. To my parents: thank you for teaching me to value knowledge. Thanks to all the people at "Rossen", especially the ones in (the not very accurately named) "hemgrupp söder", for encouraging words and for reminders of the important things in life. Thanks to Samuel and Andreas for being very good friends throughout these years, and for helping me sort out my thoughts when necessary.

Olivia, my dear — for you words really are not enough. Thank you for always being there for me and for sharing your life with me. I do not know how my life would be without you in it.

Soli Deo Gloria

PART I

MOTIVATION

1. Aim of this Thesis

This thesis concerns developments for detector electronics in PANDA, an upcoming experiment aimed at studying various aspects of strongly interacting matter. In particular, the aim of this work has been to study two aspects of the operation of the front-end digitiser module developed for the PANDA electromagnetic calorimeters (EMCs): 1) how well it will handle the high levels of radiation present in the experiment and 2) with what accuracy it can determine key features of incoming detector signals in the high-rate conditions of the experiment. Understanding these topics is especially important in PANDA, where the data-acquisition system will rely heavily on intelligent front-end electronics.

This thesis is divided into three parts. Part I provides a brief motivation of the PANDA physics programme and introduces the various subdetectors in the experiment, with a special emphasis on the EMCs. Along with this more thorough description of the EMCs, the last chapter of this part also covers relevant mechanisms for radiation-matter interaction, something that is important for understanding Parts II and III of thesis.

Part II of the thesis describes a study of single event upsets (SEUs), a type of errors in microelectronics where radiation causes a change in the state of the device. In this thesis, the susceptibility of the field-programmable gate arrays (FPGAs) used in the EMC front-end digitisers has been studied through experiments and theoretical modelling. The work presented here has been aimed at studying the energy dependence of the probability for proton- and neutron-induced SEUs in the FPGA that will be used in PANDA. Ch. 6 describes results from irradiations of the device using high-energy proton and neutron beams as well as low-energy neutron sources. To gain further understanding on the risk of SEUs during operation of PANDA, a Monte Carlo model of SEUs has been developed as part of this thesis work. The process of developing this model has gone through several stages. Paper I describes an early version of the model, which did not fit within the scope of this thesis. The two main stages of the model development are presented in Ch. 7 together with a description of how the model was fitted and compared to our experimental data. The final version of this model is also the topic of Paper II, which has been submitted for publication. Results from model predictions of the SEU rate in PANDA, based on additional simulations of the radiation field in PANDA, are given in Ch. 8.

The final part of this thesis, Part III, describes work done on the FPGA firmware for the EMC digitiser. In particular, the focus has been on the read-out of the shashlyk calorimeter, a detector which is developed to cover the most forward region in the PANDA experiment, resulting in high hit rates from particles. In accordance with the data-acquisition scheme planned for PANDA, the FPGA-based digitisers should analyse incoming detector signals in real time and extract information of interest, such as pulse height and timing information. This is a scheme known as *feature extraction*. Because of this high hit rate, there is a risk for pile-up events, where two consecutive detector signals overlap in time. Instead of rejecting such events, which would decrease the efficiency of the detector system, the aim is to reconstruct them. This poses a challenge for the real-time nature of the triggering and data acquisition system, and new methods have to be considered. In Ch. 9, a general overview of feature-extraction methods is given, with some additional details on the main algorithms used in Part III of the thesis. In order to develop and evaluate a feature-extraction method, a detailed Monte Carlo model of the shashlyk calorimeter has been developed. This model, which is the focus of Ch. 10, makes it possible to generate realistic detector signals that incorporate fluctuations in time and amplitude due to the detector geometry and read-out. Ch. 11 describes the development of an FPGA-based algorithm for real-time pulse height and time determination under high-rate conditions, and how it was validated against experimental data. Finally, Ch. 12 describes the performance of the developed algorithm both in terms of energy and time resolution and pile-up reconstruction ability. In this chapter, simulations of the conditions in PANDA are used to make predictions about the final performance of the algorithm. The contents of Part III of this thesis will be the topic of a future publication.

2. Physics Introduction

The strong interaction is one of the fundamental forces of nature, and acts between quarks and gluons — two types of elementary particles — to form composite objects known as hadrons. The proton and the neutron are hadrons, and thus an understanding of the strong force is important in order to understand the fundamental structure of the atomic nucleus.

The strong interaction is described theoretically by quantum chromodynamics (QCD), which however is not well understood at low energies, i.e. on the scale of atomic nuclei. Theoretical frameworks aimed at describing low-energy QCD exist, but experimental data is needed both as input to the models and to validate the theoretical predictions.

PANDA (Antiproton Annihilation at Darmstadt) [1] is one of the four experimental pillars of the Facility for Antiproton and Ion Research (FAIR) [2] in Darmstadt, Germany. In PANDA, an antiproton beam accelerated to a momentum between 1.5 GeV/*c* and 15 GeV/*c* will interact in a hydrogen, or possibly heavier, target, giving access to a number of different physics channels of interest when probing the low-energy regime of QCD.

2.1 The Standard Model of Particle Physics

The standard model (SM) of particle physics is used to describe the fundamental constituents of matter and the interactions that govern their behaviour. A particle has a number of intrinsic properties such as mass, electric charge and spin. Particles may be categorised according to their spin — half-integer spin particles are called *fermions* and integer spin particles are called *bosons*. Categorising particles in this way is useful because fermions obey the Pauli exclusion principle[1], while bosons do not. Thus, the spin of a particle gives information about how the particle behaves in a multi-particle system. While the theoretical framework of the SM has been very successful so far, there are still a number of open questions not fully explained by it. For instance, a quantum-mechanical description of gravity is still lacking, which would be needed to describe all known fundamental interactions within the SM.

There are both fermions and bosons among the elementary particles in the SM.

---

[1] The Pauli exclusion principle states that two identical fermions in a system cannot both occupy the same quantum state at the same time.

The SM fermions, listed in Tab. 2.1, are subdivided into quarks and leptons. The SM bosons, listed in Tab. 2.2, are subdivided into gauge bosons and scalar bosons.

Table 2.1: The elementary fermions in the SM of particle physics. Data taken from [3].

Name	Charge (e)	Mass (MeV/c^2)	Spin	Parity eigenvalue
Quarks				
Up (u)	2/3	2.16*	1/2	+1
Down (d)	-1/3	4.67*	1/2	+1
Charm (c)	2/3	1270*	1/2	+1
Strange (s)	-1/3	93*	1/2	+1
Top (t)	2/3	172900*	1/2	+1
Bottom (b)	-1/3	4180*	1/2	+1
Leptons				
Electron (e)	-1	0.511	1/2	+1
Electron neutrino (ν_e)	0	$< 2 \cdot 10^{-6}$	1/2	+1
Muon (μ)	-1	105.66	1/2	+1
Muon neutrino (ν_μ)	0	< 0.19	1/2	+1
Tau (τ)	-1	1776.9	1/2	+1
Tau neutrino (ν_τ)	0	< 18.2	1/2	+1

* The bare-quark mass.

Quarks exist in six different flavours — up, down, charm, strange, top and bottom. Each quark has a corresponding antiquark. Composite particles known as hadrons are formed by combining two or more quarks or antiquarks. Two examples of hadrons are the proton (consisting of two up quarks and one down quark) and the neutron (consisting of one up quark and two down quarks), which are the building blocks of the atomic nucleus.

Leptons also exist in six flavours — the electron, muon and tau and their associated neutrinos: the electron neutrino, the muon neutrino and the tau neutrino. As with the quarks, there are antiparticles associated with all of the leptons.

Gauge bosons are vector bosons and have a spin equal to one. The SM gauge bosons mediate the fundamental interactions between particles — the gluon mediates the strong interaction, the photon mediates the electromagnetic interaction and the Z and W bosons mediate the weak interaction.

Scalar bosons have a spin equal to zero. In the SM, there is only one scalar boson: the Higgs boson. The Higgs boson mediates the Higgs mechanism, whereby only the SM particles coupling to the Higgs boson have mass.

Table 2.2: The elementary bosons in the SM of particle physics. Data taken from [3].

Name	Charge (e)	Mass (MeV/c^2)	Spin	Parity eigenvalue
Gauge bosons				
Gluon (g)	0	0	1	-1
Photon (γ)	0	0	1	-1
Z boson (Z)	0	91190	1	N/A
W boson ($W^{\pm}$)	±1	80380	1	N/A
Scalar boson				
Higgs boson (H^0)	0	125100	0	+1

2.2 Physics of the Strong Interaction

A system of quarks and gluons, bound together by the strong force, is known as a *hadron*. As any particle in quantum mechanics, a hadron is fundamentally described by its state vector $|\psi\rangle$, which can be a product of several components; a spatial part $|\psi_{\text{space}}\rangle$, a spin part $|\psi_{\text{spin}}\rangle$, a flavour part $|\psi_{\text{flavour}}\rangle$ and a colour part $|\psi_{\text{colour}}\rangle$:

$$|\psi\rangle = |\psi_{\text{space}}\rangle\,|\psi_{\text{spin}}\rangle\,|\psi_{\text{flavour}}\rangle\,|\psi_{\text{colour}}\rangle\,, \tag{2.1}$$

or a linear combination of such states.

The main difference between a fermion and a boson is that the fermion has half-integer spin, while the boson has integer spin. The Pauli principle states that two identical fermions in a system can not both occupy the exact same quantum state. In terms of $|\psi\rangle$, this means that the state of a boson is symmetric under the exchange of two identical particles, while the state of a fermion *must be* antisymmetric under the same exchange. That is, if the space, flavour and colour parts for a fermion are all symmetric under this exchange, the spin part must be antisymmetric, and so on. For a hadron, which is a system of fermions, the constituent-quark states have to be antisymmetric with respect to each other even if the hadron itself is a boson.

One may consider the quantum mechanics of a system containing a fermion and its antifermion, i. e. $|\mathrm{f\bar{f}}\rangle$. The physics of such a system has implications for PANDA because it describes both the primary $\mathrm{\bar{p}p}$ interaction, as well as several of the bound particles which will be produced and studied in the experiment.

2.2.1 Spin and the J^{PC} Quantum Numbers

The spin state of $|\mathrm{f\bar{f}}\rangle$ may be written

$$|\psi_{\text{spin}}\rangle = |\mathrm{f\bar{f}}; S, m_S\rangle\,, \tag{2.2}$$

where S is the total spin quantum number of the system and m_S is the z-projection of S. For a single fermion or antifermion, $S = 1/2$ and the spin state is either $|1/2, 1/2\rangle$ or $|1/2, -1/2\rangle$. When forming a fermion-antifermion system, the spins can combine into four different states. Three of them — the triplet — are symmetric and have a total spin of $S = 1$:

$$\begin{aligned} |1, 1\rangle &= |\uparrow_{\mathrm{f}}\rangle\, |\uparrow_{\bar{\mathrm{f}}}\rangle\,, \\ |1, 0\rangle &= (|\uparrow_{\mathrm{f}}\rangle\, |\downarrow_{\bar{\mathrm{f}}}\rangle + |\downarrow_{\mathrm{f}}\rangle\, |\uparrow_{\bar{\mathrm{f}}}\rangle)/\sqrt{2}, \\ |1, -1\rangle &= |\downarrow_{\mathrm{f}}\rangle\, |\downarrow_{\bar{\mathrm{f}}}\rangle\,. \end{aligned} \tag{2.3}$$

The fourth combination has a total spin of $S = 0$, is antisymmetric, and is called the singlet:

$$|0, 0\rangle = (|\uparrow_{\mathrm{f}}\rangle\, |\downarrow_{\bar{\mathrm{f}}}\rangle - |\downarrow_{\mathrm{f}}\rangle\, |\uparrow_{\bar{\mathrm{f}}}\rangle)/\sqrt{2}. \tag{2.4}$$

In addition to the spin component of the angular momentum, the fermion-antifermion system also has a relative orbital angular momentum L. When these two are added, the total angular momentum J of the system is obtained:

$$J = |L - S|, |L - S + 1|, \cdots, |L + S|. \tag{2.5}$$

In addition, the state of the system can be characterised by the parity and C-parity quantum numbers — the eigenvalues of the parity and charge conjugation operators acting on the system. The parity operator reflects the spatial coordinates through the origin, and the charge conjugation operator changes the signs of all quantum charges (e.g. electric charge, baryon number, lepton number, strangeness) of the system. For the $\mathrm{f\bar{f}}$ system, the quantum numbers P and C are given by S and L:

$$P = (-1)^{L+1}, \tag{2.6}$$

$$C = (-1)^{L+S}. \tag{2.7}$$

These rules determine which quantum-number combinations are allowed for a pure $\mathrm{f\bar{f}}$ system — the non-exotic quantum numbers, shown in Tab. 2.3.

2.2.2 Colour Charge

The method of combining individual spins to form the full spin state of the system may be used for the colour state as well. A quark has one associated colour; red (r), green (g) or blue (b), while an antiquark has one associated anticolour; antired ($\bar{\mathrm{r}}$), antigreen ($\bar{\mathrm{g}}$) or antiblue ($\bar{\mathrm{b}}$). Therefore, there are nine possible colour combinations

Table 2.3: The six non-exotic J^{PC} quantum numbers of an $\mathrm{f\bar{f}}$ system with $L \leq 1$. The complementary $^{2S+1}L_J$ notation is also shown.

L	S	J	P	C	J^{PC}	$^{2S+1}L_J$
0	0	0	-1	+1	0^{-+}	$^1\mathrm{S}_0$
0	1	1	-1	-1	1^{--}	$^3\mathrm{S}_1$
1	0	1	+1	-1	1^{+-}	$^1\mathrm{P}_1$
1	1	0	+1	+1	0^{++}	$^3\mathrm{P}_0$
1	1	1	+1	+1	1^{++}	$^3\mathrm{P}_1$
1	1	2	+1	+1	2^{++}	$^3\mathrm{P}_2$

for a fermion-antifermion system, eight of which constitute an asymmetric colour octet, and one which is a symmetric colour singlet. As of yet only colour-singlet particles have been observed — which for $|\mathrm{f\bar{f}}\rangle$ corresponds to the following colour state, symmetric under the interchange of the two particles:

$$\frac{1}{\sqrt{3}}(|\mathrm{r_f}\rangle\,|\mathrm{\bar{r}_{\bar{f}}}\rangle + |\mathrm{g_f}\rangle\,|\mathrm{\bar{g}_{\bar{f}}}\rangle + |\mathrm{b_f}\rangle\,|\mathrm{\bar{b}_{\bar{f}}}\rangle). \tag{2.8}$$

One important feature of the strong interaction is that the associated gauge boson — the gluon — itself carries colour charge. In the electromagnetic interaction, for example, the photon does not carry electric charge and does not self-interact. The fact that gluons are able to interact directly, or couple, with other gluons has major consequences for the behaviour of the strong interaction, and leads to the unique concepts of colour confinement [4] and asymptotic freedom [5, 6] in QCD. Fig. 2.1 shows Feynman diagrams depicting, to first order, the interactions between a quark and an antiquark and the direct interaction between three gluons.

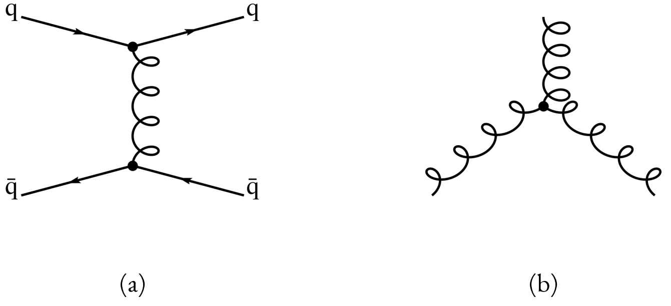

Figure 2.1: Feynman diagrams of (a) a quark-antiquark interaction mediated by a single gluon and (b) a three-gluon interaction depicting gluon self-coupling to first order.

Colour confinement means that only objects which are colour-neutral can be directly observed under normal conditions. As a consequence, it is impossible to isolate individual quarks or gluons, which by themselves are not colour-neutral. Instead, these particles are always considered as constituents of colour-neutral hadrons. A colour-neutral object may be formed in different ways: by combining all three colours (or all three anti-colours), or by combining a colour with its anti-colour (as described above). The requirement of colour neutrality means that only certain combinations of quarks and antiquarks are allowed in QCD. The original quark model includes *baryons* (hadrons consisting of three quarks), *anti-baryons* (hadrons consisting of three anti-quarks) and *mesons* (hadrons consisting of one quark and one anti-quark). Other combinations of quarks and gluons, so-called exotic hadrons, are allowed in QCD but have proven to be much more difficult to discover. Examples of exotic hadrons are tetraquarks (two quarks and two anti-quarks), pentaquarks (four quarks and one anti-quark) [7, 8], and glueballs (a bound state consisting only of gluons) [9].

The origin of colour confinement is in QCD described as an effect of the self-coupling of gluons. Had the force between a quark and an antiquark been purely electromagnetic, one could separate the particles by increasing the distance between them. However, as these are strongly interacting particles, the force between them is governed by a gluon field which due to self-coupling grows in strength as the quark-antiquark distance is increased. To separate two quarks would therefore require an infinite amount of energy, meaning that they are confined to colour-neutral objects. In fact, if enough energy is supplied to the system, a new quark-antiquark pair is produced such that the final state will consist of two colour-neutral hadrons.

2.2.3 The QCD Running Coupling

The strength of the strong interaction is described by the QCD coupling constant α_s, which determines the strength of the coupling between quarks and the gluon field. The value of α_s has been probed through a number of different experiments, which has shown that it is in fact not a constant but depends on the energy scale involved. In Fig. 2.2, a summary of measurements of α_s is shown as a function of the momentum transfer Q.

At high momentum transfer, i. e. when the interacting quarks are close to each other, the strength of the strong interaction decreases. In this regime, when $Q \gtrsim 1$ GeV/c, the quarks may be treated as approximately free particles and calculations may be performed using perturbative QCD. The fact that the quarks may be treated more and more as free particles as the momentum transfer is increased is known as *asymptotic freedom* in QCD.

The theory of perturbative QCD has been successfully applied in the analysis of data from high-energy physics experiments such as the ones at the Large Hadron

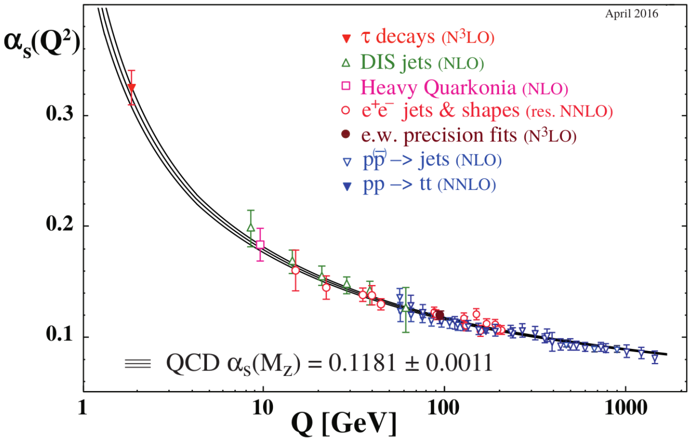

Figure 2.2: Coupling strength of the strong force as a function of the momentum transfer Q. Figure taken from [3].

Collider at CERN [3]. Due to the peculiar nature of the strong interaction, it is however not possible to apply the same methods when $Q \lesssim 1\,\mathrm{GeV}/c$. Lower momentum-transfer scales correspond to larger separations between quarks, which for example is the case in bound hadrons. As discussed in Sec. 2.2.2, increasing the separation between two quarks strengthens the gluon field present between them due to gluon self-coupling. This is confirmed by the fact that the coupling constant α_s increases at low Q as shown in Fig. 2.2. The non-perturbative regime of QCD corresponds to the distance scale of hadrons, which makes understanding it vital in order to understand hadrons. The theoretical approaches to describe such systems generally fall within one of two categories:

- **Lattice QCD** (LQCD) [10] is an ab initio description of non-perturbative QCD. In LQCD, the equations of motion for the quarks and gluons are discretised on a lattice and solved through numerical simulations.

- **Effective field theories** (EFTs) [11] utilise the symmetries of QCD. In an EFT where quarks and gluons are the relevant degrees of freedom, one can simplify calculations when some of the quarks of the system are (relatively) heavy — i. e. the c, b and t quarks. This is due to the fact that such systems may at least partly be treated non-relativistically.

In many cases, a combination of the above methods is used. However, input of parameters from experimental data is often needed to accurately solve the resulting models. Here, PANDA will be able to provide valuable information about many different hadronic systems, and thus give more insight into non-perturbative QCD.

2.3 The PANDA Physics Case

In many collider experiments aimed at studying non-perturbative QCD, colliding beams of e^+ and e^- are used [12–14]. The resulting interaction is an electromagnetic process. However, to the first order, the annihilation of these two particles results in the production of one virtual photon from which other particles may be produced. A photon has the quantum numbers $J^{PC} = 1^{--}$, which means that the total quantum numbers of the produced particles must be $J^{PC} = 1^{--}$. The production of states with other quantum numbers is possible, but is highly suppressed due to the need for multiple-photon exchange.

In $\bar{p}p$ collisions, however, virtual gluons are produced. Due to the properties of the strong interaction, the probability for multiple-gluon exchange is not lower than it is for single-gluon exchange. Thus, the hadronic nature of the $\bar{p}p$ interaction gives direct access to final states with the same J^{PC} quantum numbers as the $\bar{p}p$ system — i. e. all non-exotic combinations for a $f\bar{f}$ system, shown in Tab. 2.3. When looking at a single particle in the final state, it can have *any* quantum numbers, provided that the other particles in the final state carry the remaining quantum numbers. Therefore, PANDA will give unique access to multiple areas of research related to QCD and the strong interaction: QCD bound states, dynamics of non-perturbative QCD, hadrons in nuclear matter, hypernuclear physics, electromagnetic processes, and electroweak physics. One topic of interest is charmonium spectroscopy, which is described in more detail below.

2.3.1 Charmonium Spectroscopy

A meson consisting of $c\bar{c}$ — a charm quark and a charm antiquark — is commonly referred to as charmonium. The name is similar to that of positronium, which is a bound state of an electron and a positron. Except for the fact that the energy scale of positronium is much lower, the two systems have many properties in common. The first charmonium system to be discovered was the 1^{--} J/ψ meson, which was discovered almost simultaneously via e^-e^+ collisions at SLAC [15] and via proton-beryllium collisions at Brookhaven [16] in 1974, which sparked the so-called November Revolution in particle physics.

Like positronium, the states of $c\bar{c}$ can be characterised by their quantum numbers J^{PC}. Because of the similarities between these two systems, the spectrum of energy states in charmonium very much resembles the one for positronium. The spectrum of charmonium states is shown in Fig. 2.3.

A full theoretical treatment of a charmonium system relies on non-perturbative QCD, and thus entails lengthy calculations. However, due to the relatively high mass of the charm quark ($m_c \sim 1.3$ GeV/c^2), the $c\bar{c}$ system may be treated non-relativistically to a first approximation. In such a treatment, the charm-anticharm

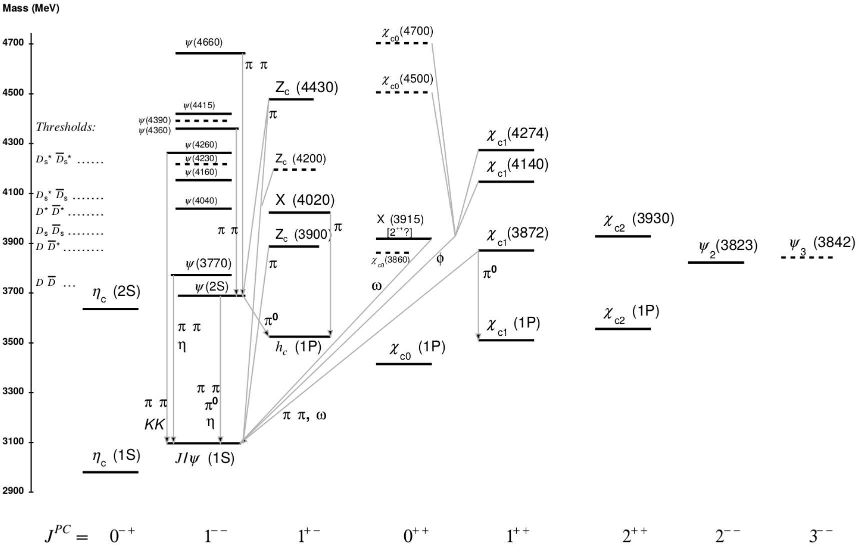
Mass (MeV)
4700
4500
4300
4100
3900
3700
3500
3300
3100
2900
Thresholds:
$D_s^* \bar{D}_s^*$
$D_s^* \bar{D}_s$
$D^* \bar{D}^*$
$D_s \bar{D}_s$
$D \bar{D}^*$
$D \bar{D}$
η_c (2S)
η_c (1S)
ψ(4660)
ψ(4415)
ψ(4390)
ψ(4360)
ψ(4260)
ψ(4230)
ψ(4160)
ψ(4040)
ψ(3770)
ψ(2S)
J/ψ (1S)
Z_c (4430)
Z_c (4200)
X (4020)
Z_c (3900)
h_c (1P)
χ_{c0}(4700)
χ_{c0}(4500)
X (3915)
[2⁺⁺?]
χ_{c0}(3860)
χ_{c0} (1P)
χ_{c1}(4274)
χ_{c1}(4140)
χ_{c1}(3872)
χ_{c1} (1P)
χ_{c2} (3930)
χ_{c2} (1P)
ψ_2(3823)
ψ_3 (3842)
π π
π
π π
η
π π
KK
π^0
ω
φ
π π, ω
J^{PC} =
0^{-+}
1^{--}
1^{+-}
0^{++}
1^{++}
2^{++}
2^{--}
3^{--}

Figure 2.3: The charmonium spectrum, ordered according to J^{PC} quantum numbers and mass. Hadronic transitions between different states are shown, whereas single-photon transitions (e. g. $\chi_{c1} \to J/\psi\,\gamma$) are not. Figure taken from [3].

potential contains a Coulomb-like term, a linear term, a hyperfine spin-spin term, a spin-orbit term and a tensor-interaction term [17]:

$$V(r) = -\frac{4}{3}\frac{\alpha_s}{r} + br + \frac{32\pi\alpha_s}{9m_c^2}\widetilde{\delta}_\sigma(r)\cdot S_c\cdot S_{\bar{c}} + \frac{1}{m_c^2}\left[\left(\frac{2\alpha_s}{r^3} - \frac{b}{2r}\right)L\cdot S + \frac{4\alpha_s}{r^3}T\right], \quad (2.9)$$

where the parameters α_s, b, m_c and $\widetilde{\delta}_\sigma$ are determined by fitting the potential to experimental data. Here, it is seen that the strength of the potential at short distances directly depends on the strong coupling constant, α_s. Although this potential model very clearly indicates the different components of the potential, such a model is not able to explain the whole charmonium spectrum, which means that more advanced methods relying on LQCD or EFTs are needed.

In PANDA, all charmonium states can be formed directly in the $\bar{p}p$ annihilation, but the detectors will not detect these states themselves but instead the particles resulting from their decays. In order to determine which angular-momentum states were actually produced in the $\bar{p}p$ interaction, the partial wave analysis (PWA) technique will be employed. In PWA, different decay modes are fit to the experimental data to determine which states were produced. A common feature of many of the charmonium decay channels is a final state with multiple electrons, positrons and photons, all of which should ideally be detected in order to facilitate a PWA.

Example: Investigating the χ_{c1}(3872) State in PANDA

In 2003, a state with an unusually long lifetime above the $D\overline{D}$ threshold was discovered at the Belle experiment in Japan [18]. It was suggested that the particle is a standard meson. However, the observed decay modes which for a meson would mean strong violations of quantum-number conservation rules suggests that the particle is more complex. This state has been named χ_{c1}(3872)[1], and with a mass of 3872 MeV/c^2 lies above the threshold for breakup of charmonium into a $D\overline{D}$ meson-antimeson pair at 3730 MeV/c^2. There are a number of proposed structures describing this state: some suggest that it is a charmonium state [19], while some suggest that it is a four-quark state[2] of some kind [21]. It is clear that further experimental study on this state is needed, which PANDA will be capable of doing. In particular, experiments at PANDA could be aimed at determining the lifetime of this state (or equivalently its width) [22], as the different models describing the exact nature of the state predict different lifetimes. The most probable decay of χ_{c1}(3872) is into a J/ψ meson and two π mesons:

$$\chi_{c1}(3872) \rightarrow J/\psi + \pi^+ + \pi^-, \tag{2.10}$$

where the J/ψ subsequently decays into a lepton pair (e.g. e^-e^+), and the π mesons decay into lepton pairs. It is therefore very important to be able to detect the final state leptons, which is the purpose of the EMC in PANDA. The particles may be distinguished from each other by analysing the shape of the resulting electromagnetic showers in the EMC [23].

---

[1] The χ_{c1}(3872) state is also known as X(3872), but here the naming convention of the 2019 update of the Review of Particle Physics [3] is used.

[2] Such a four-quark, or tetraquark, system could either consist of four quarks directly bound together or of two quark-antiquark systems bound together into a "molecule" [20].

3. The PANDA Experiment

PANDA [1] is one of the four experimental pillars of the upcoming FAIR facility in Darmstadt, Germany. In PANDA, antiprotons with momenta between 1.5 GeV/c and 15 GeV/c will interact in a fixed hydrogen or nuclear target. The maximum luminosity will be $2 \cdot 10^{32}$ cm^{-2} s^{-1}, and the optimal beam momentum spread will be $\Delta p/p \sim 10^{-5}$.

3.1 Facility for Antiproton and Ion Research

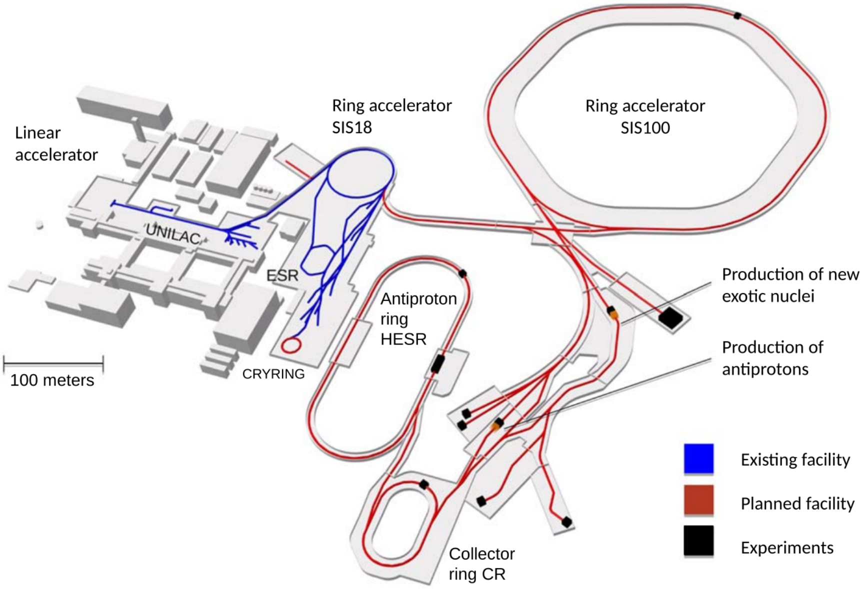
Linear accelerator
Ring accelerator SIS18
Ring accelerator SIS100
UNILAC
ESR
Antiproton ring HESR
CRYRING
100 meters
Production of new exotic nuclei
Production of antiprotons
Collector ring CR
Existing facility
Planned facility
Experiments

Figure 3.1: Overview of the FAIR facility. The first stages of the accelerator system are located in the already existing GSI facility, shown in blue. The new part of FAIR, which includes PANDA, is shown in red. Figure taken from [24].

FAIR is currently being constructed as an extension of the already existing GSI facility in Darmstadt, Germany. An overview of GSI and FAIR is shown in Fig. 3.1, where it can be seen that parts of GSI will serve as a beam injector for FAIR. During initial operation of FAIR, the antiprotons for use in PANDA will be produced as follows [25, 26]:

1. Protons are generated by an electron cyclotron resonance source, and accelerated to an energy of 70 MeV in the p-LINAC linear accelerator.

2. The protons from the p-LINAC are injected into the SIS18 synchrotron, where they are accelerated to 4 GeV.

3. The 4-GeV protons are injected into the SIS100 synchrotron, where they are accelerated to 29 GeV.

4. The 29-GeV protons are directed into a nickel and aluminium target, where up to 10^7 antiprotons per second, are produced in nuclear reactions.

5. The antiprotons are collected and pre-cooled in the Collector Ring. Due to the magnet settings at the interface between the antiproton-production target and the Collector Ring, the antiproton energy is 3 GeV at this stage.

6. The antiprotons are injected into the High Energy Storage Ring (HESR) [27], until it contains 10^{10} antiprotons. The antiprotons in the HESR can be decelerated or accelerated to energies between 0.8 GeV and 14 GeV, corresponding to momenta between 1.5 GeV/c and 15 GeV/c.

3.1.1 High Energy Storage Ring

The HESR (shown in Fig. 3.2) is a storage ring and accelerator for antiprotons, with a total circumference of 575 m. It directs an antiproton beam with a momentum between 1.5 GeV/c and 15 GeV/c through the PANDA detector system. After installation of all detectors in PANDA, the accelerator will be able to operate in two modes: the high-resolution (HR) and high-luminosity (HL) modes.

- In the HR mode, 10^{10} antiprotons circulate in the ring. This relatively low number of particles allows a very small rms-relative spread in momentum — below $4 \cdot 10^{-5}$.

- In the HL mode, 10^{11} antiprotons circulate in the ring. The beam momentum in the HL mode can be set between 1.5 GeV/c and 15 GeV/c, with a spread in momentum around 10^{-4}. The advantage of the HL mode is the higher luminosity, coming as a direct result of the larger number of particles stored in the ring.

As shown in Fig. 3.2, PANDA is situated on one of the straight sections of the HESR. The KOALA experiment [28], which will allow accurate measurements of antiproton-proton elastic scattering needed to properly normalise luminosity measurements in PANDA, is situated on the opposite straight section. In addition, the HESR could also be used in other experiments, such as the atomic-physics experiment SPARC [29].

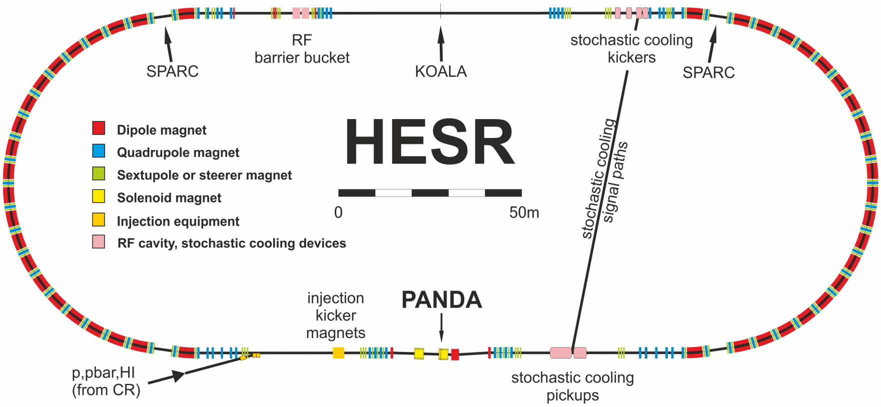
SPARC
RF
barrier bucket
KOALA
stochastic cooling
kickers
SPARC
HESR
Dipole magnet
Quadrupole magnet
Sextupole or steerer magnet
Solenoid magnet
Injection equipment
RF cavity, stochastic cooling devices
0
50m
stochastic cooling
signal paths
injection
kicker
magnets
PANDA
p,pbar,HI
(from CR)
stochastic cooling
pickups

Figure 3.2: Schematic drawing of the HESR at FAIR. PANDA is situated on one of the straight sections of the ring. The locations of the KOALA and SPARC experiments, discussed in the main text, are also shown. Figure taken from [30].

The very low spread in momentum is accomplished through stochastic and electron cooling [31]. The mean beam lifetime[1] at the HESR is expected to be between 1540 s and 7100 s [32]. Since hadronic collisions and Coulomb scattering are among the primary sources of beam loss, the lifetime of the beam strongly depends on the beam energy and target type.

The initial phase of HESR operations is known as phase 1 (P1), during which not all detectors in PANDA will be available as explained below. During P1, the beam luminosity is expected to be lower than during both the HR and HL modes, and the beam-momentum spread is expected to be between the values expected in the HR and HL modes [22]. For the HL mode, further accelerator infrastructure is needed to provide accumulation of antiprotons before they are injected into the HESR [22].

3.2 The PANDA Detector System

In PANDA, antiprotons in the HESR interact in a fixed hydrogen or nuclear target. Due to the fixed-target nature of the interaction, there can be a high boost of reaction products in the forward direction.

---

[1] The mean lifetime of the beam is defined as the time after which the beam intensity is $1/e$ of its original value.

PANDA is divided into two subsystems: the target spectrometer (TS) and the forward spectrometer (FS). Both work as magnetic spectrometers, where the TS contains a solenoid magnet and the FS contains a dipole magnet. The TS surrounds the interaction point (IP) of the experiment, while the FS enables detection of the most forward-boosted reaction products coming from the interactions.

The target is produced in a target source that is embedded in the yoke of the TS solenoid, after which it is pumped through a pipe which is installed perpendicular to the $\overline{\mathrm{p}}$ beam pipe. The location of the crossing of the target pipe and the beam pipe, at which the $\overline{\mathrm{p}}\mathrm{p}$ interaction occurs, defines the PANDA IP.

The detectors in PANDA are installed inside or in connection to the two spectrometer magnets. These detectors perform tracking, identification and calorimetry of the particles produced at the IP. Operation of PANDA will be divided into multiple phases, which are related to the HESR P1, HR and HL modes. During *phase 1* of the experiment, the majority of the detector systems will be installed and used in measurements, expected to commence in 2025. In *phase 2* of the experiment, the remaining detectors will have been installed and the HESR may have been upgraded to enable the HR mode. Subsequent phases of operation (*phase 3* and onwards) rely on the HL mode of the HESR.

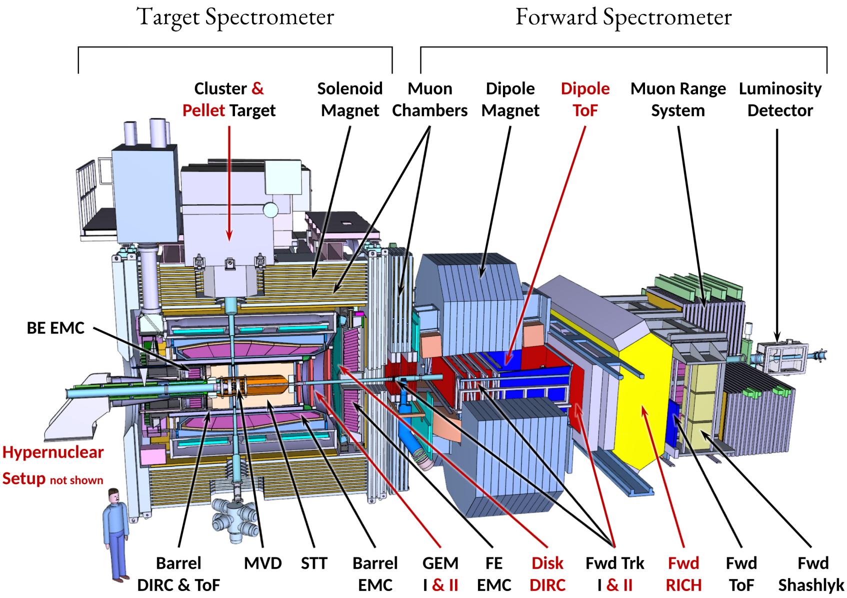
Target Spectrometer
Forward Spectrometer
Cluster & Pellet Target
Solenoid Magnet
Muon Chambers
Dipole Magnet
Dipole ToF
Muon Range System
Luminosity Detector
BE EMC
Hypernuclear Setup not shown
Barrel DIRC & ToF
MVD
STT
Barrel EMC
GEM I & II
FE EMC
Disk DIRC
Fwd Trk I & II
Fwd RICH
Fwd ToF
Fwd Shashlyk

Figure 3.3: An overview of the full PANDA experiment, including the detectors of both phase 1 and phase 2. Figure modified from [30].

3.2.1 Magnets

Solenoid Magnet

The TS consists of a solenoid magnet [33] with a length of approximately 4 m and an inner diameter of 1.9 m. A number of detectors used for tracking, particle identification and calorimetry are placed inside the magnet. To enable the required particle-tracking accuracy in the region closest to the IP, the solenoid provides a very homogeneous magnetic field of 2 T in the central region of the TS. In order to reach these specifications, the coil of the solenoid is superconducting.

In PANDA, the target is produced in a station located on top of the TS (as described in Sec. 3.2.2) and pumped through the TS from top to bottom, intersecting the IP. In order to accommodate the target pipe and still allow good field homogeneity, the solenoid coil is divided into three parts. Also, the iron yoke of the solenoid is segmented into 13 layers, with interleaving layers of mini drift tubes (MDTs) used for muon detection.

Dipole Magnet

The FS consists of a dipole magnet [33] providing a field integral of 2 Tm. It is located approximately 3.5 m downstream of the IP and has an aperture of approximately 1×3 m^2, in which a number of detector systems are located. The provided field integral makes it possible to reconstruct particle momenta at a precision of 1%.

3.2.2 Targets

Due to the wide physics program of PANDA, different target systems [34] are used. Two hydrogen-target systems, the cluster-jet target and the pellet target, are currently under development. Both target-production stations may be installed at the top of the TS, as indicated in Fig. 3.3. The target-production station produces the target, which falls through the target pipe, going through the yoke of the TS solenoid and intersecting the IP. Both target stations are able to produce hydrogen targets with an effective thickness of up to $4 \cdot 10^{15}$ atoms per cm^2, which meets the PANDA luminosity requirement. Also, both techniques allow the production of very pure targets — a requirement since contamination from other elements would result in unwanted background reactions. After crossing the IP, the target stream is pumped away at the bottom of the TS.

In phase 1 of PANDA, the cluster-jet target will be used. During phase 2 of PANDA operation, also the pellet target will be employed, allowing for a higher luminosity [34]. In addition, phase 2 will include the use of targets containing nuclei heavier than hydrogen, in experiments where $\bar{p}A$ reactions are required.

Cluster Jet Target

In this context, a hydrogen cluster is a nanoparticle formed when H_2 gas, cooled down to around 10 K, passes into vacuum through a nozzle. This produces both a supersonic beam of gas and, under the right conditions, hydrogen clusters with a sub-μm diameter. The exact velocity and shape of these clusters depend on the properties of the H_2 gas, as well as on the properties of the nozzle. The transversal diameter of the cluster-target stream is 4 mm, whereas the longitudinal diameter is 12 mm [35].

A cluster-jet target has a very homogeneous target density, which eliminates any time structures in the luminosity. In a storage-ring experiment this is very valuable since it ensures that the luminosity will not vary due to unintended variations in the target density. The density can be adjusted on a time scale of seconds or minutes, so that it can be tuned during an experiment.

Pellet Target

The pellet target is used to produce frozen hydrogen droplets, or pellets, which have a diameter of the order of μm. They are formed by injecting cryogenic liquid — H_2 in the case of a hydrogen target — into a gas of the same type as the liquid through an oscillating nozzle. Being close to triple-point condition, the jet breaks up into pellets due to the nozzle oscillations. The pellets then form a stream, with properties determined by the operational settings of the pellet source.

A pellet tracking system, which allows accurate position tracking of individual pellets and therefore vertex reconstruction with a sub-millimetre precision, is under development. The pellet target system will be run in two modes: in the pellet tracking mode, only one $\sim$20 μm pellet is in the beam, giving optimal tracking conditions; in the pellet high-luminosity mode, a large number of $<$ 10 μm pellets traverse the beam to give an average effective target thickness of $\geq 4 \cdot 10^{15}$ cm^{-2} and the highest luminosity conditions of all hydrogen-target options. The diameter of the pellet-target stream, both transversally and longitudinally, is approximately 3 mm under these conditions [35].

3.2.3 Luminosity Monitor

In order to accurately monitor the luminosity at PANDA, a luminosity monitor [36] is placed at the furthest downstream end of the FS. When antiprotons scatter elastically off protons at very small angles (3-8 mrad), the scattering cross section is dominated by the Coulomb-scattering term. Since it is possible to calculate this contribution exactly, detecting antiprotons at such small scattering angles allows accurate determination of the luminosity, which is directly related to the cross section.

The luminosity detector consists of four planes of 50 μm thin silicon pixel sensors. When an antiproton traverses these planes, it is possible to determine the particle trajectory and thus determine the antiproton scattering angle. The KOALA experiment, described in Sec. 3.1.1, will be located on the opposite side of the HESR and used to accurately measure parameters related to this cross section. By combining the luminosity-monitor measurements with the scattering cross section, the luminosity may be determined at an absolute precision of 3%.

3.2.4 Target-Spectrometer Detectors

Table 3.1: Phase 1 and 2 of the PANDA target-spectrometer detectors.

System	Primary purpose
Phase 1	
Micro vertex detector	Tracking
Straw tube tracker	Tracking
GEM I*	Tracking
Barrel DIRC	Particle identification
Barrel TOF	Particle identification
Electromagnetic calorimeter	Calorimetry
Muon detector	Particle identification
Phase 2	
GEM II*	Tracking
Endcap disc DIRC	Particle identification
Hypernuclear setup	Hypernuclear physics

* In phase 1, only one GEM plane will be installed. The other two will be added in phase 2.

Micro Vertex Detector

The innermost of the TS detectors is the micro vertex detector (MVD) [37], which is based on layers of silicon pixel and strip detectors. It is used to detect charged particles very close to the primary $\bar{p}p$ interaction point. A charged particle may be tracked very accurately when it traverses the multiple silicon layers in the MVD. Thus, the location of both the primary vertex and of secondary vertices originating from the decays of short-lived particles may be determined at a spatial resolution better than 100 μm in the longitudinal direction and a few tens ($\sim$ 20–40) of μm in the transversal direction. The MVD is divided into a 46-cm long cylindrical barrel part (which has an outer radius of 13 cm) and a flat, circular endcap — the former encircles the beam pipe around the IP while the latter covers the forward end of the MVD.

Straw Tube Tracker

The straw tube tracker (STT) [38], placed radially just outside of the MVD, consists of approximately 4500 tubes (or straws) filled with an argon-based gas mixture. Each straw contains an anode wire which runs longitudinally along the length of the straw. When charged particles bend in the solenoid field and pass through the STT, they ionise the gas in the straws. The generated charge is collected at the anode wires, and the STT may be used to reconstruct the helical trajectories of the traversing particles. The bending radius gives information about the momentum of the particle, and by measuring the amplitudes of the signals in the anode wires the STT also provides information about the specific energy loss of the traversing particles. The spatial resolution of the STT is better than 3 mm in the longitudinal direction and 150 µm in the transversal direction. The inner diameter of a single straw is 10 mm, so that the inner radius of the whole detector is 15 cm and the outer radius is 42 cm. The pressure of the gas in the straws is 1 bar, so that the STT is self-supporting.

GEM Detectors

In order to track particles emitted at forward angles not fully covered by the STT (i. e. below 22°), three planar gas electron multiplier (GEM) detectors are employed [39]. These three detectors are placed at distances of approximately 1.1, 1.4 and 1.9 m downstream of the IP. Each GEM detector contains a gas mixture in which charged particles cause ionisation and several layers of GEM foil — a foil perforated with a large number of small holes in which ionisation electrons cause electron avalanches and therefore signal amplification. The resulting current is read out at various positions around the detector, which in combination with the layered structure of the GEM allows position determination. The spatial resolution of the GEM detectors is 100 µm. In phase 1 of PANDA operation only the first GEM plane will be used whereas the others will be added in phase 2. Because they provide tracking in the forward region, while still being relatively close to the IP, the GEM detectors are important for detecting the large number of forward-going charged particles coming from the IP.

Barrel DIRC

The barrel DIRC (Detection of internally reflected Čerenkov light) detector [40] is used for particle identification of π and K mesons in the barrel region of the target spectrometer. This is needed in order to identify charmed-hadron decays, which frequently include K mesons in the final state, which should be identified and separated from a background primarily consisting of π mesons. The barrel DIRC consists of a number of silica radiators assembled into a barrel. When a charged particle travels through a radiator, Čerenkov light is emitted and reflected by mirrors. The shape of the Čerenkov light cone depends on the particle velocity, and may therefore be used to identify the particle hitting the detector. The light is detected by an array of position-sensitive photon detectors located at one end of the barrel.

Endcap Disc DIRC

The endcap disc DIRC [41] works according to the same principle as the barrel DIRC: a traversing charged particle produces Čerenkov light in a silica radiator. The endcap disc DIRC allows identification and separation of π and K mesons with momenta between 1 and 4 GeV/c. It is constructed from four silica quadrants that are put together to form a dodecagon with a thickness of 2 cm and a diameter of more than 2 m. In the centre of the detector, there is a cut-out as acceptance hole for the FS detectors. The light output of the detector is detected by photon detectors at the rim of the plate.

Barrel TOF

The barrel time-of-flight (TOF) detector [42] in PANDA is constructed as a hodoscope made out of approximately 5800 plastic-scintillator tiles, read out by silicon photomultipliers. The barrel TOF detector has several purposes: identification of charged particles at momenta below 700 MeV/c, which lies below the DIRC threshold; picosecond level timing of particle trajectories, both by itself and together with the forward TOF detector; and detection of photon conversion just before the Electromagnetic Calorimeter. In order to fit between the barrel DIRC and the EMC, the barrel TOF is less than 2 cm thick.

Electromagnetic Calorimeter

In PANDA, many of the final states include a number of photons, electrons and positrons. In order to allow proper reconstruction of such events, these particles are detected in the TS EMC [23]. The EMC allows determination of the particle energy and direction, as well as providing timing information. The EMC is able to detect particles with energies down to 10 MeV.

The TS EMC consists of a total of 15744 $PbWO_4$ scintillating crystals, and is arranged into three parts: the barrel, the forward endcap and the backward endcap. The barrel contains 11360 crystals, the forward endcap contains 3856 crystals and the backward endcap contains 528 crystals. The result is a very good solid-angle coverage around the IP. As the main topics of this thesis are related to the PANDA EMCs, a more detailed description of this detector is provided in Sec. 4.3.

Target-Spectrometer Muon Detector

A muon-detection system [43] is embedded in the TS solenoid yoke, where the iron acts as an absorber. Charged particles are detected in 13 interleaving layers of MDTs, allowing for identification of muons. These muons may originate in hadronic decays and Drell-Yan processes, both of them of interest in PANDA.

In addition to the system integrated in the solenoid a similar, but planar, system of alternating iron and MDT layers is placed between the TS and the FS. This detector has to be thicker than the one in the solenoid due to the higher momentum requirements in the forward direction of PANDA. This plane also decouples the magnetic fields of the TS and FS from each other.

Hypernuclear System

A hypernucleus is a nucleus where at least one proton or neutron has been replaced by a hyperon (a baryon containing a strange quark), such as Λ or Ξ [44]. Of particular interest for PANDA are doubly strange hypernuclei (where a Ξ hyperon is present in the nucleus) and double hypernuclei (where two Λ hyperons are present in the nucleus) [45]. Such systems may be investigated at PANDA, where hyperons may be produced by letting the $\overline{\mathrm{p}}$ beam interact in a nuclear target. In the hypernuclear system, this primary target is accompanied by a secondary target in which the produced hyperons may be captured inside nuclei to form hypernuclei. In PANDA, double-hypernuclei (i. e. nuclei where a nucleon has been replaced with a hyperon with two strange quarks in it) constitute the primary field of interest.

The PANDA hypernuclear system [45] consists of three parts: a μm-thin solid target placed in the beam; a secondary target made from silicon strip sensors, that also works as a detector to track the produced hyperons; and a high-purity germanium (HPGe) γ detector to detect photons originating in de-excitations of the produced hypernuclei. Both the silicon-detector system and the HPGe detector have to be able to withstand high levels of radiation.

3.2.5 Forward-Spectrometer Detectors

Table 3.2: Phase 1 and 2 of the PANDA forward-spectrometer detectors.

System	Primary purpose
Phase 1	
Forward tracking system	Tracking
Forward TOF	Particle identification
Forward electromagnetic calorimeter	Calorimetry
Forward muon detector	Particle identification
Phase 2	
Forward RICH	Particle identification

Forward Tracking System

The forward tracking system [46], consisting of three pairs of straw tube tracker systems, tracks the highly forward-boosted charged particles that escape the coverage of the TS tracking detectors. The detectors are placed in close proximity of the dipole magnet in the FS. They contain a total of approximately 12200 straws, which are based on the same technique as the straws in the TS STT. One of the three systems is placed upstream of the magnet, one is placed within the magnet, and one is placed downstream of the magnet. These systems allow tracking of charged particles as they are deflected inside the magnetic field of the FS dipole. This is done with a momentum resolution of 1-2%.

Forward TOF

A rectangular TOF detector [47] based on an array of plastic scintillators is located in the FS, approximately 7.5 m downstream of the IP. This detector "wall" provides timing information on particles emitted in forward directions and has a timing resolution of ~ 50 ps. Therefore, it provides particle identification as well as trigger-like conditions when working together with the barrel TOF detector in the TS.

In addition to the planar TOF wall, two dipole TOF detectors are under consideration. The dipole TOFs would be constructed in a manner similar to the TOF wall, but they would be mounted inside the dipole magnet, *along* the beam axis.

Forward RICH

A ring-imaging Čerenkov (RICH) detector [47] is placed in the FS, to provide identification of 2-15 GeV/c π and K mesons and protons going in the most forward direction. Such separation is especially useful when the $\overline{\text{p}}$ beam momentum is high and the subsequent reactions produce a large multiplicity of hadrons. The forward RICH detector contains an aerogel radiator, and charged particles incident on this material produce Čerenkov radiation which is reflected by a lightweight mirror and detected by photomultiplier tubes.

Forward Electromagnetic Calorimeter

A shashlyk-type electromagnetic calorimeter [48] is employed in the FS. Its primary purpose is to cover the most forward-directed angles from the IP, which are not covered by the TS EMC. Therefore, it can be used to detect the large number of forward-directed photons that are produced in meson decays in PANDA. It is very important to distinguish such photons from single photons produced in e.g. radiative decays of charmonium states or electromagnetic processes. The shashlyk calorimeter consists of a large number of alternating layers of lead and polystyrene-based scintillator, divided into 1512 individual cells. As the main topics of this thesis are related to the PANDA EMCs, a more detailed description of this detector is provided in Sec. 4.4.

Forward Muon Detector

In the FS, a muon range system [43] similar to the one in the TS is installed approximately 9 m downstream of the IP. It is based on the same principle as the TS muon detector, with a number of interleaving iron and MDT layers. The FS muon system is constructed to suit the higher particle momenta in the forward region and enables discrimination between muons and π mesons as well as detection of π-meson decays.

3.3 Data Acquisition

At modern accelerator-based experiments, a range of approaches are taken to treat the large amounts of data produced by the detector systems — a task known as data acquisition (DAQ). The exact method used depends on the particular nature of the experiment, regarding both the physics goals and the experimental setup. In order to achieve sufficient statistics in the measured physics channels at PANDA, an average $\bar{p}p$ interaction rate of 20 MHz is foreseen during high-luminosity operation [49]. The size of a typical event — i. e. the amount of data produced by the entire detector for each primary interaction — is expected to be 1.5-4.5 kB [50] and data rates of approximately 200 GB/s are expected. Directly storing this amount of data is not possible, both from a technological and from a financial point of view. The high data rate in PANDA, combined with the wide physics programme (relying on detection of low cross-section processes) of PANDA, have made new developments in the field of triggering necessary [51].

In order to reduce the amount of data to be stored and to discard events clearly not containing any interesting physics events, a *trigger system* is used. The trigger operates online — i. e. before the data have been written to a storage system — and determines which events to read out and which to discard. Each primary interaction will give rise to responses from different subdetectors in the experiment, and the trigger decision is based on the detector setup and responses as well as the physics channel(s) of interest. Because different experiments aim to study different physical processes and have different detector setups, trigger systems will look different from experiment to experiment. A multi-layered approach is often taken, in which a first-level trigger acts on signals from a particular detector subsystem, and higher-level triggers acts on the outputs from the multiple first-level triggers.

In PANDA, a different approach is taken to triggering, as no first-level trigger providing initial data reduction is present. Instead, the triggering and DAQ systems are based on so-called online event filtering. In this approach, incoming data from the different detector subsystems will be continuously processed in real time by front-end electronics to identify events potentially corresponding to interesting physics. Instead of looking for a pre-determined set of signatures from specific detectors, this approach allows combining the incoming signals from multiple detector systems in the trigger decision, and results in a more flexible trigger. To facilitate data storage, the online event filter has to provide data reduction by a factor of 100–1000 [50]. A schematic view of the PANDA DAQ is shown in Fig. 3.4 and its different components are described below.

Clock Distribution

In the triggering scheme used in PANDA, the different subdetectors will operate independently and should also determine the time of each event before the event is processed. Therefore, a global clock is needed to synchronise the DAQ chain. This will be achieved using the SODANET protocol, where global time information is transmitted to the DAQ chain via optical links [49, 52]. The common clock provided by SODANET has a jitter of approximately 20 ps, and the propagation of the time information will be constantly monitored to correct for fluctuations.

Front-End Electronics

The front-end electronics (FEE) read out the signals from all individual detector elements in PANDA. These modules act autonomously and constitute the first stage of data reduction in the DAQ chain. By processing detector signals in real time, these intelligent FEE modules can detect signals of interest and reject noise. Only the information from the signals of interest is transmitted from the FEE. One particular instance of the front-end electronics is the EMC digitiser, which is described in more detail in Sec. 4.5 as it constitutes the basis for the main topics of this thesis.

Data Concentrators

The data from the FEE are transmitted to data concentrators, which combine and buffer data from multiple sources. In addition to combining and buffering data, the data concentrators can perform signal-processing tasks such as pattern recognition and clustering of signals from different detector elements. Through the SODANET protocol, the data concentrators receive timing information that is used to group data into time slices, so called *bursts*, which are related to the accelerator properties [53]. The data from all data concentrators belonging to a particular burst are transmitted to a compute node.

Compute Nodes and Event-Selection Farm

The burst-sorted data from the data concentrators are transmitted to compute nodes [54], which can perform tasks such as ring imaging from Čerenkov-detector signals,

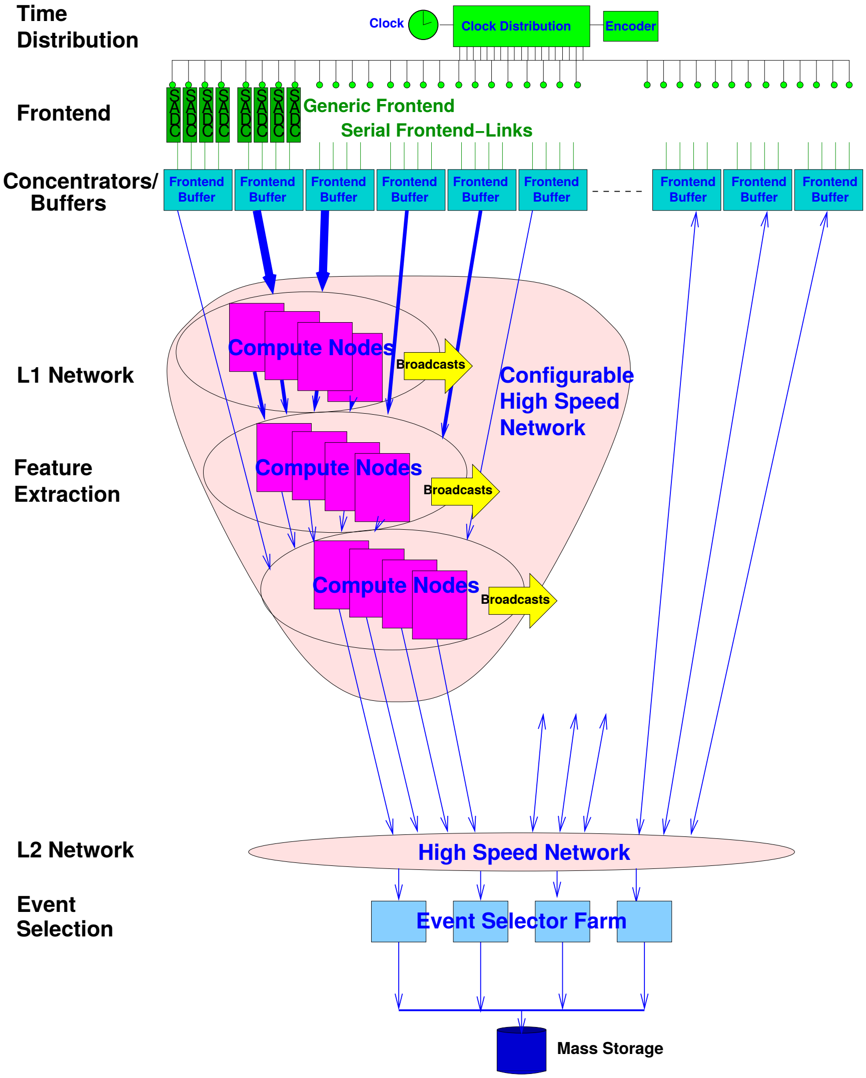
Time Distribution
Clock
Clock Distribution
Encoder
Frontend
SADC
Generic Frontend
Serial Frontend–Links
Concentrators/ Buffers
Frontend Buffer
L1 Network
Compute Nodes
Broadcasts
Configurable High Speed Network
Feature Extraction
Compute Nodes
Broadcasts
Compute Nodes
Broadcasts
L2 Network
High Speed Network
Event Selection
Event Selector Farm
Mass Storage

Figure 3.4: Schematic view of the PANDA data acquisition system. In the front-end electronics, detector signals are processed. Data from all identified signals are transmitted to the data concentrators, where data from multiple front-end modules are collected and buffered. At this stage additional signal processing, such as clustering of signals, may be performed. The buffered data in the concentrators may be accessed by subsequent elements in the system. Figure taken from [51].

displaced-vertex searches in MVD signals, as well as analysing more global detector-signal signatures. At this stage, signatures of interesting physics may be implemented to provide an accurate trigger decision and proper background rejection. Depending on the set trigger condition, the compute nodes associated with the detectors relevant for the trigger will do the initial processing. If an interesting event is found, this decision is broadcast to the rest of the compute nodes which read out their corresponding concentrators.

Data selected by the compute nodes are transmitted to an event-selection farm, where a final selection of the events of interest before storing the data on disk is performed using offline-grade algorithms. In the end, the expected data rate for storage is expected to be approximately 200 MB/s [49].

4. The PANDA Electromagnetic Calorimeters

In the world of radiation-detection systems, calorimetry is the art of measuring the properties of particles by completely absorbing them [55]. The electromagnetic calorimeters (EMCs) are key components of the PANDA experiment as they make it possible to measure the energies of photons, electrons and positrons. As described in Sec. 2.3.1, these particles are for instance very common in the final states of decays of charmonium states, illustrating the need for EMCs with good energy, position and time resolution and high efficiency. In this chapter, the working principles of the different calorimeter systems in PANDA are described starting from the physics of radiation-matter interactions. The main topic of this thesis has been developments for the FPGA-based front-end digitiser used in parts of the EMC, and towards the end of the chapter this digitiser is introduced and described.

4.1 Radiation Interaction with Matter

When radiation passes through matter, it can interact through a number of different processes. At a fundamental level, these interactions are mediated by the gauge bosons described in Ch. 2. Although the physical processes involved in these interactions depend on the properties of the incident particle, some general concepts can be used to describe the passage of radiation through a target material. These concepts are introduced here as they are essential for understanding not only the working principles of the PANDA EMC, but the rest of this thesis.

4.1.1 Reaction Rate and Cross Sections

Consider a particle beam with a density of n_p particles per unit volume, where all particles have the same velocity v. The particle flux ϕ is given by

$$\phi = n_p v. \tag{4.1}$$

If this beam is directed onto a target material containing N scattering centres, the reaction rate W_r of a particular reaction type r may be written

$$W_r = \phi N \sigma_r, \tag{4.2}$$

where the cross section σ_r has been introduced to quantify the reaction probability for this particular beam and target. In nuclear and particle physics, the cross section is commonly given in units of *barns* (1 barn = 10^{-24} cm^2).

Depending on the particular situation, multiple different reaction types can occur in the target. The total reaction rate W is the sum of the individual reaction rates:

$$W \equiv \sum_r \phi N \sigma_r = \phi N \sum_r \sigma_r = \phi N \sigma, \tag{4.3}$$

where the total cross section σ has been defined as the sum of the individual reaction cross sections. The total number of occurring reactions is obtained by integrating W over the measurement time, so that the flux ϕ is replaced by the time-integrated fluence Φ.

4.1.2 Charged Particles

Charged particles, such as electrons, positrons, protons or ions, can interact with the atomic electrons and nuclei in the target material through the Coulomb interaction, thereby transferring energy to the target. If the energy transfer is large enough, target atoms are ionised.

The average energy loss per amount of material traversed by the particle is called the *mass stopping power*, which at intermediate energies is generally dominated by the energy loss due to interactions with atomic electrons. The mass stopping power of charged particles heavier than the electron and positron due to this process is described by the Bethe formula [3]:

$$-\left\langle \frac{\mathrm{d}E}{\mathrm{d}x} \right\rangle = K z^2 \frac{Z}{A} \frac{1}{\beta^2} \left[\frac{1}{2} \ln\left(\frac{2 m_\mathrm{e} c^2 \beta^2 \gamma^2 W_\mathrm{max}}{I^2} \right) - \beta^2 - \frac{\delta(\beta\gamma)}{2} \right], \tag{4.4}$$

where x is given in units of g cm^{-2}, and is obtained by multiplying the actual distance travelled by the particle with the target density. K is a constant[1], z is the incident-particle charge, Z is the atomic number of the target material, A is the atomic mass of the target material (given in units of g mol^{-1}), m_e is the electron mass, c is the speed of light, β is the particle speed divided by the speed of light, γ is the Lorentz factor, W_max is the maximum energy that may be transferred in a single collision, I is the mean excitation potential of the target and δ is a correction factor which is important at higher energies. The average range of a certain particle in a certain material can be calculated from the stopping power.

For electrons and positions, ionisation is the dominating energy-loss mechanism at energies below approximately a few tens of MeV [3]. However, Eq. 4.4 is not entirely valid for these particles because further relativistic corrections are needed due to their low masses and because of their similarity (or for the electron, identity) with the electrons from the ionisation process. At low energies, there are small contributions from other effects, such as Møller and Bhabha scattering[1] (the energy loss due to these processes is highest at a few MeV) or positron annihilation. As the particle energy increases, radiative energy loss becomes important. The dominant radiative-loss mechanism is bremsstrahlung, in which the particle is deflected by a target nucleus causing production of bremsstrahlung photons as a result. Another process possibly contributing to the radiative energy loss of high-energy charged particles is Čerenkov radiation, which is emitted if the charged particle travels faster than the speed of light in the target material. This effect is small, but can be utilised when constructing charged-particle detectors. The bremsstrahlung contribution to the stopping power is proportional to the energy E and squared charge z^2 of the particle, but inversely proportional to the squared mass m^2 of the particle [58]:

---

[1] $K = 4\pi N_\mathrm{A} r_\mathrm{e}^2 m_\mathrm{e} c^2 = 0.307$ MeV mol^{-1} cm^2.

$$-\left\langle \frac{\mathrm{d}E}{\mathrm{d}x} \right\rangle_{\text{bremsstrahlung}} \propto \frac{Ez^2}{m^2}. \tag{4.5}$$

Therefore this effect is negligible for heavier particles except at very high energies — for instance, the stopping power of protons in silicon due to bremsstrahlung becomes equal to the one due to ionisation at approximately 135 TeV [58].

The stopping power of electrons, calculated from the sum of the Bethe formula and bremsstrahlung losses, in three materials commonly used in radiation detectors is shown in Fig. 4.1. The increase in stopping power at high energies shows the effect of bremsstrahlung. Additionally, the increase in stopping power with target atomic number Z shows why lead is a suitable component in calorimeters, where the task is to make the incident particle stop inside the detector volume. Silicon is commonly used in tracking detectors, where the aim is to detect the presence of the particle but not to stop it. Germanium is used in high-resolution photon detectors, mainly in nuclear physics.

In addition to the interaction processes involving charged particles listed above, charged particles may also cause nuclear reactions in the target material. Such reactions are described in more detail in Sec. 4.1.4.

Linear Energy Transfer

In dosimetry, the term Linear Energy Transfer (LET) is commonly used to describe ionisation due to a charged particle. The *restricted* LET is defined as the energy lost through ionisation per unit distance, where the liberated charges have an energy below Δ. In many applications, only ionisation very close to the particle track is of

---

[1] Note that although the *energy loss* of a positron through Bhabha scattering is highest at a few MeV, Bhabha scattering at much higher energies is commonly used when measuring the luminosity at e^+e^- colliders [56, 57].

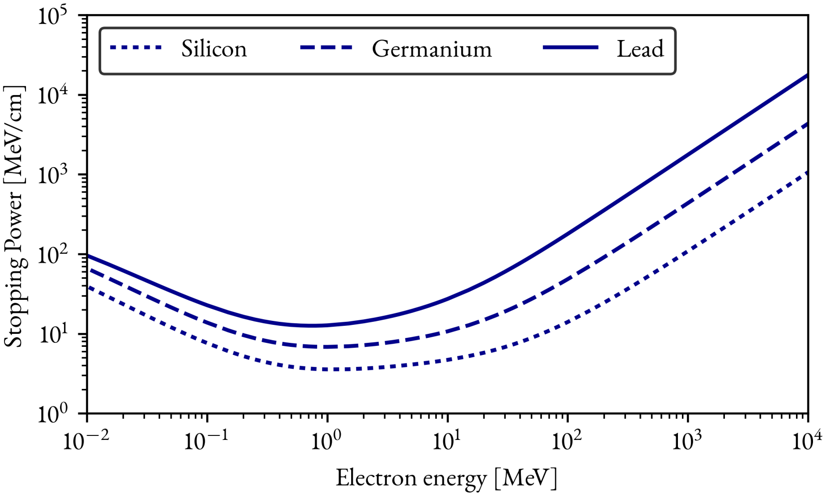

Figure 4.1: Stopping power of of electrons in silicon ($Z = 14$), germanium ($Z = 32$) and lead ($Z = 82$) as a function of the electron energy. The increase in stopping power with target atomic number Z is clear. Data taken from [59].

interest. By imposing a limit Δ, for instance energetic electrons (so called delta-rays) can be excluded. In the limit $\Delta \to \infty$, the now *unrestricted* LET is equal to the electronic stopping power defined above.

4.1.3 High-Energy Photons

A photon passing through matter loses energy mainly through four different processes: Rayleigh scattering, photoelectric absorption, Compton scattering and pair production. For a specific target material, the cross sections for these different reactions directly depend on the photon energy, as shown in Fig. 4.2.

Rayleigh scattering, or coherent scattering, is the elastic scattering of photons off atoms. This process, which in contrast to the three other processes described here can be described without the need for quantum mechanics, is only relevant for low photon energies. In the context of this work, this process can be of relevance for scintillation light, but not for the direct interactions of the high-energy photons in the accelerator environment itself. In photoelectric absorption, the energy of the incident photon is transferred to an atomic electron in the target. The energy acquired by the electron can lead to excitation of the atom or, if the energy is large enough, to ionisation. This effect is dominant at low photon energies. In Compton scattering, the incident photon collides with an atomic electron, thereby losing part of its energy. The process gives energy to the electron, which is liberated from

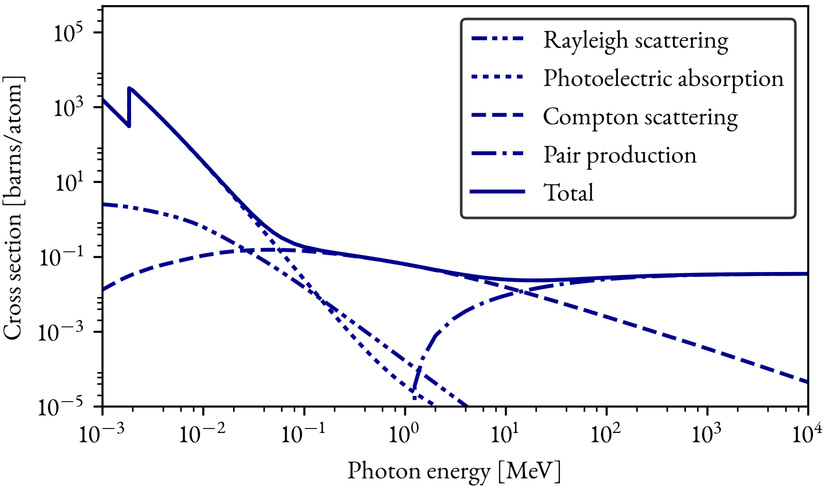

Figure 4.2: Cross sections for Rayleigh scattering, photoelectric effect, Compton scattering and pair production in natural silicon, as a function of the photon energy. The sum of the four contributions is also shown, and indicates in which energy regions the different processes are dominant. Data taken from [60].

its atom. In pair production, the incident photon has enough energy to produce an electron-positron pair (the threshold for this reaction is twice the electron rest mass). In order to conserve momentum in this process, it must occur in the vicinity of a target nucleus, which recoils after the pair production.

4.1.4 Nuclear Reactions

The most probable interactions of a projectile in a target material are those involving the atomic electrons of the target. However, virtually all particles are able to interact with atomic nuclei, although these reaction channels are very improbable for some particles. Here, only nuclear reactions initiated by an incident proton or neutron (i. e. a nucleon) will be discussed, since these are relevant for the work presented in Part II of this thesis. Because they need to proceed through the electromagnetic interaction instead of the strong interaction, the cross sections for nuclear reactions initiated by photons, electrons or positrons are generally at least two or three orders of magnitude smaller than nucleon-induced reactions [61]. For this reason, the contribution from such reactions is in the context of this thesis considered to be negligible.

In a nuclear reaction, the system containing a projectile nucleon *a* and a target nucleus *A* is called the incident channel. The resulting system after the interaction is called the exit channel, and consists of particles b and B (note that the exit channel may consist of more than two particles). The full reaction can be stated as:

$$A(a, b)B. \tag{4.6}$$

If the projectile is a proton, it will be affected by the electrostatic Coulomb field of the target nucleus. In order for a nuclear reaction to take place, the proton has to have sufficient kinetic energy to overcome the Coulomb barrier of the nucleus. For a proton incident on a nucleus with atomic number Z and mass number A, the approximate height E_C of the Coulomb barrier is given by [62]:

$$E_C \approx (1.44\,\mathrm{MeV\,fm})\frac{Z}{R_0(1+A^{1/3})}, \tag{4.7}$$

where $R_0 \approx 1.25$ fm. This relation is based on a classical description of the proton and nucleus in which the two particles are approximated as two uniformly-charged spheres with well-defined radii. For a ^{28}Si target, Eq. 4.7 yields a Coulomb-barrier height of approximately 4 MeV. Therefore, the incident proton needs an energy higher than this to initiate a nuclear reaction[1]. If the projectile is a neutron, it is unaffected by the Coulomb barrier and may initiate a nuclear reaction at any energy.

A number of mechanisms can be involved in the nucleon-nucleus interaction. These may be classified according to either the time scale of the reaction or the composition of the exit channel. In the time-based classification, one commonly distinguishes between direct reactions, which happen on a timescale of approximately 10^{-22} seconds, and compound-nucleus reactions, which happen on a timescale of 10^{-16} to 10^{-18} seconds [63]. In a direct reaction, the projectile interacts only with a limited number of target-nucleus nucleons. In a compound-nucleus reaction, the projectile is absorbed by the nucleus and the energy is shared between a large number of nucleons in the nucleus. After a relatively long time, the nucleus may remove excess energy by "boiling off" particles in a process known as evaporation.

When classifying reactions based on the exit-channel composition, it is important to remember that some exit channels can be the result of either a direct reaction or a compound-nucleus reaction. For instance, consider the case where a proton hits a nucleus. If the exit channel of the reaction consists of a proton and an alpha particle, one scenario is that the proton knocked out an alpha particle from the nucleus in a direct reaction. However, the second scenario is that the proton was absorbed by the nucleus, which subsequently de-excited by boiling off a proton and an alpha particle — this would be a compound-nucleus reaction. In an experiment, one could distinguish between the two for example by measuring the exit angles of the reaction products. Remembering that a certain exit-channel composition does not necessarily give information about the underlying process of the reaction, one can divide reactions into several categories:

---

[1] In a quantum-mechanical treatment of the problem, a proton with a lower energy could tunnel through the Coulomb barrier. Therefore, the actual effective height of the barrier is lower than 4 MeV.

- Elastic scattering: An incident proton may scatter elastically off the nucleus due to the Coulomb interaction with its electric field. This purely electromagnetic effect, known as Rutherford scattering, is accompanied with scattering due to the strong interaction. For the neutron, only the strong-interaction scattering is responsible for its elastic scattering. Elastic scattering results in the nucleon leaving the interaction point and a recoil nucleus ionising the atoms around it until it stops. The energy of the recoiling nucleus depends on the kinetic energy of the incoming nucleon as well as on the scattering angle ϑ of the nucleon. The relation between the scattering angles and particle energies may be derived using relativistic kinematics [64]. In Fig. 4.3, the energy of the recoiling ^{28}Si nucleus in a p+^{28}Si elastic scattering event is shown for different incident-proton energies as a function of the scattering angle in the lab frame. It is evident that the largest energy transfer is expected when the proton scatters at $\vartheta_{\text{lab}} = 180°$, and that the recoil from such a scattering event can be quite energetic and therefore highly ionising in the target material.

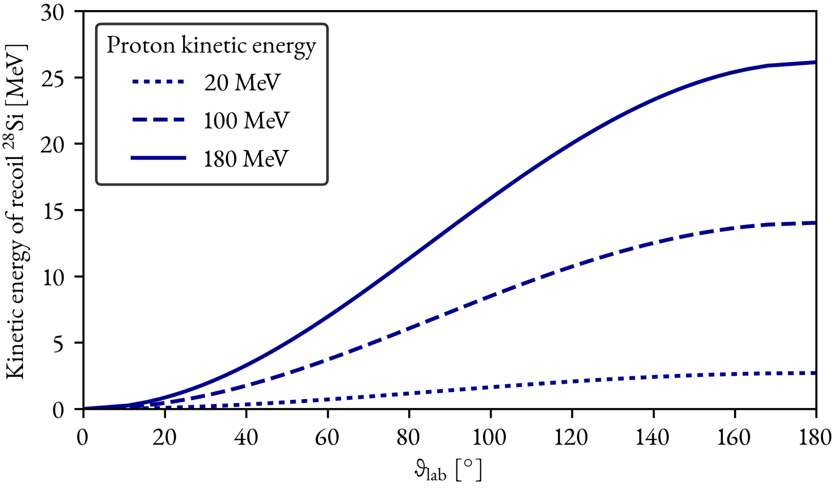

Figure 4.3: Kinetic energy of the recoil silicon nucleus after a proton-^{28}Si elastic scattering as a function of the proton scattering angle ϑ_{lab} at different incident-proton energies. Data taken from [64].

- Inelastic scattering: In a scattering event, energy is transferred to the nucleus (either through the Coulomb interaction or through the strong interaction). Inelastic scattering occurs when this energy transfer is such that the nucleus is excited, and the kinetic energy in the exit channel is not the same as in the incident channel. The excited nucleus subsequently de-excites via emission of γ photons. Inelastic scattering results in a scattered nucleon, a recoil nucleus and one or more de-excitation photons.

- Charge exchange: When the projectile nucleon interacts with a nucleon in the periphery of the target nucleus, pion exchange between those two may exchange the projectile nucleon for the target nucleon. That is, if the projectile is a proton, it may be turned into a neutron, and vice versa. Thus, the mass number of the nucleus is kept constant, while the resulting free particle after the interaction will have changed.

- Absorption: The projectile is absorbed by the target nucleus.

- Pickup reaction: One or more nucleons in the nucleus are transferred to the projectile.

- Knockout reaction: The projectile nucleon gives enough energy to one or more nucleons in the nucleus to eject them from it.

- Fusion and fusion-evaporation: Energy from primary nucleon-nucleon interactions is spread out over a large part of the nucleus. Through this process, the projectile nucleon can lose enough energy to be absorbed by the nucleus (i. e. causing fusion). Also, the energy transfer to some part of the nucleus might be large enough that one or more nuclear fragments can leave the nucleus through evaporation. Such a reaction can result in a breakup of the nucleus, with the result of two recoiling heavy fragments.

4.1.5 Electromagnetic Showers

As shown in Fig. 4.2, a photon with an energy above a few MeV mainly interacts with matter through pair production. Therefore, a high-energy photon incident upon a target will with a high probability cause the production of an electron-positron pair. These generated particles will in turn lose energy radiatively due to their high energies, causing the emission of bremsstrahlung photons. This combination of energy-loss processes of electrons, positrons and photons causes an avalanche of particles, known as an electromagnetic shower, in the material. An electromagnetic shower may also be initiated by a high-energy electron or positron incident upon the target, although the exact nature and shape of the shower will be slightly different in these cases compared to when the primary particle is a photon [65].

During the shower development, low-energy photons and electrons will be produced continuously. For these particles, the bremsstrahlung or pair-production processes may be highly improbable or impossible, and they will lose energy through ionisation, Compton scattering and/or photoelectric effect. At some point during the shower development, when the energy of a particle goes below the critical energy E_C, the multiplication process can no longer be sustained, and the shower development stops. The critical energy in a solid target with atomic number Z is approximately given by [3]:

$$E_C = \frac{610\ \mathrm{MeV}}{Z + 1.24}. \tag{4.8}$$

It is useful to define the radiation length X_0 of a target material, which is a material-dependent constant describing the mean distance an electron travels to lose all but $1/e$ of its energy through bremsstrahlung [3]. It is common to give the dimensions of electromagnetic showers in units of X_0, and Eq. 4.8 relies on the approximation that the energy loss through bremsstrahlung is $|\mathrm{d}E/\mathrm{d}x|_{\mathrm{bremsstrahlung}} \approx E/X_0$. The lateral profile of the shower has been found to be described by the Molière radius R_M, which is the radius of a cylinder that on average contains 90% of the energy deposition of the shower [3]:

$$R_M = 21\ \mathrm{MeV}\frac{X_0}{E_C}. \tag{4.9}$$

The longitudinal and lateral profile of an electromagnetic shower initiated by a 6-GeV electron in lead is shown in Fig. 4.4.

4.2 Requirements for the PANDA Calorimeters

The purpose of the PANDA EMCs is to detect photons, electrons and positrons. An incident particle will ideally deposit its full energy by producing an electromagnetic shower in the calorimeter. Detection of this shower gives information about the energy of the particle and its angle of incidence on the detector. Also, the location and time of the interaction with the detector may be determined.

Calorimeters used for radiation detection may be classified as either *homogeneous* or *sampling* calorimeters. In a homogeneous calorimeter, energy deposited anywhere in the entire detector volume can contribute to the generated signal. Sampling calorimeters, on the other hand, consist of multiple materials which are not all sensitive to deposited energy. Typically, a sampling calorimeter consists of two materials: one of them passive, in which an electromagnetic shower develops, and one active, where the particles produced in the passive material generate a signal. Depending on the active material, the output signal from a homogeneous or sampling calorimeter can be generated for example through scintillation, emission of Čerenkov radiation or direct ionisation.

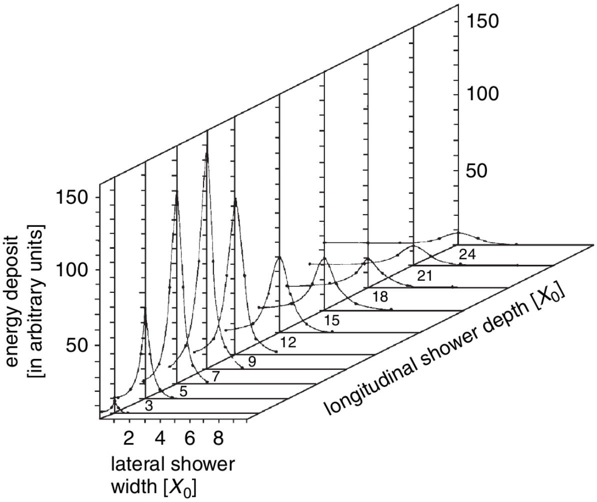

Figure 4.4: The lateral distribution of an electromagnetic shower initiated by a 6-GeV electron in lead at different depths in the target. The dimensions are given in units of radiation length X_0. Figure taken from [66].

The planned physics programme at PANDA places a number of requirements on the calorimeter system, including energy resolution, energy range, angular coverage and radiation hardness. In order to fulfil these requirements, a homogeneous calorimeter consisting of lead tungstate ($PbWO_4$) scintillator crystals will be used in the TS region, while a shashlyk-type sampling calorimeter based on interleaved layers of lead and plastic scintillators will be installed in the FS region. As will be discussed in subsequent sections, the TS EMC is subdivided into three separate detectors: the backward-endcap, the barrel and the forward-endcap EMC. The requirements on the different subsystems are listed in Table 4.1.

One of the main requirements on the EMC is a good solid-angle coverage, which with the planned configuration will be approximately 99% of 4π in the $\bar{p}p$ centre-of-mass frame of reference. This is necessary to facilitate reconstruction of the many final states containing photons, electrons and positrons [23]. The remaining solid angle will be taken up by the $\bar{p}$ and target beam pipes, mechanical structures and cabling. The different parts of the EMC are shown in Fig. 4.5, where the roles of the different detectors in achieving this good coverage is clear. The properties of the TS and FS calorimeter systems are described in more detail in the subsequent sections.

Table 4.1: Requirements on the EMC detectors in PANDA. Data taken from [23, 48].

Property	Required values			
	Backward endcap	Barrel	Forward endcap	Shashlyk
Relative energy resolution σ_E/E	$\leq 1\% \oplus \frac{2\%}{\sqrt{E/\mathrm{GeV}}}$	$\leq 1\% \oplus \frac{2\%}{\sqrt{E/\mathrm{GeV}}}$	$\leq 1\% \oplus \frac{2\%}{\sqrt{E/\mathrm{GeV}}}$	$\leq 1\% \oplus \frac{(2-3)\%}{\sqrt{E/\mathrm{GeV}}}$
Photon-energy threshold [MeV]	10	10	10	10
Single-detector threshold [MeV]	3	3	3	3
Energy-equivalent noise [MeV]	1	1	1	1
Maximum detectable energy [MeV]	700	7300	14600	15000
Polar-angle coverage (lab frame) [°]	≥ 140	≥ 22	≥ 5	≥ 0
Solid-angle coverage (lab frame) [% 4π]	5.5	84.7	3.2	0.74
Hit rate per detector* [MHz]	0.06	0.06	0.5	~ 1
Radiation hardness [$\mathrm{Gy\,y^{-1}}$]	10	10	125	1000

* Hit rate per individual crystal or cell.

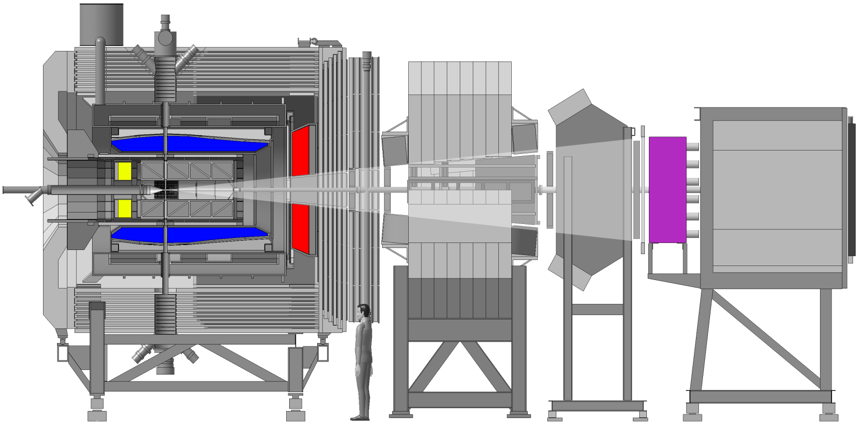

Figure 4.5: Schematic drawing of PANDA, with the backward-endcap (yellow), barrel (blue), forward-endcap (red) and shashlyk (purple) EMCs highlighted. Figure modified from [67].

4.3 Target-Spectrometer Electromagnetic Calorimeter

The TS EMC is divided into three parts: the cylindrical barrel, and the forward and backward endcaps. In this section the scintillator material, photodetectors and preamplifiers are discussed in some detail. The readout electronics will differ between the three detectors, and as the focus of this work is the FPGA-based digitiser developed for the forward-endcap and shashlyk EMCs, it will be described in more detail in Sec. 4.5.

4.3.1 PWO-II Crystals

The requirements placed on the scintillator material used in the TS EMC are, as specified in Tab. 4.1: (a) high density to permit a small thickness of the EMC, (b) fast response time, (c) good energy resolution in the dynamic energy range of the EMC, and (d) radiation hardness. Lead tungstate ($PbWO_4$ or PWO), successfully used in the CMS experiment at CERN [68], has been chosen as the scintillator material for the TS EMC. The detector material used at CMS was found to fulfil all of the above requirements except for the one on the energy resolution, coming as a result of the low light yield of PWO. An improved crystal material, referred to as PWO-II, has been developed for PANDA and has around twice the light yield of the first-

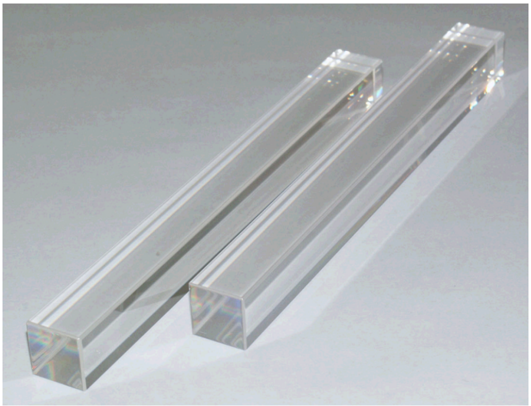

Figure 4.6: Photograph of two PWO-II crystals, developed for use in the TS EMC. The dimensions of a single crystal is $20 \times 20 \times 200$ mm^3. Figure taken from [51].

generation PWO material [23]. Fig. 4.6 shows two examples of finalised PWO-II crystals.

The EMC will consist of 15744 PWO-II crystals. The barrel consists of 11360 crystals, the forward endcap consists of 3856 crystals and the backward endcap consists of 528 crystals. All crystals will be 200 mm long but will be tapered to different extents in order to fit the detector geometry while still facing a point close to the $\bar{p}p$ interaction point. This point is chosen such that the probability that a particle generated at the interaction point passes the EMC between adjacent crystals is minimised. The constraints on the radial thickness of the TS EMC are due to the fact that the detector will be placed inside the TS solenoid. The crystals will be operated at a temperature of -25°C, which increases the scintillator light output by a factor of about four as compared to operation at +25°C. At -25°C, the light yield is approximately 80 photoelectrons per MeV, which is about 2.5% of the value for a sodium iodide scintillator. Because of the forward-boosting of reaction products from the IP, the highest requirements on energy range and rate capability concern the forward endcap, as is clear from Table 4.1.

4.3.2 Photodetectors

Two types of photodetectors will be employed in the TS EMC — large-area avalanche photodiodes (APDs) and vacuum phototetrodes (VPTTs) — both chosen due to their ability to operate under the high magnetic field of approximately 2 T present in the EMC. The photodetectors are attached to the end faces of the crystals. Each crystal in the backward endcap and in the barrel will be equipped with two APDs, as will the 3088 peripheral crystals in the forward endcap. Since VPTTs handle high rate better than APDs, the inner 768 crystals of the forward endcap will be equipped with one VPTT each.

4.3.3 Preamplifiers

The performance requirements on the TS EMC, in combination with the choices of detector material and photodetectors, place high demands on the preamplifiers which have to be both compact and able to amplify small signals from the PWO crystals. Also, the preamplifiers should be radiation tolerant, and capable of handling high rates. To this end, two types of preamplifiers have been developed for use in the EMC: the APFEL-ASIC preamplifier [69] which will be used in the backward endcap and the barrel, and the Basel-LNP preamplifier [70] which will be used in the forward endcap.

4.4 Forward-Spectrometer Electromagnetic Calorimeter

The FS EMC is a shashlyk-type [71] sampling calorimeter located approximately 7 metres downstream of the IP, covering the very forward region of the solid angle around the IP. In this section the features of the detector and its readout are discussed in some detail, while the FPGA-based digitiser used as the FEE for the shashlyk calorimeter will be described in more detail in Sec. 4.5. A more detailed discussion of the components of the FS EMC is presented in Part III of this thesis.

4.4.1 Shashlyk Cells

The FS EMC is not subject to as strict geometrical constraints as the TS EMC, since it does not have to be placed within any magnet. Therefore, there has been more flexibility in designing this detector. However, there are still constraints on its size coming from the layout of the other subdetectors in the FS. At the same time, a detector area of over 4 m^2 is required to give the required solid-angle coverage [48]. To cover such an area with homogeneous scintillators would be expensive, and because of the less strict geometrical requirements a sampling calorimeter having a resolution similar to that of PWO-II is being developed.

Shashlyk-type calorimeters are sampling calorimeters read out by a number of wavelength-shifting (WLS) fibres that run through the calorimeter layers longitudinally, transporting the scintillation light to photodetectors. Shashlyk calorimeters are or have been used in a number of high-energy physics experiments, such as PHENIX [72], HERA-B [73], LHCb [74] and COMPASS [75]. Due to the relatively low yield of scintillation photons per deposited energy, this detector type has not been previously used in the MeV energy range, as is needed in PANDA. The design of the PANDA shashlyk calorimeter is heavily based on the developments for the KOPIO experiment [76], for which development of a shashlyk calorimeter for the MeV range took place before the experiment was eventually cancelled. The development of the PANDA shashlyk calorimeter has to a large extent been focused on optimising the light yield and light-yield uniformity of the system, as these parameters have a large effect on the energy resolution at the energy scale of interest [48].

The PANDA shashlyk calorimeter will consist of 1512 individual shashlyk cells, with each cell having a surface area of $5.5 \times 5.5\ \mathrm{cm}^2$. A hole corresponding to 6×6 cells is required for the beam pipe to pass through the centre of the calorimeter. Each cell is constructed from 380 layers of interleaved lead, plastic scintillators and Tyvek [77] sheets. The lead acts as the absorber of the calorimeter, the scintillator as the active medium and the Tyvek increases light-collection efficiency. The total thickness of the calorimeter amounts to 0.875 metres.

The scintillator plates are manufactured at IHEP Protvino, Russia, and consist of a mixture of polystyrene, 1.5% para-terphenyl (pTP) and 0.04% POPOP. In order to collect the scintillation light, nine WLS fibres run through each cell longitudinally (making a 180-degree bend at the front of the cell) and couple to a photomultiplier tube (PMT) at the back of the detector for signal read-out.

4.4.2 Photodetectors

Each shashlyk cell in the FS EMC will be read out by a PMT, which intrinsically has a higher gain than the APDs and VPTTs used in the TS EMC and can be used in the FS EMC due to the absence of a magnetic field. For the FS EMC, the Hamamatsu R7899 PMT [78] has been selected as it has a good pulse-height linearity over a wide range of currents [48]. This property is needed both because the short duration of the signals from the calorimeter causes a high peak current and because the calorimeter should be able to detect particles with a large range of energies. The PMTs will be supplied high voltage from custom-made Cockcroft-Walton power supplies [48]. Because of the high gain of the PMTs, no preamplifiers are needed before signal digitisation, and so the signals from the PMTs are transmitted directly to the FEE digitisers. At the FEE inputs, additional shaping of the analogue signals may be performed.

4.5 Front-End Digitiser

In Sec. 3.3, the principles of the PANDA DAQ scheme were described. In this scheme, the FEE plays a vital role in processing detector signals in real time, and for the forward-endcap and shashlyk EMCs this will be done by FPGA-based digitiser modules. These modules digitise the signals from the preamplifiers (in the forward endcap case) and the PMTs (in the shashlyk case), and the digital signals are processed by FPGAs. In the case of the forward-endcap EMC, the digitisers are placed outside the cold volume of the EMC, but still inside the TS detector volume as the amount of cabling to the outside of the detector has to be constrained [79]. A total of 217 boards will read out the data from the forward-endcap EMC, while 22 boards are envisioned for the shashlyk EMC [79]. Fig. 4.7 shows a digitiser module for the forward endcap.

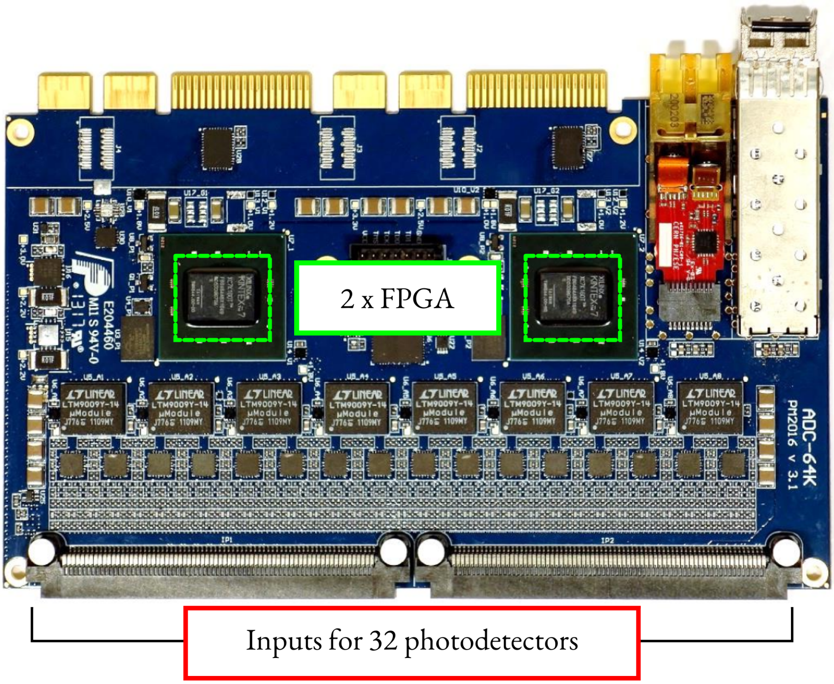

Figure 4.7: The forward-endcap EMC digitiser module. On each module, there are inputs for 32 photodetectors, and the digitised detector signals are processed by two Kintex-7 FPGAs. Figure courtesy of [80].

32 photodetectors may be connected to each digitiser board in the forward endcap. The digitisation of the signals is performed by sampling analogue-to-digital converters (ADCs), which in the forward-endcap case are Linear Technology 14-bit ADCs [81] operating at a sampling rate of 80 MHz. The sampling rate in the shashlyk EMC will be higher, due to the shorter signals from the PMTs compared to those from the TS-EMC preamplifiers. The key components in the signal processing done on the digitised data by each module are two Xilinx Kintex-7 FPGAs, which are based on 28-nm technology [82]. The FPGAs can be used to perform for instance noise calibration, pedestal subtraction and hit detection [23]. They may be reprogrammed any number of times after initial operation, which can be done directly from a programmable read-only memory (PROM) located on the board. An overview of the forward-endcap EMC readout is shown in Fig. 4.8. For the shashlyk EMC, the readout scheme will be identical, with the exception of the cooled detector

volume, the preamplifiers and the use PMTs instead of APDs.

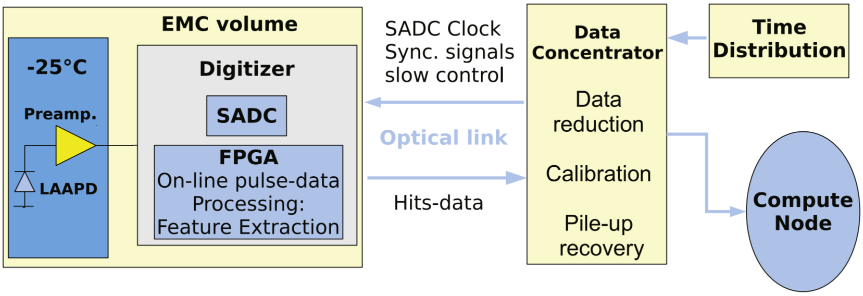
EMC volume
-25°C
Preamp.
LAAPD
Digitizer
SADC
FPGA
On-line pulse-data Processing: Feature Extraction
SADC Clock
Sync. signals
slow control
Optical link
Hits-data
Data Concentrator
Data reduction
Calibration
Pile-up recovery
Time Distribution
Compute Node

Figure 4.8: Schematic diagram of the readout chain in the forward-endcap EMC. The front-end digitiser boards are located inside the detector volume, but outside the cooled PWO crystals and preamplifiers. For the shashlyk calorimeter, the same readout scheme will be used, with the exception of the cooled detector volume and the preamplifiers and using PMTs instead of large-area APDs (LAAPDs). Figure taken from [83].

This thesis will focus on two topics which arise due to the operating conditions of the digitiser modules. In Part II, a study of the risk of radiation-induced SEUs in the digitiser FPGAs during operation of PANDA is described. Such errors could cause different kinds of data corruption or sudden component failure in the digitisers. Due to the vital part played by the FEE digitisers in the PANDA DAQ scheme, the risk of such errors should be understood and minimised to avoid data loss. To this end, SEUs in the Kintex-7 FPGA have been studied through experiments and Monte Carlo modelling. In Part III, the development of an FPGA-based algorithm for real-time signal processing in the shashlyk EMC is described. To develop and test this algorithm, a Geant4-based Monte Carlo model of the shashlyk EMC has been developed. As shown in Table 4.1, hit rates of up to 1 MHz are expected in this detector, leading to a high risk of pile-up events. In order to have a low detector dead time even at rates as high as this, and maintaining a resolution as good as possible, pile-up events should be recovered online.

PART II

SINGLE EVENT UPSETS IN THE FRONT-END DIGITISER FPGA

5. Single Event Upsets

The Xilinx Kintex-7 FPGA, which is used in the EMC front-end digitiser module, is based on static random-access memory (SRAM) [84]. As such, it has a very high storage density and allows the user to reconfigure the firmware of the device any number of times after initial operation [85]. This chapter describes the properties of semiconductor devices and the operation of an SRAM cell; keys to understanding the radiation effects which are discussed in this part of the thesis.

5.1 Semiconductor Devices

The most commonly used semiconductor in SRAM memories is silicon. The silicon atom has four valence electrons, so that its crystal lattice structure is built up by atoms forming covalent bonds with four neighbouring atoms. The electrical properties of the crystal may be changed by replacing one silicon atom in the lattice by a dopant atom, for example arsenic or boron. Replacing silicon atoms with arsenic atoms, which have five valence electrons, results in free negative charge, and an *n-type semiconductor*. The arsenic ion, which is positively charged, is called a donor atom. Boron, on the other hand, has three valence electrons. Replacing silicon atoms with boron atoms results in free positive charge (due to the missing electrons), and a *p-type semiconductor*. The boron ion, which is negatively charged, is called an acceptor atom.

In a semiconductor, electrons and holes are constantly created due to excitations in the lattice. Thus, electrons and holes can both act as charge carriers in such a material. When doped, the concentration of one type of charge carriers increases. This means for example that electrons are majority carriers in an n-type semiconductor, while holes are minority carriers.

5.1.1 The P–N Junction

By placing n-type silicon next to p-type silicon, a p–n junction is formed. When this happens, electrons from the n-side diffuse to the p-side, where they recombine with holes. Similarly, holes from the p-side diffuse to the n-side where they recombine with electrons. As shown in Fig. 5.1, the diffusion currents and subsequent recombinations result in a *depletion layer* in the p–n interface, where there are no free charge carriers but only ionised donor and acceptor atoms. Due to the diffused charge carriers, there will be an electric field across the depletion layer, directed from the n-side to the p-side. This field creates a barrier for the diffusing majority charge carriers so that diffusion and recombination will eventually stop. This leads to an equilibrium between the diffusion currents and the resulting electric field, and a fixed depth of the depletion layer. Note that while the movement of majority charge carriers from both sides is effectively blocked by the electric field, minority carriers can still be accelerated across the depletion layer. However, the so-called drift current resulting from this is relatively small.

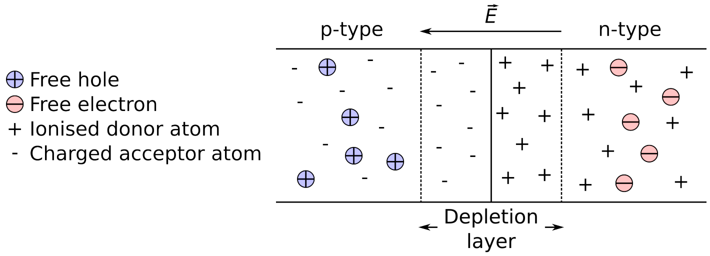

Figure 5.1: The p–n junction. Initially, majority charge carriers drift across the interface and recombine with ions. This results in a net concentration of positive ions on the n-side and of negative ions on the p-side, which in turn results in an electric field counteracting the original drift. Thus, the depletion layer is formed.

When applying a bias to the p–n junction, the allowed amount of current across it is changed. The three possible states — unbiased, forward biased and reverse biased — of the junction are shown in Fig. 5.2. When the p–n junction is unbiased,

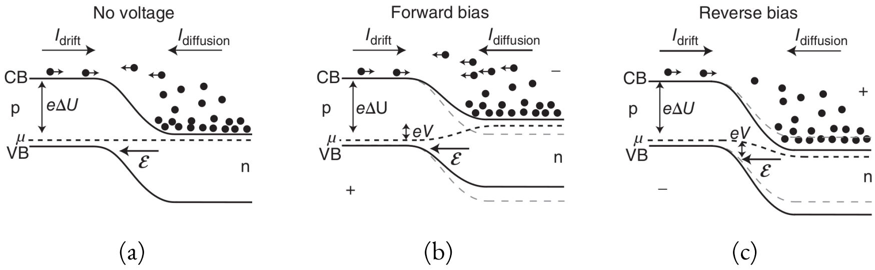

(a) (b) (c)

Figure 5.2: The potential difference in a p–n junction when (a) unbiased, (b) forward biased and (c) reverse biased. Here, only electrons are shown for clarity. When the device is unbiased, a depletion layer is formed. Forward-biasing lowers the potential difference, and a net current flows. When the junction is reverse biased, no current flows. Figures taken from [86].

minority carriers on the p-side (i.e. electrons) may get close to or into the depletion layer, where they will be accelerated toward the n-side by the electric field, thereby forming a drift current I_{drift}. Simultaneously, majority electrons on the n-side, having sufficient thermal energy to pass over the potential barrier of the depletion layer may diffuse to the p-side, forming a diffusion current $I_{\text{diffusion}}$. However, these currents are not large enough to upset the equilibrium. This is shown in Fig. 5.2a.

When forward-biasing the p–n junction, the p-side is connected to the positive end of a voltage source. This introduces an electric field directed from the p-side to the n-side, thereby decreasing the potential difference between the sides. This makes it easier for electrons to diffuse into the p-side and holes to diffuse into the n-side — i. e. $I_{\text{diffusion}}$ increases. This is shown in Fig. 5.2b.

Finally, reverse-biasing the p–n junction means that the n-side is connected to the positive end of a voltage source. The electric field due to this is directed in the same way as the electric field already existing in the depletion layer (from the n-side to the p-side), enforcing the potential barrier between the sides. This decreases $I_{\text{diffusion}}$, and is shown in Fig. 5.2c.

The net current across the p–n junction is the difference between the diffusion current and the drift current. Since the drift current is independent of the applied voltage, the net current directly depends on the diffusion current, and therefore on whether the junction is forward or reverse biased: if it is forward biased, current can flow easily; if it is reverse biased, no current will flow. The p–n junction thus acts as a diode when placed in an electric circuit.

5.1.2 The MOS Transistor

The metal-oxide-semiconductor field-effect transistor (MOSFET or MOS) is one of the most common circuit elements in integrated circuits, and is the core component of SRAM memories. A MOS transistor consists of different regions of n-type and p-type silicon[1]. In each transistor, there is a *source* and a *drain*. A conducting *gate* is placed on top of the body, between the source and the drain, with a layer of silicon dioxide (SiO_2) insulating it from the body. In accordance with the working principle of the p–n junction, applying a bias at the gate alters the ability for current to flow from the source to the drain, and therefore determines whether the transistor is *on* (conducting) or *off* (not conducting). There are two types of MOS transistors: n-type MOS (nMOS) and p-type MOS (pMOS) transistors, which are shown in Fig. 5.3.

nMOS

In an nMOS transistor, the body consists of p-type silicon while the source and drain both consist of heavily doped n-type silicon. The body is connected to ground so that the p–n junction between the source or drain and the body is reverse-biased

---

[1] MOS transistors based on other semiconductor materials have been developed, but will not be discussed in this work.

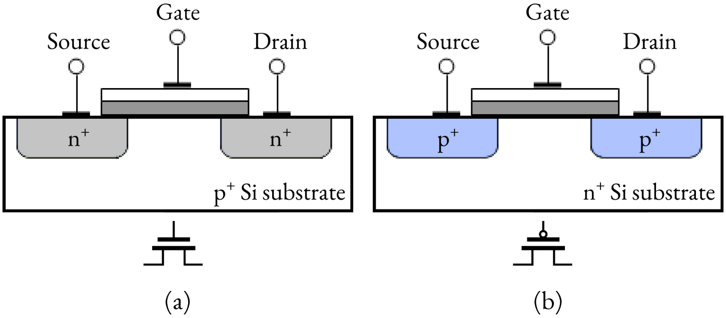

Figure 5.3: The two types of MOS transistors: a) the nMOS transistor and b) the pMOS transistor. Their respective symbols in electrical circuits are also shown on the bottom.

when no voltage is applied at the gate — i. e. no current flows from the source to the drain and the transistor is off. When a positive voltage is applied to the gate, electrons in the body are attracted to the region under the gate. Eventually, a channel between the source and the drain becomes so electron-rich that the effect of the p–n junctions is reverted and a current of electrons may flow. Thus, the nMOS transistor turns on when a positive voltage is applied at the gate.

pMOS

In a pMOS transistor, the situation is opposite to that in the nMOS transistor. The body consists of n-type silicon while the source and drain both consist of heavily doped p-type silicon. The body is connected to a positive voltage $+V_{\mathrm{DD}}$ so that the p–n junction between the source or drain and the body is reverse-biased when a positive voltage is applied at the gate — i. e. no current flows from the source to the drain and the transistor is off. When the gate voltage is lowered, holes in the body are attracted to the region under the gate. Eventually, a channel between the source and the drain becomes so hole-rich that the effect of the p–n junctions is reverted and a current of holes may flow. Thus, the pMOS transistor turns on when no voltage is applied at the gate.

5.2 The CMOS Inverter

When nMOS and pMOS transistors are combined, they form a complementary metal-oxide semiconductor (CMOS) device. The simplest such device, which also forms the basis of the CMOS SRAM memory, is the CMOS inverter. The inverter consists of one nMOS and one pMOS transistor connected as shown in Fig. 5.4. Here, the *substrate* of the device is made out of p-type silicon, and the pMOS transistor is enclosed in an n-type *well*. The nMOS source and drain are placed directly into the substrate. The nMOS and pMOS bodies are connected to ground and $+V_{\mathrm{DD}}$, respectively, via *taps* placed within the two transistors. Not shown here is a CMOS inverter with an n-type substrate — such a device would have a p-type well.

As the name suggests, the inverter inverts the value of an input signal A, which is connected to the gates of the two transistors. The value on A determines which of the two transistors is on, and which is off. The output signal Y is connected to the two drains of the transistors. The nMOS source is connected to ground, while the pMOS source is connected to a positive voltage V_{DD}.

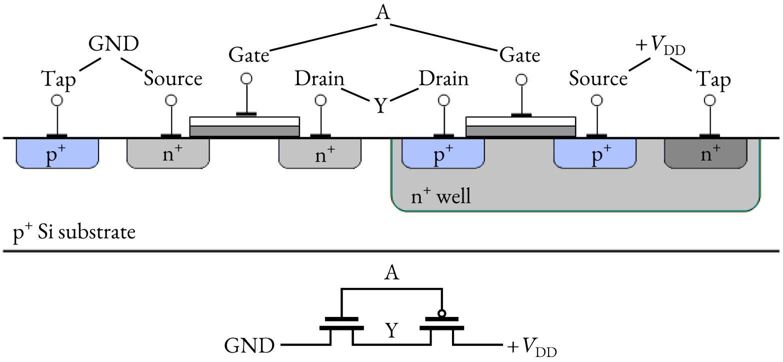

Figure 5.4: Schematic drawing of a CMOS inverter, based on a p-substrate technology. The inverter inverts the value of an input signal A, which is connected to the gates of the two transistors. The output signal Y is connected to the drains of the transistors.

The truth table for the CMOS inverter is shown in Tab. 5.1. When the input voltage A is low (0), the nMOS will be off and the pMOS will be on. This means that current will flow through the pMOS and the voltage at Y will be equal to the the voltage V_{DD} which is connected to the pMOS source. That is, the voltage at Y will be high (1). When the input voltage A is high, on the other hand, the nMOS will be on and the pMOS transistor will be off. Then, current flows through the nMOS transistor and the voltage at Y will be equal to ground which is connected to the nMOS source. That is, the voltage at Y will be low (0). It can be seen how the inverter changes a low input to a high output and a high input to a low output.

Table 5.1: Truth table for the CMOS inverter.

A (input)	Y (output)
0	1
1	0

5.3 The 6-Transistor SRAM Cell

The most common type of SRAM memory cell is the 6-transistor (6T) cell, which is shown in Fig. 5.5. As the name suggests, the 6T cell consists of six transistors: two access transistors A_1 and A_2, two nMOS transistors D_1 and D_2 and two pMOS transistors P_1 and P_2. A_1 and A_2 allow reading and writing content to the memory cell, while two cross-coupled inverters containing the D and P transistors hold the desired cell bit value, which is either 0 or 1. For stability, the state of the cell is stored by inverter 1 as Q, while the complement of the state is stored by inverter 2 as $\overline{\mathrm{Q}}$. The wordline and bitline signals (WL and BL, respectively) are used to read and write the cell as described below.

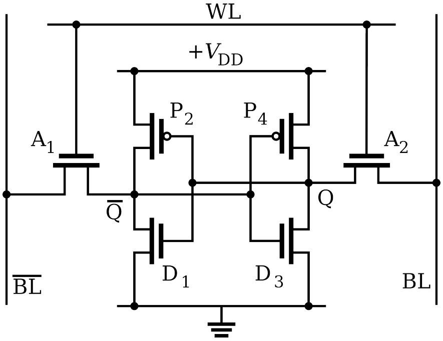

Figure 5.5: Schematic overview of a 6T SRAM cell, showing the two access transistors A_1 and A_2, and two cross-coupled inverters containing nMOS transistors D_1 and D_2 and pMOS transistors P_1 and P_2.

5.3.1 Reading from an SRAM Cell

Consider the case where the bit value of the cell is 0, i. e. $\mathrm{Q} = 0$ and $\overline{\mathrm{Q}} = 1$. To read the value of the cell from outside, the bitlines BL and $\overline{\mathrm{BL}}$ are floating at a high voltage. When the wordline WL is also put to high, the access transistors A_1 and A_2 both turn on. As current flows from BL through A_1 and D_1, the voltage at Q increases slightly. This rise is a compromise between the pull-down through D_1 and the current coming from A_1 — therefore D_1 must be stronger than A_1 to keep the value of Q low. This relationship is called read stability.

5.3.2 Writing to an SRAM Cell

Again consider the case where the bit value of the cell is 0. To write a value of 1 to the cell, the bitline BL is at a high floating voltage, while $\overline{\mathrm{BL}}$ is pulled down to a low voltage. By asserting the wordline WL, the access transistors turn on, and since the cell value should change now, the value of $\overline{Q}$ must be forced down by $\overline{BL}$. However, the transistor P_2, which is connected to a high voltage, resists this change, meaning that the access transistor A_2 must be stronger than P_2 to force the change to happen.

5.4 The Kintex-7 Configuration Memory

An SRAM memory is normally constructed as an array of SRAM cells, connected by wordlines and bitlines. The individual cells are arranged into n-bit words, so that a single bit in the array can be read or written by first setting the correct wordline to high (to select the correct word) and then setting the correct bitline to high or low depending on the desired memory-cell state. Therefore, each memory cell is assigned an address which is used to uniquely identify it in the memory.

The configuration memory of the Kintex-7 FPGA is arranged as an array of memory *frames*, which are structures consisting of 101 32-bit words each [87], as shown in Fig. 5.6. Therefore, the memory structure within a frame follows the general principle of an SRAM array. When the FPGA is programmed, a bitstream is loaded into the configuration memory. The bitstream contains information on the use of for instance routing, logical components and look-up tables in the device. The configuration memory occupies the largest portion of the FPGA resources, and holds the function of the device [85]. Because of this, a malfunction in one or several bits can have very severe consequences for the operation of the device. Such an error could for example lead to an error in the routing, which can cause erroneous treatment of data passing through the device, leading to corruption of the data. In PANDA, the high flux of ionising particles at the location of the FPGA-equipped front-end modules can be a major source of such errors. Therefore, the cause of radiation-induced errors, their effect in the device used, and ways to mitigate them must be well understood.

5.5 Radiation Damage in a CMOS Device

Research on radiation damage in integrated circuits (ICs) was initiated in the 1960s [89], and has been a growing field of study since then, due to the increased use of and continuous development of small-scale electronics. The questions in this field of research are connected both to electronics — because different IC components work differently — and physics — because the different methods of interaction between particles and matter must be understood. This work focuses on a specific subset of radiation effects: SEUs in the Kintex-7 configuration memory. However, the different types of radiation effects in a microelectronic device are summarised here.

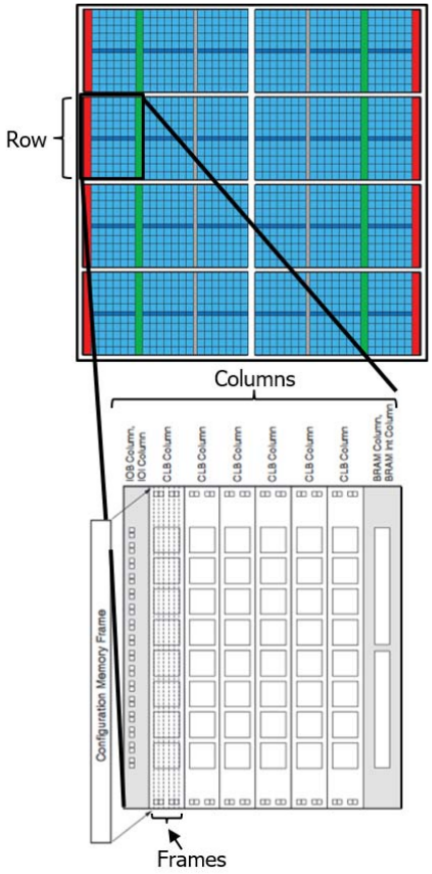
Row
Columns
IOB Column,
IOI Column
CLB Column
CLB Column
CLB Column
CLB Column
CLB Column
CLB Column
BRAM Column,
BRAM Int Column
Configuration Memory Frame
Frames

Figure 5.6: Layout of the Kintex-7 FPGA, showing the structure of the configuration memory frames. Figure taken from [88].

5.5.1 Charge Generation and Collection

In the context of SEUs, it is helpful to introduce the concepts of direct and indirect ionisation. These concepts are related to the energy-loss mechanisms introduced in Ch. 4, but here particles are separated based on whether or not they can cause ionisation by themselves. Since only electrically charged particles can cause direct ionisation in a material, they are the only ones that can cause SEUs directly. Heavy ions, which have a high stopping power, typically induce SEUs through direct ionisation. Charged particles with a lower stopping power, such as protons, may cause SEUs through direct ionisation to a lesser degree (if at all). Electrically neutral particles, such as the neutron, do not cause ionisation by themselves. They can, however, cause SEUs through for example nuclear reactions where the outgoing reaction product is charged and causes direct ionisation. Such processes are indirectly ionising. It is worth noting that directly ionising particles can also cause indirect ionisation, such as proton-induced nuclear reactions.

The cross sections for various proton-silicon nuclear reactions, as a function of the incident-proton energy, are shown in Fig. 5.7. It is clear that there is a maximum in the total cross section at a proton energy of approximately 20 MeV. However, the elastic-scattering cross section, which is non-zero at lower energies, is not included here. The cross section for a proton- or neutron-induced SEU is related to the total-reaction cross section, but it also depends on the kinematics of the particles in the exit channel of the reaction. As seen in Fig. 4.3, a collision between a 20-MeV proton and a silicon nucleus can result in a recoiling nucleus with a kinetic energy of up to 2.7 MeV, which corresponds to a range of approximately 2 μm in silicon [90]. It is evident that a higher incident-nucleon momentum can result in a higher recoil energy and therefore a longer recoil range.

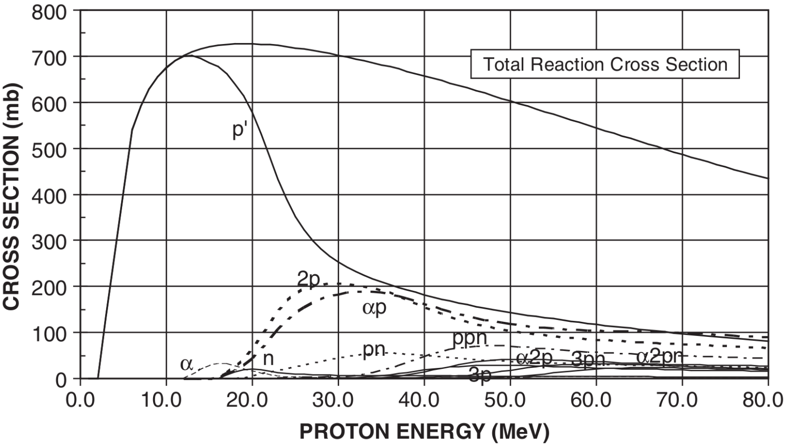

Figure 5.7: Cross sections for various proton-silicon nuclear reactions, excluding elastic scattering. Figure taken from [91].

When an ionising particle travels through a CMOS SRAM structure, it will leave a trail of free charges along its path. In the SRAM cell, there are several depletion layers belonging to the different p–n junctions in the cell. These depletion layers are present between the source regions and the body, between the drain regions and the body, and between the well regions and the body. As charges are liberated in the material, they may be collected at the transistor nodes, thus forming a current and potentially disrupt the state of the memory cell.

The charges liberated inside a depletion region may be efficiently collected by the electric field that is present. This swift collection results in a drift current, which is accompanied by a much slower diffusion current, formed by charges diffusing into the depletion layer where they are collected. This is shown in Fig. 5.8. While the original depletion region of the junction is relatively small, the region with a high electric field may be extended by an incoming particle which distorts the original field. This is known as the funnelling effect [92], and is shown in Fig. 5.8.

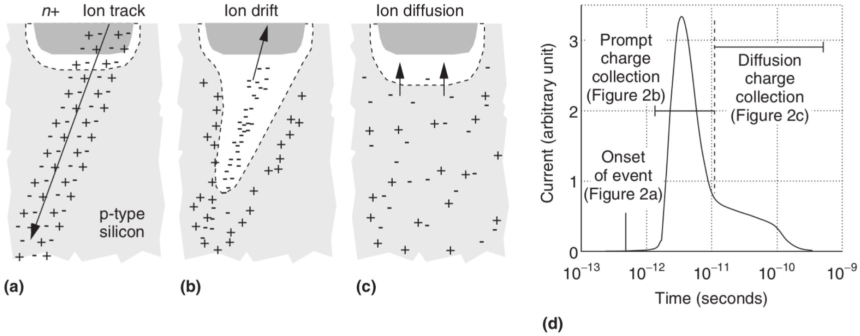
n+
Ion track
Ion drift
Ion diffusion
p-type silicon
(a)
(b)
(c)
Prompt charge collection (Figure 2b)
Diffusion charge collection (Figure 2c)
Onset of event (Figure 2a)
Current (arbitrary unit)
0
1
2
3
10^-13
10^-12
10^-11
10^-10
10^-9
Time (seconds)
(d)

Figure 5.8: Charge collection by an n^+ node in a transistor. In a), an ionising particle liberates charge in the material. The drift current, i.e. the swift collection of charge by the electric field, is shown in b). In c), the much slower diffusion current is illustrated. The white region is the depletion layer, which is extended in b) due to the funnelling effect. The time structure of the resulting current is shown in d) (note the logarithmic scale on the horizontal axis). Figure taken from [93]. © 2005 IEEE.

The current densities associated with the flow of electrons, J_n, and holes, J_p are described by the carrier transport equations [94]:

$$J_\mathrm{n} = -e\mu_\mathrm{n} nE - eD_\mathrm{n}\nabla n, \tag{5.1}$$

$$J_\mathrm{p} = e\mu_\mathrm{p} pE - eD_\mathrm{p}\nabla p, \tag{5.2}$$

where e is the elementary charge, μ is the carrier mobility, n and p are the concentrations of negative and positive charges, and D is the diffusion coefficient. Note that the diffusion current does not depend on whether any electric fields are present. As shown in Fig. 5.8, the drift current reaches the sensitive node at a much earlier stage than the diffusion current. Because of this, the current reaching the node is often modelled as a double-exponential in circuit models [92].

5.5.2 Sensitive Regions in an SRAM

In a 6T SRAM cell (see Sec. 5.3), the drain nodes are the most sensitive to SEU errors, since the state of the whole cell is kept by the voltages at the drains of the two inverters. We first consider the case where the gate voltage in one of the inverters is A = 0 and an ionising particle hits the nMOS drain. Because of the value of A, the nMOS transistor is initially turned off. Therefore, the voltage Y at the nMOS drain is Y = 1 initially. Since the p-type body is connected to ground, the drain-body p–n junction is reverse biased by default, meaning that there is an electric field present in the depletion layer between the drain and the body. Negative charges liberated by the ionising particle will therefore be collected at the drain. This creates a current at the nMOS drain, which flows from the nMOS drain, through the pMOS drain and source, which is connected to a voltage of $+V_{\mathrm{DD}}$. The pMOS transistor here acts as the restoring transistor to remove the excess charge, and while doing so a voltage drop results at the pMOS drain while the charge is being removed. This voltage drop looks similar to the write pulse of the SRAM cell, discussed in Sec. 5.3, and propagates to the transistor gates of the other inverter of the cell. If the restoring transistor does not manage to remove the excess charge fast enough, the voltage drop will cause the other inverter to flip, changing the bit value of the entire cell. This is what is known as an SEU.

To determine which regions in the SRAM are most sensitive to SEUs, one may consider the four possible drain states in the cell: on- and off-nMOS, and on- and off-pMOS transistors. Since the off-nMOS has already been discussed, the following list describes the responses of the three other states to an ionising particle:

- On-nMOS drain: the source and drain of this transistor are both connected to ground, as is the p-type body. Therefore, there is no strong electric field between the drain and the body due to biasing of the junctions. Thus, electrons will only be drawn to the drain by the intrinsic field in the depletion layer. The resulting drift current of electrons to the drain results in a slight forward-bias of the drain-body junction (since the drain potential is lowered by the collected electrons). However, the lowering of the on-nMOS drain potential does not result in an SEU. This is because the nMOS source is connected to ground and the logic state of the transistor (logic low) is simply enforced by the transient current.

- On-pMOS drain: the source and drain of this transistor are both connected to $+V_{\mathrm{DD}}$, as is the n-type body. Therefore, there is no strong electric field between the drain and the body due to biasing. The situation here is the same as in the on-nMOS case, with the only difference that the collected charges are positive and that the state which is enforced is a logic high.

- Off-pMOS drain: the source of this transistor is connected to $+V_{\mathrm{DD}}$ while the drain is connected to ground. The p-type body is connected to $+V_{\mathrm{DD}}$ so that the reverse-biased drain junction very efficiently collects positive charges. The result is the same as in the case of the off-nMOS transistor, described in detail above, so that the charge collection in the case of the off-pMOS also leads to an SEU.

While this reasoning demonstrates that the off-drain transistors in the SRAM cell are generally the ones most sensitive to SEUs, there are other effects which are not discussed here. For example, drains located in wells may have a different sensitivity than the drains placed directly within the substrate [92].

5.5.3 Critical Charge

There are obviously a number of parameters that determine how sensitive a particular device is to SEUs. However, one can generally say that since an SEU is caused by the induced transient current, it is important to study the magnitude and time-structure of this current. The exact amount of charge Q_{coll} that is collected at the sensitive node depends on complex factors such as the geometry of the device, the voltages in the memory cell and the materials present in it. The risk of an SEU occurring does however not only depend on Q_{coll}, but also on how the cell handles the excess charge. Here, the electrical properties of the components come into play, so that the connection between the amount of generated charge by the ionising particle and the SEU risk becomes very complex. For this reason, it is common to define a critical charge Q_{crit} as the amount of collected charge required to cause an SEU:

$$Q_{coll} \geq Q_{crit} \Rightarrow \text{SEU},$$

$$Q_{coll} < Q_{crit} \Rightarrow \text{NO SEU}.$$

By combining the concept of critical charge with the topics discussed earlier in this chapter, one can in a simple model use the fact that the amount of generated charge directly depends on the LET of the ionising particle travelling through the device. Therefore, the SEU sensitivity is in such a model directly connected to the LET, so that the charge liberated by a low-LET particle will affect the potential in the struck node, but not enough to cause the cell to flip. A high-LET particle will liberate enough charge to cause the cell to flip. Somewhere between these extremes is a LET value corresponding to an amount of generated charge just able to flip the cell. This is called the threshold LET value. This is illustrated in Fig. 5.9 for three particular incident particles, where LET values of 9 and 40.5 MeV cm^2 mg^{-1} are not able to cause the bit to flip, whereas a LET value higher than 42 MeV cm^2 mg^{-1} is able to cause the bit to flip.

While the concept of critical charge simplifies the task of modelling SEUs in circuits, one should note that it is a simplification that neglects the time structure of the generated current[92]. However, to determine the time structure of the current, as well as other parameters related to the circuit itself, more detailed knowledge of the memory device is needed. In this work, this is not well known, and therefore the concept of critical charge will be the basis of the discussions in subsequent chapters.

The constantly ongoing decrease in IC feature size means that the capacitance, charge storage and noise margin of a single SRAM cell have decreased with time as well. Since lower values on these parameters result in a lower amount of charge

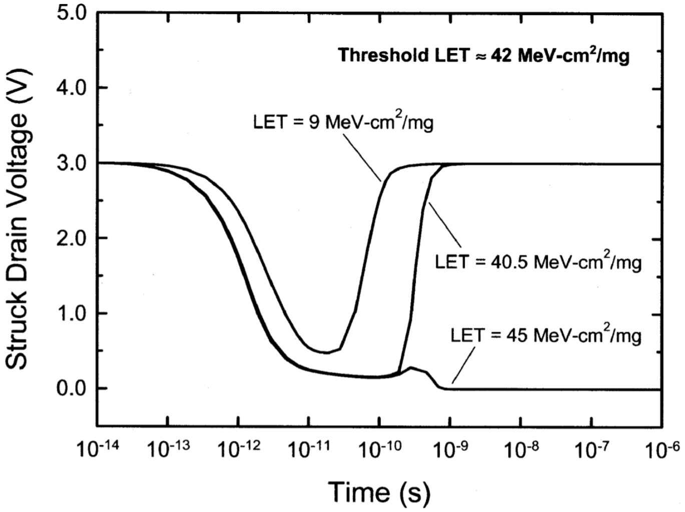

Figure 5.9: Struck drain voltage as a function of time for three different LET values. An ionising particle with a low LET will only generate a small amount of free charge, which is not enough to cause an SEU. However, it might be enough to temporarily alter the potential at the collecting node. A high-LET particle generates a comparatively large amount of charge, which when collected causes the bit-value of the cell to change. This is seen as the permanent change in the drain voltage. Figure taken from [92]. © 2003 IEEE.

needed to disrupt the memory cell, the critical charge has also decreased with decreasing feature sizes [95]. For a 28-nm device, the critical charge has been estimated to be less than 0.5 fC [96], which corresponds to approximately 3000 electrons.

5.6 SEU Bit Multiplicity

Depending on the structure of the trajectory of an SEU-causing ionising particle and on the feature size and charge-collection capability of the device, more than one bit can be upset by a single particle [97]. Such an event is called a multi-bit upset (MBU), whereas an SEU only affecting one bit is known as a single-bit upset (SBU). MBUs have been studied extensively in the past, as they are more difficult to mitigate than SBUs [97]. In the Kintex-7 configuration memory, MBUs may be further categorised as inter-frame and intra-frame MBUs [98], where inter-frame MBUs are events where multiple bits spread out over several configuration-memory frames have been affected and intra-frame MBUs are events affecting multiple bits within a frame.

5.7 The SEU Cross Section

The SEU cross section σ_{SEU} is a measure of the probability of an SEU occurring in a particular IC device. It is used to characterise the sensitivity of a device in different radiation environments, and is commonly normalised to the number of memory cells, or bits, in the device to allow direct comparison between different technologies. To determine σ_{SEU} with as good accuracy as possible, accelerated testing of the device — that is, irradiating the device at a particle flux higher than the one expected during operation — is the recommended method [99]. In such a measurement, the number of SEUs that occur should be monitored. Then, using the concepts outlined in Sec. 4.1.1, the SEU cross section per bit is defined as:

$$\sigma_{\mathrm{SEU}} = \frac{N_{\mathrm{SEU}}}{\Phi N_0}, \tag{5.3}$$

where N_{SEU} is the number of SEUs that have occurred during the irradiation, Φ is the total particle fluence during the irradiation, and N_0 is the number of bits in the device memory.

One way to determine σ_{SEU} is through irradiation with various heavy ions. These particles are highly ionising, and can therefore easily cause SEUs through direct ionisation. As different ions have different LETs, such a measurement gives σ_{SEU} as a function of LET. This information can be valuable when comparing different devices, and when the device is expected to be subjected to high fluxes of high-LET particles during operation. Also, since most of the SEUs caused by heavy ions are due to direct ionisation (where the charge generation along the track of the particle is related to the LET), heavy-ion irradiation can be used to deduce information about the charge collection in the device [100].

In addition to heavy-ion irradiations, high-energy protons and neutrons have long been used to characterise the SEU sensitivity of a device. As the primary source of SEUs in the PANDA EMC is not expected to be heavy ions, studying the response of the FPGA to protons and neutrons, which mainly cause SEUs through indirect ionisation, is of interest. The rest of this work will focus on determining the cross sections for SEUs induced by protons and neutrons of various energies, both through experiments and theoretical modelling.

6. Experiments

In order to investigate the sensitivity of the FPGA configuration memory to SEUs induced by neutrons and protons of different energies, a series of irradiations of the front-end digitiser were performed:

- In June 2016, the board was irradiated with a beam of neutrons having a continuous energy spectrum up to 180 MeV at the The Svedberg Laboratory (TSL) in Uppsala, Sweden.
- In November 2016, the board was irradiated with monoenergetic protons with energies of 80, 100 and 184 MeV at the Kernfysisch Versneller Instituut — Center for Advanced Radiation Technology (KVI-CART) in Groningen, the Netherlands.
- In December 2017 and January 2018, the board was irradiated with neutrons from radium-beryllium (RaBe) and americium-beryllium (AmBe) neutron sources at Stockholm University. The neutrons had continuous energy spectra up to approximately 12 MeV.

This chapter describes the experiments, the subsequent data analysis and the experimental results.

6.1 Experimental Setup

In all experiments, the digitiser board was placed perpendicular to the direction of the particle flux, as shown in Fig. 6.1. It was positioned such that the beam was centred on one of the two FPGAs, and was fully powered on throughout all irradiations. Only the FPGA on which the beam was centred was monitored for SEUs.

6.1.1 Xilinx Soft Error Mitigation Controller

During the irradiations, the Xilinx Soft Error Mitigation (SEM) controller [101] was implemented in the FPGA firmware to detect and correct SEUs. As discussed in Sec. 5.4, the FPGA configuration memory is divided into a large number of frames, each consisting of 101 32-bit words. In the way SEM was configured during the

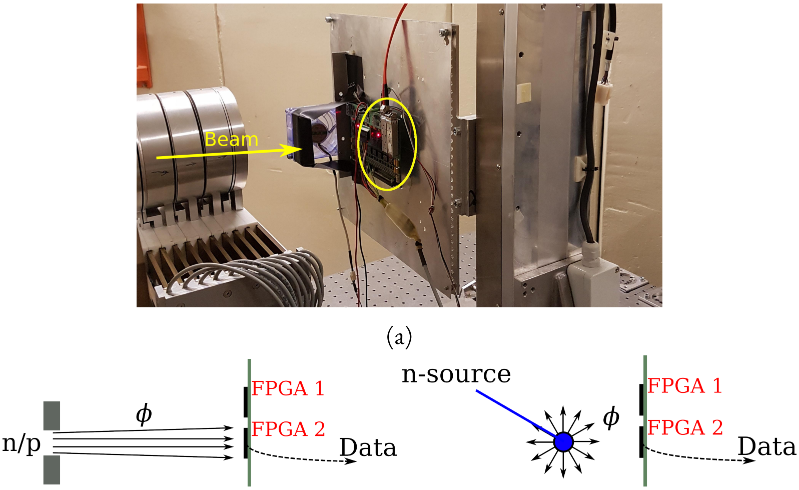

(a)

(b)

(c)

Figure 6.1: a) Photograph of the experimental setup during the proton irradiations. The digitiser board was positioned such that the beam was centred on one of the two FPGAs (indicated by the yellow ellipse). In b), the setup during the neutron- and proton-beam irradiations is shown. In c), the setup during the neutron-source irradiations is shown.

experiments, the majority of all SEUs occurring in the configuration memory were corrected with the use of an error-correcting code (ECC) algorithm. Specifically, all SBUs as well as all inter-frame MBUs could be corrected. More complex errors, such as intra-frame MBUs, could not be corrected by SEM.[1] In fact, SEM reported the number of *errors* due to SEUs, which did not correspond to the actual number of upset bits in all cases. Three types of errors were reported by SEM:

- A *correctable* error was an error which was found and corrected by SEM. In all cases, a correctable error corresponded to a single upset bit, either as part of an inter-frame MBU or as a standalone SBU.
- An *uncorrectable* error was an error which was found but not corrected by SEM. An uncorrectable error therefore corresponded to an intra-frame MBU, where more than one bit were upset.
- A *CRC-only* error was a more complicated uncorrectable error, where SEM did not manage to track the location of the error. Such errors most likely also corresponded to more than one upset bit.

---

[1] SEM can be configured to correct also more complex SEUs as well — this is a topic of future work.

As the FPGA was powered on, SEM was initialised by reading the correct state of the device firmware. After initialisation, SEM continuously monitored the memory to detect any unexpected changes due to SEUs. During the irradiations, the state of SEM was continuously read out via a serial link. When an error occurred the time of the error was reported, as was the location of the error in the memory in case the error was correctable.

6.1.2 Proton Irradiation

The digitiser board was irradiated with protons of three different energies at the AGOR Facility for Irradiations of Materials (AGORFIRM) at KVI-CART [102]. The AGOR cyclotron was used to accelerate protons to an energy of 190 MeV. The primary beam was collimated using a circular collimator with a diameter of 120 mm, and was centred on one of the two FPGA. As the digitiser board was placed in air, after the AGORFIRM beamline, the maximum proton energy at its location was 184 MeV. The digitiser board was irradiated with protons of this energy, as well as with 80 and 100 MeV protons which were obtained by placing aluminium degraders in front of the digitiser. The energy resolution of the beam was a few MeV [102, 103]. Before each of the three measurements, the system was calibrated so that the proton fluence could be determined. The average fluence rate (the number of incident particles per unit area and time) during the proton irradiations was $7 \cdot 10^5$ cm^{-2} s^{-1}.

6.1.3 High-Energy Neutron Irradiation

The digitiser board was irradiated with a beam of neutrons at the ANITA neutron source at TSL [104]. The neutron beam was produced by directing a 180-MeV proton beam from a cyclotron into a 2.4-cm thick tungsten target. The proton beam was fully stopped inside the target, and neutrons were produced in nuclear reactions. The resulting neutron beam was collimated with a circular iron collimator with a diameter of 100 mm. The digitiser board was placed 250 cm downstream of the tungsten target, where the beam covered approximately half of the digitiser.

Since the neutrons were produced through spallation in a tungsten target, they had a continuous energy distribution, with the maximum neutron energy approximately equal to the energy of the original proton beam. The energy spectrum of the TSL neutron beam has been parameterised [104], and is shown in Fig. 6.2. The neutron fluence rate at the location of the digitiser board was determined on a second-by-second basis by measuring the current from the full-stop proton target. According to standard procedure [105], only neutrons with energies above 10 MeV were included in the fluence determination. This low-energy cutoff has traditionally been motivated by the assumption that neutrons with energies below 10 MeV do not contribute to the SEU rate. The average fluence rate during the high-energy neutron irradiation was $1 \cdot 10^6$ cm^{-2} s^{-1}.

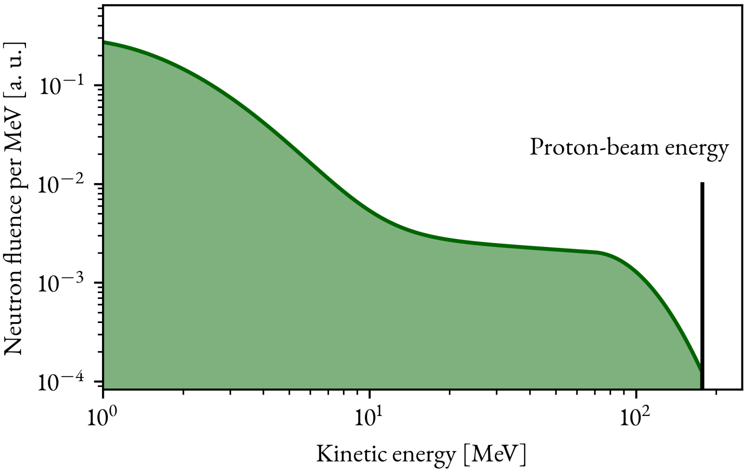

Figure 6.2: Neutron energy spectrum at the location of the digitiser at TSL, normalised to one. The maximum neutron energy corresponds to the energy of the primary proton beam, 177 MeV. Data taken from [104].

6.1.4 Low-Energy Neutron Irradiations

During two separate measurements, the digitiser board was irradiated with neutrons from two ^{9}Be(α, n) neutron sources at Stockholm University: a 9 GBq RaBe neutron source and a 10 GBq AmBe neutron source (activities are nominal values supplied by the producers).

Both ^{226}Ra and ^{241}Am are α-emitters. When they are combined with ^{9}Be, the emitted α particles may be captured by the ^{9}Be nucleus, leading to the emission of neutrons in the decay of formed unstable states of ^{13}C. The energy of an emitted neutron depends on the energy of the α particle, and whether the nuclei that are involved in the reaction are left in excited states. The maximum neutron energy is approximately 12 MeV for both sources [106], which is seen in Fig. 6.3, where both neutron spectra are shown. Due to the similarities in the nuclear reactions involved, the two spectra are very similar, with the major difference being that the fraction of neutrons with low energies is larger for the RaBe source.

The neutron intensities from the two sources were determined using two separate neutron activation analysis measurements: first, the relative intensity of the two sources was determined to be $I_{\mathrm{n}}(\mathrm{AmBe})/I_{\mathrm{n}}(\mathrm{RaBe}) = 0.53 \pm 0.02$ through neutron activation of indium (the uncertainty corresponds to one standard deviation). Second, the absolute neutron intensity of the RaBe source was determined to be $(1.4 \pm 0.3) \cdot 10^{6}\ \mathrm{s}^{-1}$ through neutron activation of antimony. Combining these

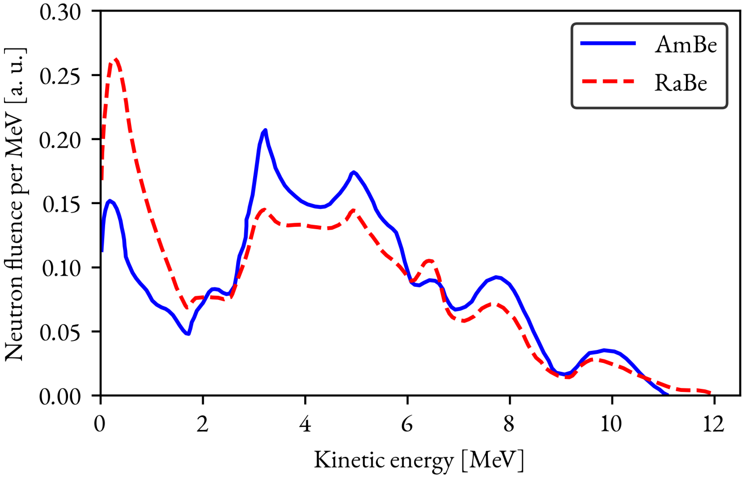

Figure 6.3: Neutron-energy spectra for RaBe and AmBe neutron sources. The integrals of the spectra have been normalised to one. Data taken from [106].

two measurements, the neutron intensity of the AmBe source was determined to be $(0.7 \pm 0.2) \cdot 10^6$ s^{-1}.

During both irradiations, the digitiser board was placed 5 cm from the neutron source. Both sources were placed in leak-tight metal capsules. Due to the long and complex decay chain of ^{226}Ra, a photon fluence approximately 6000 times larger than the neutron fluence was present during the RaBe irradiation. This was determined from the known activity of the radium in the source, where each disintegration yields on average 2.2 photons throughout the radium decay chain [107]. These photons have energies up to several MeVs, and since the cross section for SEUs caused by these photons is unknown, the possibility that photons contribute to an observed SEU rate cannot be excluded. During the AmBe irradiation, the photon flux was much smaller due to the simpler decay of ^{241}Am, with the majority of the emitted photons from the AmBe source having an energy of 60 keV. During the AmBe irradiation, a 2 mm Pb sheet was placed between the source and the digitiser in order to reduce the fluence of 60-keV photons by a factor of approximately 10^5 [60]. The attenuation of neutrons due to the Pb sheet was approximately 1% [108]. In addition to the SEU cross section measured with the AmBe source shielded by the Pb sheet, the cross section was determined when the sheet was removed. No difference in the cross section was observed, and so the cross section determined from the Pb-shielded measurement was used in the analysis. The average flux of neutrons at the location of the digitiser during the RaBe irradiation was $4 \cdot 10^3$ cm^{-2} s^{-1}, and

$2 \cdot 10^3$ cm^{-2} s^{-1} during the AmBe irradiation.

Although any potential contribution to the SEU rate from photons is unknown, the mean energy deposition of electrons in silicon is expected to increase at low electron energies, as shown in Fig. 4.1. Therefore, the low-energy electrons generated in interactions between photons from the source and silicon are the most dangerous in the context of SEUs. The cross section for SEUs induced by 1- and 20-MeV electrons in 28-nm and 45-nm devices have been measured in the past [109, 110]. Together with previous measurements of the Kintex-7 neutron cross section [98], these results indicate that the cross section for 1 MeV electrons in the device is approximately 10^6 times smaller than the neutron cross section. The energies of the electrons generated when photons interact in the device follow a distribution that depends on the energies of the photons from the source. Assuming that the probability that these secondary electrons cause an SEU is approximately given by the 1-MeV electron SEU cross section, it may be combined with the probability that a photon generates an electron close enough to a memory cell, to give the SEU cross section for photons. The probability that an incident photon interacts in a silicon volume with a size equal to the maximum electron range was determined to be approximately 10% using photon cross sections and particle-range data [59, 60], so that an upper limit on the resulting flux of secondary electrons could be determined. Combining this with the electron SEU cross section, the cross section for photon-induced SEUs is expected to be approximately 10^7 times smaller than the neutron cross section. Because of this, and as no difference was seen in the SEU cross section when the AmBe source was shielded with a Pb sheet, any contribution from photons to the observed SEU rate was assumed to be negligible during both irradiations.

6.2 Data Analysis

The SEU cross section per configuration-memory bit was determined using Eq. 6.1:

$$\sigma_{\mathrm{SEU}} = \frac{N_{\mathrm{SEU,\,exp}}}{\Phi_{\mathrm{exp}} \cdot N_0}, \tag{6.1}$$

where $N_{\mathrm{SEU,\,exp}}$ is the number of bits upset during the irradiation, Φ_{exp} is the particle fluence (i. e. the flux integrated over the duration of the measurement) and N_0 is the total number of bits in the FPGA configuration memory. In the following sections, the input quantities of Eq. 6.1 will be described in more detail. The determination of the expected values and standard deviations of the experimental cross sections is also described. This was done using Monte Carlo techniques, in which the input parameters and their uncertainties are treated on a fundamental level [111].

6.2.1 Number of Upset Bits

During the irradiations, SEM reported correctable, uncorrectable, and CRC-only errors. The total number of errors of each type — $N_{\text{corr}}^{\text{obs}}$, $N_{\text{uncorr}}^{\text{obs}}$ and $N_{\text{CRC}}^{\text{obs}}$ — observed during the six measurements are shown in Tab. 6.1.

Table 6.1: Beam properties and number of errors of each type observed during the six irradiations.

Particle	E [MeV]	$\langle \Phi_{\text{exp}} \rangle$ [cm^{-2}]	$N_{\text{corr}}^{\text{obs}}$	$N_{\text{uncorr}}^{\text{obs}}$	$N_{\text{CRC}}^{\text{obs}}$
Proton (KVI-CART)	80	$1.2 \cdot 10^9$	312	19	4
Proton (KVI-CART)	100	$1.7 \cdot 10^9$	391	18	4
Proton (KVI-CART)	184	$1.4 \cdot 10^9$	269	14	2
Neutron (TSL)	< 180	$2.1 \cdot 10^9$	549	22	2
Neutron (RaBe)	< 12	$3.0 \cdot 10^9$	91	2	0
Neutron (AmBe)	< 12	$4.3 \cdot 10^9$	117	2	0

Because the actual number of upset bits corresponding to uncorrectable and CRC-only errors were not reported by SEM, $N_{\text{SEU, exp}}$ had to be estimated from the number of observed errors. In general, the bit multiplicity M may be defined as the number of upset bits per error — correctable, uncorrectable or CRC-only. The number of upset bits $N_{\text{SEU, exp}}$ is then related to the number of correctable, uncorrectable and CRC-only errors N_{corr}, N_{uncorr} and N_{CRC}:

$$N_{\text{SEU, exp}} = \sum_{i=1}^{N_{\text{corr}}} M_{\text{corr}}^{(i)} + \sum_{i=1}^{N_{\text{uncorr}}} M_{\text{uncorr}}^{(i)} + \sum_{i=1}^{N_{\text{CRC}}} M_{\text{CRC}}^{(i)}, \tag{6.2}$$

so that the actual bit multiplicities for all individual errors are summed to give the total number of upset bits. Three probability density functions (PDFs) — g_{corr}, g_{uncorr} and g_{CRC} — describing the probability that an error of a certain type corresponds to M upset bits may be defined. Since SEM could correct SBUs and intercell MBUs, the number of bits associated with the correctable errors was equal to the number of correctable errors, and was determined directly from the SEM logfile. Therefore, $g_{\text{corr}}(M) = \delta_{1,M}$. The PDFs describing the multiplicities for uncorrectable and CRC-only errors were estimated using previously published data on intra-frame MBUs in Kintex-7 [98]. These data were taken during an irradiation with neutrons below 600 MeV and included bit multiplicities up to $M = 6$. In general, the multiplicity PDFs are expected to depend on the incident-particle type and energy [97], but since the mechanisms by which neutrons and protons cause SEUs are similar, the previously published results were taken to describe a scenario similar to the experiments in this work. Here, g_{uncorr} and g_{CRC} are assumed to be identical. The multiplicity PDFs for the three error types are given in Tab. 6.2. In Sec. 6.2.4, these PDFs together with the data in Tab. 6.1 are used to determine the SEU cross sections.

Table 6.2: Probabilities for different bit multiplicities $\mathcal{M}$ for the error types reported by SEM.

Error type	Multiplicity $\mathcal{M}$					
	1	2	3	4	5	≥ 6
Correctable	100%	0%	0%	0%	0%	0%
Uncorrectable*	0%	76%	14%	6%	3%	2%
CRC-only*	0%	76%	14%	6%	3%	2%

* Data taken from [98].

6.2.2 Particle Fluence

The systematic uncertainties in the beam fluences were estimated to be 10% for both the high-energy proton and high-energy neutron irradiations. For the two low-energy neutron irradiations, they were estimated to be 30%, based on the estimated uncertainties in the neutron-emission rates and the placement of the source inside the leak-tight capsules and relative to the digitiser. The uncertainties in the fluences were modelled as normal distributions centred at the means of the measured fluences, $\langle \Phi_{\text{exp}} \rangle$.

6.2.3 Number of Configuration-Memory Bits

The total number of bits in the FPGA configuration memory was given in the SEM logfile, and served to normalise the cross section to a per-bit value. As this value was assumed to be known without any uncertainty, it simply entered the calculation as a scaling constant.

6.2.4 SEU Cross Sections

Inserting Eq. 6.2 into Eq. 6.1, a general expression for the SEU cross section is given by:

$$\sigma_{\text{SEU}} = \frac{\sum_{i=1}^{N_{\text{corr}}} \mathcal{M}_{\text{corr}}^{(i)} + \sum_{i=1}^{N_{\text{uncorr}}} \mathcal{M}_{\text{uncorr}}^{(i)} + \sum_{i=1}^{N_{\text{CRC}}} \mathcal{M}_{\text{CRC}}^{(i)}}{\Phi_{\text{exp}} \cdot N_0}, \tag{6.3}$$

where each input quantity has an associated PDF, as described in Secs. 6.2.1, 6.2.2 and 6.2.3. A summary of the input-quantity PDFs is given in Tab. 6.3.

Table 6.3: Summary of the PDFs related to the input-quantities needed for determining the SEU cross section for a particular measurement.

Quantity	Associated PDF	PDF parameter values
N_{corr}	Poisson(λ)	$\lambda = N_{\mathrm{corr}}^{\mathrm{obs}}$, number of correctable errors
M_{corr}	g_{corr}	Full PDF given in Tab. 6.2
N_{uncorr}	Poisson(λ)	$\lambda = N_{\mathrm{uncorr}}^{\mathrm{obs}}$, number of uncorrectable errors
M_{uncorr}	g_{uncorr}	Full PDF given in Tab. 6.2
N_{CRC}	Poisson(λ)	$\lambda = N_{\mathrm{CRC}}^{\mathrm{obs}}$, number of CRC-only errors
M_{CRC}	g_{CRC}	Full PDF given in Tab. 6.2
Φ_{exp}	Normal(μ, σ^2)	$\mu = \langle \Phi_{\mathrm{exp}} \rangle$, the measured fluence σ = 10–20% of the measured fluence*
N_0	N/A	Number of configuration-memory bits, constant

* The uncertainty in the fluence was different for the different measurements, as described in Sec. 6.2.2.

Using Monte Carlo techniques, input-quantity values were generated from their respective PDFs for each of the six measurements. Each set of generated values was used to determine the resulting SEU cross sections via Eq. 6.3. As this procedure was repeated a predefined number of times, the input-quantity PDFs were propagated through Eq. 6.3 to give the PDFs for the SEU cross sections. These PDFs include the expected value of the cross section and the total uncertainty, to which both statistical and systematic effects contribute. The resulting PDF for the 80-MeV proton SEU cross section is shown in Fig. 6.4, where the expected value and standard deviation are indicated. The expected values and standard deviations of all obtained PDFs, which were the results of the six irradiations, are shown in Tab. 6.4. Here, also the expected values of the total number of observed SEUs, $\langle N_{\mathrm{SEU,\,exp}} \rangle$, which were processed in the analysis, are given. In Figs. 6.5 and 6.6, the results are compared with previous measurements of the Kintex-7 cross sections.

One must be aware that there are differences between the experiments presented here and those reported earlier, both in terms of the exact FPGA part number, the accelerator facility used and the error-detection and -correction method used. In the previous experiments, FPGA part numbers XCK70T [88, 112] and XCK325T [98, 113–115] were used, compared to XCK160T in the present work. All of these are Kintex-7 FPGAs, and the FPGA part number determines the amount of available resources in the FPGA. In the previous measurements, 30-MeV [115], 35-MeV [112], 62-MeV [88], 64-MeV [113], 105-MeV [114] and 180-MeV protons [98] and TSL neutrons [98] were used. Error detection and correction was performed using a configuration-memory readback after irradiation [98, 113, 114], using the SEM core

[112], using custom-made firmware [115] and by using external memory-scrubbing circuitry to detect and correct SEUs [88].

Table 6.4: Results of the experiments. The expected value of the total number SEUs and the expected value and standard deviation of each cross section are shown. The uncertainties include both the statistical and systematic uncertainties.

Particle	E [MeV]	$\langle N_{\text{SEU, exp}} \rangle$	SEU cross section [cm^2 bit^{-1}]
Proton (KVI-CART)	80	367 ± 21 [*]	$(7.5 \pm 0.9) \cdot 10^{-15}$
Proton (KVI-CART)	100	444 ± 23	$(6.4 \pm 0.7) \cdot 10^{-15}$
Proton(KVI-CART)	184	307 ± 19	$(5.4 \pm 0.6) \cdot 10^{-15}$
Neutron (TSL)[†]	< 180	607 ± 27	$(7.1 \pm 0.8) \cdot 10^{-15}$
Neutron (RaBe)	< 12	96 ± 10	$(9 \pm 4) \cdot 10^{-16}$
Neutron (AmBe)	< 12	122 ± 11	$(8 \pm 4) \cdot 10^{-16}$

[*] All uncertainties correspond to one standard deviation.

[†] Determined using the neutron fluence above 10 MeV.

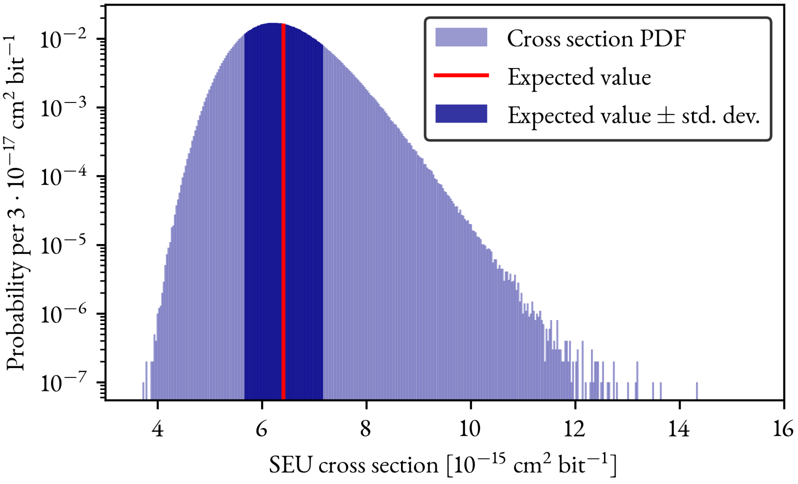

Figure 6.4: PDF corresponding to the 100-MeV proton SEU cross section, as determined from the Monte Carlo method described in Sec. 6.2.4. Note the logarithmic scale on the vertical axis.

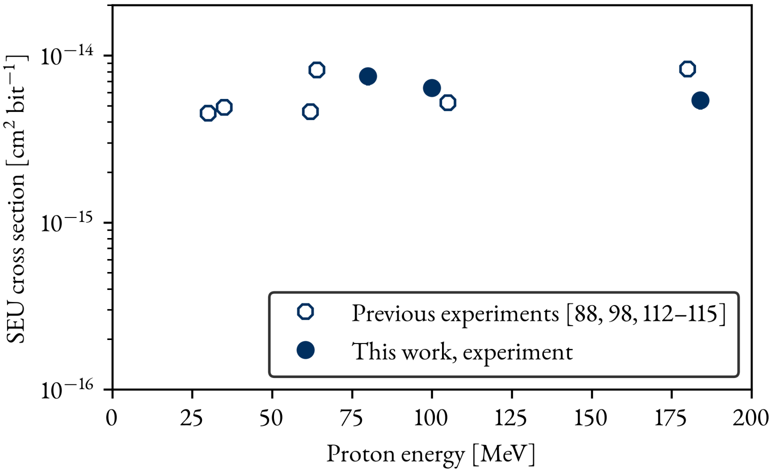

Figure 6.5: SEU cross section per configuration-memory bit, measured during the proton irradiations at 80, 100 and 184 MeV. The results from this work are compared with previous results on Kintex-7. Note the logarithmic scale on the vertical axis.

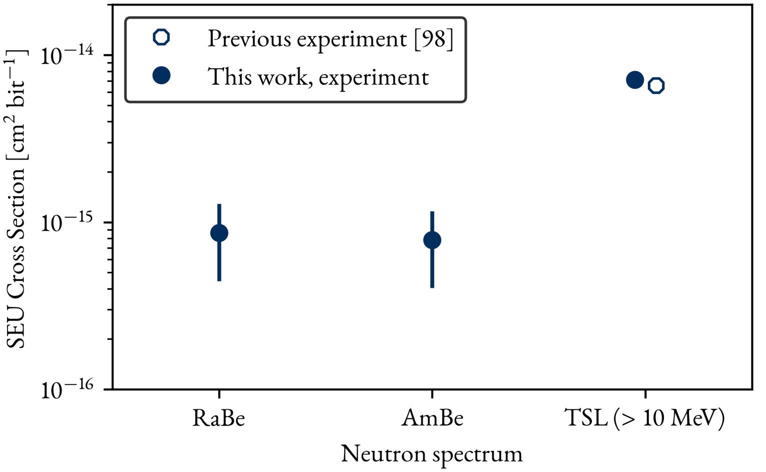

Figure 6.6: SEU cross section per configuration-memory bit, measured during the three neutron irradiations. The results from the TSL irradiation in this work are compared with previous results on Kintex-7. Note the logarithmic scale on the vertical axis.

7. Theoretical Modelling

The experimental results presented in Ch. 6 show that the Kintex-7 configuration memory is susceptible to SEUs induced by both protons and neutrons. However, the exact consequences for the operation of the front-end digitiser in the PANDA EMC are not clear from these results. In order to decide on how to mitigate SEUs in the device, an estimate of the error rate during operation in the EMC is needed. While it is common to use a single "worst-case" SEU cross section obtained through irradiations to obtain such an estimate, the methods developed here aim at giving a more complete picture of the energy-dependence in the proton and neutron cross sections. As part of this work, two Monte Carlo models of SEUs have been developed, which describe the memory cell as consisting of several volumes sensitive to energy deposition. This work was initiated with the work presented in Paper I, where an initial model is described. As this initial model differs from the subsequently developed models, it will not be discussed further in this thesis. The two models presented here should be seen as two additional stages in the evolution of the model. The first of these models is based on well-known methods in Monte Carlo simulations of SEUs, and was found to have some shortcomings that were subsequently addressed in the second of the two models. The second model, which is also described in Paper II, was developed with the aim of describing charge collection in a memory cell in a more realistic way than in traditional Monte Carlo models of SEUs. In both models, the energy deposition in the cell by protons and neutrons was simulated, and the free parameters of the models were obtained by fitting the model to the experimental data. Once the model was fitted to experimental data, it was used to predict the SEU rate in PANDA.

7.1 Modelling Single Event Upsets

Over the past 40 years, since the threat of SEUs was first recognised, a number of techniques for modelling SEUs has been developed and used to predict the error rates of different components in different radiation environments. As technology has evolved, the sensitivity of devices to different particles and charge-collection mechanisms has also changed, motivating an active research in the field. In order to give a full description of SEUs in microelectronics, a model should be able to incorporate seven aspects of relevance [116]:

1. The radiation field that the device is exposed to during operation should be quantified.
2. The material around the sensitive device should be described.
3. The energy deposited by the incident radiation should be modelled.
4. Generation of charge in the device.
5. Transport of charge in the device.
6. Response of the device transistors to the generated charge.
7. Response of the circuit to the collected charge.

Different models describing SEUs approach these requirements differently. In order to accurately model the interaction between radiation and matter (including the device itself), Monte Carlo methods are commonly used [116–118]. Charge transport in semiconductor devices may be calculated using technology computer-aided design tools [119], and circuit responses determined from circuit models [120]. Since these different modelling techniques are required to describe the generation of SEUs in a device, several tools provide a combination of them [116, 121, 122].

One of the most common models used when modelling SEUs in microelectronics is the rectangular parallelepiped (RPP) method [123]. It is based on the assumption that a sensitive region in the SRAM cell can, in the context of SEUs, be described as a sensitive volume (SV) having the shape of an RPP as shown in Fig. 7.1. As ionising particles travel through the SV, they deposit energy and generate free charges. As discussed in Sec. 5.5.1, an SEU occurs if enough charge is collected by a sensitive transistor. In the RPP model, the situation is simplified by assuming that the quantity of importance is the amount of charge *generated* in the RPP. If the amount of generated charge exceeds the critical charge $Q_{\mathrm{crit,\,RPP}}$, an SEU is said to have occurred. In this model, the SEU sensitivity of the device depends on the SV size and on the critical charge: a larger SV allows a larger amount of charge to be collected, resulting in a higher SEU sensitivity. A lowered critical charge also results in a higher SEU sensitivity as the probability for charge generation above the critical value increases.

Even though they only provide a simplified description of SEUs, for example excluding detailed descriptions of charge-transport mechanisms, models describing a single memory cell as a single RPP were very successful in predicting SEU rates for a very long time [123, 125–129]. However, the validity of using such models for describing devices with feature sizes below 100 nm has been questioned [130]. At such small length scales, liberated charges can be shared between adjacent transistors and memory cells, causing the assumption that a single memory cell may be modelled as a single SV to break down. These effects are, at least in part, due to

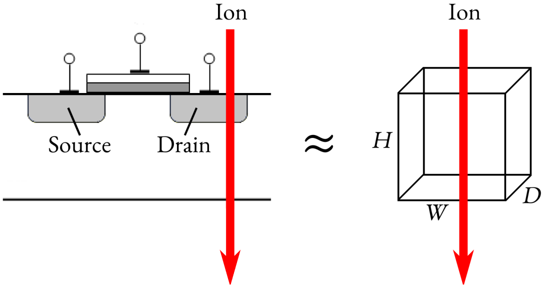

Figure 7.1: The RPP model. The sensitive part of the transistor is the drain, which is modelled as an RPP-shaped SV centred at the drain location. An ion passing through the SV generates charges, and in the RPP model the SEU sensitivity depends on the size of the SV and on the critical charge. Figure taken from [124].

the fact that transistors may collect charge through both drift and diffusion from within the memory structure [124]. Therefore, the RPP model is unphysical as it assumes that the charge-collection efficiency is constant and very high in a localised RPP volume, and zero outside. This shortcoming has been pointed out by others [131–133], and as will be seen in later sections, was the motivation for developing model 1 into model 2.

In this work, the aim has been to develop a model of SEUs in FPGAs that incorporates radiation-transport simulations and requires very little knowledge of the fundamental properties of the FPGA memory. These properties include the exact material composition of the device and information about the circuitry and voltages in the FPGA. In this chapter, two stages in the development of such a model are described. As they are fully independent models, they will be referred to as *model 1* and *model 2*. Model 1 is based on a traditional RPP approach, although incorporating some sub-cell structure of the memory instead of treating the whole cell as a single RPP. Model 2 provides an extension to the RPP model, and includes modelling of charge collection through both drift and diffusion. As such, it aims at a more realistic description of the phenomenon while still maintaining the requirements on model simplicity. Both models are based on the radiation-transport modelling toolkit Geant4 (Geometry And Tracking 4) [134, 135], and common features in the Geant4 setup will be described in the following sections, before the two models are described in more detail.

7.2 Geant4 Setup

Geant4 is a free toolkit that uses Monte Carlo methods to simulate the transport of particles in matter. It is mainly used for modelling detector systems in high-energy and nuclear physics, but can also be used to model radiation effects in microelectronics [116–118, 122]. Depending on the application of the toolkit, the properties of the the radiation-transport simulation can be optimised and tuned to give realistic results for the relevant particle types, energies and length scales. In this work, Geant4 was used to simulate proton and neutron interactions in matter, while the charge-generation and charge-collection modelling was developed independently. The output of the Geant4 modelling thus couples to the subsequent parts of the SEU model to allow SEU predictions for any incident-particle scenario.

7.2.1 Geometry Definition

To model the interactions of particles inside the SRAM cell, a simplified geometrical model of the cell was constructed in Geant4. As CMOS feature sizes have decreased over recent years, the area of a single SRAM cell has continuously scaled down. The scaling trend makes it possible to approximate the cell area A_{cell} at a given feature size F [136]:

$$A_{\text{cell}} \simeq 150F^2. \tag{7.1}$$

The Kintex-7 has a feature size of $F = 28$ nm, which by using this equation corresponds to a cell area of 0.12 μm^2.

Based on the physical layout of a general SRAM cell at feature sizes similar to the one in the Kintex-7 [137], the ratio between the width and the length of the cell is ~ 2.5. This agrees well with data on cells having feature sizes similar to the Kintex-7 [138]. Combining this with the cell area determined from Eq. 7.1, the width and length of the cell used in the theoretical modelling were set to 550 nm and 220 nm, respectively. In accordance with the same physical layout, the four sensitive transistor drains of the cell were assumed to be located in a row along the centre of the cell.

In order to fully model an SRAM cell in the input to a model, details about its complex physical structure would be needed. This includes, for example, information about the materials used in the metal interconnects located above the SRAM transistors. Since no such information was available for the Kintex-7, the geometry in this model consisted of a $(100 \times 100 \times 30)$ μm^3 volume of natural silicon, V_0, in which protons and neutrons interacted.

When a particle is tracked through the geometry in Geant4, the distance it travels between two subsequent interactions is called a *step*. Each step has associated information, such as the start and end points of the step, and the energy deposited in the geometry during the step. In this simulation, the information connected to all simulated steps in a (4 × 4 × 30) μm^3 subvolume of V_0 — V_{sub} — was stored. The modelled SRAM cell is located inside V_{sub}, and the size of V_{sub} was chosen such that it was sufficiently larger than the feature size of the FPGA while also being small enough to limit the resulting amount of data. Therefore, while all particles were tracked throughout V_0, only the steps within V_{sub} were stored for further analysis.

7.2.2 Particle Beams

When a Geant4 simulation is run, a primary particle is generated. This particle, and all resulting secondary particles, are tracked through the geometry. When all particles have been absorbed or escaped the geometry, another primary particle is generated. The generation of a single primary particle and tracking of all related secondary particles is known as an *event*. The simulation was run for a predefined number of events, N_{sim}. Before the simulation was run, the beam direction was set to be perpendicular to the face of the memory cell, to match the experimental conditions. The three proton beams were defined as fully monoenergetic beams with energies of 80, 100 and 184 MeV. The neutron-beam spectra were defined as having continuous energy spectra according to Figs. 6.2 and 6.3. While the SEU cross section for the TSL measurement was determined assuming that only neutrons above 10 MeV contribute to the SEU rate, the full spectrum as shown in Fig. 6.2 was included in the simulation. In order to compare the modelled TSL cross section with the experimental data, it was scaled after the simulation to account for the fact that the experimental cross section was determined using only a fraction of the actual neutron fluence.

In this context, nuclear reactions induced by protons and neutrons are one of the main sources of SEUs. As discussed in sec 5.5.1, the recoiling silicon nucleus after an elastic scattering of a 20-MeV proton in silicon has a range of approximately 2 µm. As the primary-particle energy in some of the experiments in this work is significantly higher than 20 MeV, even longer recoil-nucleus ranges are expected. Therefore, it is possible even for particles generated relatively far away from a memory cell to reach it and cause an SEU. To ensure that such particles were included in the simulation, the transversal area of the beam had to be sufficiently large. The particle fluence in the simulation, Φ_{sim}, is given by:

$$\Phi_{\text{sim}} = \frac{N_{\text{sim}}}{A_{\text{beam}}}, \tag{7.2}$$

where A_{beam} is the transversal area of the simulated beam. While it was desirable to have an area as large as possible, a sufficiently large Φ_{sim} was needed to decrease the statistical uncertainty in the simulation. Therefore, an increase in A_{beam} had to be matched by an increase in N_{sim}. A too large value on N_{sim} would become computationally unfeasible and therefore A_{beam} had to be limited. By investigating how the results of the model — i. e. the simulated cross section — depended on the beam area, a beam area was chosen. Secondary particles could always be generated in interactions of a primary particle at the edge of the beam, and an increase in $\mathcal{A}_{\text{beam}}$ therefore generally caused an increase in the resulting cross section (as contributions from nuclear fragments generated far from the cell contribute to some extent). However, this effect is most dramatic at beam areas not much larger than the memory-cell area, partially because the ranges of generated particles are finite and partially because the solid angle subtended by the memory cell is very small for a particle generated far away. A square beam with $\mathcal{A}_{\text{beam}} = (30{\times}30)\ \mu\text{m}^2$ was found to be sufficient in this respect, while also allowing the simulation to be performed in reasonable time.

7.2.3 Particle Interactions

On the most fundamental level, the result of a Geant4 simulation depends on a large number of physics models and data sets, which determine the probabilities for different interactions to occur. A collection of such models and data is known as a physics list, which may be chosen based on which particles are involved in the simulation, as well as on the energy scale and the desired spatial resolution. For model 1, the Geant4 reference physics list QGSP_BIC_HP_EMY was used. It is a combination of several models for particle interactions: the QGSP model describes high-energy hadronic interactions, the BIC model is a binary-cascade model of neutron and proton interactions with nuclei below $\sim$ 10 GeV, HP uses low-energy neutron data to simulate low-energy neutron interactions, and EMY is a recent extension of the standard electromagnetic-physics list that is well suited for low-energy applications [139]. For model 2, the reference physics list QGSP_BIC_HP_EMZ, which provides even more detail in simulations of low-energy electromagnetic interactions[1], was used.

7.3 Model 1

As stated above, model 1 is based on the traditional RPP model, with the exception that structure inside the memory cell is also modelled instead of assuming a single RPP for the entire cell. This model consists of a memory cell containing four cubic SVs, each being centred at the location of the corresponding transistor drain. The cell is only sensitive to energy deposition inside the SVs, as it is assumed that no charges generated outside of them would be collected at the transistors. The four SVs had the same size, which depended on a single parameter — the length of the SV side, d_{SV}.

[1] For a list of differences between the EMY and EMZ electromagnetic-physics lists, the reader is referred to [140].

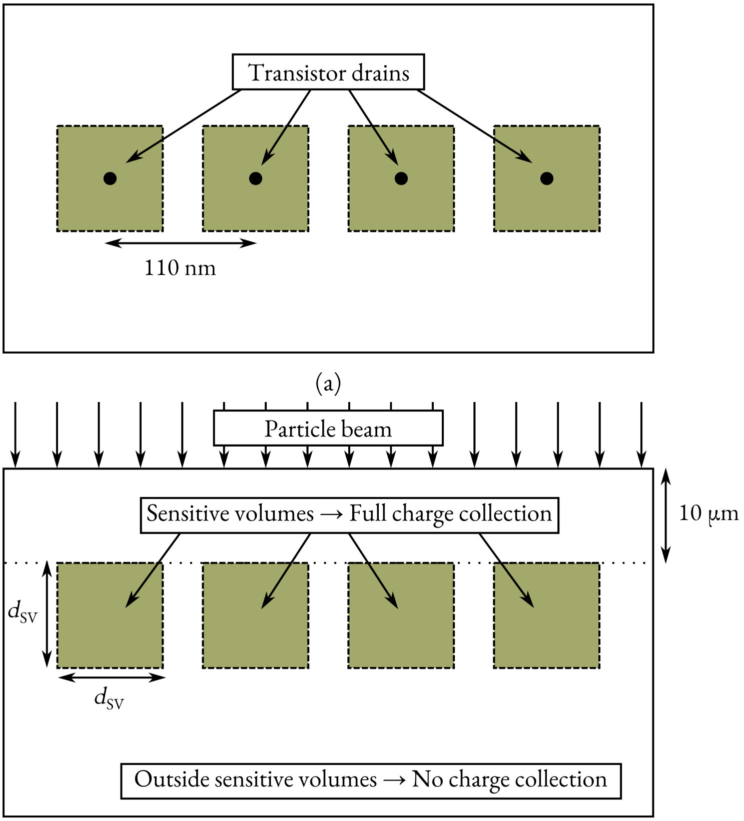
Transistor drains
110 nm
Particle beam
Sensitive volumes → Full charge collection
10 µm
d_{SV}
d_{SV}
Outside sensitive volumes → No charge collection

(a)

(b)

Figure 7.2: Geometry of the memory cell in model 1. In (a), the top view of the cell is shown, and the assumed locations of the four transistors are indicated. In (b), the side view of the cell is shown. The dimensions in the figures are not to scale.

7.3.1 Sensitive Volumes

The SVs were not defined directly in the Geant4 geometry in order to maintain flexibility in the choice of d_{SV}. Instead, all step data within V_{sub} were stored, the location of the memory cell and the SVs could be mathematically defined within V_{sub} and then the energy deposits could be determined by analysing the step data. The layout of the SVs, as implemented in the analysis, is shown in Fig. 7.2. The transversal placement of the SVs in the cell was modelled after the considerations in Sec. 7.2.1, so that the SVs were placed on a line, 110 nm apart from each other. The distance between the centres of two SVs therefore corresponded to the distance between two transistor drains. This distance is indicated in Fig. 7.2. The top of each SV was fixed to a plane illustrating the memory-cell surface, which was located at a depth of 10 µm into V_0. Therefore, a change in d_{SV} only caused the SV to extend on the back side of the cell into the CMOS substrate.

7.3.2 Energy Deposition

The energy depositions in the SVs were determined on an event-by-event basis by analysing the saved steps. Each step was described as a vector starting at $\boldsymbol{r}_{\mathrm{start}}$ and ending at $\boldsymbol{r}_{\mathrm{end}}$. For each step, it was determined whether the step intersected any of the SVs and if it did, the point(s) of intersection with the SV boundaries were identified. In Fig. 7.3, a step intersecting an SV is shown, and the two intersection points $\boldsymbol{r}_1$ and $\boldsymbol{r}_2$ are indicated. If a step started or ended within an SV, a single intersection point $\boldsymbol{r}_1$ was identified.

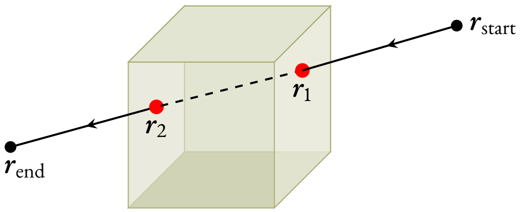
$\boldsymbol{r}_{\mathrm{start}}$
$\boldsymbol{r}_1$
$\boldsymbol{r}_2$
$\boldsymbol{r}_{\mathrm{end}}$

Figure 7.3: A Geant4 step intersecting one of the SVs. The step is characterised by its endpoint locations $\boldsymbol{r}_{\mathrm{start}}$ and $\boldsymbol{r}_{\mathrm{end}}$, and intersects the SV at two locations: $\boldsymbol{r}_1$ and $\boldsymbol{r}_2$. The energy deposited in the SV was determined by comparing the total length of the step to the distance between the two intersection points.

Once the intersection point(s) between the step and a particular SV have been identified, the fraction u of the total step distance intersecting the SV was given by:

$$u = \frac{|\boldsymbol{r}_2 - \boldsymbol{r}_1|}{|\boldsymbol{r}_{\mathrm{end}} - \boldsymbol{r}_{\mathrm{start}}|}. \tag{7.3}$$

In addition to the endpoints of the step, the amount of energy $E_{\mathrm{dep,\,step}}$ deposited to the silicon during the step was also stored. Using the result of Eq. 7.3, the amount of energy deposited inside the SV in question, $E_{\mathrm{dep,\,SV}}$, was determined:

$$E_{\mathrm{dep,\,SV}} = uE_{\mathrm{dep,\,step}}. \tag{7.4}$$

When all steps associated with an event had been fully analysed, the energy deposited in each SV per event was determined. Fig. 7.4 shows the energy-deposition distributions for one of the four SVs due to 100-MeV protons at different d_{SV}, after analysing all events. The energy spectra clearly show the two contributions to proton-induced SEUs: direct ionisation by protons and indirect ionisation due to nuclear reactions. In direct-ionisation events, the amount of deposited energy is lower than ~ 5 keV, while indirect-ionisation events are much fewer in number but deposit significantly higher amount of energy. In fact, the energy deposition due to direct ionisation by protons is to a first approximation equal to $(\mathrm{d}E/\mathrm{d}x)d_{\mathrm{SV}}$, so that it is proportional to d_{SV}.

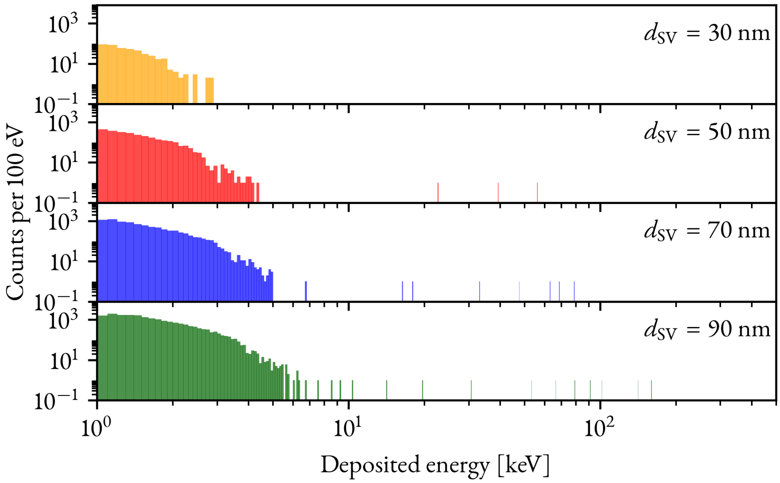

Figure 7.4: Histograms of the deposited energy in one of the four SVs at different SV sizes after simulating $1.5 \cdot 10^{11}$ 100-MeV protons incident on the silicon geometry.

7.3.3 Critical Energy

In the RPP model, the assumption that the charge is collected uniformly within the SV is made, so that an SEU occurs if the amount of generated charge in the SV exceeds $Q_{\mathrm{crit,\,RPP}}$. Assuming that the number of produced electron-hole pairs per unit of deposited energy is $1/3.6\ \mathrm{eV}^{-1}$ for silicon [141] and is constant throughout the SV, the critical energy E_{crit} may be defined:

$$E_{\mathrm{crit}} \equiv \frac{Q_{\mathrm{crit,\,RPP}}}{280e}\ \mathrm{keV}, \tag{7.5}$$

where e is the elementary charge. Now, E_{crit} replaces $Q_{\mathrm{crit,\,RPP}}$ as one of the free parameters of the model and the SEU sensitivity depends on the amount of deposited energy, and not charge, in the SVs.

7.3.4 Number of Upsets

In the model, the total energy deposited in each SV for a full event, and how it compared with E_{crit} determined whether that event was classified as an SEU. Also, the initial state of the memory cell — i. e. whether it holds a value of 1 or 0 — is of importance, as it determines which of the four transistor drains are sensitive to charge collection, as discussed in Sec. 5.5.2. Assuming that only the drains of the two off-transistors are sensitive to charge collection, the sensitive SVs under the two initial-state situations is given by Tab. 7.1.

Table 7.1: The two possible initial-state situations in the model. Depending on what value the memory cell initially holds, different transistors and therefore different SVs are sensitive.

Initial cell state	Sensitive drains	Sensitive SVs
1	D_1 and P_2	1 and 3
0	P_1 and D_2	2 and 4

The conditions for an event to be classified as an SEU under the two initial-state situations are given by:

$$\begin{aligned}(E_{\text{dep, SV 1}} \geq E_{\text{crit}}) \vee (E_{\text{dep, SV 3}} \geq E_{\text{crit}}) &\Rightarrow \text{SEU (bit value: } 1 \rightarrow 0),\\ (E_{\text{dep, SV 2}} \geq E_{\text{crit}}) \vee (E_{\text{dep, SV 4}} \geq E_{\text{crit}}) &\Rightarrow \text{SEU (bit value: } 0 \rightarrow 1),\end{aligned} \tag{7.6}$$

so that an energy deposition exceeding E_{crit} in either of the two sensitive SVs results in an SEU. The total number of detected SEUs in the two initial-state situations, $N^{\text{on}}_{\text{SEU, model}}$ and $N^{\text{off}}_{\text{SEU, model}}$, was determined. By assuming that the SEU sensitivity is independent of the initial-state situation, the two situations were treated as two separate measurements. The total number of detected SEUs, $N_{\text{SEU, model}}$ was the sum of the two contributions:

$$N_{\text{SEU, model}} = N^{\text{on}}_{\text{SEU, model}} + N^{\text{off}}_{\text{SEU, model}}. \tag{7.7}$$

7.3.5 SEU Cross Section

The SEU cross section predicted by the model, $\sigma_{\text{SEU, model}}$, was determined from:

$$\sigma_{\text{SEU, model}}(E_{\text{crit}}, d_{\text{SV}}) = \frac{N_{\text{SEU, model}}(E_{\text{crit}}, d_{\text{SV}})}{2\Phi_{\text{sim}}}, \tag{7.8}$$

where the factor 2 in the denominator is due to the fact that $N_{\text{SEU, model}}$ is the sum of two measurements (i. e. the two initial-state situations), so that the total fluence is twice the simulated fluence. The parameter space of E_{crit} and d_{SV} was divided into a rectilinear grid, where each cell had an area of 0.5 nm × 10 eV. At each grid point, $N_{\text{SEU, model}}$ was evaluated and $\sigma_{\text{SEU, model}}$ was mapped. In Fig. 7.5, the model-predicted cross section for SEUs induced by 100 MeV protons is shown as a function of E_{crit} and d_{SV}.

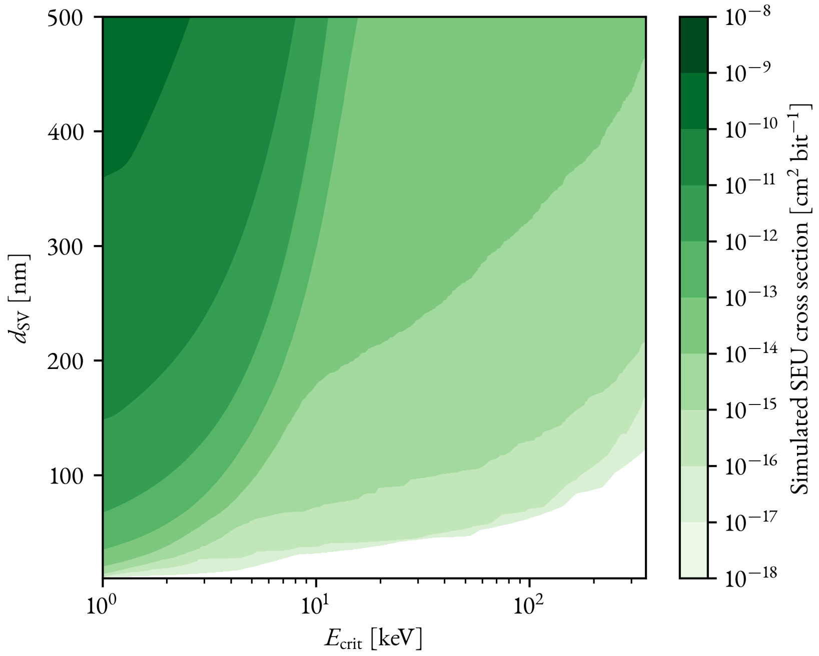

Figure 7.5: The 100-MeV proton SEU cross section predicted by the model, as a function of the critical energy and the SV side. Note the logarithmic scale on the horizontal axis.

7.4 Model 2

Although model 1 may be used to predict SEU rates in its own right, it has the disadvantage that it is unphysical on a fundamental level as described in Sec. 7.1. As will be seen in Sec. 7.5.2, determining the parameters in model 1 from a fit to the experimental data results in unrealistically large SV dimensions. This, together with the unphysical nature of the RPP model, motivated the extension of the model into what is known as *model 2*. Model 2 shares several assumptions about the memory-cell structure with model 1, such as the number and orientation of the transistors and the dimensions of the SRAM cell. Therefore, the two possible memory-cell states and the corresponding sensitive drains given in Table 7.1 still hold.

7.4.1 Sensitive Volumes

The main difference between the two models lies in the definition of the SVs. In model 1, an SV is an RPP volume below each transistor, assumed to collect charge with an efficiency of 100%. In model 2, an SV still represents a volume below a transistor in which charge is collected with an efficiency of 100%. This represents the charge-drift process, where the electric field around the transistor yields a high charge-collection efficiency. In addition, the SV is sensitive to charge collected from the silicon further below the SV volume itself. This represents the charge-diffusion process, where charges may diffuse to the high-field regions below the transistors after which they are collected efficiently.

In model 1, the amount of charge collected by a transistor is assumed to be proportional to the amount of energy E_{dep} deposited in the corresponding SV. Due to the inclusion of multiple charge-collection processes in model 2, this assumption is no longer valid, and the amount of charge Q_{coll} collected by a transistor has to be used as a parameter of interest. The layout of the SVs, as implemented in model 2, is shown in Fig. 7.6. The overall layout of the memory cell, including transistor locations, follows the same reasoning as for model 1 (see Sec. 7.3.1). Apart from the non-zero charge-collection efficiencies below the SVs, there are two differences from the geometry in model 1: the memory cell is in model 2 located 15 μm into the silicon block instead of 10 μm, and the SVs are cylindrical instead of cubic. The diameter and height of a SV cylinder in model 2 are the same, so that the SV dimensions are again defined by a single parameter d_{SV}. Note that while this parameter still contains information about the SV size, as it did in model 1, the actual shape of the SV is different here. The switch from cubic to cylindrical SVs was motivated by the inclusion of charge diffusion in the model, and are detailed in Sec. 7.4.2.

7.4.2 Charge Collection

As in model 1, the particle step information was available from the Geant4 simulation on an event-by-event basis, and each step was described as a vector starting at $\boldsymbol{r}_{\mathrm{start}}$ and ending at $\boldsymbol{r}_{\mathrm{end}}$. In model 2, the charge-collection efficiency for an SV is non-zero below the SV, describing charge diffusion, and zero above the SV as no charge collection from above the memory cell is assumed. The number of electron-hole pairs N_{eh} generated along a step corresponding to an energy deposition E_{dep} is given by:

$$N_{\mathrm{eh}} = kE_{\mathrm{dep,\,step}}, \tag{7.9}$$

where $k = 1/3.6\ \mathrm{eV}^{-1}$ for silicon, as was also assumed in model 1. Due to the directions of the electric fields around the transistors, it was assumed that the two nMOS transistors only collect negative charge efficiently, and that the two pMOS transistors only collect positive charge. As a first-degree approximation, the probability that a charge generated below the SVs would diffuse to a particular SV is given by the solid angle Ω_i subtended by the base of that SV. Combining this with the 100% collection efficiency inside the SV and the 0% collection efficiency above the memory-cell surface, the combined efficiency of SV i collecting a charge generated

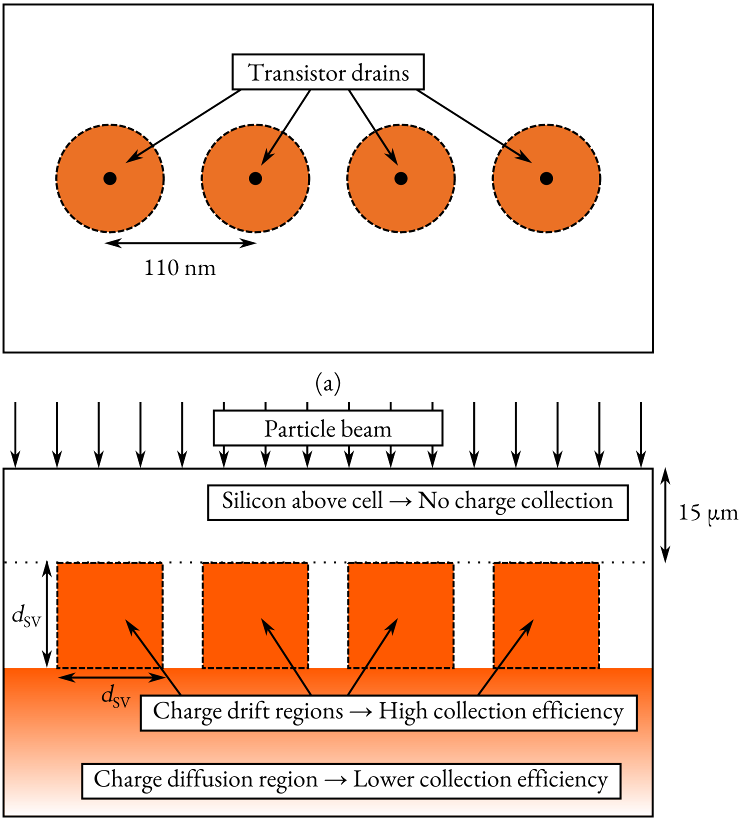
Transistor drains
110 nm
Particle beam
Silicon above cell → No charge collection
15 μm
d_{SV}
d_{SV}
Charge drift regions → High collection efficiency
Charge diffusion region → Lower collection efficiency

(a)

(b)

Figure 7.6: Geometry of the memory cell in model 2. In (a), the top view of the cell is shown, and the assumed locations of the four transistors are indicated. In (b), the side view of the cell is shown. The cell sensitive to energy deposition both inside the four sensitive volumes and, to some extent, below the sensitive volumes where there is a possibility for generated charge to diffuse to the transistors. The dimensions in the figures are not to scale.

at a position (x, y, z) is given by:

$$\varepsilon_{\text{coll},\,i}(x, y, z) = \begin{cases} 1, & \text{inside cylinder } i, \\ \Omega_i(x, y, z)/4\pi, & \text{below cylinder } i, \\ 0, & \text{otherwise.} \end{cases} \tag{7.10}$$

In Fig. 7.7, a step intersecting an SV is shown, and the two endpoints $\boldsymbol{r}_{\text{start}}$ and $\boldsymbol{r}_{\text{end}}$ of the step are shown. The cylindrical SV shape is motivated by the fact that the solid angle subtended by the circular base of such a cylinder from a point (x, y, z)

may be calculated analytically [142], while this would be much more difficult in case of cubic SVs.

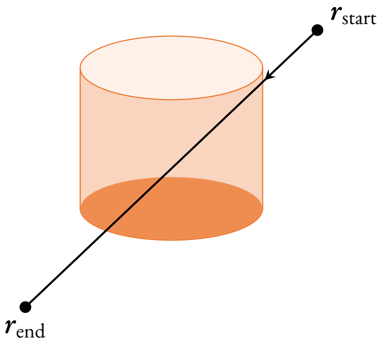
$\boldsymbol{r}_{\text{start}}$
$\boldsymbol{r}_{\text{end}}$

Figure 7.7: A Geant4 step intersecting one of the SVs. The step is characterised by its endpoint locations $\boldsymbol{r}_{\text{start}}$ and $\boldsymbol{r}_{\text{end}}$. The charge collected by the SV was determined by integrating the amount of charge generated along the step over the charge-collection efficiency.

Since each particle step is described by a straight line between two points $\boldsymbol{r}_{\text{start}}$ and $\boldsymbol{r}_{\text{end}}$, one may introduce a parameter t to parameterise the line:

$$\boldsymbol{r}(t) = \boldsymbol{r}_{\text{start}} + t(\boldsymbol{r}_{\text{end}} - \boldsymbol{r}_{\text{start}}), 0 \leq t \leq 1. \tag{7.11}$$

By integrating the charge-collection efficiency along each such step, incorporating the electron-hole production, the total amount of generated charge q_{coll} along the step was determined:

$$q_{\text{coll, i}} = \int_0^1 dt\, N_{\text{eh}} \cdot e \cdot \varepsilon_{coll,\, i}(\boldsymbol{r}(t)), \tag{7.12}$$

where e is the elementary charge. By solving this integral, the amount of negative *or* positive charge (according to the SV type) collected by the i:th SV was calculated. By summing the contributions from all steps during a particular event, the total amount of collected charge Q_{coll} during an event was determined for each SV. Fig. 7.8 shows the charge-collection distributions for one of the four SVs due to 100-MeV protons at different d_{SV}, after analysing all events. There are obvious similarities with the energy-deposition distributions for model 1 (shown in Fig. 7.4), as the majority of the distribution corresponds to direct-ionisation events giving rise to small Q_{coll} values while a few events giving higher Q_{coll} correspond to indirect ionisation.

In model 2, the critical charge Q_{crit} is reintroduced as a model parameter. In model 1, it was replaced by the critical energy, but since charge collection is now actually modelled it provides a realistic connection to the actual upset mechanisms in the cell. The model still relies on only two parameters, which now are Q_{crit} and the cylinder dimension-parameter d_{SV}.

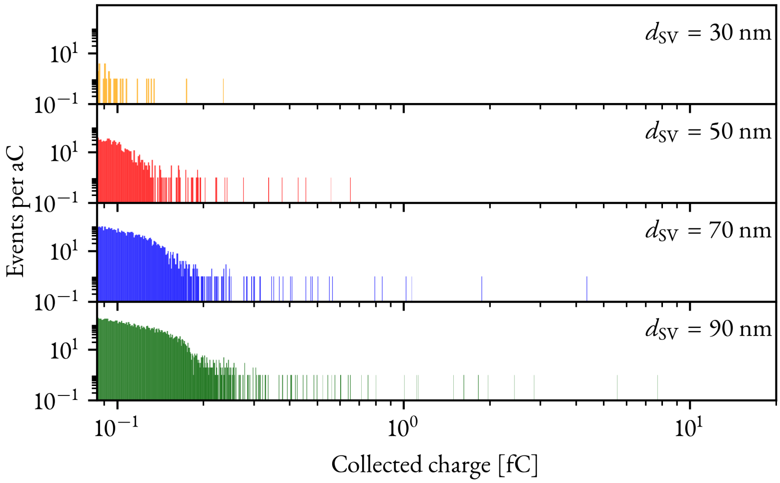

Figure 7.8: Histograms of the collected charge in one of the four SVs at different SV sizes after simulating $2 \cdot 10^{11}$ 100-MeV protons incident on the silicon geometry.

7.4.3 Number of Upsets

As stated earlier, model 2 views the sensitivity of the memory-cell transistors in the same way as model 1, i. e. that two of the SVs correspond to pMOS drains and the other two to nMOS drains (see Table 7.1). The conditions for an event to be classified as an SEU in model 2 under the two initial-state situations are given by:

$$\begin{aligned} (Q_{\text{coll, SV 1}} \geq Q_{\text{crit}}) \vee (Q_{\text{coll, SV 3}} \geq Q_{\text{crit}}) &\Rightarrow \text{SEU (bit value: } 1 \rightarrow 0) \\ (Q_{\text{coll, SV 2}} \geq Q_{\text{crit}}) \vee (Q_{\text{coll, SV 4}} \geq Q_{\text{crit}}) &\Rightarrow \text{SEU (bit value: } 0 \rightarrow 1), \end{aligned} \tag{7.13}$$

so that a charge collection exceeding Q_{crit} in either of the two sensitive SVs results in an SEU. The total number of detected SEUs in the two initial-state situations, $N^{\text{on}}_{\text{SEU, model}}$ and $N^{\text{off}}_{\text{SEU, model}}$, was determined. By assuming that the SEU sensitivity is independent of the initial-state situation, the two situations were treated as two separate measurements. The total number of detected SEUs, $N_{\text{SEU, model}}$ was the sum of the two contributions:

$$N_{\text{SEU, model}} = N^{\text{on}}_{\text{SEU, model}} + N^{\text{off}}_{\text{SEU, model}}. \tag{7.14}$$

7.4.4 SEU Cross Section

The SEU cross section predicted by model 2, $\sigma_{\text{SEU, model}}$, was determined from:

$$\sigma_{\text{SEU, model}}(Q_{\text{crit}}, d_{\text{SV}}) = \frac{N_{\text{SEU, model}}(Q_{\text{crit}}, d_{\text{SV}})}{2\Phi_{\text{sim}}}, \tag{7.15}$$

where the factor of 2 in the denominator is due to the fact that $N_{\mathrm{SEU,\,model}}$ is the sum of two measurements (i. e. the two initial-state situations), so that the total fluence is twice the simulated fluence. The parameter space of Q_{crit} and d_{SV} was divided into a rectilinear grid, where each cell had an area of 1 nm × 0.525 aC. At each grid point, $N_{\mathrm{SEU,\,model}}$ was evaluated and $\sigma_{\mathrm{SEU,\,model}}$ was mapped. In Fig. 7.9, the model-predicted cross section for SEUs induced by 100 MeV protons is shown as a function of Q_{crit} and d_{SV}.

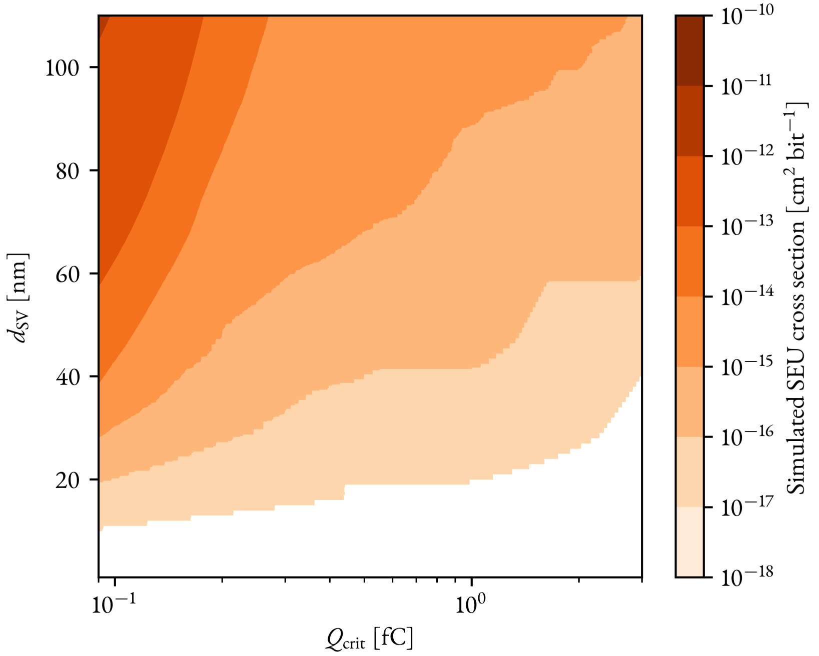

Figure 7.9: The 100-MeV proton SEU cross section predicted by model 2, as a function of the critical charge and the SV side. Note the logarithmic scale on the horizontal axis.

7.5 Fit to Data

From Figs. 7.5 and 7.9, it is evident that the results of both models are highly dependent on the choice of the model-parameter values: the resulting cross sections differ by up to ten orders within the studied parameter ranges. In order to predict SEU cross sections based on the models, the values of the free parameters had to be determined by fitting the models to the experimental data. Although the two models were analysed and fitted separately, the procedure used to determine the optimal parameter values was the same in both cases. Therefore, the details of the analysis procedure will be given here, and results from the specific models will be given separately. However, as noted in the beginning of this chapter, the purpose of this is not to perform a strict comparison of the models but rather to demonstrate the process that led to the improvement of model 1 into model 2. Fitting the model was done by means of Bayesian inference, which enables determination of the full parameter PDF — i. e. how likely any parameter-value pair is, given the observed data — and subsequent cross-section predictions. The foundation of Bayesian inference is Bayes' theorem:

$$p(\vartheta|\boldsymbol{N}_{\mathrm{SEU,\,exp}}) = \frac{p(\boldsymbol{N}_{\mathrm{SEU,\,exp}}|\vartheta)p(\vartheta)}{p(\boldsymbol{N}_{\mathrm{SEU,\,exp}})}, \tag{7.16}$$

where $p(\vartheta|\boldsymbol{N}_{\mathrm{SEU,\,exp}})$ is the *posterior probability*, $p(\boldsymbol{N}_{\mathrm{SEU,\,exp}}|\vartheta)$ is the *likelihood*, $p(\vartheta)$ is the *prior probability* and $p(\boldsymbol{N}_{\mathrm{SEU,\,exp}})$ is the *marginal likelihood*. $\boldsymbol{N}_{\mathrm{SEU,\,exp}}$ is a vector containing the total number of experimentally observed SEUs during the six measurements and ϑ is a vector of the model parameters. In model 1, $\vartheta = (E_{\mathrm{crit}},\ d_{\mathrm{SV}})$, and in model 2, $\vartheta = (Q_{\mathrm{crit}},\ d_{\mathrm{SV}})$. The posterior probability is the probability that the model parameters take on particular values given the observed number of counts, and the likelihood is the probability that the observed data is reproduced by the model given the particular parameter values. The prior probability incorporates any previous knowledge about the parameter values (such as physical constraints), and the marginal likelihood is the likelihood summed over all possible parameter values. As the data are fixed, the marginal likelihood is simply a constant ensuring that the posterior probability integrates to unity. Furthermore, if we assume no prior knowledge of the parameter values, $p(\vartheta)$ is constant and may be included in the normalisation constant. The unnormalised posterior probability becomes:

$$p(\vartheta|\boldsymbol{N}_{\mathrm{SEU,\,exp}}) \propto p(\boldsymbol{N}_{\mathrm{SEU,\,exp}}|\vartheta) = \prod_{i=1}^{6} p(N^{(i)}_{\mathrm{SEU,\,exp}}|\vartheta), \tag{7.17}$$

where the separation of the total likelihood into the product of the individual likelihoods for the six data points comes from the fact that the experimental data are independent from each other. Obtaining the posterior probability describing ϑ therefore comes down to determining the six likelihood functions.

7.5.1 Likelihood Functions

Eq. 6.1, which was used to determine the experimental cross sections, relates a particular cross section to the number of observed SEUs, $N_{\mathrm{SEU,\,exp}}$, the particle fluence, Φ_{exp} and the number of bits in the FPGA memory, N_0. The cross section predicted by the model, $\sigma_{\mathrm{SEU,\,model}}$, may be inserted into Eq. 6.1 to calculate the expected value of the predicted number of experimentally observed SEUs, $N^*_{\mathrm{SEU,\,exp}}$:

$$\langle N^*_{\mathrm{SEU,\,exp}}\rangle(\vartheta) = \sigma_{\mathrm{SEU,\,model}}(\vartheta)\,\Phi_{\mathrm{exp}}N_0. \tag{7.18}$$

Assuming that the number of observed SEUs follows Poisson statistics, the likelihood of observing the number of SEUs given in Tab. 6.4, $\langle N_{\mathrm{SEU,\,exp}}\rangle$, in the case of some parameter values ϑ is given by a Poisson distribution with the mean $\langle N^*_{\mathrm{SEU,\,exp}}\rangle$. This distribution quantifies the uncertainty in the experiment, as a higher number of observed SEUs would lead to a lower uncertainty in the Poisson distribution. The statistical uncertainty in the model was also incorporated into the fitting procedure by noting that it is given by the Poisson uncertainty in $N_{\mathrm{SEU,\,model}}$, as it depends on the number of counted SEUs in the model. That is, the output of the model under some parameter values is a particular SEU count, $\langle N_{\mathrm{SEU,\,model}}\rangle$, which has an associated uncertainty given by Poisson statistics. This in turn gives the uncertainty in $\sigma_{\mathrm{SEU,\,model}}$. By increasing the number of simulated events N_{sim}, the uncertainty in the model predictions can be decreased. The uncertainties in both the experiments and models were included by applying the technique introduced in Ch. 6 — propagation of input-parameter PDFs. For each value of the two parameters, the following procedure was performed:

1. A value on $N_{\mathrm{SEU,\,model}}$ was generated from the Poisson distribution given by $\langle N_{\mathrm{SEU,\,model}}\rangle$. The corresponding modelled cross section $\sigma_{\mathrm{SEU,\,model}}$ was determined from Eq. 7.8.
2. A value on Φ_{exp} was generated as described in Ch. 6. N_0 was obtained from the experimental data.
3. $\langle N^*_{\mathrm{SEU,\,exp}}\rangle$ was determined from Eq. 7.18. The predicted number of experimentally observed SEUs, $N^*_{\mathrm{SEU,\,exp}}$, was determined by generating a value from the Poisson distribution with mean $\langle N^*_{\mathrm{SEU,\,exp}}\rangle$.
4. The procedure was repeated a large number of times so that the likelihood of obtaining a predicted number of SEUs exactly equal to the expected value of the observation, $p(\langle N_{\mathrm{SEU,\,exp}}\rangle|\vartheta)$, was determined with high precision.

The likelihood values as a function of the model parameters were determined for both models, for all six experiments, using this procedure. During the model development, the neutron intensities from the low-energy neutron sources and the associated uncertainties were re-determined as detailed in Ch. 6. Because of this, there is a difference in the experimental data used to determine the likelihood functions in the two models, and this will affect the fit. The likelihood functions for 100-MeV protons in both models are shown in Figs. 7.10. A general trend in the obtained likelihood functions is that when the SV size is increased, also the critical energy or charge has to be increased to remain true to the observed data. This is due to the fact that more energy will be deposited in a large SV, and to still fit the experimental data also the sensitivity of the SV has to be decreased (corresponding to an increased critical energy/charge).

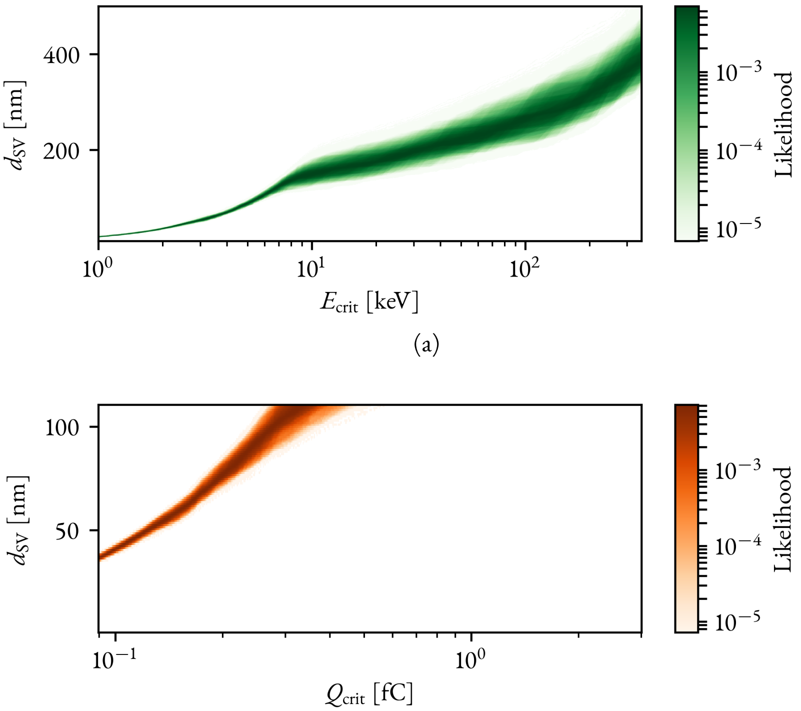

(a)

(b)

Figure 7.10: Likelihood values as a function of the model parameters for 100-MeV protons using a) model 1 and b) model 2. The likelihood is the probability of obtaining the experimentally observed cross section in the model under different values of the model parameters.

7.5.2 Posterior Distributions

The posterior distribution gives the probability that the *true* parameters of the model take on particular values, given the observed data. The posterior distributions for the two models were determined by normalising the products of the corresponding individual likelihood functions to one, and are shown in Fig. 7.11.

It can be seen that the posterior distribution for model 1 is somewhat bimodal — there are two distinctly separated maxima in the PDF. However, as Bayesian inference allows using the full posterior distribution for further analysis, this does not cause any issues. A more serious problem, which ultimately caused the evolution of model 1 into model 2, is the fact that both of the maxima in the model 1 posterior correspond to $d_{SV} > 110$ nm, as indicated in Fig. 7.11b. Since 110 nm is the predefined distance between two transistors in the cell, an SV size larger than this results in overlapping SVs. This is unphysical, since each SV should only correspond to charge collection by one particular transistor drain. In model 2, the posterior distribution was only analysed for $d_{SV} \leq 110$ nm, and in this case there is only one clear maximum of the PDF. The properties of the posterior distributions for the two models are summarised in Tables 7.2 and 7.3.

Table 7.2: The means, standard deviations and covariance of the two parameters in model 1, obtained by analysing the posterior distribution.

Parameter	Mean	Standard deviation
E_{crit}	160 keV	40 keV
d_{SV}	300 nm	30 nm
$\mathrm{cov}(E_{crit}, d_{SV}) = 1154.6$ keV^2 nm^2		

Table 7.3: The means, standard deviations and covariance of the two parameters in model 2, obtained by analysing the posterior distribution.

Parameter	Mean	Standard deviation
Q_{crit}	0.23 fC	0.03 fC
d_{SV}	87 nm	7 nm
$\mathrm{cov}(Q_{crit}, d_{SV}) = 0.192$ fC^2 nm^2		

7.6 Comparison with Experimental Data

The results of the model, in terms of SEU cross sections, may be determined by combining $\sigma_{SEU,\,model}$ with the posterior probability distribution. In the context of Bayesian inference, this may be done using posterior predictive checking [143]. The posterior, which was determined by the actually observed experimental data, is in this procedure used to generate a PDF describing the data that *could have been observed* if the model is correct. The probability for a particular *replicated* data value may therefore be determined. For one of the measurements, the probability that the replicated cross section $\sigma^{\text{rep}}_{\text{SEU, model}}$ takes a particular value given the experimental result, $\langle N_{\text{SEU, exp}}\rangle$, is given by Eq. 7.19:

$$p(\sigma^{\text{rep}}_{\text{SEU, model}}|\langle N_{\text{SEU, exp}}\rangle) = \sum_{\vartheta} p(\sigma^{\text{rep}}_{\text{SEU, model}}|\vartheta)p(\vartheta|\langle N_{\text{SEU, exp}}\rangle), \tag{7.19}$$

where $p(\sigma^{\text{rep}}_{\text{SEU, model}}|\vartheta)$ may be directly determined from $p(N^{\text{rep}}_{\text{SEU, model}}|\vartheta)$ using Eq. 7.8, and the sum runs over all possible parameter values.

The expected values and standard deviations of all replicated cross sections based on the analyses of the two models, compared with the experimental data, are shown in Figs. 7.12 and 7.13. Because the fit of model 1 to the experimental data yields an unphysically large SV size, model 2 was developed. From this point onwards, i. e. in the next chapter, only model 2 will be used to predict SEU cross sections.

7.7 Discussion

As shown in Figs. 7.12 and 7.13, both models reproduce both proton- and neutron-induced SEU cross sections. Whereas model 1 was fitted to experimental data determined using nominal neutron intensities of the low-energy neutron sources, re-measured intensities were used in the model 2 fit. There is some discrepancy between the model and the data at some of the particle energies — for instance the proton cross section increases with the proton energy in the model predictions, while it appears to decrease based on the experimental data. However, there are not enough experimental data to draw any conclusions about whether this difference is significant. For a discussion about the quality of the fit of model 2, the reader is referred to Paper II. The cross sections from previous work neither give sufficient information about the trend in the energy dependence. However, support for an increasing trend (as is predicted by the model) is given in Sec. 6.2.4, where an increase in the SEU cross section until it reaches a plateau level is motivated.

The dimensions of the SVs in model 2 are such that the SVs are well separated, supporting the initial assumption of the model — that each SV corresponds to a localised volume in which charges drift to a single transistor. The feature-size dependence on the critical charge Q_{crit} has been studied in the past [96]. These results show that Q_{crit} for a transistor in the Kintex-7 configuration memory could be below 0.5 fC, with which the value predicted by model 2 (0.23 fC) is in agreement. The fact that the geometry in the model only consists of silicon most likely affects the obtained values on both Q_{crit} and d_{SV}. The real device contains a number of metallic layers above the silicon in the CMOS. If the proton or neutron reaction cross section is larger in one of these overlayers, the result could be a higher number of SEUs. These effects are discussed in Paper II.

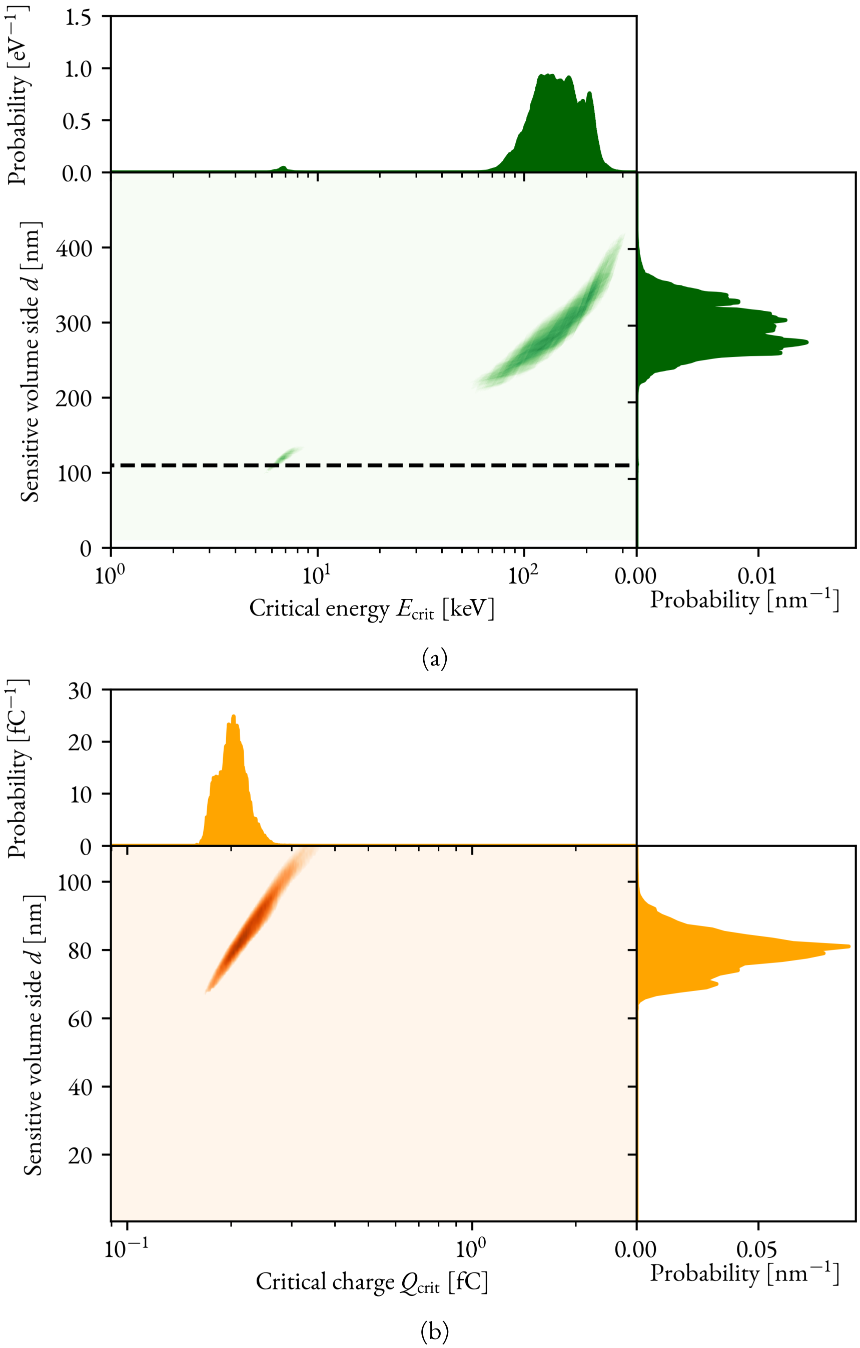

Figure 7.11: The posterior probability distribution of the model parameters using a) model 1 and b) model 2. The posterior probability gives the probability that the true parameters of the model take on particular values, given the observed data. The horizontal dashed line in b) indicates $d_{\rm SV}$ = 110 nm, above which adjacent SVs start to overlap, thus making the model unphysical.

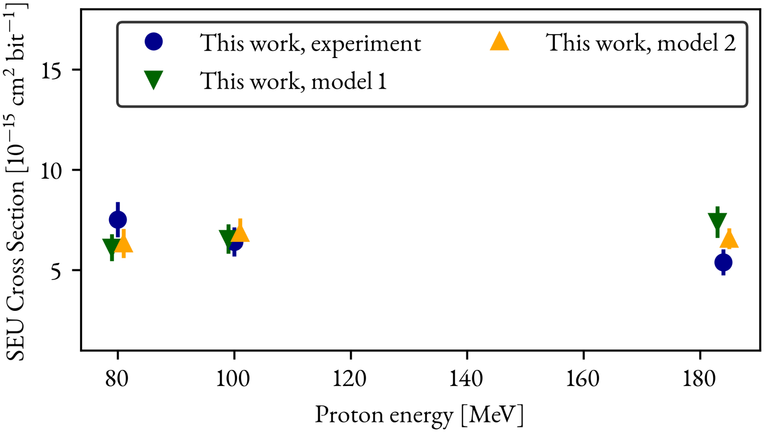

Figure 7.12: The model-determined cross sections for proton-induced SEUs, compared with the experimental results. Note that model 1 was fitted to experimental cross section based on earlier estimates of the intensities of the low-energy neutron intensities, as explained in Sec. 7.5.1.

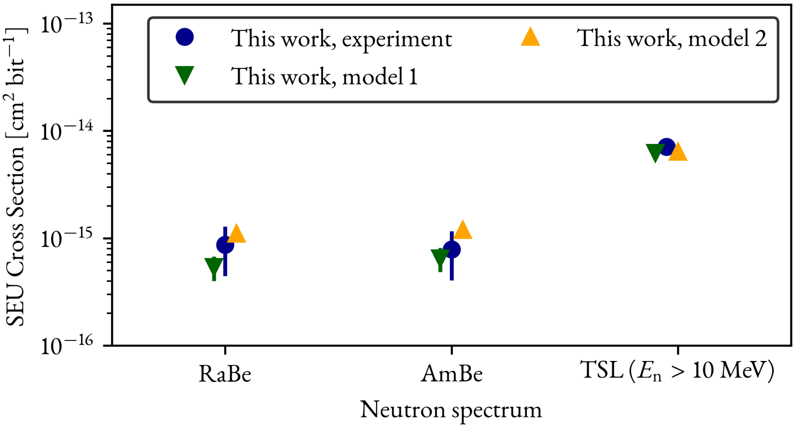

Figure 7.13: The model-determined cross sections for neutron-induced SEUs, compared with the experimental results. Note that model 1 was fitted to experimental cross section based on earlier estimates of the intensities of the low-energy neutron intensities, as explained in Sec. 7.5.1.

8. Results and Discussion

The model described in Ch. 7 may, after determination of Q_{crit} and d_{SV}, be used to predict SEU cross sections. By simulating the interaction of a proton or neutron beam of any energy inside the modelled SRAM cell, the SEU cross section for that particular particle beam can be determined by using Eq. 7.19. In this process, the direct result of the Monte Carlo simulation — i. e. $N_{\text{SEU}}(Q_{\text{crit}}, d_{\text{SV}})$ — is combined with the posterior distribution of the two parameters to predict σ_{SEU}. In this chapter, the results of such predictions are presented, both for monoenergetic proton and neutron beams of different energies and for the expected neutron spectrum at the location of the digitiser boards in the PANDA EMC. Additionally, the SEU rate during operation of PANDA is estimated.

8.1 Monoenergetic Protons and Neutrons

The energy dependence of the proton and neutron SEU cross sections was studied by applying the model predictions to simulations of monoenergetic beams of protons and neutrons. The resulting SEU cross sections are shown as a function of the incident-particle energy in Fig. 8.1, where they are also compared with a parametric model for neutron-induced SEUs described in the work of Wirthlin *et al.* [98]. The observed discrepancy between the model in the present work and this previously described model may be due to the fact that the parametric model in [98] was fitted to high-energy data only.

The energy dependences of the predicted cross sections agree well with what is expected from the reasoning in Sec. 6.2.4: the cross sections increase with energy above a threshold level, until reaching a plateau. At high energies, the proton and neutron cross sections are very similar, which is expected as the nuclear-reaction mechanisms in silicon at these energies are similar for both nucleons. As the fluence of low-energy protons is assumed to be very small at the locations of the digitisers (see Paper II), the cross section for low-energy protons has not been determined with the model.

Potential uncertainties in the energy-dependence of the modelled cross section, for instance regarding the SEU risk posed by thermal neutrons, are discussed in Paper II.

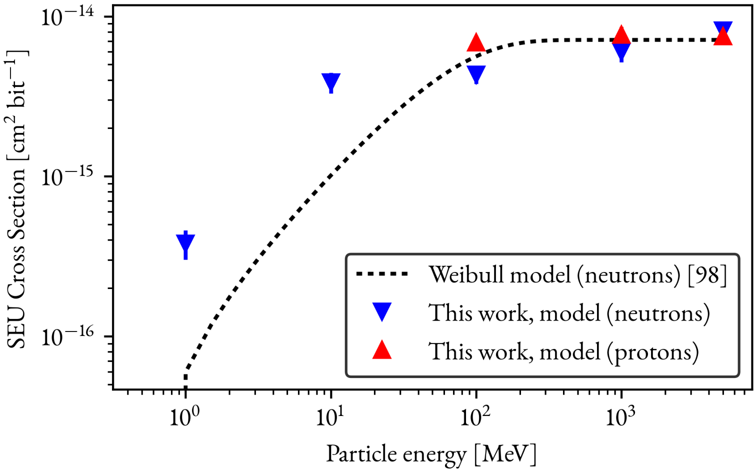

Figure 8.1: The energy dependences of the cross sections for proton- and neutron-induced SEUs in the Kintex-7 FPGA, as predicted by the SEU model developed in this work. The model predictions are compared with a model for neutron-induced SEUs, proposed in [98].

8.2 Neutron-Induced SEUs in PANDA

As discussed in Ch. 4, the digitiser boards will be placed inside the EMC detector volume, where they will be exposed to a rather high particle fluence. The SEU rate during operation of PANDA may be estimated by employing the SEU model in this work. Here, this procedure has been performed for neutrons reaching the digitiser boards around the forward endcap of the EMC. In addition to the SEU model, the expected neutron fluence and energy spectrum at this location are needed to estimate the SEU rate. To determine these, the PandaRoot framework [144] has been used. PandaRoot is a software framework that includes the PANDA detector geometries and allows event generation from an initial $\bar{p}p$ collision using the dual parton model (DPM) [145] event generator. The generated particles are tracked through the detector volumes using Monte Carlo techniques and the responses of the PANDA subsystems may be simulated.

In this work, the different operating conditions of PANDA during initial experiments have been considered. Therefore, two PandaRoot simulations were performed: at $\bar{p}$ momenta of 1.5 and 15 GeV/c, respectively. This was done to identify any potential variation in the SEU rate with beam momentum. As described in Paper 2, the PandaRoot simulations were used to model the neutron energy spectra for these two $\bar{p}$ momenta at the locations of the forward-endcap digitiser boards.

By combining the modelled radiation field with the model-predicted SEU energy dependence, the rate of neutron-induced SEUs in the forward endcap could be predicted. The predicted SEU rate and resulting mean time between upsets (MTBU) are shown in Tab. 8.1. For more details, the reader is referred to Paper II.

Table 8.1: The model-predicted rate of neutron-induced SEUs in the forward-endcap EMC and the corresponding mean time between upsets per FPGA.

Beam momentum [GeV/c]	SEU rate [h^{-1}]	Mean time between upsets [h]
1.5	0.006	165 ± 38
15	0.008	123 ± 30

8.3 Discussion

The results in the previous section show that the worst case average MTBU in the forward-endcap FPGAs under initial operation of PANDA is expected to be 123 ± 30 hours per FPGA. Since the forward endcap will be read out by 217 front-end digitisers, each containing two FPGAs, the resulting MTBU for the whole endcap is predicted to be 17 ± 4 minutes. As stated in Sec. 8.1, one potential issue with the SEU model is that its ability to model SEUs induced by thermal neutrons is unknown. However, due to considerations in the manufacturing process, the thermal-neutron cross section of the Kintex-7 is kept low.

In order to assess the need for SEU mitigation techniques in the FPGA firmware, the severity of errors has to be determined. An SEU occurring in a part of the configuration memory which is not utilised by the used firmware, and which has no effect on any vital parts of the memory, does not have to be corrected immediately. On the other hand, an SEU causing a bit flip in a sensitive part of the memory — for instance the location of a state machine used in the data processing — has to be corrected immediately. In order to determine which parts of the memory are critical, the design of the firmware has to be finalised.

As was the case during the experiments described in Ch. 6, the Xilinx SEM core may be implemented in the FPGA firmware during operation of PANDA to protect against some SEUs. In fact, the functionality of the SEM core may be extended compared to what was the case during the test irradiations, so that some MBUs may be corrected in addition to the SBUs. As may be determined from the data Tab. 6.1, the average probability of an SEU being part of an uncorrectable error is approximately 10%. Assuming that this ratio holds also for the PANDA SEU cross sections, the MTBU for uncorrectable SEUs in the whole forward endcap is 170 ± 40 minutes.

Part III

Feature Extraction for the Shashlyk Calorimeter

9. Feature Extraction

The purpose of the PANDA shashlyk calorimeter is to measure the energies of highly forward-boosted photons, electrons and positrons. As with all calorimeters, the shashlyk detector and readout are constructed in a way such that for instance the size of the output signal is proportional to the energy deposited in the detector. Key properties of the detector, such as potential non-uniformities in the scintillation-light collection and a position dependence in the detector response, have been studied in the past [146]. After a dedicated research & development campaign, these issues were resolved by improving the mechanical rigidity of the cell, changing the WLS-fibre type and including reflective material for improved light collection. After these improvements, the energy and time resolution of the shashlyk calorimeter were found to fulfil the performance requirements presented in Table 4.1.

As was explained in Ch. 3, powerful FPGA-based front-end electronics will be used in the shashlyk EMC as part of the PANDA DAQ chain. These digitiser modules will sample the detector signals, and signal-processing algorithms will be implemented in the FPGA firmware to enable real-time analysis of the incoming signals. Due to data-rate constraints, the entire sampled detector signals will not be transmitted from the digitisers. Rather, so-called feature-extraction methods [83] will be implemented in the FPGA to extract key parameters of detector signals in real time. In addition to information about the incident-particle energy, the FPGA should also determine the timing of signals from the detector. Since the digitisers will receive global timing information through the SODANET protocol, time information determined locally on an FPGA may be related to signals from other detector subsystems. Merging of data from these multiple sources will be done at a later stage in the DAQ chain, where information extracted by the digitiser FPGAs may also be used to reconstruct the hit position of a particle.

Throughout the history of radiation-detection systems, several methods to determine pulse-height and timing information from detector signals have been used. Many of these methods were developed for implementation in analogue electronics, and as digital signal processing techniques have become the standard in modern systems one may either port these algorithms to the digital domain or develop purely digital algorithms. Today, when fast and powerful components such as FPGAs are commonly used in these systems, it is possible to implement increasingly powerful real-time algorithms. In this part of the thesis, the development of a method combining two well-known algorithms is described. The developed algorithm enables real-time determination of pulse height and timing, and provides a way of reconstructing pile-up events. In the following sections, these three tasks will be introduced, current status of the field briefly reviewed and the components of the proposed algorithm described.

9.1 Energy and Timing Measurements

Before proceeding to describe the algorithms chosen for this work, the current status of the field will be described, with the focus being on digital algorithms. There are several areas of research where these topics are of interest. In gamma-spectroscopy applications, the task is to accurately measure the energies of photon impinging on the detector. Today, such applications often suffer from high count rates, and so the task of handling pile-up events is a common one. Methods for pulse-height and timing measurements are commonly used in high-energy physics. However, as discussed in Sec. 3.3, most such systems do not employ the same free-running DAQ approach as PANDA, and so entire sampled detector signals are often available for offline analysis, allowing for removal of pile-up effects. Yet another area of research connected to these topics concerns medical applications such as positron emission tomography, where good energy and time resolution, often at high count rates, is usually required to minimise treatment times.

9.1.1 Pulse-Height Measurements

Fundamentally, the amount of light output from a scintillator should be proportional to the energy deposition in the detector. As this scintillation light is converted into charge, the total amount of charge should be proportional to the energy deposition. By integrating the current output from the detector, one obtains a measurement of the energy. A number of analogue methods have been developed to perform this integration to yield an optimal energy resolution — commonly a detector system includes a preamplifier to integrate the current pulses and an amplifier to amplify and shape the integrated signal [147]. A common feature of such systems is that the amplitude of the final signal is made to be proportional to the input charge, so that the energy can be measured by measuring the pulse height. Using a peak-sensing ADC, the pulse height is detected and digitised for spectroscopic analysis. In Fig. 9.1, a typical detector signal is shown and its height indicated. It is clear that noise and fluctuations may obscure the true pulse maximum, which is the motivation for pulse-processing methods.

In the case of purely analogue methods, optimal performance in terms of for instance the signal-to-noise ratio (SNR) is the aim of integrating and shaping circuits. Fast digital systems make it possible to take a different approach to pulse-height determination, by directly digitising the preamplifier signal and applying digital fil-

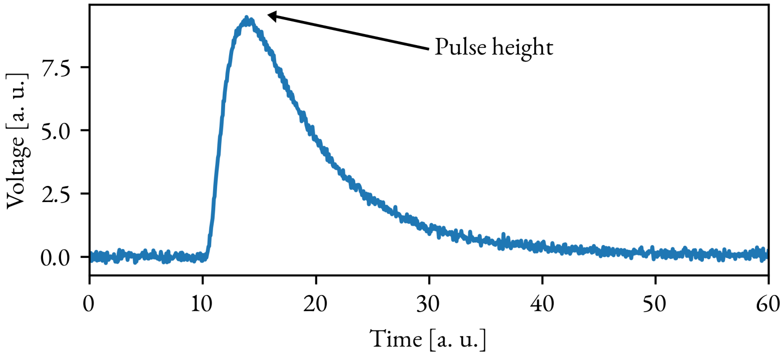

Figure 9.1: The purpose of pulse-height algorithms is to determine the height of a detector signal, as this is proportional to the energy deposition in the detector. Here, a typical detector signal is shown and its pulse height indicated.

ters directly on that signal. Digital filters commonly used to maximise the SNR to obtain a good energy resolution include trapezoidal filters [148, 149], cusp filters [150] and digital implementations of CR-RC filters [151]. Filters such as these are commonly developed starting from an analogue filter, but are in many cases easier to implement in the digital domain. These filters often assume that the input signal is well described as a single decaying exponential function. This assumption is usually valid for signals from preamplifiers. In the case of the PANDA shashlyk calorimeter, however, the signals from the PMTs are digitised directly (potentially with some analogue shaping at the input stage of the digitiser), so that the sampled signal is not well described by such an elementary function. In addition, most of these digital algorithms suffer from the same issue as their analogue counterparts: they are unable to withstand high-rate conditions [152]. This is not acceptable in PANDA, where a high rate is expected in the shashlyk calorimeter, and pile-up reconstruction is desired. Therefore, a method capable of measuring the pulse height of non-exponential pulses with a good SNR at high-rate conditions is necessary.

Finally, fully digital systems are capable of sampling and extracting entire pulse waveforms, which has been utilised in spectroscopic applications by fitting the extracted waveforms offline to obtain pulse-height information [153, 154]. Advantages of such methods are for instance that information about the entire pulse shape is available for analysis, and that the pulse shape does not have to be described by a simple exponential function but may be fitted with a custom pulse-shape function. Due to the need for real-time processing of signals in PANDA due to high data rates, such methods are not appropriate for application to the present work. Nonetheless, there exists a well-known algorithm which may be used to perform a simplified fit to incoming data in real time: the so-called optimal filter (OF) [155]. It is purely digital as it has no direct analogue counterpart, and has been successfully used mainly in particle-physics experiments for a long time [156–158]. It has been developed to determine the amplitude and timing of detector signals given a known pulse shape. As it is one of the algorithms used in this work, it will be described in more detail in Sec. 9.3.

9.1.2 Timing Measurements

In addition to measuring the energy of the particle interacting in the calorimeter, measuring its time of arrival is a key task for the EMC digitisers. In order to relate an event to responses from other subdetectors in PANDA, accurate information about its timing is necessary. The goal of any timing algorithm is to produce a logic signal at a time directly related to the time-of-arrival of the measured signal. In Fig. 9.2, a typical detector signal is shown and its start time indicated. As was the case for the pulse-height determination, noise and fluctuations makes the task of determining the pulse timing more difficult. As with algorithms developed for energy determination, timing algorithms have often been developed starting from analogue predecessors. Such is the case for digital implementations of the leading edge discriminator (LED) and the constant fraction discriminator (CFD).

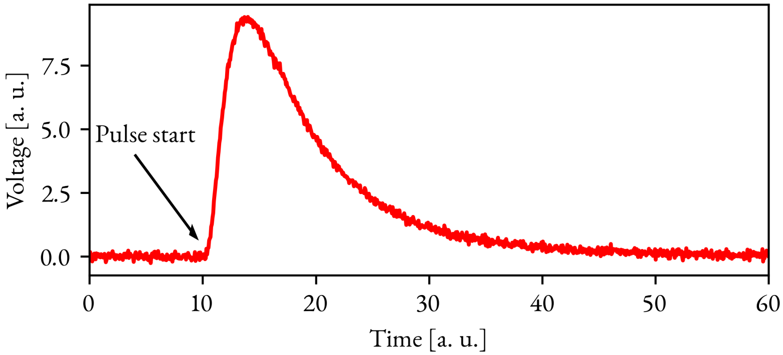

Figure 9.2: The purpose of timing algorithms is to determine the timing of a detector signal. Here, a typical detector signal is shown and its start time indicated.

A LED outputs a logic signal when the input exceeds a *fixed* threshold, i. e. on the leading edge of the detector signal [159]. The LED method suffers from two sources of noise: jitter and time walk. Jitter is due to noise and statistical fluctuations in the detector and readout electronics, and to some extent affects all timing algorithms. Time walk is a more severe shortcoming of the LED method, and appears when input signals have very different amplitudes from each other. If the rise time of all signals is the same, the constant threshold of the LED will mean that a larger pulse will cross the threshold earlier than a small pulse, even if the time of arrival of the initiating particle was the same. While this effect is not very pronounced if the pulse amplitudes are fairly constant, the LED method would cause a deterioration if used in the shashlyk readout, where pulses having a wide range of amplitudes are expected.

To reduce the impact of the time-walk effect, the CFD was developed [160]. In contrast to the LED, which relies on a fixed threshold for timing determination, the idea behind the CFD method is to trigger at a *fraction* of the pulse amplitude. In this way, the strong pulse-height dependence of the determined time is removed. In an analogue implementation of a CFD, this is achieved by splitting the input signal into two branches — one which is delayed and one which is inverted and attenuated. By triggering at the time when these two branches are equal (or equivalently when their sum crosses zero), the timing signal is generated at a specific fraction of the input-signal amplitude. The actual value of the fractional triggering level is specified by setting the delay time and the attenuation factor. It has been found that the jitter induced by the CFD method is minimised when the triggering occurs at the maximum slope of the signal rising edge. The CFD algorithm may be easily implemented in digital signal processing (DSP) systems, and was due to its simplicity and favourable properties chosen as one of the main algorithms for use in the present work. The digital implementation of the CFD algorithm is described in more detail in Sec. 9.2.

In addition to the digital implementation of analogue algorithms, several purely digital algorithms have been developed. These include methods based on weighted averages of pulse samples [161], moment analysis [162], pulse-shape fitting [161] or interpolation techniques [163]. At least some of these more advanced methods suffer from the same computational complexity as the more advanced algorithms for pulse-height determination. The OF algorithm, briefly introduced in the previous section, provides a way of estimating the pulse timing in real time while avoiding the computational complexity of some of these methods. It will be described in more detail in Sec. 9.3.

9.1.3 Pile-Up Events

For many years, the issue of pile-up events has posed a problem in radiation-detection systems. In a gamma-spectroscopy system, pile-up causes distortion of the measured spectrum, and for this reason methods to detect and discard pile-up events before storage were developed [164–166]. Through the advent of digital-signal processing systems, new possibilities to handle such events have opened up [167]. This includes methods developed to not only reject pile-up events, but to some extent reconstruct the underlying signals to extract signal features. Such methods have a greater throughput than pileup-rejection methods where events are discarded, but may result in a loss of resolution as the resolution of reconstructed events is worse than the resolution of undisturbed events. In Fig. 9.3, a typical pile-up event is shown. The purpose of a pile-up reconstruction algorithm is to “disentangle” the constituent pulses so that their respective heights and start times may be determined.

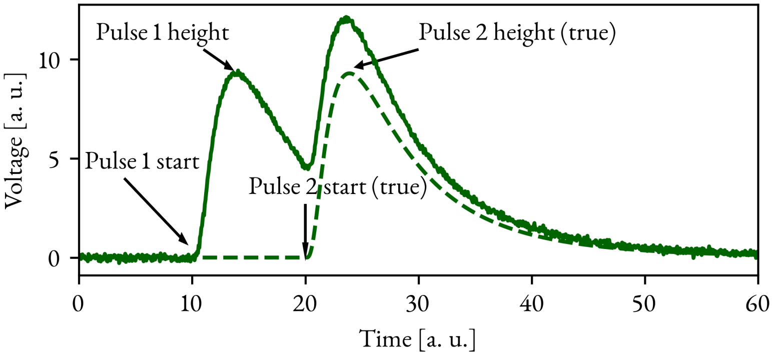

Figure 9.3: The purpose of pile-up recovery algorithms is to reconstruct piled-up pulses so that the heights and timings of the constituent pulses may be determined. Here, a typical pile-up event, where a second pulse arrives before the end of the first pulse, is shown.

In order to achieve the requirements of at most 1% event loss due to pile-up placed on the PANDA EMCs, pile-up reconstruction algorithms are necessary. One algorithm commonly used for this purpose is the moving window deconvolution method [168], a trapezoidal filter which runs in real time and is implementable in an FPGA. However, it relies on the assumptions that the signals are well described by a simple exponentially decaying function. As was the case for the many pulse-height algorithms relying on the same assumption, this is not valid in the shashlyk EMC, and other methods have to be investigated. Many of the methods not requiring a simple exponential pulse shape rely on pulse fitting [169] or deconvolution [170]. Such methods are often computationally intensive and require offline processing of the saved waveforms. Real-time pulse fitting methods have been developed [171], but also these require multiple iterations to converge to optimal pulse-height and timing parameters.

Out of the recently proposed strategies to reconstruct pile-up events, the method presented in this thesis is most similar to the one presented in [172]. It also shares features with a proposed method for pile-up reconstruction in the PANDA EMC [173, 174], which includes pulse-tail subtration but also requires purely exponential pulse shapes and cannot be directly applied in the shashlyk EMC. In this thesis, the well known CFD and OF algorithms are combined with the purpose of constructing a real-time method, implementable in an FPGA, which is capable of improving the energy and time resolution while also enabling pile-up reconstruction. A digital implementation of the CFD is used to extract a first estimate of the pulse timing, and the OF is used to refine the timing determination and provide a measurement of the pulse height. Due to the high channel density on the EMC digitiser, this method has to require limited resources in the FPGA. In the subsequent sections, the CFD and OF algorithms are described in more detail, and the principles behind the combined algorithm developed in this work are outlined. The results of the method are presented in the following chapters.

9.2 Constant-Fraction Discriminator

The CFD reduces the time-walk effect as it determines the pulse timing by measuring the time at which the pulse reaches a fixed fraction of its maximum height. The fractional triggering is achieved by splitting the input signal into two branches, one which is delayed by a fixed time t_d, and another which is inverted and attenuated by a factor f relative to the original pulse height. All of these operations rely on the determination of the signal baseline level $V_0(t)$, which is the voltage under the signal, which is not actually related to the particle interaction in the detector. While the baseline can in the most general sense be time-dependent, it is commonly assumed to be constant. For proper operation of the CFD algorithm, the baseline has to be subtracted from the input signal. After summing the delayed and the attenuated/inverted branches, the resulting signal shape is given by:

$$V_{\mathrm{CFD}}(t) = (V(t - t_d) - V_0(t - t_d)) - f(V(t) - V_0(t)), \tag{9.1}$$

where V is the raw signal from the detector. The timing of the signal is determined by measuring the time at which V_{CFD} crosses zero. The working principle of this method is shown in Fig. 9.4.

The CFD method was in its original form a purely analogue one, but it may be directly transferred into the digital domain by simply considering a sampled detector signal. Given a set of such samples $S[n]$ (where n denotes the sample number), the digital CFD (DCFD) output is, analogous to Eq. 9.1, given by:

$$V_{\mathrm{DCFD}}[n] = (S[n - D] - B[n - D]) - f(S[n] - B[n]), \tag{9.2}$$

where B is the signal baseline and D is the time delay used in the delayed branch. In the simplest digital form of the DCFD, D is an integer, although methods have been developed to consider also fractional-sample delays [175]. In this work, only integer-value delays will be considered. Because of the discrete nature of the DCFD algorithm, the true DCFD zero crossing is normally located between two sampling-clock cycles. Because of this, some form of interpolation between the samples below and above the zero crossing may be employed to extract T_{DCFD}, the DCFD time.

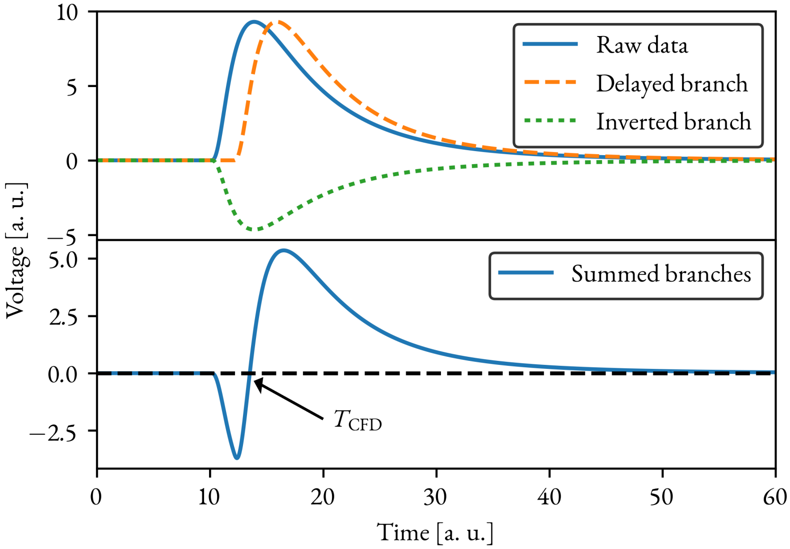

Figure 9.4: Principle of using the constant fraction discriminator method to determine the timing of a detector signal. The raw signal is (after baseline subtraction) split into two branches: one which is delayed and one which is inverted and attenuated. The zero-crossing point of the sum of the two branches yields a time stamp which is independent of the pulse height of the original signal.

9.3 Optimal Filter

One of the more common signal-processing algorithms used in high-energy physics is the so-called optimal filter (OF) [155]. The OF filter is an example of a finite impulse response (FIR) filter [176], a type of filters which will now be briefly introduced.

9.3.1 Finite Impulse Response Filters

As with any filter used in signal processing, the aim of a FIR filter is to modify an input signal to reduce unwanted features (such as noise) or enhance features of interest in the signal. A schematic view of a FIR filter is shown in Fig. 9.5, where N delay-line elements are used to obtain a set of $N+1$ samples of a sampled input signal $\boldsymbol{x}$ (giving $x[n], x[n-1], x[n-2], ..., x[n-N]$). Each of these samples is multiplied by one of $N+1$ corresponding coefficients $\boldsymbol{b}$, and the results of the multiplications are summed to give an output $y[n]$. Each sample used in the filter is known as a *tap*, so that an Nth order FIR filter has $N+1$ taps.

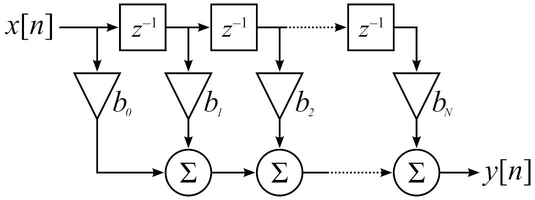

Figure 9.5: Schematic drawing of the principle of a finite impulse response (FIR) filter, in which $N + 1$ taps of the input signal $\boldsymbol{x}$ are multiplied with coefficients b_0, b_1, b_2, ..., b_N. The filter output $y[n]$ is the sum of the multiplied values.

9.3.2 Principles of the Optimal Filter

In the rest of this thesis, the notation used to denote the FIR-filter operations used in the OF will differ from the more general notation just introduced. In particular, the total number of samples and coefficients used in the filter will be denoted M, the filter tap indices will run from 1 to M and the input signal will be denoted $S_n \equiv S[n]$ (where n is the sample number). The OF algorithm may be used to estimate the amplitude and timing of a detector signal, under the assumption of white noise. It relies on knowledge about the pulse shape $g(t)$, which has an amplitude normalised to 1. Although the OF will be given in the form of a FIR filter later in this section, it is helpful — especially so for the work in this thesis — to introduce it as being equivalent to fitting the incoming data with a linearised version of the known pulse shape in a χ^2 fit. The aim of this procedure is to estimate the pulse height and timing. Given a sampled waveform such that a series of samples $\boldsymbol{S} = S_1, S_2, ..., S_M$ are obtained, the agreement between the data and the assumed pulse shape may be quantified using a χ^2 metric:

$$\chi^2 = \sum_{i=1}^{M} \sum_{j=1}^{M} (S_i - Ag(t_i - \tau) V_{ij} (S_j - Ag(t_j - \tau)), \tag{9.3}$$

where the normalised pulse template $g(t)$ is evaluated at the sample times $t_i (i = 1, ..., M)$, is scaled by an amplitude parameter A and shifted in time by τ. τ is the deviation of the phase of the pulse from some *assumed* time of arrival. V_{ij} is the inverse of the covariance matrix for the different samples. This matrix depends on any correlation between subsequent samples in the incoming data. By minimising Eq. 9.3, the values of A and τ giving the best agreement with the observed pulse may be determined. Assuming that τ is small, one may linearise $g(t - \tau)$ using a Taylor expansion:

$$g(t_i - \tau) \approx g(t_i) - \tau g'(t_i), \tag{9.4}$$

where $g'(t_i) = \mathrm{d}g/\mathrm{d}t$. By defining $\alpha_1 \equiv A$ and $\alpha_2 \equiv A\tau$, introducing the notation $g_i \equiv g(t_i)$ and $g'_i \equiv g'(t_i)$ and combining Eqs. 9.3 and 9.4, one obtains:

$$\chi^2 = \sum_{i=1}^{M} \sum_{j=1}^{M} (S_i - \alpha_1 g_i + \alpha_2 g'_i) V_{ij} (S_j - \alpha_1 g_j + \alpha_2 g'_j), \tag{9.5}$$

so that the task of estimating α_1 and α_2 is now reduced to a linear problem.

It can be shown [155] that minimising the χ^2 in Eq. 9.5 yields expressions for α_1 and α_2 that depend only on the pulse template $\boldsymbol{g}$, the matrix $\boldsymbol{V}$ and the input data $\boldsymbol{S}$, and that this minimisation may also be performed in the time domain using a FIR filter. This makes it easy to implement in an FPGA. In the time domain, α_1 and α_2 may be estimated using two FIR filters with sets of coefficients $\boldsymbol{a}$ and $\boldsymbol{b}$:

$$\alpha_1 \equiv A = \sum_{i=1}^{M} a_i S_i \tag{9.6}$$

$$\alpha_2 \equiv A\tau = \sum_{i=1}^{M} b_i S_i \tag{9.7}$$

To satisfy these relationships while assuming purely white noise, the sets of coefficients $\boldsymbol{a}$ and $\boldsymbol{b}$ should be chosen according to:

$$\boldsymbol{a} = \lambda \boldsymbol{V}\boldsymbol{g} + \varkappa \boldsymbol{V}\boldsymbol{g}' \tag{9.8}$$

$$\boldsymbol{b} = \mu \boldsymbol{V}\boldsymbol{g} + \varrho \boldsymbol{V}\boldsymbol{g}', \tag{9.9}$$

where λ, $\varkappa$, μ and ϱ are defined as follows:

$$\lambda = \frac{\boldsymbol{g}'^{\mathrm{T}}\boldsymbol{V}\boldsymbol{g}'}{(\boldsymbol{g}'^{\mathrm{T}}\boldsymbol{V}\boldsymbol{g}') \cdot (\boldsymbol{g}^{\mathrm{T}}\boldsymbol{V}\boldsymbol{g}) - (\boldsymbol{g}'^{\mathrm{T}}\boldsymbol{V}\boldsymbol{g}) \cdot (\boldsymbol{g}'^{\mathrm{T}}\boldsymbol{V}\boldsymbol{g})} \tag{9.10}$$

$$\varkappa = \frac{-\boldsymbol{g}'^{\mathrm{T}}\boldsymbol{V}\boldsymbol{g}}{(\boldsymbol{g}'^{\mathrm{T}}\boldsymbol{V}\boldsymbol{g}') \cdot (\boldsymbol{g}^{\mathrm{T}}\boldsymbol{V}\boldsymbol{g}) - (\boldsymbol{g}'^{\mathrm{T}}\boldsymbol{V}\boldsymbol{g}) \cdot (\boldsymbol{g}'^{\mathrm{T}}\boldsymbol{V}\boldsymbol{g})} \tag{9.11}$$

$$\mu = \frac{\boldsymbol{g}'^{\mathrm{T}}\boldsymbol{V}\boldsymbol{g}}{(\boldsymbol{g}'^{\mathrm{T}}\boldsymbol{V}\boldsymbol{g}') \cdot (\boldsymbol{g}^{\mathrm{T}}\boldsymbol{V}\boldsymbol{g}) - (\boldsymbol{g}'^{\mathrm{T}}\boldsymbol{V}\boldsymbol{g}) \cdot (\boldsymbol{g}'^{\mathrm{T}}\boldsymbol{V}\boldsymbol{g})} \tag{9.12}$$

$$\varrho = \frac{-\boldsymbol{g}^{\mathrm{T}}\boldsymbol{V}\boldsymbol{g}}{(\boldsymbol{g}'^{\mathrm{T}}\boldsymbol{V}\boldsymbol{g}') \cdot (\boldsymbol{g}^{\mathrm{T}}\boldsymbol{V}\boldsymbol{g}) - (\boldsymbol{g}'^{\mathrm{T}}\boldsymbol{V}\boldsymbol{g}) \cdot (\boldsymbol{g}^{\mathrm{T}}\boldsymbol{V}\boldsymbol{g})} \tag{9.13}$$

Thus, since the ideal pulse shape $g(t)$ (and its time-discretised version $\boldsymbol{g}$) and the matrix $\boldsymbol{V}$ are known, the sets of coefficients $\boldsymbol{a}$ and $\boldsymbol{b}$ may be calculated offline and multiplied with any incoming data to give estimates for A and $A\tau$ according to Eqs. 9.6 and 9.7. The fact that these coefficients are constant makes the OF algorithm very well suited for real-time applications. When the method is applied in real time, it will constantly re-evaluate the output of the FIR filters based on the M input samples. When the input data and waveform template are optimally aligned, the output reaches its maximum and the estimates of α_1 and α_2 correspond to the best estimates for the analysed pulse.

Because the OF algorithm incorporates information from several samples into the determination of the pulse height and timing, as well as prior information about the expected pulse shape, it can provide accurate parameter estimation. In contrary to the CFD algorithm, it does not rely directly on linear interpolation for timing determination and should be able to more accurately describe a non-linear rising pulse edge. However, this relies on both the assumption that the pulse shape from the detector is fairly stable, that the pulse template g actually contains the pulse maximum, and that a good initial estimate of the pulse timing is provided. In a collider experiment with a bunched beam structure, the assumed time of arrival of signals may be obtained by synchronising the clock used to sample the input signal with the bunch-crossing frequency. In this case, the assumed time of arrival is readily given by the sampling clock. In PANDA, this is not possible due to the free-running nature of the DAQ (all electronics are time-synchronised using the SODANET protocol, which is not directly derived from the antiproton-proton interaction rate). Because of this, the method proposed in this thesis uses the CFD algorithm to provide an initial timing estimate of the pulse timing, after which a small τ may be assumed. In practice, this means that the coefficient sets $\boldsymbol{a}$ and $\boldsymbol{b}$ depend on the timing determined by the CFD, since the time-discretised pulse template $\boldsymbol{g}$ will be different for different assumed pulse timings. The solution to this issue will be described in Ch. 10.

9.3.3 Pile-up Recovery

The previous sections introduced the two DSP algorithms forming the basis of the rest of this thesis. Together, they may be used to solve the two main tasks of the EMC digitiser: pulse height and timing determination. The CFD method provides a first estimate of the pulse timing but gives no information about the pulse height. By using the CFD timing estimate as an input to the OF algorithm, the timing determination may be refined and the pulse height determined. However, as it is generally used, the OF algorithm does not enable pile-up reconstruction. Indeed, if the pulse template $\boldsymbol{g}$ describes an ideal pulse shape and the input data corresponds to two (or more) overlapping pulses, the algorithm will attempt to "fit" a single pulse to the multi-pulse data and the pulse height and timing determination will most likely not be correct.

To obtain robust operation of the OF method even under pile-up conditions, correlations introduced by pile-up events (which are essentially time-shifted and scaled pulse templates superimposed on each others) may be incorporated into the covariance matrix [177]. Such methods depend on the average pile-up probability, which in turns depends on the primary-interaction rate. They may be used to suppress pile-up events when using the OF to make a trigger decision, but in a feature-extraction application such as the PANDA EMC, where the full waveform will not be stored for offline analysis, they are not suitable. A method based on the traditional OF aimed at simultaneous determination of α_1 and α_2 for two pile-up pulses has been developed in the past [178], but comes with higher requirements on hardware resources.

In this work, we propose another approach, which is illustrated in Fig. 9.6. As the OF algorithm may be viewed as a way of minimising the χ^2 in Eq. 9.5, there is no reason why the “range” of the fit has to be large enough to cover the entire pulse, except that information from more samples will go into the determination of α_1 and α_2. Since the most important information about the pulse — its height and its timing — is contained within the first part of the pulse, the pulse-template $\boldsymbol{g}$ may be truncated in time to correspond to a narrower fit range. The main requirements on this range are that it should cover the rising edge and the maximum of the template pulse. By limiting the fit range, the influence that potential pile-up events arriving on the tail of the primary pulse would have on the amplitude and time determination are reduced. Limiting the fit range corresponds to decreasing the number of FIR coefficients $\mathcal{M}$, which also reduces the hardware requirements. If α_1 and α_2 may indeed be successfully determined from the initial part of a pulse, they will have been determined before the arrival of any pile-up pulses. Since the pulse template $g(t)$ is known, it may be scaled and shifted according to the parameters determined from the fit to the initial pulse, and subtracted from the subsequent input data. This way, the *reconstructed* tail of the first pulse will constitute the baseline of subsequent pile-up pulses and may be used as such in both the CFD and OF analyses of subsequent data. The analysis procedure of any pile-up events is exactly the same as for the initial pulse, only assuming a non-constant baseline. With this method, reconstruction of pile-up events should be possible as long as they are separated well enough that they don’t influence the OF fit range. The development of this method is described in detail in the next chapter.

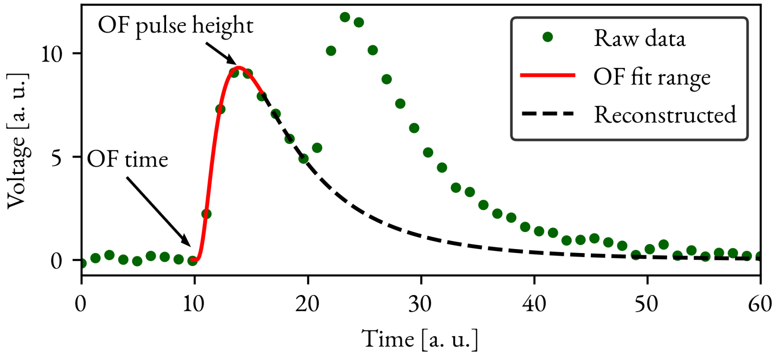

Figure 9.6: Principle of the feature-extraction algorithm proposed in this work. Digitised detector data are analysed by a combination of the CFD and OF algorithms. After an initial timing estimate by the CFD method, a "truncated" OF algorithm covering the initial part of the detector signal is used to determine the height and timing of the first pulse. The determined pulse parameters may be used to calculate a reconstructed pulse shape, which forms the baseline of any pile-up pulses.

10. Detector Modelling

To develop and benchmark an algorithm for feature extraction in the PANDA shashlyk calorimeter, a detailed Monte Carlo model of the detector and its readout has been developed. This model has been developed using existing experimental data from measurements of the response of a 4 × 4 prototype of the calorimeter. After validating the model against these experimental data, it was used to generate realistic detector signals on which the developed algorithm was applied.

10.1 Prototype Tests

In 2014, the response of an 4 × 4 calorimeter prototype to photons with energies up to 800 MeV was measured at the tagged-photon facility at the MAMI (Mainzer Mikrotron) electron accelerator in Mainz, Germany [146, 179]. These experiments were performed and analysed by the PANDA groups from Gießen, Germany and Protvino, Russia. During these measurements, the full digitised waveforms were extracted for each event, allowing for flexible offline analysis. These measurements provided valuable information about for example the energy and time resolution of the calorimeter. For the work presented in this thesis, these measurements also provide information about the detector pulse shape.

The MAMI electron-accelerator system used during the prototype tests consists of a thermionic electron gun, a 4-MeV linear accelerator and three racetrack microtrons. At the end of acceleration, the electrons had an energy of 855 MeV. The calorimeter prototype was placed in the MAMI A2 hall, where the electron beam was directed into a 10-μm copper foil acting as a radiator to produce bremsstrahlung photons. After bremsstrahlung photons are produced, the electrons are deflected by a dipole magnet (the tagger), and directed onto a plastic-scintillator hodoscope where their energies are determined. In this way, a quasi-monoenergetic beam of tagged photons is obtained as the electron energy detected at the hodoscope is directly related to the energy of the corresponding bremsstrahlung photon. By requiring a coincidence between a signal in the prototype and a signal in the hodoscope, the detector response to different photon energies may be measured.

Fig. 10.1a shows a photograph of the 4×4 prototype used at MAMI. During the prototype tests, the calorimeter was mounted on a movable table, so that its position relative to the photon beam could be modified. Using this setup, the response of the calorimeter at different beam positions could be measured. A subset of these data was used in the analysis presented in this work — as shown in Fig. 10.1b, the measurements of relevance here are the ones where the beam was aimed into the centre of one particular cell (*position a*) and also when aimed at the interface between two cells (*position b*).

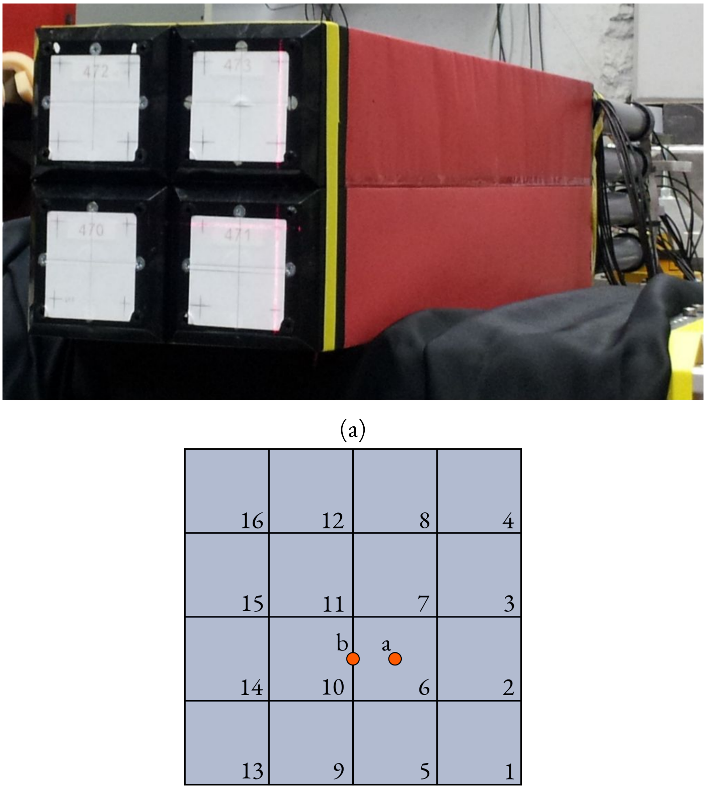

(a)

(b)

Figure 10.1: a) Photograph of the 4 × 4 shashlyk prototype used during the 2014 tests and b) a schematic drawing of the numbering scheme used to identify the cells in the prototype. In this work, measurements taken when the photon beam was directed into positions a (centre of cell 6) and b (interface between cells 6 and 10) were used. Photograph taken from [146].

A VME-based Wiener AVM16 160 MHz, 12-bit sampling ADC [180] was used to digitise the signals from the calorimeter prototype, and readout was triggered by a coincidence between a signal in any calorimeter cell and a signal in any of 15 electron-hodoscope channels selected to correspond to photon energies evenly distributed below 800 MeV. Each acquired waveform consisted of 162 samples, corresponding to 1012.5 ns. At each occurring trigger, the data from all 16 calorimeter cells were read out. In Fig. 10.2, three examples of collected waveforms are shown. Due to an impedance mismatch between the PMT outputs and the ADC inputs present during the prototype tests, reflection of the signals occurred. The resulting undershoot is clearly visible in the acquired waveforms. The amplitude of the undershoot was assumed to be proportional to the amplitude of the original pulse, and the undershoot region of the waveforms was excluded in the analysis.

Another instrumental effect discovered during the original analysis of these data was a non-linearity in the response of the used sampling ADC at photon energies higher than 400 MeV. This had the effect that only data corresponding to tagged-photon energies below 400 MeV could be used in the analysis. For this reason, data from the first eight tagger channels only — corresponding to photon energies of 55, 78, 95, 125, 156, 182, 239, 301 and 342 MeV — will be used in the analysis here.

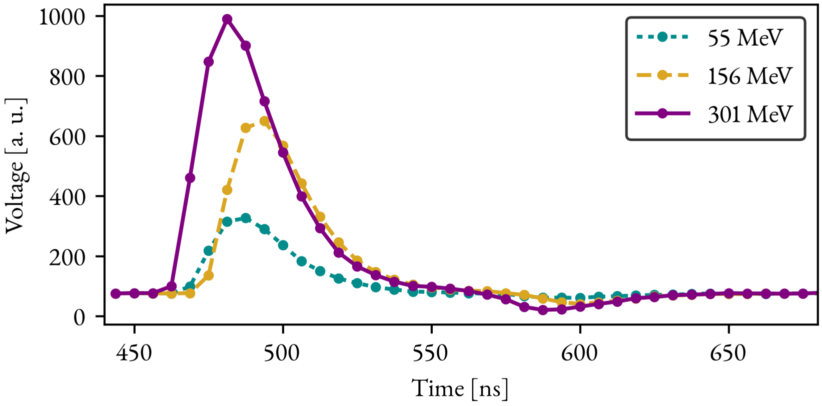

Figure 10.2: Examples of waveforms acquired during the 2014 prototype tests at three different tagged-photon energies. The undershoot visible just before 600 ns is a result of an impedance mismatch during the experiment, and this region of the waveform was excluded in the analysis.

10.2 Geant4 Simulation

In order to develop feature-extraction algorithms for the shashlyk calorimeter, a Monte Carlo model of the 4 × 4 prototype has been developed. The starting point of this model is a Geant4 simulation of photons interacting in the 4 × 4 prototype. A schematic side view of a single shashlyk cell is shown in Fig. 10.3 — this was the basis for the modelled detector geometry, with the exception of the WLS fibres which were assumed to provide a negligible contribution to the energy deposition in the cell due to the relatively small fibre diameter of 1 mm. The Tyvek sheets placed between the layers in the calorimeter are not shown in Fig. 10.3 but were included in the modelling as they contribute to the thickness of the detector and therefore could influence the shower development and potential leakage.

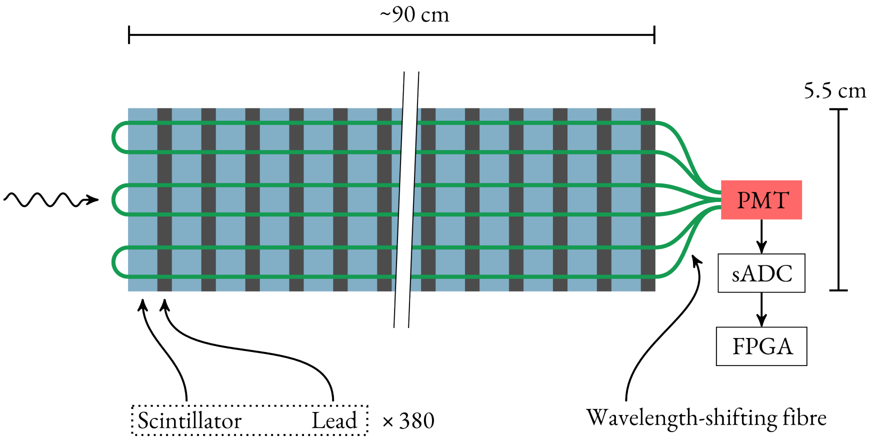

Figure 10.3: Schematic side view of a single shashlyk-calorimeter cell. Each cell consists of 380 layers of interleaved scintillators and lead, giving a total thickness of approximately 90 cm. The Tyvek sheets placed between the layers are not shown here, but are taken into account in the total thickness. WLS fibres are used to read out the scintillation light, which is detected and converted to a current in a PMT. The signal from the PMT is digitised and may be processed by an FPGA.

The MAMI facility provided a tagged photon beam, and as each scintillator in the tagger hodoscope has a finite width, the tagged photons corresponding to a particular tagger channel will have a (narrow) energy distribution, which was taken into account when simulating the beams. Due to the bremsstrahlung process, the tagged-photon beam had a finite size when reaching the prototype, and this was modelled as a beam having an intensity distribution given by a 2D normal distribution with a standard deviation of 3.6 mm, in accordance with [146].

Each of the 380 layers of an individual cell was modelled as consisting of a 175-μm Tyvek sheet, a 1500-μm scintillator plate, another 175-μm Tyvek sheet and a 275-μm lead plate. An air gap of 1 μm was assumed between each of these components. A schematic drawing of such a layer is shown in Fig. 10.4. The wavelength-shifting fibres were not included in the Geant4 geometry, as they were assumed to have a negligible impact on the energy-deposition profile. In addition, no mechanical holding structures were included. The matrix was constructed by stacking 4×4 such cells side by side, with a 0.5-mm air gap between each pair of cells. Fig. 10.5 shows the energy-deposition distributions for the different parts of cell 6 after centring a 55-MeV photon beam on that cell. These distributions show the sum of the contributions from all layers in the cell, and show that the energy deposited in the Tyvek sheets is small,

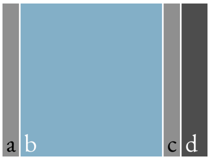

Figure 10.4: Schematic drawing of a single shashlyk-calorimeter layer, as implemented in the Geant4 simulation. Each layer consists of a 175-µm Tyvek sheet (a), a 1500-µm scintillator plate (b), another 175-µm Tyvek sheet (c) and a 275-µm lead plate. Between each layer there is a 1 µm air gap.

but non-zero. Also shown is the distribution of the total energy deposition in the cell, i. e. the sum of all contributions from the scintillators, absorbers and Tyvek sheets. The asymmetry of the energy-deposition distribution indicates that there is a substantial lateral leakage of the electromagnetic shower.

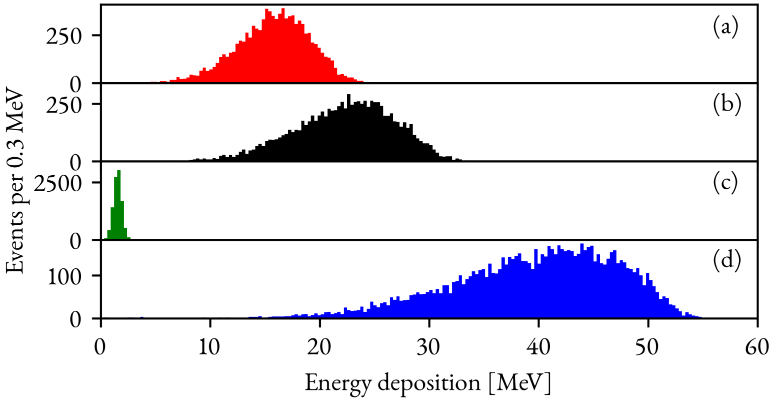

Figure 10.5: Spectra of simulated energy depositions in the (a) scintillator plates, (b) lead absorber plates, (c) Tyvek sheets in cell 6 in the 4 × 4 matrix, after simulating $1 \cdot 10^4$ 55-MeV photons directed into the centre of that cell. In (d), the total energy deposition in the entire cell is shown.

The Geant4 simulation provides access to event-by-event sampling fluctuations intrinsic to the calorimeter, but in order to model the full response of the calorimeter, including the PMT and readout electronics, proper treatment of time and amplitude fluctuations in the system is necessary. These considerations are described in the following subsections.

10.3 Calorimeter Response Function

In order to obtain realistic pulse shapes based on the results of the Geant4 simulation, the entire detector and readout have to be modelled. As shown in Fig. 10.6, one may divide the detector and readout of a single shashlyk cell into four main components that affect the pulse size and shape:

1. The 380 scintillator plates in the cell, which convert the energy deposited into scintillation light.
2. The WLS fibres, which absorb the scintillation light, re-emits it at a longer wavelength and transport the wavelength-shifted light to the photomultiplier tube.
3. In the PMT, electrons are produced from the scintillation photons using a photocathode, and multiplies these electrons to generate a measurable current at the anode.
4. The ADC interface is assumed to consist of a parallel RC circuit which converts the current from the PMT anode to a voltage and a digitisation step where the resulting voltage is digitised.

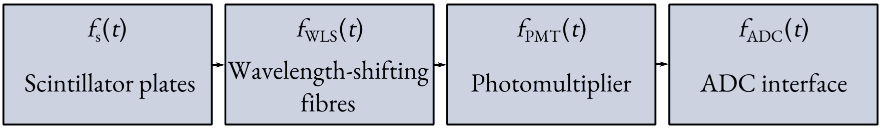

Figure 10.6: Flowchart depicting the components of the calorimeter detector and readout that affect the pulse size and shape.

The four components of this single-cell system may be characterised by their time-domain transfer functions f_s, f_{WLS}, f_{PMT} and f_{ADC}, so that the total transfer function f_{TOT} of the shashlyk cell is given by the convolution of these:

$$f_{\mathrm{TOT}}(t) = \left[\sum_{i=1}^{380} (f_{\mathrm{s,\,i}}(t) * f_{\mathrm{WLS,\,i}}(t)) \right] * f_{\mathrm{PMT}}(t) * f_{\mathrm{ADC}}(t), \tag{10.1}$$

where the response functions of all 380 layers have been summed for the scintillators and WLS fibres, since the total light yield is the sum of the contributions from the individual layers. The convolution operation $*$ between two functions $f(t)$ and $g(t)$ is defined as:

$$(f * g)(t) \equiv \int_{-\infty}^{\infty} f(\tau) g(t - \tau) \mathrm{d}\tau. \tag{10.2}$$

The time-domain response function describes the digitised pulse shape from the detector as a function of the amount of energy deposited in the scintillators. The different components of the response function will now be discussed in detail.

10.3.1 Scintillator Response Function

The scintillator response function f_s describes the time and amplitude structure of the scintillation light given a certain energy deposition in each of the 380 scintillation plates. Assuming that there is no leakage of scintillation light between the different layers, one may treat each layer independently and sum the responses at a later stage.

The time structure of scintillation light from a plastic scintillator with a very similar composition to the one used in the PANDA shashlyk calorimeter has been studied before for use in the CDF experiment [181]. Given the similarity in the composition (2% pTP and 0.03% POPOP in the previous study compared with 1.5% pTP and 0.04% POPOP in PANDA), we assume the same time structure. The resulting response function of the i:th layer, $f_{\mathrm{s,\,i}}$, is given by:

$$f_{\mathrm{s,\,i}}(t) = \begin{cases} s_i \frac{\beta}{1+R} \left[\frac{\exp(-t/\tau_2)-\exp(-t/\tau_1)}{\tau_2-\tau_1} + R\frac{\exp(-t/\tau_3)}{\tau_3} \right], & \text{if } t \geq 0 \\ 0, & \text{otherwise,} \end{cases} \tag{10.3}$$

where the values on the parameters $R = 0.24$, $\tau_1 = 1.04$ ns, $\tau_2 = 1.54$ ns and $\tau_3 = 7.8$ ns were obtained from [181]. s_i is the amount of energy deposited in scintillator layer i and β is the average number of generated scintillation photons per unit of deposited energy in the scintillator. For an energy deposition in a particular layer at a specific time, the scintillator response function yields the time distribution of the produced scintillation photons.

10.3.2 Wavelength-Shifting Fibre Response Function

The WLS fibres used in the PANDA shashlyk calorimeter are 1-mm diameter Kuraray Y-11(200)M green-shifting WLS fibres [182]. As discussed in Sec. 4.4, each shashlyk cell is read out by nine such fibres, each making a 180-degree turn at the front of the cell. As a result, each scintillator layer is pierced by 18 fibres. Several properties of the WLS fibres are of interest:

- The purpose of the fibres is to absorb scintillation photons and re-emit photons at a longer wavelength. This process has an associated decay time intrinsic to the fibre, and has previously been measured to be $\tau_{\mathrm{WLS}} = 7.3$ ns [183].
- Light transported through a fibre will be attenuated due to losses from the fibre. This effect has previously been measured to correspond to an exponential attenuation with an attenuation coefficient of $\mu = 0.33\ \mathrm{m}^{-1}$ [184]. In

addition, the quite sharp 180-degree fibre bend at the front of the cell was assumed to result in an additional loss of 30% of the photons passing through it, so that the transmission probability of light travelling that way is $p_{\mathrm{x}} = 0.7$.

- The speed of the light transported through a fibre depends on the refractive index of the fibre, which was taken to be $n = 1.59$ [182].

In the following calculations, it will be assumed that the total length of a single fibre is given by $2l$, where l is the thickness of the entire calorimeter. After being absorbed and re-emitted in a WLS fibre, a scintillation photon may travel in any of the two directions in the fibre: either directly towards the PMT or towards the fibre bend at the front of the cell. In the first case, the photon has to travel a distance $d_{1,\,i}$ (the distance from the i:th scintillator layer to the back of the calorimeter), while it in the second case has to travel a distance $d_{2,\,i} = l + (l - d_{1,\,i})$. The different path lengths result in different attenuations, in addition to the extra attenuation affecting the light passing through the fibre bend. The full response function of a WLS fibre from layer i is given by:

$$f_{\mathrm{WLS,\,i}} = f_{\mathrm{WLS,\,1,\,i}} + f_{\mathrm{WLS,\,2,\,i}}, \tag{10.4}$$

where $f_{\mathrm{WLS,\,1,\,i}}$ contains information about the photons transported directly from the scintillator layer to the PMT (a distance $d_{1,\,i}$) and $f_{\mathrm{WLS,\,2,\,i}}$ contains information about the photons transported via the fibre bend (a distance $d_{2,\,i}$).

Combining the different sources of photon attenuation with the exponential time structure introduced by the WLS, the response function for photons transported directly to the PMT is given by:

$$f_{\mathrm{WLS,\,1,\,i}}(t) = \begin{cases} 0.5\xi \exp(-\mu d_{1,\,i}) \frac{\exp(-(t-T^{1,\,i}_{\mathrm{WLS}})/\tau_{\mathrm{WLS}})}{\tau_{\mathrm{WLS}}}, & \text{if } t \geq T^{1,\,i}_{\mathrm{WLS}} \\ 0, & \text{otherwise}, \end{cases} \tag{10.5}$$

where $T^{1,\,i}_{\mathrm{WLS}}$ is the time it takes for the re-emitted photons to travel from the i:th layer to the PMT, given by the speed of light corrected for the fibre refractive index. The factor 0.5 represents the fact that only half the number of produced photons will travel this path, and the factor ξ represents additional (but position-independent) losses[1]. Note that this response function does not include any reference to the actual number of scintillation photons — when solving the convolution in Eq. 10.1 this will be included from the scintillator response function.

The situation is very similar for the case where the absorbed and re-emitted photon from the i:th layer travels to the PMT via the fibre bend, only that $d_{1,\,i}$ is replaced by $d_{2,\,i}$ and an extra factor p_{x} is included to account for the light loss at the fibre bend:

---

[1] A typical position-independent loss in efficiency could come from imperfect photon transmission from the scintillator to the WLS.

$$f_{\mathrm{WLS},\,2,\,\mathrm{i}}(t) = \begin{cases} 0.5\xi p_{\mathrm{x}} \exp(-\mu d_{2,\,i}) \frac{\exp(-(t-T^{2,\,i}_{\mathrm{WLS}})/\tau_{\mathrm{WLS}})}{\tau_{\mathrm{WLS}}}, & \text{if } t \geq T^{2,\,i}_{\mathrm{WLS}} \\ 0, & \text{otherwise,} \end{cases} \tag{10.6}$$

where also the different travel time, $T^{2,\,i}_{\mathrm{WLS}}$, for the photons taking this longer path has been included.

Since each scintillator layer will be read out by a number of fibres, the response function should be scaled accordingly. However, since this can be represented by a constant factor, it can be absorbed by ξ in the above equations.

10.3.3 Photomultiplier Response Function

In the PANDA shashlyk calorimeter, a 10-dynode Hamamatsu R7899 PMT is used to read out the light from the WLS fibres. The first part of the PMT is the photocathode, where electrons are produced when photons impinge on it. The probability of this process occurring is given by the quantum efficiency q, which depends primarily on the material of the photocathode. The produced electrons are accelerated by electric fields and multiplied at the PMT dynodes and the resulting current is read out at the PMT anode. The average total gain G_{PMT} of the PMT was assumed to be $2 \cdot 10^6$ [78].

Two effects of the PMT on the time structure of the pulse are assumed. First, the multiplication process in the PMT leads to a time spread in the anode pulse, which was modelled as a normal distribution having a 10-90% rise time of 1.6 ns and a mean transit time of 17 ns [78, 185]. Secondly, transit-time spread (TTS) in the PMT was modelled as a normal distribution having a full-width at half maximum of 0.6 ns [78]. To combine these effects in a single response function, these two normal distributions were convolved, a procedure resulting in a wider normal distribution. Combining these effects with the PMT gain, the average PMT response function may be written as:

$$f_{\mathrm{PMT}}(t) = \frac{qG_{\mathrm{PMT}}}{\sqrt{2\pi(\sigma_{\mathrm{a}}^2 + \sigma_{\mathrm{TTS}}^2)}} \exp(-0.5(t - T_{\mathrm{PMT}})^2/(\sigma_{\mathrm{a}}^2 + \sigma_{\mathrm{TTS}}^2)), \tag{10.7}$$

where T_{PMT} is the mean transit time in the PMT, σ_{a} is the standard deviation of the anode pulse and σ_{TTS} is the standard deviation of the TTS.

10.3.4 ADC-interface Response Function

The interface between the PMT anode and the input of the sampling ADC is assumed to correspond to a parallel RC circuit, where the voltage difference V across the resistor is measured and changes as current from the PMT flows into the circuit [186]. The time dependence of this voltage is given by the differential equation:

$$\frac{\mathrm{d}V(t)}{\mathrm{d}t} = \frac{i(t)}{C} + \frac{V(t)}{RC}, \tag{10.8}$$

where $i(t)$ is the current from the anode and R and C are the resistance and capacitance in the RC circuit, respectively. Solving this differential equation with a delta-function input current yields the transfer function of the circuit:

$$f_{\mathrm{ADC}}(t) = \begin{cases} \frac{G_{\mathrm{ADC}}}{C} \exp(-t/\tau_{\mathrm{RC}}), & \text{if } t \geq 0 \\ 0, \text{ otherwise}, \end{cases} \tag{10.9}$$

where G_{ADC} is the analogue-to-digital conversion gain of the ADC (which includes digitisation of the analogue signal), and $\tau_{\mathrm{RC}} = RC$ is the anode time constant. This essentially leads to some shaping of the anode pulse.

10.4 Model Calibration

As shown in Eq. 10.1, the response function $f_{\mathrm{TOT}}(t)$ of the entire cell is given by the convolution of the scintillator, WLS fibre, PMT and ADC-interface response functions. There exists an analytical solution to this convolution problem, and one may calculate the average response of the whole cell to an event where energy depositions $[s_1, s_2, ..., s_{380}]$ occur at times $[T_1, T_2, ..., T_{380}]$ in the 380 different scintillator layers. The energy-deposition times may be calculated relative to the time T_0 when the incident photon hits the front of the detector by assuming that the electromagnetic shower develops through the cell at a speed of c. The only free parameters of $f_{\mathrm{TOT}}(t)$ are a time offset T_0, a scaling factor G and the anode-circuit time constant τ_{RC}. The scaling factor G is the integral of f_{TOT} and incorporates all normalisation and gain factors — including the number of scintillation photons produced per unit of energy deposition, and thus acts as an overall scaling constant. The parameter τ_{RC} is thus assumed to be the only free parameter affecting the shape of the digitised pulse.

To fully model the calorimeter, the different contributions to the time structure of its signal have to be understood. In the following sections, the determination of the relative contribution to the total scintillation-photon yield by each layer, the number of generated photoelectrons and the anode time constant will be described. In addition, an energy calibration of the model will be described.

10.4.1 Layer Contribution to Scintillation-Photon Yield

Due to sampling fluctuations in the calorimeter, the energy deposition s_i in a particular scintillator layer, and therefore also the calorimeter response to a photon of a particular energy, will in reality differ on an event-by-event basis. As a first step in calibrating the model, one may study the contribution of the scintillation photons generated in layer i to the *total* number of photons reaching the PMT. In this case, the time structure of the signal does not matter since we are only interested in a total photon yield. By combining the time-independent parts of Eqs. 10.3–10.6, one obtains an expression for the average relative contribution r_i of layer i to the total number of photons at the PMT:

$$r_i = \frac{\langle s_i \rangle \exp(-\mu d_{1,\,i}) + \langle s_i \rangle p_\mathrm{x} \exp(-\mu d_{2,\,i})}{\sum_{i=1}^{380} [\langle s_i \rangle \exp(-\mu d_{1,\,i}) + \langle s_i \rangle p_\mathrm{x} \exp(-\mu d_{2,\,i})]}, \tag{10.10}$$

where $\langle s_i \rangle$ is the average energy deposition in scintillator layer i. $d_{1,\,i}$ and $d_{2,\,i}$ are known for each layer, and p_x and μ describe scintillation-light attenuation, as discussed in Sec. 10.3.2. The factor $\langle s_i \rangle / \sum \langle s_i \rangle$ was determined for each layer for each of the nine tagged-photon energies by simulating the interactions of $1 \cdot 10^7$ photons directed onto position a of the cell (see Fig. 10.1b). The result is shown in Fig. 10.7, where the average relative energy deposition per layer is shown as a function of layer number for three different incident-photon energies. Here, layer number 1 corresponds to the layer closest to the front of the detector, while layer 380 is the one closest to the PMT.

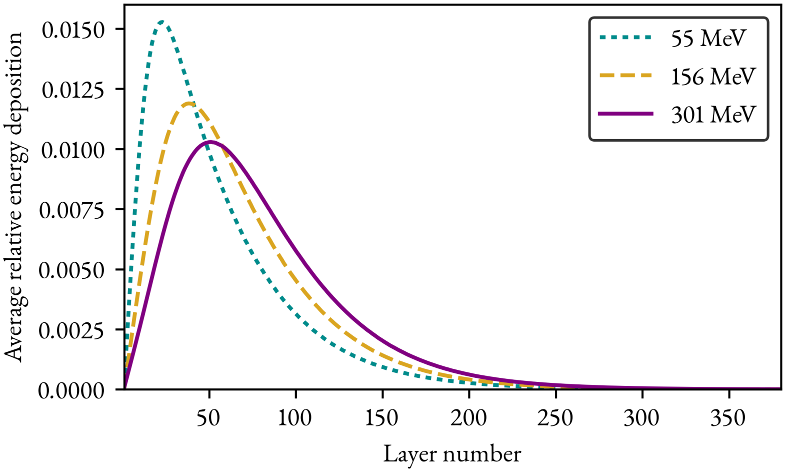

Figure 10.7: Simulated shower shape in a single shashlyk cell at three different incident-photon energies.

As the average contribution of each layer to the total light yield of the detector has been determined, the average time-independent component of the full response function $f_{\mathrm{TOT}}(t)$ up to the point of the photocathode is known. By summing the time-dependent response functions of all 380 scintillator layers and their corresponding WLS fibres, weighted by their respective r_i values, also the time-component of the response function until the photocathode stage may be calculated. Convolving this with the PMT and ADC-interface responses as discussed above, an *average* detector response $\widetilde{f}_{\mathrm{TOT}}(t; E_\gamma, G, T_0, \tau_{\mathrm{RC}})$, which depends on the incident-photon energy E_γ and the three free parameters discussed above, is obtained.

10.4.2 Number of Generated Photoelectrons

In order to model fluctuations in the detector, the time-independent scaling factor G present in the total transfer function has to be decomposed into its various components. One of the most important factors determining the statistical noise in the detector is the number of photoelectrons generated at the PMT photocathode per unit energy deposition in the detector. Earlier studies of the shashlyk calorimeter have shown that if an energy E_{TOT} is deposited in the entire cell (i. e. in scintillators, absorbers and Tyvek sheets), $k = 3.6\ \mathrm{MeV}^{-1}$ photoelectrons are on average generated at the photocathode [146]. This gives:

$$\langle P \rangle = kE_{\mathrm{TOT}}, \tag{10.11}$$

where $\langle P \rangle$ is the average total number of generated photoelectrons. In order to relate this to the energy deposited in the scintillator layers, the Geant4 model was used to determine the average fraction between the total energy deposition in all 380 scintillator layers s_{TOT} and E_{TOT}. This was done by simulating a large number of photons for each tagged-photon energy and determining the ratio between the two for each event. As shown in Fig. 10.8, the ratio $s_{\mathrm{TOT}}/E_{\mathrm{TOT}}$ appears to be quite constant over the entire energy range, and the average fraction $\langle s_{\mathrm{TOT}}/E_{\mathrm{TOT}} \rangle$ was determined by fitting a horizontal line to the data.

One may now rewrite Eq. 10.11 in terms of the energy deposition in the scintillator layers:

$$\langle P \rangle = k \left\langle \frac{E_{\mathrm{TOT}}}{s_{\mathrm{TOT}}} \right\rangle s_{\mathrm{TOT}}, \tag{10.12}$$

where both k and $\langle E_{\mathrm{TOT}}/s_{\mathrm{TOT}} \rangle$ are now known constants. At the same time, it is also known that if N scintillation photons hit the photocathode, the average number of generated photoelectrons $\langle P \rangle$ is given by:

$$\langle P \rangle = qN, \tag{10.13}$$

where q is the quantum efficiency of the photocathode. Using Eqs. 10.3, 10.5 and

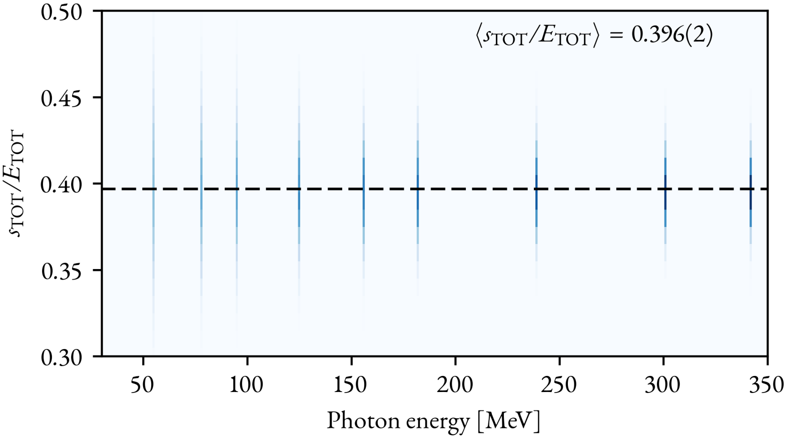

Figure 10.8: Event-by-event fraction between the total energy deposition in all 380 scintillator layers s_{TOT} and the total energy deposition in the whole cell (including lead plates and Tyvek) E_{TOT}, determined from the simulation as a function of the incident-photon energy. The average of this fraction is approximately constant across the entire investigated energy range, with $\langle s_{\mathrm{TOT}}/E_{\mathrm{TOT}} \rangle$ determined by fitting a horizontal line (dashed) to the data. The uncertainty (in parentheses) corresponds to the one-standard deviation uncertainty in the fit parameter.

10.6 we also know:

$$N = \beta\xi \sum_{i=1}^{380} [0.5 s_i \exp(-\mu d_{1,\,i}) + 0.5 s_i p_{\mathrm{x}} \exp(-\mu d_{2,\,i})], \tag{10.14}$$

which may be combined with Eqs. 10.12–10.14 so that one finally obtains:

$$s_{\mathrm{TOT}} = \frac{q\beta\xi}{k} \left\langle \frac{s_{\mathrm{TOT}}}{E_{\mathrm{TOT}}} \right\rangle \sum_{i=1}^{380} [0.5 s_i \exp(-\mu d_{1,\,i}) + 0.5 s_i p_{\mathrm{x}} \exp(-\mu d_{2,\,i})] \tag{10.15}$$

Here, s_{TOT} and the s_i of all individual scintillator layers may be determined on an event-by-event basis from the Geant4 simulation. As shown in Fig. 10.9, a first-degree polynomial intersecting the origin was fitted to these data to yield a value on $\frac{q\beta\xi}{k} \left\langle \frac{s_{\mathrm{TOT}}}{E_{\mathrm{TOT}}} \right\rangle$. From this, $q\beta\xi$ was determined to be 13.8 MeV^{-1}. By determining $q\beta\xi$ in this way, Eq. 10.14 may now be solved for *any* set of s_i values to give the average total number of generated photoelectrons $\langle P \rangle$.

10.4.3 Anode Time Constant

Since τ_{RC} is the only free parameter which should be the same for all measured signals, its value may be determined by performing a fit to a number of experimentally

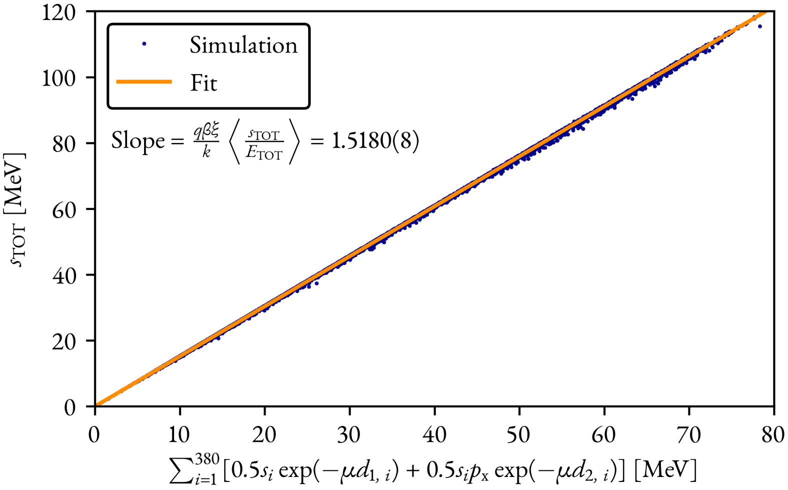

Figure 10.9: Simulated total energy deposition in all 380 scintillator layers as a function of $\sum_{i=1}^{380}[0.5 s_i \exp(-\mu d_{1,\,i}) + 0.5 s_i p_{\mathrm{x}} \exp(-\mu d_{2,\,i})]$, which is related to the number of scintillation photons reaching the PMT photocathode. A first-degree polynomial intersecting the origin has been fitted to determine $q\beta\xi$. See text for details. The uncertainty (in parentheses) corresponds to the one-standard deviation uncertainty in the fit parameter.

measured signal waveforms. This was done by performing a global fit of $\widetilde{f}_{\mathrm{TOT}}(t)$ to 90 measured waveforms — 10 from each of the selected tagged-photon energies. In this fit, τ_{RC} was treated as a global parameter that should be the same for all fitted waveforms, while G and T_0 were allowed to vary freely between the individual waveforms. For each waveform, 10 samples around the signal maximum were included in the fit to exclude the undershoot present in the experimental data. For each waveform E_γ was known, and therefore the appropriate $\langle s \rangle$ values. This procedure yielded a value of $\tau_{\mathrm{RC}} = 17.1$ ns. This value could also depend on possible signal shaping at the input of the sampling ADC, which was unknown for the device used during the 2014 prototype tests. One example of the fitted pulse shape is shown in Fig. 10.10.

10.4.4 Energy Calibration

By the reasoning given above, it is now possible to relate the energy deposition in the detector to an average photoelectron yield per energy deposition. The average gain of the PMT is known, as is the multiplication of the individual dynode stages. Indeed, the only parameter not yet specified is the amplitude-scaling factor intro-

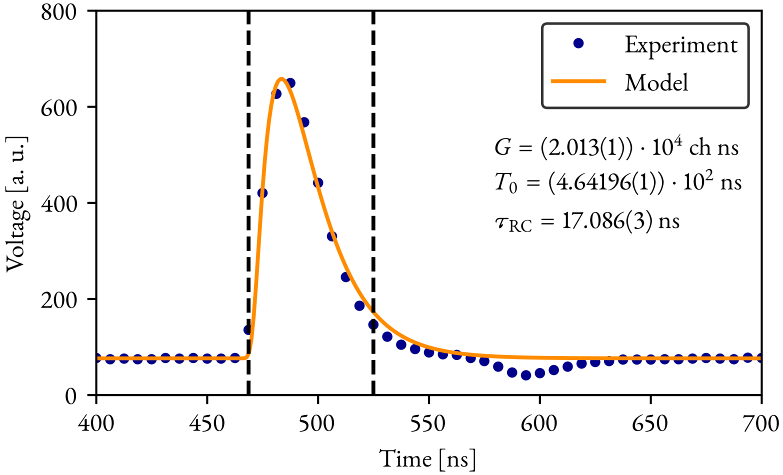

Figure 10.10: One of the 90 experimentally obtained waveforms to which the average shashlyk response function was fitted. The dashed lines show the region used in the fit, which was chosen to avoid effects on the pulse shape due to the undershoot. The integral G and time-offset T_0 parameters were allowed to vary freely between the individual waveforms, and τ_{RC} was a global parameter that should be the same for all fitted waveforms. The uncertainties (in parentheses) correspond to the one-standard deviation uncertainties in the fit parameters.

duced by the response function of the ADC-interface. This scaling factor is defined as G_{ADC}/C in Eq. 10.9, and is related to the overall scaling factor G of the response function of the whole detector as:

$$G = \int_{-\infty}^{\infty} f_{TOT}(t)\,\mathrm{d}t = \frac{G_{ADC}}{C}\tau_{RC}\langle P\rangle G_{PMT} = \frac{G_{ADC}}{C}\tau_{RC}k\left\langle\frac{E_{TOT}}{s_{TOT}}\right\rangle s_{TOT}G_{PMT}, \tag{10.16}$$

where G is given in units of (ADC channels)·ns and Eq. 10.12 has been used for the second equality. G_{ADC} is given in units of ADC channels per voltage, and C in units of inverse voltage (since the amount of charge at the PMT anode is given in units of number of electrons). As such, G_{ADC}/C has units of ADC channels.

By fitting a large number of experimentally obtained waveforms with the convolved detector response function as in Sec. 10.4.3 (only now with τ_{RC} known and fixed), a histogram of the determined values of the G parameter from the fits was created for each of the nine tagged-photon energies. Similarly, nine histograms of the s_{TOT} values from the Geant4 simulation were created. Due to leakage of the electromagnetic shower to adjacent cells, these distributions are more or less asymmetric. The Novosibirsk function [187, 188] was used to fit these asymmetric distributions.

The Novosibirsk function is given by:

$$f(E; \mathcal{A}, \tau, \widetilde{\sigma}_E, E_0) = \mathcal{A} \exp \left[-\frac{1}{2} \left(\frac{\log^2(1 + \mathcal{A}\tau(E - E_0))}{\tau^2} + \tau^2 \right) \right], \tag{10.17}$$

where

$$\mathcal{A} \equiv \frac{\sinh(\tau \sqrt{\log 4})}{\widetilde{\sigma}_E \tau \sqrt{\log 4}}. \tag{10.18}$$

The shape of the Novosibirsk function depends on a "tail parameter" τ and a width $\widetilde{\sigma}$. Its mode is defined by the μ_0 parameter. This function will be used throughout the rest of this thesis when fitting distributions of energy depositions in the shashlyk cell. Here, Novosibirsk functions were fitted to both the distributions of G values (determined from pulse-shape fits) for a particular photon energy and the corresponding distributions of s_{TOT}. The relationship between the modes of these Novosibirsk fits is shown in Fig. 10.11. From the slope of the fitted line, G_{ADC}/C was determined to be $1.5 \cdot 10^{-6}$ ADC channels.

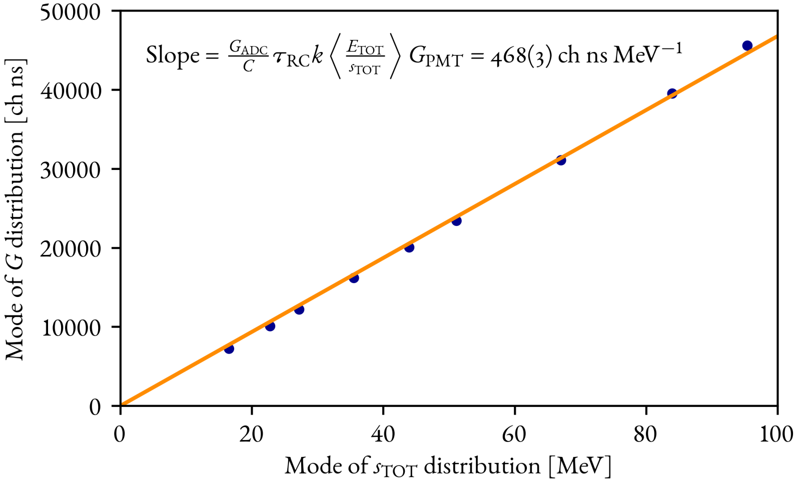

Figure 10.11: The overall scaling factor G as a function of the total amount of energy deposited in the shashlyk cell, as determined by fitting Novosibirsk functions to the respective distributions. The slope of the fit makes it possible to determine G_{ADC}/C. The uncertainty (in parentheses) corresponds to the one-standard deviation uncertainty in the fit parameter.

10.5 Signal Generation

The calibrations of the model make it possible to generate realistic detector signals incorporating all the discussed noise sources on an event-by-event basis. For a Geant4-simulated event resulting in energy depositions $[s_1, s_2, ..., s_{380}]$ in the scintillator layers, this is done as follows:

1. Pick a T_0 value from the uniform distribution $[60\text{ ns}, 100\text{ ns}]$. This was done to cover all timing phases relative to the 6.25 ns ADC sampling clock.

2. For the i:th scintillator layer, the average number of electrons produced at the photocathode due to the energy deposition s_i depends on the attenuation of scintillation photons in the WLS fibres: $\langle P_i \rangle = q\beta\xi[0.5s_i \exp(-\mu d_{1,\,i}) + 0.5s_i p_x \exp(-\mu d_{2,\,i})]$. For a particular event, the actual number of generated photoelectrons was determined by picking a random number from a Poisson distribution with the mean $\langle P \rangle$. This process was repeated for all 380 layers.

3. Each generated photoelectron may have been caused by a photon travelling either a distance $d_{1,\,i}$ or $d_{2,\,i}$ through the WLS fibre. The average relative probability of a photon having travelled the distance $d_{1,\,i}$ is for example given by $\exp(-\mu d_{1,\,i})/[\exp(-\mu d_{1,\,i}) + p_x \exp(-\mu d_{2,\,i})]$, and by picking a random value from the uniform distribution $[0, 1]$ and comparing with this (i. e. drawing from a binomial distribution), the path of the scintillation light causing a particular photoelectron was determined.

4. The time of generation of each photoelectron was determined by picking a time from the time distributions given by the scintillator and WLS-fibre response functions in Eqs. 10.5 and 10.6.

5. The mean electron transit time through the PMT was determined from the normal distribution used to model the transit-time spread.

6. In order to track the multiplication of the electrons through the PMT, the gains of the individual dynode stages were taken into account to determine the number of electrons reaching the PMT anode. Here, Poisson statistics was assumed to govern the electron-multiplication process at the dynodes.

7. Since the number of electrons at the anode is very large, the time structure of the anode pulse was modelled as a normal distribution as discussed in Sec. 10.3.3, normalised to the determined number of electrons at the anode.

8. Finally, the resulting current from the anode was convolved with the ADC-interface response function in Eq. 10.9, which includes digitisation in the ADC and shaping, assumed to be due to the anode circuitry.

The electronic noise was modelled as white noise having an r.m.s. given by the experimental data. By modelling individual detector responses according to this procedure, realistic sources of noise and fluctuations are included on an event-by-event basis.

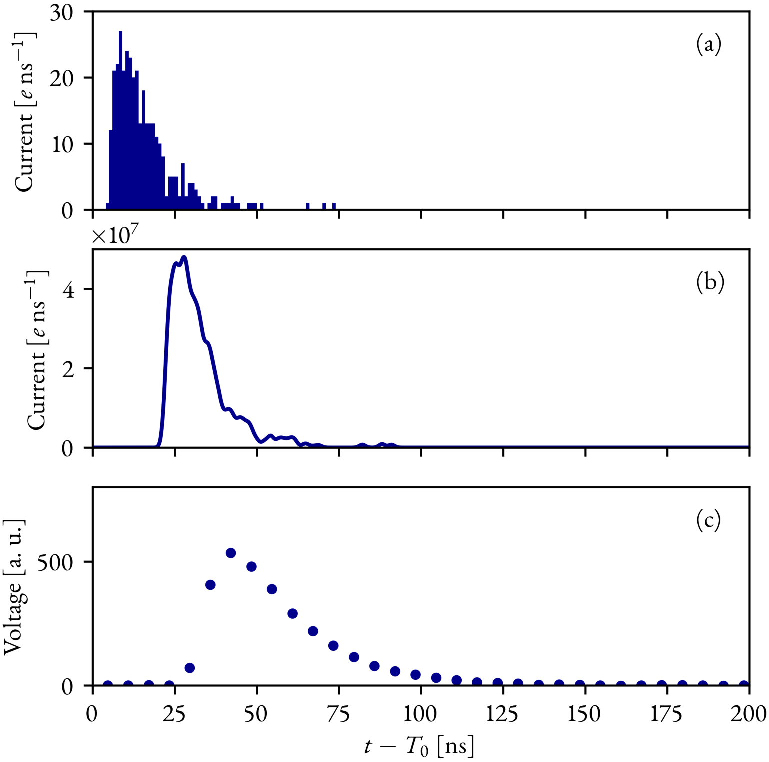

Figure 10.12: Example of a simulated event, at an incident-photon energy of 156 MeV. a) shows the current of generated photoelectrons (the cathode current), b) the current at the PMT anode and c) the final, digitised pulse in the ADC.

10.6 Model Validation

By using the model to simulate the response of the calorimeter to the tagged-photon beams used during the prototype tests, the simulated waveforms may be analysed in the same way as the experimentally obtained waveforms. This makes model validation possible, regarding both the energy and timing resolution of the prototype.

For these validations, $8 \cdot 10^5$ simulated waveforms were generated at each of the nine tagged-photon energies.

10.6.1 Energy Resolution

The single-cell pulse-height distributions of both the simulated and the experimental waveforms were obtained by histogramming the maximum of each waveform. As shown in Fig. 10.13, a Novosibirsk distribution was fitted to each of the two distribution, and the relative energy resolution was defined as $\widetilde{\sigma}_E/E_0$, where E_0 is the mode of the Novosibirsk distribution and $\widetilde{\sigma}_E$ characterises its width.

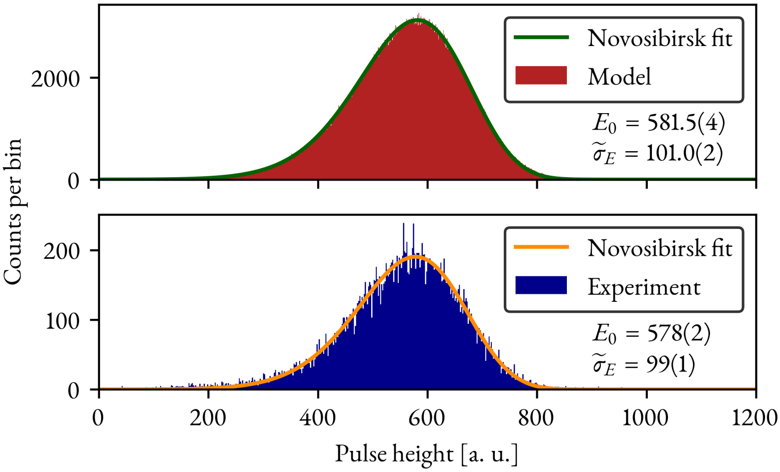

Figure 10.13: Comparison between the pulse-height distribution corresponding to 156-MeV photons, as determined from model-generated (in red) and from experimental data (in blue), respectively. The uncertainties (in parentheses) correspond to the one-standard deviation uncertainties in the parameters of the fitted Novosibirsk distributions.

Fig. 10.14 shows a comparison between the obtained model and experiment relative energy resolutions for all nine tagged-photon energies. The agreement between the model and the experiment is in general very good, with the exception for the lowest-energy datum point.

10.6.2 Time Resolution

The time resolution of the 4 × 4 shashlyk prototype has previously been investigated [179], by analysing the data from the measurements taken with the photon

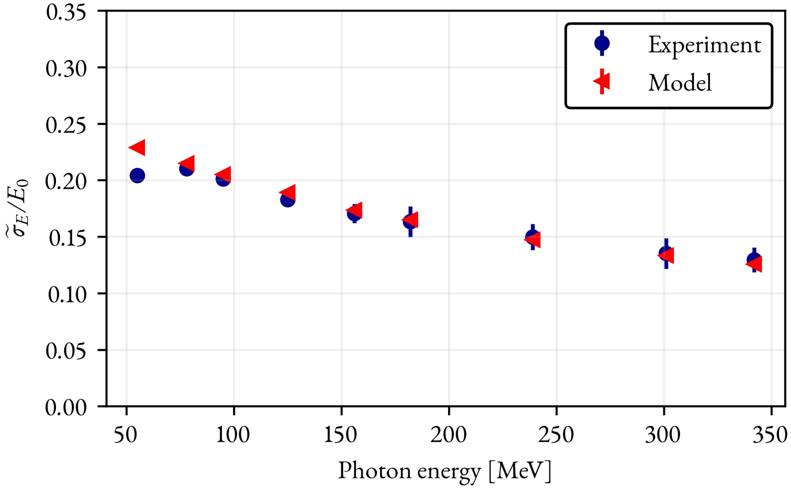

Figure 10.14: Comparison between the determined relative energy resolution from experimental data and the model-generated data, as a function of incident-photon energy. The error bars correspond to the one-standard deviation uncertainties in the fitted Novosibirsk distributions.

beam directed onto position b (see Fig. 10.1b) of the matrix, i. e. onto the interface between two adjacent cells. The acquired waveforms from each of the two cells were analysed offline using the CFD timing algorithm, discussed in Sec. 9.2. For a particular event, the pulse timings T_1 and T_2 were determined for the two detector signals. Under the requirement that the two pulses corresponded to similar *energy depositions* (within 10% of each others), the time resolution of a single detector was determined from the time difference ΔT between T_1 and T_2. This relies on the assumption that similar energy depositions would correspond to similar time resolutions. After analysing a large number of events, a distribution of ΔT values is obtained. Assuming that the responses of the two cells are uncorrelated, the time resolution was determined from:

$$\sigma_{\mathrm{T}} = \frac{\sigma(\Delta T)}{\sqrt{2}}, \tag{10.19}$$

where $\sigma(\Delta T)$ is the standard deviation of the distribution of ΔT. By performing exactly the same analysis procedure on the model-generated waveforms, for each of the two beam positions, the time resolution as given by Eq. 10.19 was determined. Note that the time resolution is determined as a function of the amount of energy deposited in each of the two adjacent cells.

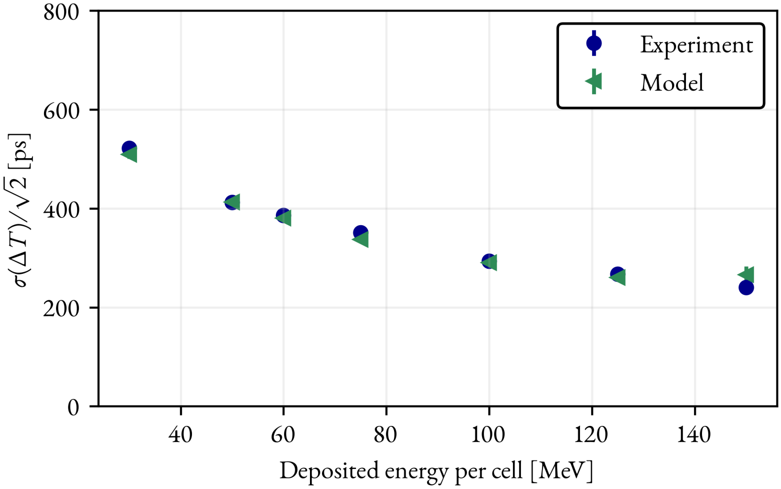

Figure 10.15: Comparison between the determined time resolution from experimental data and the model-generated data, determined from the time difference between signals in adjacent cells. The time resolution is shown as a function of the energy deposition per cell, which was selected by requiring that the two pulses corresponded to energy depositions within 10% of each others. The error bars correspond to the one-standard deviation uncertainties in the fitted normal distributions.

11. Algorithm Development

The end goal for the algorithm introduced in Ch. 9 is implementation in an FPGA. In order to test the performance of the proposed method, it has been implemented in the hardware-description language VHDL and used in a simulation environment to analyse waveforms generated by the model described in Ch. 10. Each generated pulse corresponds to a particular photon-interaction time T_0 and a certain energy deposition in the cell E_{TOT}, which are known from the model. This enables benchmarking of the model under realistic conditions.

The OF (optimal filter) algorithm, introduced in Sec. 9.3, relies on three assumptions about the detector signal:

- The signal is a pulse with a fixed shape, scaled by an amplitude A and shifted by a time τ.
- The phase shift τ is assumed to be small, and describes the deviation of the pulse timing from an assumed time t_0.
- The noise under a single detector pulse can be approximated as white noise.

The tasks of determining the pulse-shape template, obtaining an estimate of t_0, implementing the filter in VHDL and evaluating its performance will be described in this chapter.

11.1 Pulse-Shape Template

While the Monte Carlo model provides a way of parameterising the detector pulse shape through the detector response function, this description inherently relies on the shower shape in the detector. As the shower shape depends on the incident-photon energy, and the OF relies on an energy-independent fixed pulse shape, another approach has to be taken to obtain a function describing the overall pulse shape. This is also of importance for realistic applications of the method, as a full time-based Monte Carlo model of a detector is not generally available. To describe the average pulse shape, the lognormal function was used:

$$f_{\mathrm{L}}(t) = \begin{cases} \frac{A_{\mathrm{L}} \exp(\mu - 0.5\sigma^2)}{t - T_{\mathrm{L}}} \exp\left[\frac{[\log(t - T_{\mathrm{L}}) - \mu]^2}{2\sigma^2}\right], & \text{if } t > T_{\mathrm{L}} \\ 0, & \text{otherwise,} \end{cases} \tag{11.1}$$

where A_L is the amplitude of the pulse, μ and σ are parameters determining the shape of the function, and T_L is the start of the pulse. By performing a global fit of this function to 180 model-generated pulses (20 from each tagged-photon energy), μ and σ were determined. In Fig. 11.1, a comparison between a generated signal and the fitted lognormal function is shown. Setting $A_\mathrm{L} = 1$, the result is an amplitude-normalised pulse shape which can be used as the pulse-shape template in the OF algorithm.

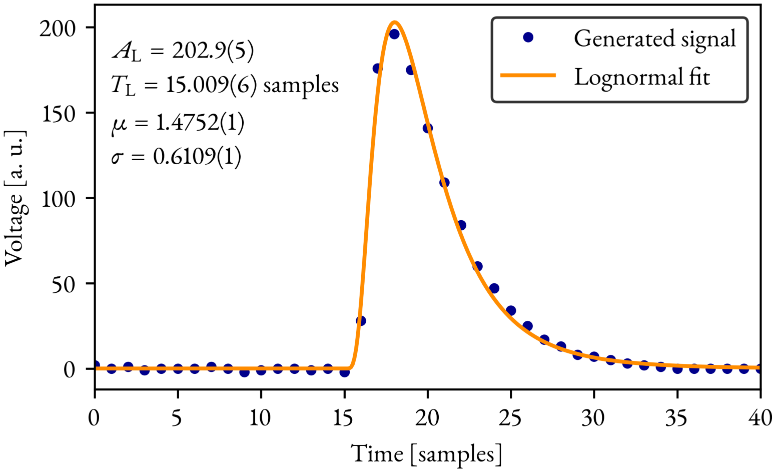

Figure 11.1: Fit of the lognormal function (Eq. 11.1) to a model-generated detector signal. The resulting fit parameters are shown. The amplitude A_L and time-offset T_L parameters were allowed to vary freely between the individual waveforms, and μ and σ were global parameters that should be the same for all fitted waveforms. The uncertainties (in parentheses) correspond to the one-standard deviation uncertainties in the fit parameters.

11.2 Binary-Search Constant Fraction Discriminator

Now that the shape of the pulse template has been defined, the aim of the feature-extraction algorithm described here is to provide estimates of A_L of T_L for each analysed detector signal. It is clear that there is a direct correspondence between A_L and A_OF, the amplitude parameter determined using the OF algorithm. It is also clear that T_L is related to τ_OF, although there is not a direct correspondence in this case due to the linearisation needed in the construction of the OF. That is, τ_OF gives the (small) time difference between an assumed time T^0_OF and the actual timing of the signal: $T_\mathrm{L} = T^0_\mathrm{OF} + \tau_\mathrm{OF}$. Therefore, the first issue faced when constructing the filter is to find a good estimate of T^0_{OF}.

As discussed in Sec. 9.3.2, one way of finding T^0_{OF} in an experiment where the beam structure is bunched is by synchronising the sampling clock of the ADC with the bunch-crossing frequency. This way, $T^0_{\mathrm{OF}} = 0$ relative to the sampling clock and the OF algorithm may be applied directly. This approach is not possible in PANDA, where the bunch-crossing frequency is not provided by the accelerator and real-time feature extraction is vital. Therefore, a separate method is needed to obtain an estimate of T^0_{OF}. In the method described here, a binary-search implementation (from now on referred to as B-CFD) of the linear CFD is proposed for this purpose. The basis for the B-CFD algorithm is still Eq. 9.2, where the CFD data are calculated from the incoming (baseline-subtracted) data samples. However, the B-CFD method differs from the standard linear CFD method in how the CFD samples are treated. Instead of requiring a division operation to locate the time of the CFD zero crossing, each sample is subdivided into four regions in time and the *window* in which the zero crossing occurs is located. This was done by directly evaluating the value of the linear interpolation at three fixed sub-sample fractions (0.25, 0.5 and 0.75). In practice, this was achieved by redefining the width of a sample to be $t_1 - t_0 = 2$, so that the value of the interpolated line at half of the sample is given by:

$$V_{\mathrm{CFD}}(1) = \frac{V_{\mathrm{CFD}}(2) - V_{\mathrm{CFD}}(0)}{2-0}(1-0) = \frac{V_{\mathrm{CFD}}(2) - V_{\mathrm{CFD}}(0)}{2}, \qquad (11.2)$$

where $V_{\mathrm{CFD}}(0)$ and $V_{\mathrm{CFD}}(2)$ are the CFD data for the two samples surrounding the zero crossing. As this operation only requires division by two, i. e. a single bit-shift, it is very suitable for implementation in an FPGA. By determining whether $V_{\mathrm{CFD}}(1)$ lies above or below the zero crossing, the half-sample window containing the zero crossing was located. By further subdividing this smaller window into two regions and applying Eq. 11.2 again, the quarter-sample region containing the zero crossing was located. The B-CFD timing $T_{\mathrm{B\text{-}CFD}}$ of the signal was determined as the centre time of the located zero-crossing window (so $T_{\mathrm{B\text{-}CFD}} = 0.125, 0.375, 0.625$ or 0.875 samples relative to the CFD sample before the zero crossing). The working principle of the B-CFD method is shown in Fig. 11.2. It is worth noting that a B-CFD delay of 2 samples is used, contrary to the 4-sample delay used in the previous analyses of the experimental data. This was the result of an optimisation procedure of the OF algorithm, and was not found to affect the time resolution adversely.

The B-CFD method provides a way of estimating the phase of the signal relative to the ADC sampling clock. However, the determined $T_{\mathrm{B\text{-}CFD}}$ has to be related to the assumed pulse timing T^0_{OF} needed by the OF method. To establish a connection between these, the lognormal function of Eq. 11.1 was fitted to $9 \cdot 10^5$ generated signals of different amplitudes. By also applying the B-CFD algorithm on each analysed signal, $\langle T_{\mathrm{B\text{-}CFD}} - T_{\mathrm{L}} \rangle$ was determined for each of the four sub-sample windows. For any subsequent signal i analysed in real time, the initial time estimate for the OF

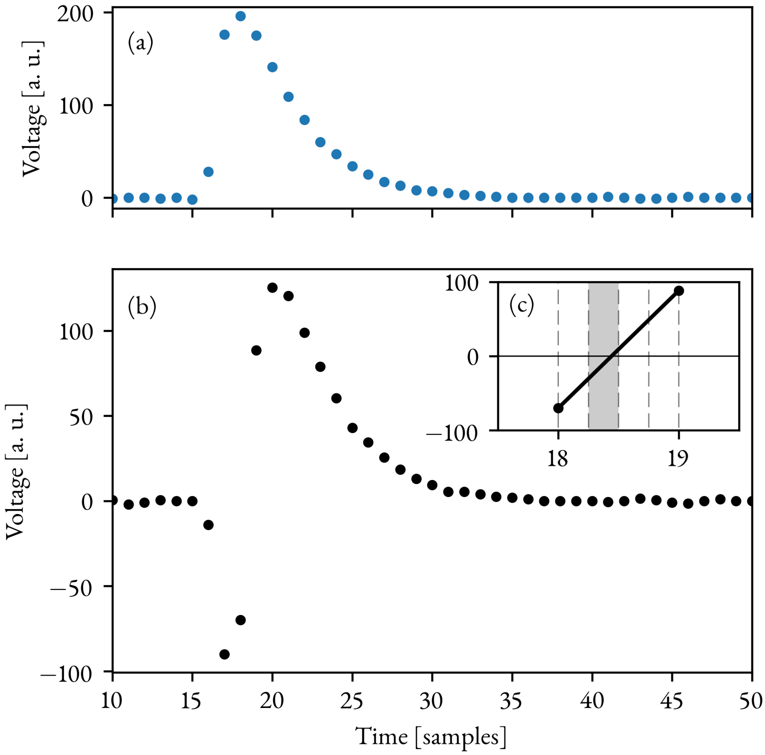

Figure 11.2: Working principle of the binary-search CFD (B-CFD) method. a) shows the raw sampled data from the detector, b) is the CFD data given by Eq. 9.2 using t_d = 2 samples and f = 0.5, and c) shows the two samples surrounding the CFD zero-crossing. Using a binary-search algorithm, the quarter-sample wide window (marked in grey) containing the zero crossing is located. The resulting time estimate is the centre of the located zero-crossing window, $T_{\text{B-CFD}}$ = 18.375 samples.

method is given by:

$$T^0_{\mathrm{OF},\,i} = T_{\text{B-CFD},\,i} - \langle T_{\text{B-CFD}} - T_\mathrm{L} \rangle. \tag{11.3}$$

Tab. 11.1 lists the obtained $\langle T_{\text{B-CFD}} - T_\mathrm{L} \rangle$ values for the four B-CFD windows at a CFD delay of $t_\mathrm{d} = 2$ samples.

Table 11.1: The average difference between the 2-sample delay B-CFD timing estimate and the lognormal time parameter for each of the four B-CFD windows, determined by analysing $9 \cdot 10^5$ generated signals.

B-CFD window	$\langle T_{\text{B-CFD}} - T_\mathrm{L} \rangle$ [samples]
1	3.454
2	3.460
3	3.417
4	3.413

In order to determine the coefficients needed for the OF algorithm, the template pulse shape has to be discretised in time: $f_\mathrm{L}(t) \rightarrow g[t_i]$. It is clear that the phase of $f_\mathrm{L}(t)$ relative to the discrete time steps affects the values of $g[t_i]$, so that four different sets of OF coefficients — one for each B-CFD window — has to be constructed. As soon as the phase of the signal has been estimated using the B-CFD method, the correct OF coefficients may be applied to the data to determine the final pulse-time correction τ_OF as well as the pulse amplitude A_OF.

11.3 Optimising the Filter Length

As described in Sec. 9.3.2, the OF uses M sampled values of the input signal, and multiplies these values with sets of coefficients $\boldsymbol{a}$ and $\boldsymbol{b}$. Implementation of an M-coefficient OF in an FPGA therefore requires the device to perform $2M$ simultaneous multiplications. The Kintex-7 FPGA used in the EMC digitiser has 600 DSP48 blocks, which contain dedicated resources for signal-processing operations such as multiplications. Because each FPGA in the digitiser will be used to analyse signals from 16 detectors, at most 37 DSP48 blocks are available per channel. If the system is used in dual-gain mode, each mode has to be analysed separately, cutting the maximum number of DSP48 available per signal in half. Since $2M$ simultaneous multiplications are necessary, there is a hard limit of $M \leq 9$ in the current implementation, and the OF has to be optimised.

Since the OF method is analogous to performing a χ^2 fit to the sample data, limiting the number of OF coefficients corresponds to limiting the region of the χ^2 fit. When choosing a fit region, one has to select both the starting point of the fit and the width of the fitting range. In the OF case, one has to select which samples of the incoming data to use in the “fit”. Because the B-CFD method is used to estimate the phase of the signal, the “fit range” must be related to the B-CFD zero crossing. Defining B_Z as the time of the first 2-delay CFD sample *after* the zero crossing, one can relate the timing of *any* sample to this. Therefore, we define B_0 to be the time (relative to B_Z) of the first sample used in the OF analysis subsequent to a B-CFD zero crossing being found. If $\mathcal{M}$ is the number of OF coefficients, the data samples to be processed by the OF are located at times $B_0, B_0 + 1, ..., B_0 + (\mathcal{M} - 1)$ relative to B_Z.

When determining the optimal values of B_0 and $\mathcal{M}$, care has to be taken to not degrade the resolution of the system. This could for instance happen if the samples processed by the OF do not include the peak of the detector signal, which would lead to a worsened energy resolution. Due to Eq. 9.7, the OF time determination is directly dependent on a correct amplitude determination, and therefore the time resolution can be assumed to be a solid estimate of the performance of the algorithm. To study the dependence of the time resolution on B_0 and $\mathcal{M}$, the simulated interactions of $5 \cdot 10^4$ photons of each of the tagged-photon energies aimed at position a in the matrix (see Fig. 10.1b) were used to generate signals that were processed by a C++ implementation of the method. The time resolution was in this case defined as the standard deviation of the $(T_{\mathrm{OF}} - T_0)$ distribution. The time resolution for 156-MeV tagged photons as a function of B_0 and $\mathcal{M}$ is shown in Fig. 11.3. A few things are worth noting:

- At $(B_0 = -6, \mathcal{M} = 4)$, the samples processed by the OF lie before the peak of the pulse, leading to a worsened resolution.
- As B_0 is moved closer to B_Z, fewer samples on the rising edge of the pulse are included in the fit, leading to a worsened resolution.
- An OF with $B_0 = -6$ can generally be replaced by an OF with $B_0 = -5$ and one less coefficients. This is because $g[B_Z - 6] \approx 0$.

Based on the results shown in Fig. 11.3, as well as an analysis of the results for the other tagged-photon energies, it was found that the optimal samples to use are given by $B_0 = -3$ and $\mathcal{M} = 4$. Making the OF shorter in this way has a positive effect on both the resource requirements and the pile-up reconstruction ability of the method. Fig. 11.4 shows the range of samples used by the 4-coefficient OF using the four samples up to and including the first sample above the 2-sample delay B-CFD zero crossing.

11.4 Pile-Up Reconstruction

One of the primary objectives of the method developed in this work is to enable separation and reconstruction of pile-up events. We here propose a method where

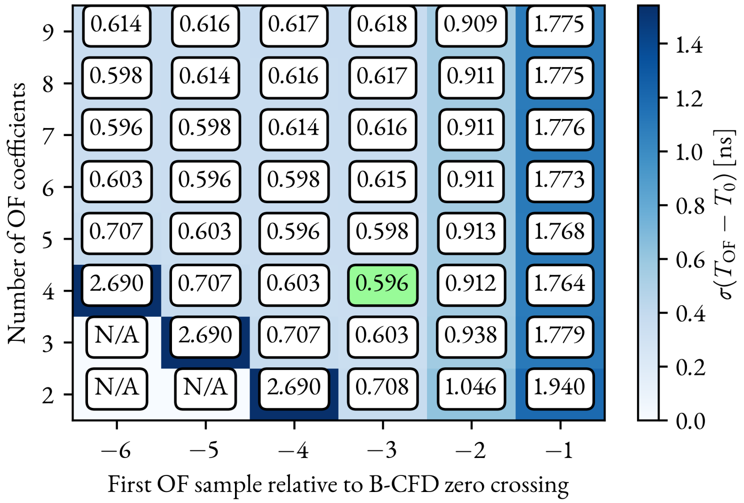

Figure 11.3: The time resolution of the OF-based method at a photon energy of 156 MeV, as a function of the initial sample and number of coefficients in the OF. The initial sample is numbered relative to the first sample after the B-CFD zero crossing. The optimum, both in terms of time resolution and number of OF coefficients, is marked in green.

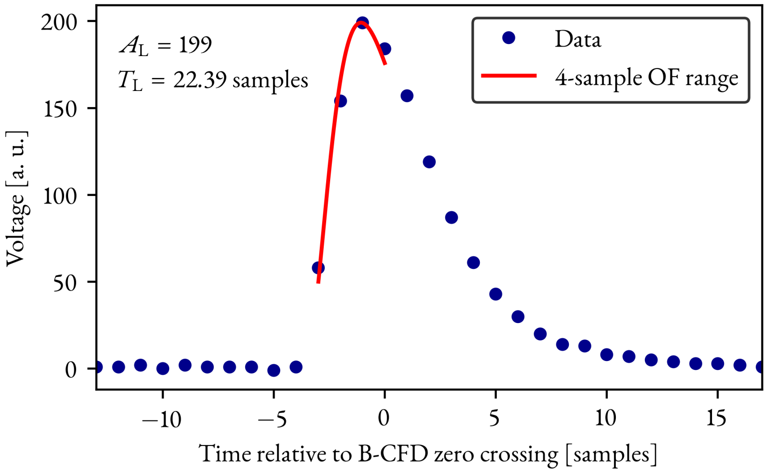

Figure 11.4: Example of a generated waveform and the "fit range" used in the OF method suggested here. The pulse-height and timing parameters determined by the filter are shown.

the B-CFD and OF methods outlined in the previous sections are used to analyse the detector signals in real time, and the extracted pulse parameters are used to subtract the subsequent "tail" of the pulse to allow detection and analysis of possible piled up pulses. The advantage of only using the initial part of the pulse in the OF algorithm now becomes clear, as it lowers the risk of pile-up pulses "contaminating" the OF calculation and allows a completely separate treatment of the first pulse.

The key to this algorithm is that the pulse tail is subtracted from *all* pulses successfully analysed by the B-CFD and OF methods, irrespective of whether there is a subsequent pile-up pulse or not. To do this, the tail has to be reconstructed solely from the A_{OF} and τ_{OF} parameters of the first identified, and the reconstructed tail forms a new baseline which may be subtracted from subsequent incoming data. The template pulse shape g, used by the OF method, contains information about the shape of the tail. The reconstruction of the pulse tail may be done using the methods outlined in Sec. 9.3.3, where the pulse template is discretised in time at four different phases. In theory, this discretised template may now be scaled and shifted by the parameters from the OF. However, it was found that there was a discrepancy between the lognormal function defining $g(t)$ and the generated pulse shapes. The discrepancy between the reconstructed pulse shape (using the A_{OF} and τ_{OF} parameters determined by the OF) and one generated pulse shape is shown in Fig. 11.5.

By determining the average amplitude-normalised difference between the re-

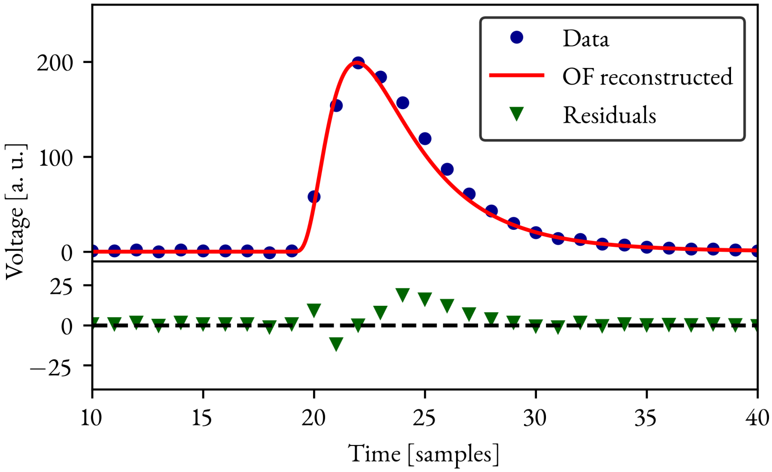

Figure 11.5: A generated waveform (blue points), the pulse shape fitted by the proposed method (orange line) and the residuals after taking the difference between the two. The average residuals were determined by performing a large number of such fits, and could then be subtracted to yield better pile-up reconstruction capabilities.

constructed pulse and the generated data and interpolating it using a spline method, a correction function $g_{\text{corr}}(t)$ to the reconstructed pulse was obtained. Since the interpolated spline is differentiable, $g'_{\text{corr}}(t)$ could be determined and $g_{\text{corr}}(t)$ was linearised in exactly the same way as the pulse template $g(t)$. The reconstructed pulse shape $g_{\text{rec}}(t)$ is given by:

$$g_{\text{rec}}(t_i - \tau) \approx g_{\text{OF}}(t_i) + g_{\text{corr}}(t_i) - \tau(g'_{\text{OF}}(t_i) + g'_{\text{corr}}(t_i)). \tag{11.4}$$

This procedure was repeated for each of the four B-CFD subsample phases (as in Sec. 11.2, the time-discretised pulse template is different for each of these cases). The end result is four sets of linearised reconstructed-pulse templates, which may be scaled, shifted and subtracted from an analysed waveform as soon as A_{OF} and τ_{OF} have been determined. The result of this pile-up algorithm is discussed in Ch. 12.

11.5 VHDL Implementation

The algorithm described in this chapter has been implemented in a VHDL code, which has been used to simulate the processing of both generated and experimental waveforms. As this has been purely a simulation study, no optimisations with regards to the implementation in an FPGA have been considered. Fig. 11.6 shows a schematic representation of the developed VHDL algorithm, which aims at estimating the amplitude A_{OF} and time τ_{OF} of detector pulses by analysing the sampled-signal values S. The implementations of the five components in the design — the baseline follower, the baseline trigger, the B-CFD algorithm, the OF algorithm and the baseline selector — will now be discussed in more detail.

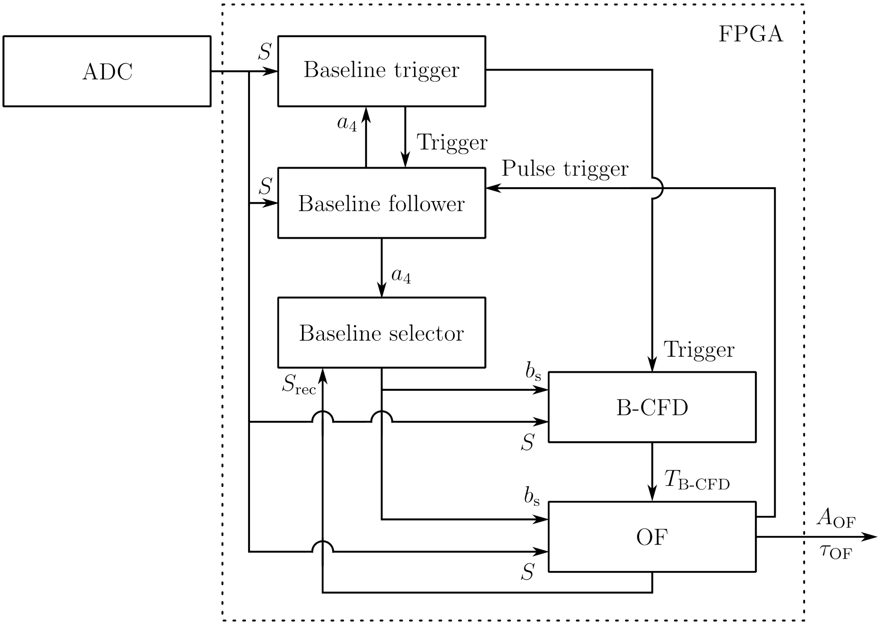

Figure 11.6: Flowchart of the VHDL implementation. A "pulse trigger" is issued when the OF has succeeded in determining the pulse height and timing.

11.5.1 Baseline Follower

Successful operation of both the B-CFD and OF methods relies on an accurate measurement of the *baseline* of the signal, i. e. the voltage level of the detector output when no pulses are present. In a realistic detector system, the baseline may fluctuate due to electronic noise or interference, and the noise level may change throughout a measurement. Therefore, the first task for the implemented algorithm is to continuously follow and estimate the baseline of the signal. The implemented baseline follower receives the raw sampled data S from the ADC, as well as trigger signals from the baseline-trigger and OF components. The purpose of these trigger signals is to prevent pulse data from influencing the baseline estimation.

The baseline follower is based on a 4-sample moving average (MA) filter, which is used to reduce the fluctuations and calculate an averaged baseline a_4. In order to implement the MA filter, the sampled data were pushed into a 10-sample buffer where any four values could be used to calculate a_4. The length of the buffer was chosen such that if a trigger signal from the baseline trigger is received, earlier sample data may be retrieved from the buffer and used to calculate a_4. The length of the buffer therefore depends on both the length of the MA filter and on the characteristics of the detector pulse shape. The baseline follower can be in one of three states, which may update every clock cycle:

- *Setup*: the baseline buffer is filled with sampled data S during a fixed initialisation time. No pulse detection can take place when in this state. After a fixed number of clock cycles, the state changes to *awake*.

- *Awake*: if no trigger is received from the baseline trigger, and a sufficient number of clock cycles have passed since the last OF trigger, the incoming signal is assumed to consist of pure baseline. The measured sample S is pushed into the buffer and the latest four samples in the buffer are used to calculate the averaged baseline a_4. If a baseline trigger is received, earlier data are collected from the baseline buffer and used to calculate a_4. The baseline-buffer contents are shifted so that the last four samples correspond to the ones used to calculate a_4 and the state changes to *sleeping*.

- *Sleeping*: no sampled data is pushed into the baseline buffer. The baseline estimate from before the baseline trigger is used as a constant estimate of the baseline. When the trigger signal from the baseline trigger disappears, the state changes to *awake*.

11.5.2 Baseline Trigger

The baseline calculation done by the baseline follower should be paused as soon as a possible detector pulse is identified. To this end, a 2-sample MA is used to continuously smooth the sampled data S, and the resulting average a_2 is compared to a fixed threshold v_0 above the baseline a_4 measured by the baseline follower. If $a_2 > a_4 + v_0$, the processed data potentially corresponds to the rising edge of a detector pulse. When this occurs, a trigger signal is sent to the baseline follower, which goes into its *sleeping* state as outlined above. This trigger signal remains at a high value until $a_2 < a_4 + v_1$, where v_1 is another fixed threshold level depending on the characteristics of the falling edge of the pulse.

The trigger signal from the baseline trigger is distributed to the other components in the design, so that further feature-extraction processing is only possible if the baseline trigger is at a high value. One may note that in the case of pile-up events, the baseline trigger may be triggered by the rising edge of the first pulse and not get cleared until the falling edge of the second pulse. Since the final triggering is handled by the OF algorithm, which will be active for the whole time the baseline trigger is active, this does not affect the triggering capabilities of the method.

11.5.3 Baseline Selector

The baseline estimate from the baseline follower assumes that underneath each pulse from the detector there is a flat baseline. This baseline estimate will be sent to the baseline selector, which by default transmits that baseline estimate to the B-CFD and OF components. However, as described in Sec. 9.3.3, a pulse identified by the OF should be reconstructed and subtracted to enable detection and reconstruction of potential pile-up pulses. In this situation, the reconstructed tail of the first identified pulse constitutes a new baseline estimate that should be subtracted from subsequent data. For each pulse identified by the OF, the reconstructed pulse tail is also calculated and sent to the baseline selector. When this happens, the flat baseline assumed by default is replaced by the reconstructed tail, and the selected baseline b_s that is assumed by the B-CFD and OF modules accounts for the reconstructed pulse.

11.5.4 Binary-Search CFD

Implementing the B-CFD method, as it is defined in Eq. 11.2, is straightforward in VHDL. The implemented B-CFD algorithm receives both raw data from the ADCs and baseline information from the baseline selector. By feeding baseline-subtracted data into a buffer larger than the B-CFD delay parameter, the B-CFD output is re-evaluated on every sampling-clock cycle. Since the B-CFD attenuation factor is set to 2, the necessary division is implemented using a bit-shift operation. To avoid spurious triggers due to noise, a threshold is imposed on the signal slope around the zero crossing, so that the B-CFD only triggers if the pulse is large enough. The B-CFD may *only* issue a trigger if the baseline trigger is active. If all of these conditions are met — i. e. the baseline trigger is active and the B-CFD algorithm finds a "large enough" zero crossing — the B-CFD issues a trigger to the OF algorithm and sends information about in which B-CFD window the zero crossing is located. This provides an initial timing estimate for the OF.

11.5.5 Optimal Filter

The OF was implemented in VHDL by storing the necessary OF coefficients $\boldsymbol{a}$ and $\boldsymbol{b}$ in arrays. As discussed below, the coefficients had to be quantised before implementation in VHDL. The precision of this quantisation potentially affects the achievable resolution, and was therefore not resource-optimised in the present proof-of-concept study. For the OF multiplications, $2 \times M$ DSP48 blocks were instantiated in the code. As soon as a trigger arrives from the B-CFD, along with information about the B-CFD timing, the appropriate sets of FIR coefficients are selected and used as inputs to the multipliers. If the OF-determined pulse height is large enough (a threshold may be imposed also here), a "pulse trigger" is issued. This tells the rest of the system that a pulse has been identified, and may be used as a trigger to read out the event.

In order to reconstruct the pulse tail, two arrays containing the pulse template and its derivative were defined. As soon as the OF finds a pulse and determines its amplitude and timing, the reconstructed pulse should be subtracted using Eq. 11.4. This required the instantiation of further DSP48 blocks, but still few enough to fit within the FPGA resources. The reconstructed samples are sent to the baseline selector, where they replace the constant baseline as the input to the B-CFD and OF algorithms. The processing of a pile-up pulse will proceed exactly as above, with its B-CFD time being determined and the OF used to estimate the pulse height and timing. In addition to the fixed lower threshold on the amplitude of OF-detected pulses, which is always employed, pile-up pulses are subject to one further constraint: due to the extra noise introduced by the tail reconstruction (visible in Fig. 11.5), a pile-up pulse detected by the OF is only accepted if its amplitude is larger than a fixed fraction of the *previous* pulse. This way, triggering on noise due to reconstruction of large pulses is avoided. This however comes with a loss in detection efficiency for small signals arriving on the tail of large signals.

Coefficient Quantisation

In order to implement the OF in an FPGA, the filter coefficients have to be quantised. In this work, where the FPGA implementation was only studied in simulation, the precision of the quantisation was chosen so that each filter multiplication only requires a single DSP48 block. As a consequence, the $\boldsymbol{a}$ and $\boldsymbol{b}$ coefficients were quantised with a precision of 25 bits per coefficient, with 10 of these bits reserved for precision in the determined value of τ_{OF}. After a more thorough study of the presented method under various experimental conditions, the coefficient quantisation should be optimised by studying the dependence of the energy and time resolution of different coefficient precisions. Correspondingly, the pulse-template values used for tail reconstruction were also quantised with a precision such that one DSP48 block is sufficient for each multiplication.

11.6 Method Validation

To validate the method described in this chapter, the Xilinx Vivado logic simulator [189] was used to set up a simulation of the VHDL-implemented method. Both experimental and modelled waveforms may be used as inputs to this simulation, so that data corresponding to a particular beam energy and position can be analysed independently to determine pulse height and timing information. For each such situation, the response to 1000 individual waveforms was simulated.

11.6.1 Energy Resolution

The energy resolution was determined when using the method described in this chapter on both experimental and model data. In previous analyses of the experimental data, the pulse maximum (i. e. the highest ADC output in the waveform) has been used as a measure of the pulse height — this was also the basis for the validation of the detector model presented in Ch. 10. Therefore, it is interesting to compare the results obtained with the OF method and the results obtained using the maximum-sample method. This was done for both the experimental (Fig. 11.7) and model (Fig. 11.8) data, separately. Here, the relative energy resolution is again defined as $\widetilde{\sigma}_E/E_0$, where $\tilde{\sigma}_E$ and E_0 are the width and mode parameters of the fitted Novosibirsk distributions.

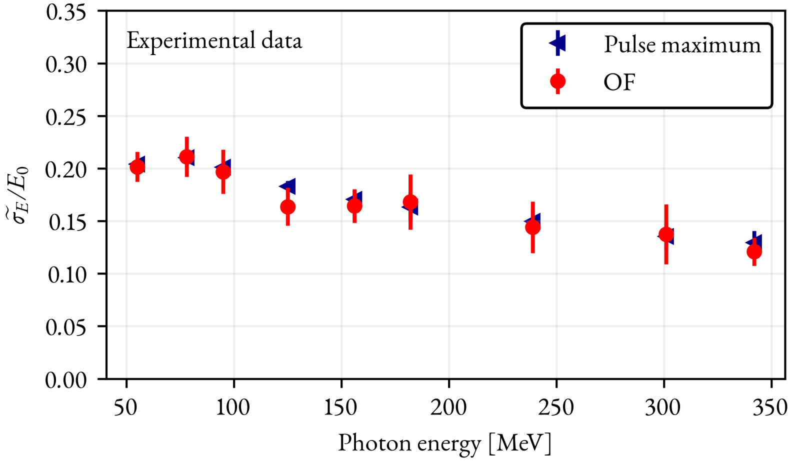

Figure 11.7: Relative energy resolution of a single cell as a function of photon energy, determined from experimental data using the pulse-maximum method and the method proposed in this work. The error bars correspond to the one-standard deviation uncertainties in the fitted Novosibirsk distributions.

11.6.2 Time Resolution

When it comes to the time resolution of a calorimeter, the end goal is to measure the time when an incident particle hits the detector with as good precision as possible. Here, we call this time T_0. During the prototype tests described in Ch. 10, with a

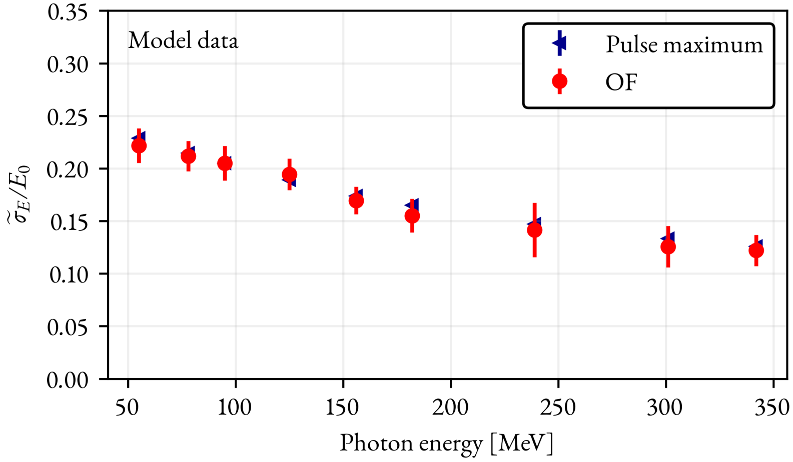

Figure 11.8: Relative energy resolution of a single cell as a function of photon energy, determined from model-generated data using the pulse-maximum method and the method proposed in this work. The error bars correspond to the one-standard deviation uncertainties in the fitted Novosibirsk distributions.

continuous (non-pulsed) photon beam, T_0 is of course not known. Therefore, the time resolution of a single cell was estimated by aiming the beam into the interface between two cells and analysing the distribution of time differences $\Delta T = T_1 - T_2$ between signals in two adjacent cells. In this section, the results from the OF method are compared with the results from the linear-CFD method both when the time resolution is obtained from $\sigma(\Delta T)$ (this comparison is made for both experimental and model data) and when the time resolution is obtained from $\sigma(T_1 - T_0)$ (this comparison is only made for model data).

Time Resolution from $\sigma(\Delta T)$

Here, the time resolution was determined by directing the photon beam onto the interface between two cells and determining the time difference ΔT between the signals in the two detectors (requiring the energy depositions in the two cells to be within 10% of each others). In this case, the resolution of a single cell was determined from the standard deviation of the ΔT distribution using Eq. 10.19. In Fig. 11.9 the single-cell time resolution determined from experimental data in this way is shown as a function of the energy deposition per cell. A similar comparison, but for model data, is shown in Fig. 11.10.

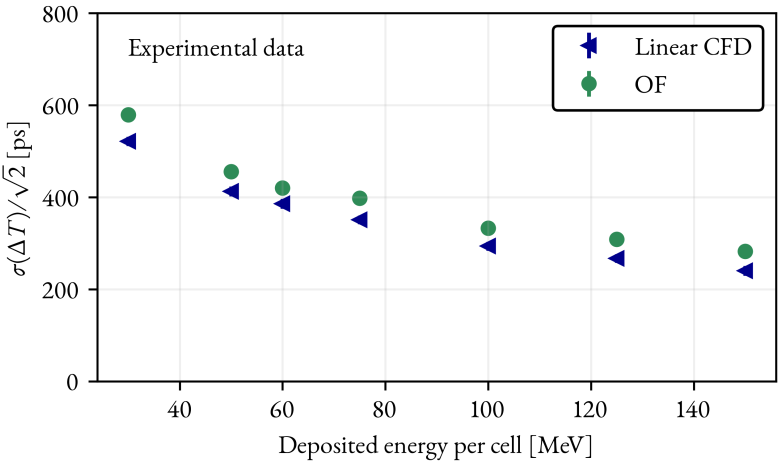

Figure 11.9: Time resolution of a single cell as a function of energy deposition in the cell, determined from experimental data using the linear CFD method and the method proposed in this work. Here, the photon beam was directed into the interface between two adjacent cells. The single-cell resolution was assumed to be $\sigma_T = \sigma(\Delta T)/\sqrt{2}$, where ΔT is the time difference between two signals in the adjacent cells. The error bars correspond to the one-standard deviation uncertainties in the fitted normal distributions.

Time Resolution from $\sigma(T_1 - T_0)$

In addition to determining the time resolution from the ΔT distribution, the model also enables determination the timing of pulses in a cell *relative to when the photon hit the detector*, T_0. That is, if the timings of the signals from the two adjacent cells are T_1 and T_2, then these may be compared with the photon-interaction time T_0, so that a true timing spectrum of each cell may be determined instead of having to rely on determining $\Delta T = T_1 - T_2$. Therefore, Fig. 11.11 also shows the time resolution of a cell determined from $\sigma(T_1 - T_0)$ and $\sigma(T_1 - T_0)$ using the linear CFD and the OF method.

11.7 Discussion

It is not obviously clear from the results in the previous section that the OF-based method presented in this thesis performs better than the previously used algorithms. With respect to the energy resolution, the methods perform equally well, as shown in Figs. 11.7 and 11.8. The attainable energy resolution with the OF method could

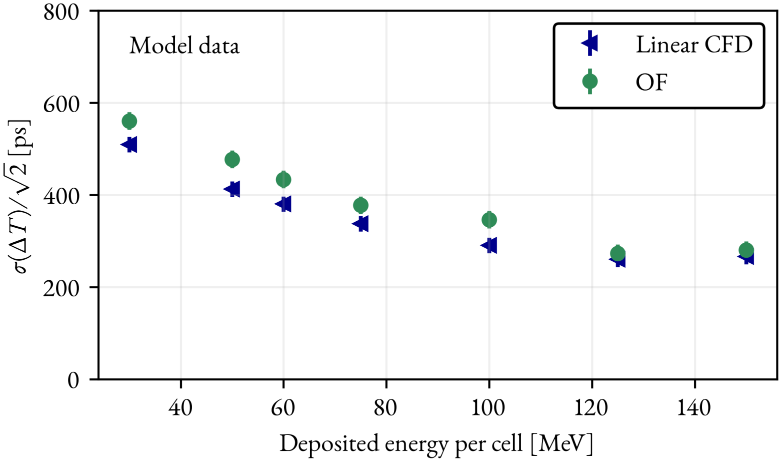

Figure 11.10: Time resolution of a single cell as a function of energy deposition in the cell, determined from model-generated data using the linear CFD method and the method proposed in this work. Here, the photon beam was directed into the interface between two adjacent cells. The single-cell resolution was assumed to be $\sigma_T = \sigma(\Delta T)/\sqrt{2}$, where ΔT is the time difference between two signals in the adjacent cells. The error bars correspond to the one-standard deviation uncertainties in the fitted normal distributions.

potentially be improved by modifying the pulse-shape template — since the pulse is rather short the effect of the fit quality of the used lognormal function around the pulse maximum could be investigated. This would be a topic for further work, since the shashlyk-EMC pulse shape is not yet well specified.

The time-resolution situation is a bit more complex. If one would just look at the experimental data, as analysed with both the linear-CFD and OF methods, the simple CFD seems to outperform the OF method, as shown in Figs. 11.9 and 11.10. However, the time resolution was in this case determined from the time difference between signals detected at times T_1 and T_2 in adjacent cells, as information about when the photon actually hit the calorimeter (T_0) is not available from the experiment. In contrast, this information *is* available from the Monte Carlo model described in Ch. 10, and so the time resolution may be determined from the model data using both methods. When determining the true time resolution $\sigma(T_1 - T_0)$ of a particular cell, the OF-based method yields a better resolution than the linear-CFD method, as shown in Fig. 11.11. This will also be clear from the results presented in Ch. 12. It appears that assuming that the time resolution of a single cell is given by $\sigma(\Delta T)/\sqrt{2}$ overestimates the performance of the detector, as shown in Fig. 11.12.

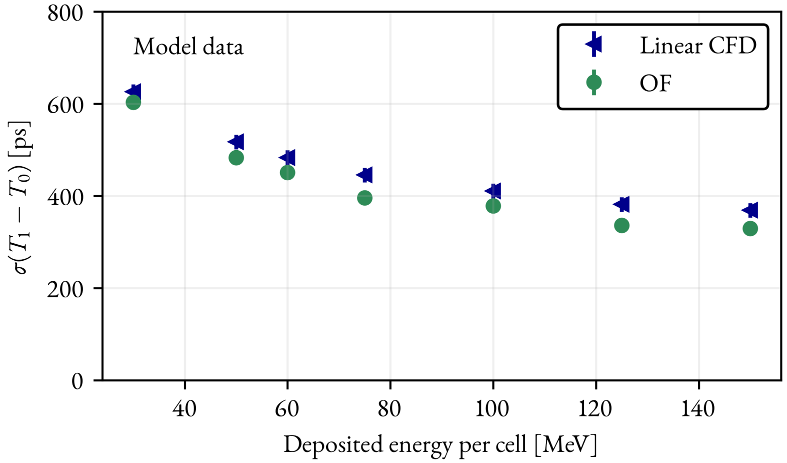

Figure 11.11: Time resolution of a single cell as a function of energy deposition in the cell, determined from model-generated data using the linear CFD method and the method proposed in this work. Here, the photon beam was directed into the interface between two adjacent cells. The single-cell resolution was determined by comparing the pulse timing T_1 with the time of arrival T_0 of the photon at the calorimeter. The error bars correspond to the one-standard deviation uncertainties in the fitted normal distributions.

The difference in the determined time resolution is especially seen for the CFD case, where this assumption indicates a time resolution $\sim$ 100 ps better than the true resolution of the cell. This behaviour can be understood by using the linear-CFD method to measure the pulse timings T_1 and T_2 in the two detectors, and plotting $(T_2 - T_0)$ as a function of $(T_1 - T_0)$ for all analysed events, as shown in Fig. 11.13.

It is clear that there exists a correlation between the pulse timings T_1 and T_2 determined with the linear CFD. Since these are random variables and $\Delta T = (T_2 - T_0) - (T_1 - T_0)$, the standard deviation in ΔT may be written:

$$\sigma(\Delta T) = \sqrt{\sigma(T_2 - T_0)^2 + \sigma(T_1 - T_0)^2 - 2\varrho\sigma(T_2 - T_0)\sigma(T_1 - T_0)}, \tag{11.5}$$

where ϱ is the Pearson correlation coefficient between $(T_2 - T_0)$ and $(T_1 - T_0)$. If one assumes that $\sigma(T_2 - T_0) = \sigma(T_1 - T_0)$, i. e. that the resolutions of the two cells are the same, Eq. 11.5 simplifies to:

$$\sigma(\Delta T) = \sigma(T_1 - T_0)\sqrt{2(1 - \varrho)}. \tag{11.6}$$

In the previously used method to determine the time resolution, it was assumed that the time resolutions of the two cells are identical and that their responses are

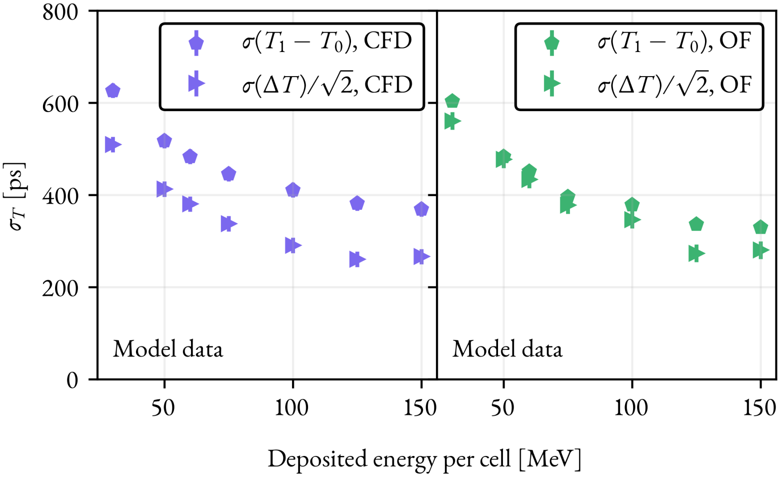

Figure 11.12: Comparison between the time resolution of a single cell determined from $\sigma(\Delta T)/\sqrt{2}$ and $\sigma(T_1 - T_0)$ as a function of energy deposition in the cell, using both the linear CFD method and the method proposed in this work. Here, the photon beam was directed into the interface between two adjacent cells. When using the linear CFD method (left figure), the $\sigma(\Delta T)/\sqrt{2}$ method severely overestimates the performance of the detector relative to the "true" time resolution $\sigma(T_1 - T_0)$. The error bars correspond to the one-standard deviation uncertainties in the fitted normal distributions.

uncorrelated (i. e. $\varrho = 0$). Since it now appears that the correlation is non-zero, the assumption that the time resolution of a single cell may be directly obtained from $\sigma(\Delta T)$ is invalid and results in an underestimation of the time resolution. The reason for the non-zero correlation is shown in Fig. 11.14, where the dependence of $(T_1 - T_0)$ and $(T_2 - T_0)$ on the phase of T_0 relative to the sampling clock is shown. It is clear that the determined times T_1 and T_2 are correlated, and that there is a dependence on when (relative to the ADC sampling clock) the photon hit the detector. This dependence is due to the fact that the linear interpolation needed for the linear CFD introduces some bias in the timing estimate, and that this bias depends on the phase of the signal.

To further investigate the source of this correlation, and to enable comparison with the new OF-based method, the interactions of a large number of 156-MeV photons directed onto position a of the matrix (i. e. onto the centre of one cell) were modelled. For each event, the pulse timing T_1 relative to the photon-interaction time T_0 was determined. Also, the phase of T_0 relative to the sampling clock was determined. Because the detector signal is continuously sampled, the sampled data will represent slightly different parts of the actual signal, depending on when the

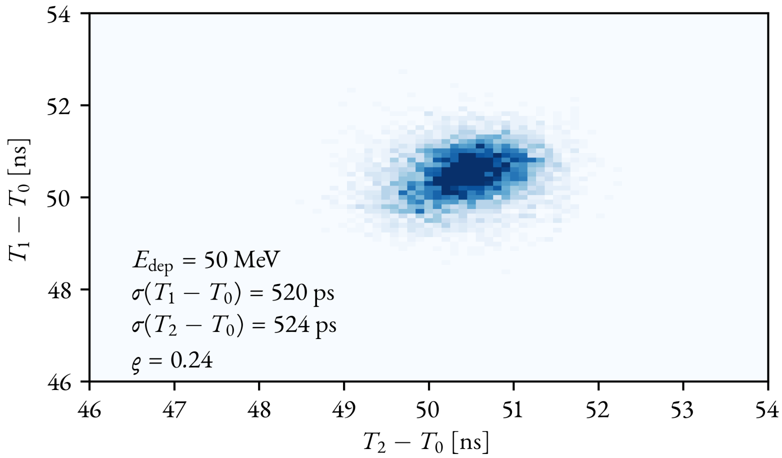

Figure 11.13: Pulse timings T_1 and T_2 in two adjacent cells relative to the photon-arrival time T_0, as determined using the linear-CFD method to analyse $8 \cdot 10^5$ model-generated pulses. These events correspond to cases where 50 MeV was deposited in each of the two cells.

photon interacts in the detector. This analysis was performed using both the linear-CFD and OF-based methods, and the results are shown in Figs. 11.15 and 11.16. It can be seen clearly that when using the linear-CFD method, the time response of the cell depends strongly on the phase of T_0. This is explained by the fact that a linear interpolation is used on the rising edge of the pulse, an approximation which depends on the phase since the pulse shape is not actually fully linear in this region. For the case where the photon beam is directed into the interface between two cells, the result is that the time responses will be correlated as T_0 is the same for both cells. When using the OF-based method proposed in this thesis, the phase-dependence of the response is suppressed since the OF does not assume linear interpolation between samples to determine the timing. One can clearly see some non-random structures in Fig. 11.16 — these are due to the subdivision of a sample into four regions needed for the B-CFD algorithm. Further optimisations could be done to find an optimal combination of sampling frequency and number of B-CFD windows.

In conclusion, the OF method proposed in this thesis yields a considerably better time resolution than the standard linear CFD method. This improvement is not directly observed when applying the two methods to experimental data due to correlations in the time response of adjacent cells. This correlation is very pronounced for the linear-CFD method, and has led to an underestimation of the time resolution of a single cell. There is no significant improvement in the energy resolution

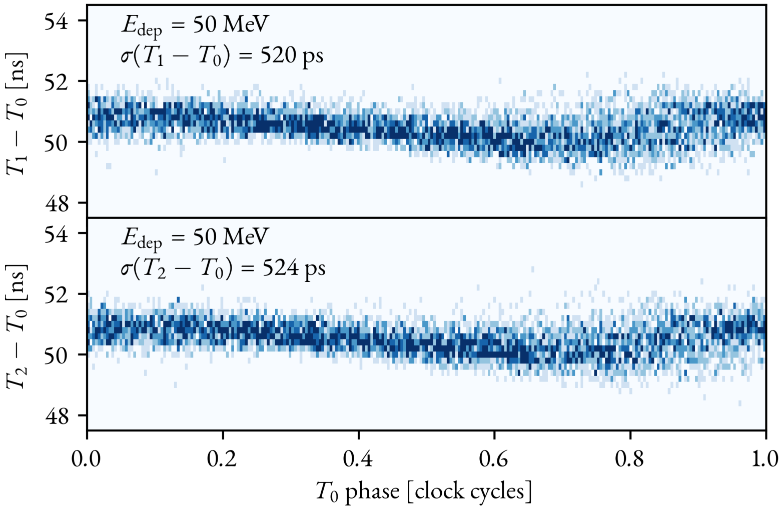

Figure 11.14: Pulse timings T_1 and T_2 in two adjacent cells relative to the photon-arrival time T_0, as determined using the linear-CFD method to analyse $8{\cdot}10^5$ model-generated pulses. These events correspond to cases where 50 MeV was deposited in each of the two cells. The correlated dependence of $(T_1 - T_0)$ and $(T_2 - T_0)$ on the phase of T_0 is clearly visible.

using the OF-based method, and this could potentially be improved by optimising the pulse-template function.

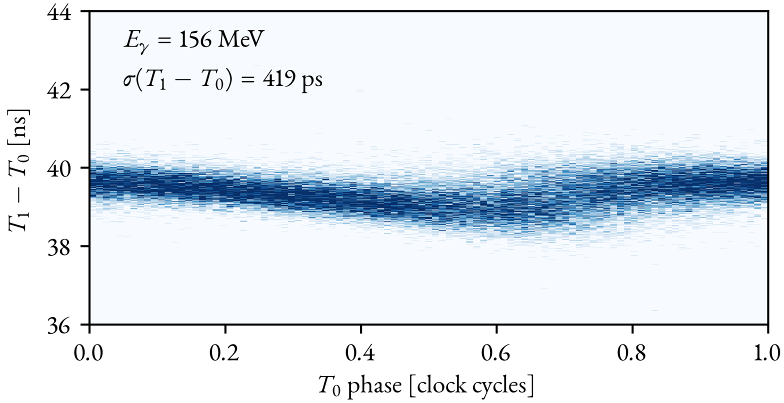

Figure 11.15: Pulse timing, relative to photon-arrival time T_0, as a function of the phase of T_0 relative to the sampling clock. The pulse timings correspond to $5 \cdot 10^4$ model-generated 156-MeV photons directed into the centre of the investigated cell, and were determined using the linear-CFD method. A noticeable dependence of the pulse timing on the phase of T_0 can be seen, and is explained by the linear approximation in the CFD not capturing the pulse-shape characteristics on the rising edge.

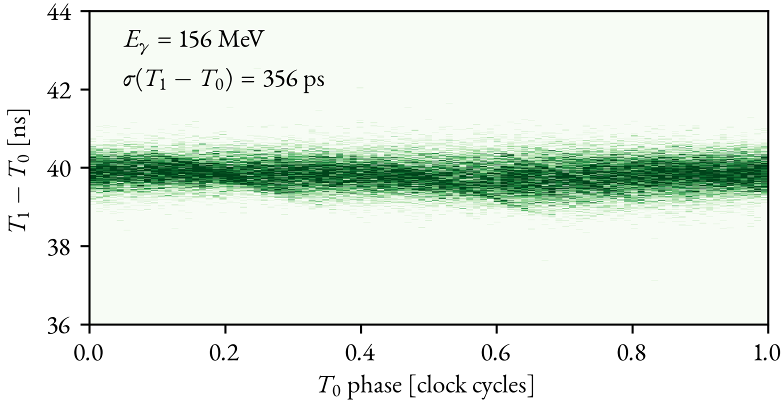

Figure 11.16: Pulse timing, relative to photon-arrival time T_0, as a function of the phase of T_0 relative to the sampling clock. The pulse timings correspond to $5 \cdot 10^4$ model-generated 156-MeV photons directed into the centre of the investigated cell, and were determined using the OF-based method proposed in this thesis. The OF captures the non-linear nature of the pulse shape, so that the phase-dependence in the time determination is suppressed. The non-random structures seen in the figure are due to the B-CFD algorithm, which subdivides the sample into four windows, and uses those windows as first approximations to the pulse timing.

12. Results and Discussion

In the previous chapter, promising results from the method presented in this thesis were presented. In particular, the time resolution provided by the OF-based method described here is better than what can be achieved using a standard linear-CFD method. In this chapter, the energy resolution, time resolution and pulse-detection efficiency of the method will be evaluated using model-generated detector signals. In contrast to previous chapters, where comparison to experimental results was important, all results in this chapter are based on simulations of a fully monoenergetic beam directed into the centre of one of the shashlyk cells in the matrix.

In this chapter, the pile-up reconstruction performance of the method is evaluated. Pile-up reconstruction is one of the primary aims of the method, and the performance of the method in this respect has been studied as a function of pulse height and pulse separation time. As a final result of this study, the pile-up performance under PANDA conditions has been studied and the results compared with the PANDA requirements presented in Ch. 4.

12.1 Monoenergetic Photons

By simulating the interaction of a pencil beam of monoenergetic photons at position b of the matrix (see Fig. 10.1b), and processing the resulting pulses with the VHDL implementation of the developed method, the relative energy resolution, the time resolution and the pulse-detection efficiency could be determined as a function of incident-photon energy E_γ. For the present study, the interactions of photons with energies of 10, 30, 50, 100, 200, 300, 500, 1000 and 1500 MeV were modelled.

12.1.1 Energy Resolution

The relative energy resolution, determined as in previous chapters from the width and mode parameters of Novosibirsk distributions fitted to the obtained pulse-height distributions, is shown as a function of E_γ in Fig. 12.1. Here, the results of the present method are compared to the energy resolutions obtained using the existing method (using the pulse maximum as a measure of the energy). No significant improvement in the energy resolution by using the OF-based method can be seen. As the detector signal from the calorimeter is rather short, the accuracy in the $\mathcal{A}$ parameter of the OF is most likely dependent on the assumed pulse template. Here, a lognormal function was used to describe the pulse shape (see Fig. 11.1). A more detailed analysis of the optimal pulse-shape template could potentially improve the energy resolution of the model.

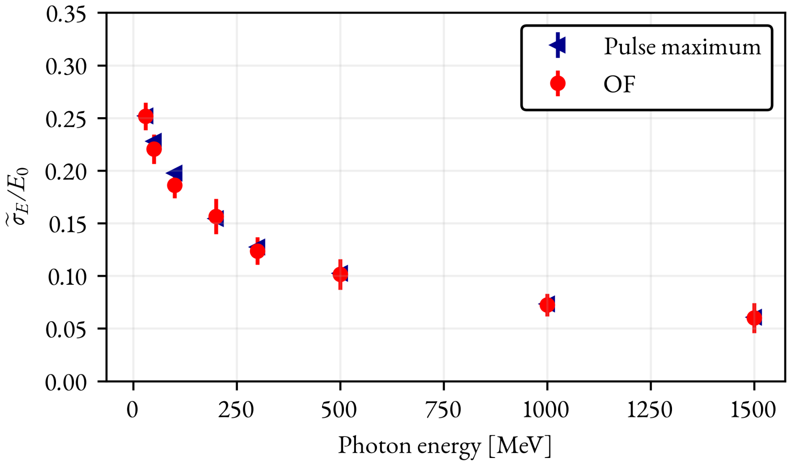

Figure 12.1: Relative energy resolution of a single shashlyk cell as a function of incident-photon energy. Determined by modelling interactions of monoenergetic photon beams in the centre of a shashlyk cell. The generated waveforms have been analysed using the existing method (where the pulse height is measured as the maximum of the sampled signal) and the OF-based method described in this thesis. The error bars correspond to the one-standard deviation uncertainties in the fitted Novosibirsk distributions.

12.1.2 Time Resolution

The timing of each detected pulse, relative to the photon-interaction time T_0, was determined for each pulse. As in previous chapters, the time resolution was determined by fitting a normal distribution to the resulting timing distribution. The time resolution of the single shashlyk cell is shown as a function of E_γ in Fig. 12.2. Here, the results of the present method are compared to the time resolutions obtained using the linear-CFD method. As indicated already in Ch. 11, the proposed OF-based method provides an improvement in the time resolution of the calorimeter. The energy-dependence of the time resolution of a scintillation detector coupled to a PMT may to first order be approximated as [190, 191]:

$$\sigma_\mathrm{T} = \sqrt{\left(\frac{a}{\sqrt{E_\gamma}}\right)^2 + b^2}, \tag{12.1}$$

where the $a/\sqrt{E_\gamma}$ term is due to statistical fluctuations in the scintillation process and b describes energy-independent noise or jitter. By fitting Eq. 12.1 to the linear-CFD data in Fig. 12.2, the fit parameters were found to be $a = (113 \pm 2)$ ps/$\sqrt{\mathrm{GeV}}$ and $b = (260 \pm 13)$ ps. By fitting the same equation to the OF data in Fig. 12.2, the fit parameters were found to be $a = (114 \pm 2)$ ps/$\sqrt{\mathrm{GeV}}$ and $b = (120 \pm 18)$ ps. Here, it can be seen that the major difference between the two methods is that the constant noise contribution to the time resolution is decreased by more than 50% by using the method proposed in this thesis. The major contribution to this improvement in time resolution is likely due to the removal of the phase-dependent response of the timing method, described in Sec. 11.7. This improvement becomes extremely important at high energies where the statistical fluctuations are negligible.

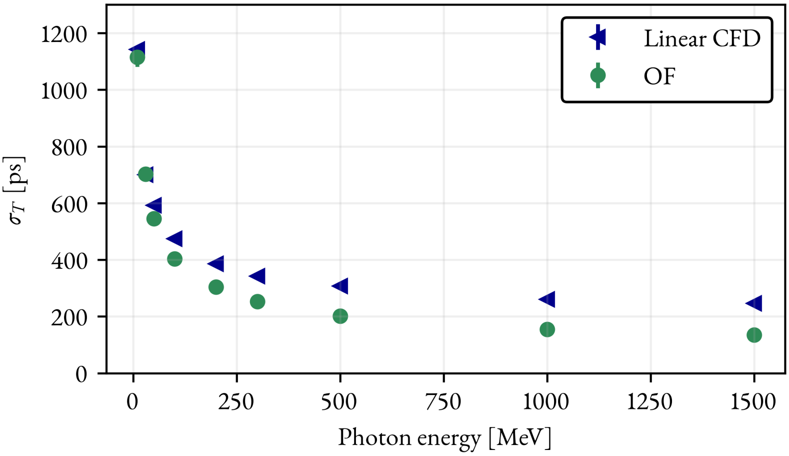

Figure 12.2: Time resolution of a single shashlyk cell as a function of incident-photon energy. Determined by modelling interactions of monoenergetic photon beams in the centre of a shashlyk cell. The generated waveforms have been analysed using the existing method (a linear CFD) and the OF-based method described in this thesis. The error bars correspond to the one-standard deviation uncertainties in the fitted normal distributions.

12.1.3 Pulse-Detection Efficiency

As discussed in the previous chapter, the VHDL implementation of the developed algorithm includes some thresholds, which have to be set by the user. These affect the baseline trigger, B-CFD and OF parts of the algorithm, and are set such that the occurrence of false triggers is minimised. In order to achieve the single-cell threshold of 3 MeV, specified by the PANDA requirements, the pulse-height distribution was calibrated in energy using the energy-deposition information available for each generated pulse and the thresholds in the VHDL were set to correspond to 3 MeV. The pulse-detection efficiency ε is defined as the ratio between the number of detected pulses and the number of generated pulses used as input to the VHDL simulation:

$$\varepsilon = \frac{N_{\mathrm{det}}}{N_{\mathrm{gen}}}. \tag{12.2}$$

Fig. 12.3 shows the pulse-detection efficiency as a function of E_γ. The decrease in efficiency at low photon energies is simply due to the fact that in a fraction of those events the actual energy deposition in the cell will be below the threshold of 3 MeV, for instance due to leakage of the electromagnetic shower to adjacent cells.

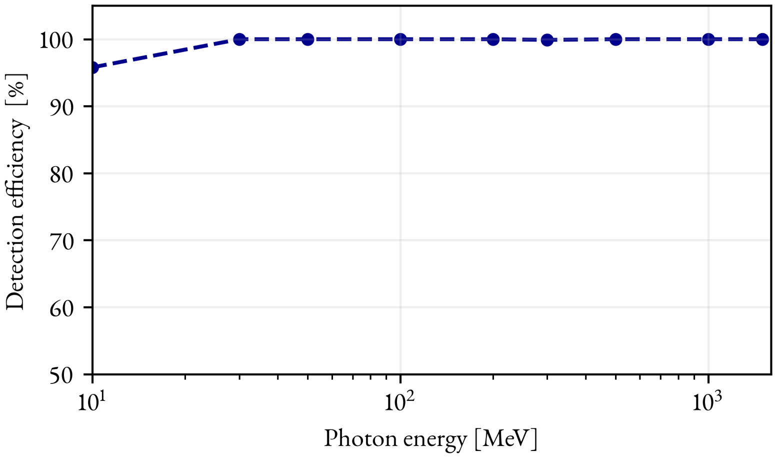

Figure 12.3: Pulse-detection efficiency of the OF-based method in this work as a function of incident-photon energy. The decrease in efficiency at low photon energies is due to the low-energy tail in the energy-deposition distribution, meaning that a fraction of the photons in this situation will deposit less than 3 MeV, which is the specified lower threshold.

12.2 Pile-Up Reconstruction

To systematically evaluate the pile-up reconstruction capabilities of the method, generated pile-up events were used as inputs to the VHDL simulation. When generating a pair of pile-up pulses, the amplitudes of the two pulses and their separation in time could be specified. Since the pile-up reconstruction performance should be evaluated for specific E_γ separately, the amplitude of one of the two pulses was obtained from the simulation corresponding to the specific E_γ. For reasons that will be made clear in Sec. 12.3, the energy of the other of the two pulses was *not* taken to correspond to a particular E_γ. Instead, pulses corresponding to particular *energy depositions* $E^0_{\text{dep}} = 1, 3, 5, 10, 20, 30, 50, 80, 100, 200, 300, 400, 600, 700, 3500$ and 7000 MeV were used. Since the model was calibrated to experimental data for photon energies below 800 MeV, pulses corresponding to multi-GeV energy depositions would not fit within the ADC range. To emulate this, the ADC range was assumed to be 14 bits and the amplitudes of any pulses exceeding this were truncated as shown in Fig. 12.4.

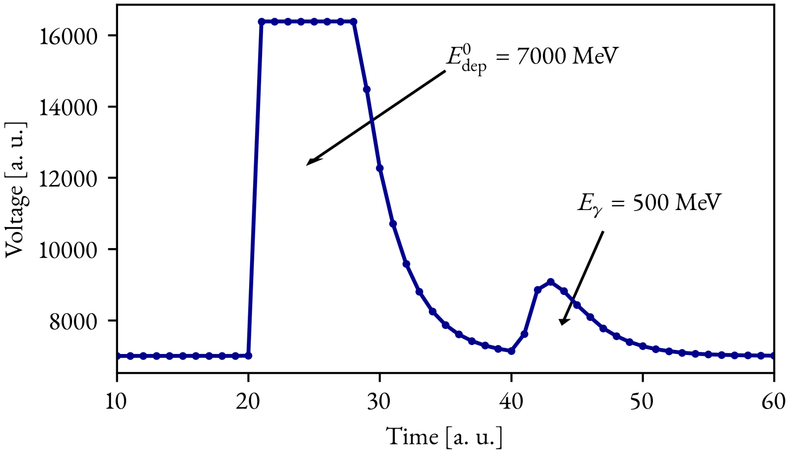

Figure 12.4: Example of a modelled pile-up event where the maximum range of the ADC is reached. The first of the two pulses is due to an energy deposition of 7000 MeV in the cell, while the second is due to an incident-photon energy of 500 MeV. An energy deposition of 7000 MeV gives an amplitude exceeding the 14-bit range of the ADC. In the model, such pulses were assumed to saturate at at the ADC maximum.

Since the signal that should be successfully reconstructed — the "signal of interest" — is the one corresponding to a photon-beam energy E_γ, the other of the two pulses (corresponding to an energy deposition E^0_{dep}) will be referred to as the "nuisance signal". That is, the nuisance signal constitutes background events in the detector, in which presence the detection probability and reconstruction performance for an additional photon of energy E_γ should be evaluated. Of course, in reality also the signal which here is called the nuisance signal should be reconstructed by the algorithm. The time difference Δt between the two pulses constituting the pile-up event could be specified for each generated event, and was defined as:

$$\Delta t = t_\gamma - t^0_{\text{dep}}, \tag{12.3}$$

where t_γ is the time when the photon of energy E_γ (i. e. the signal of interest described above) hits the detector and t^0_{dep} is the time when the photon giving rise to an energy deposition E^0_{dep} in the cell (i. e. the nuisance signal described above) hits the detector. Because the performance of the method might be different depending on which of the two pulses arrives first, Δt values from -250 ns to 250 ns were investigated. Fig. 12.5 shows three modelled pile-up events at $E^0_{\text{dep}} = 100$ MeV and $E_\gamma = 100$ MeV and three different Δt values; 125 ns, 37.5 ns and 0 ns. The first of these cases corresponds to well separated pulses, the second to highly piled-up pulses and the third to completely overlapping pulses. Completely overlapping signals will be identified a single pulse with a larger amplitude, and so the two events cannot be separated.

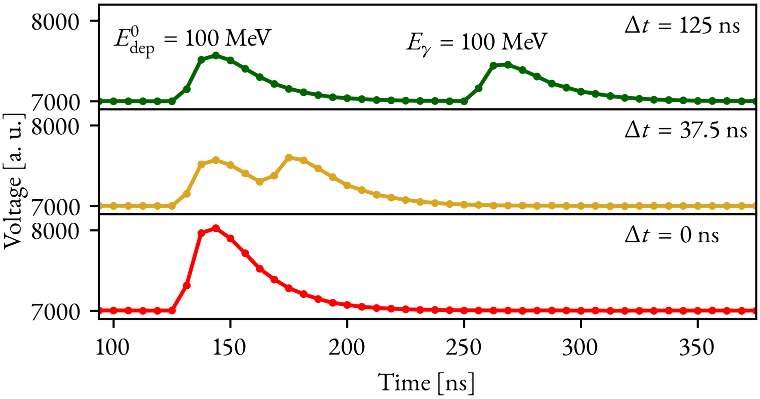

Figure 12.5: Modelled pile-up events at different time differences. The first pulse is a so-called nuisance signal corresponding to an energy deposition of 100 MeV. The second pulse is the signal of interest and is in this case due to an incident photon with an energy of 100 MeV. Here, time differences Δt of 125 ns (well separated pulses), 37.5 ns (highly piled-up pulses) and 0 ns (completely overlapping pulses). When the two pulses completely overlap a single pulse with the summed amplitude will be observed.

Figs. 12.6 and 12.7 show the energy and time resolution of the reconstructed signal of interest in the three cases shown in Fig. 12.5, as determined by the VHDL implementation of the feature-extraction method. As before, the pulse-height distributions have been fitted with Novosibirsk distributions giving mode and width parameters for the distribution, whereas the resulting timing distributions have been fitted with normal distributions. Two things are worth noting:

- Even at considerable pile-up (as in the $\Delta t = 37.5$ ns case), the method succeeds in determining the pulse height and timing with almost as good precision as for well-separated pulses.

- For fully overlapping pulses, the pulse-height distribution is shifted to higher amplitudes. At the same time, both the relative energy resolution and the time resolution is better in this case than in the well-separated case. This is because the completely overlapping pulses appear as a single pulse with a higher amplitude, for which the resolution is generally better than for a low-energy photon, as seen in Figs. 12.1 and 12.2.

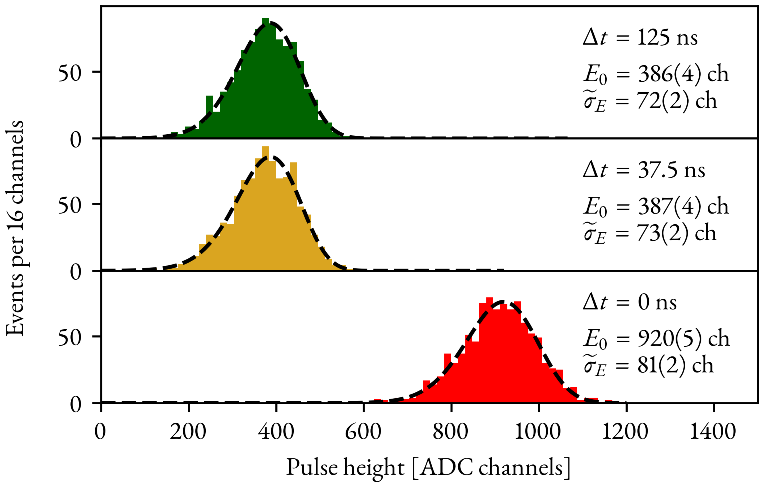

Figure 12.6: Pulse-height distributions for reconstructed signals of interest corresponding to an incident-photon energy of 100 MeV under three different pile-up scenarios. The parameters of the fitted distributions, along with the uncertainties in the fit parameters (in parentheses), are shown. In all three cases, the nuisance signal corresponded to an energy deposition of $E^0_{\text{dep}} = 100$ MeV.

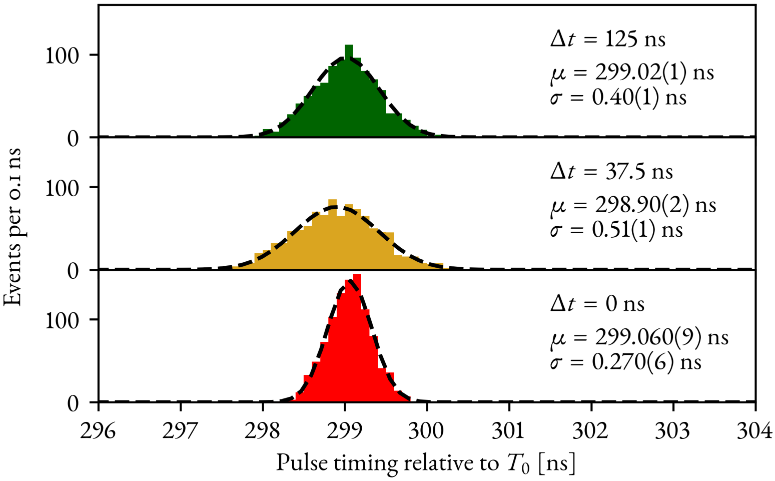

Figure 12.7: Timing distributions for reconstructed signals of interest corresponding to an incident-photon energy of 100 MeV under three different pile-up scenarios. The parameters of the fitted distributions, along with the uncertainties in the fit parameters (in parentheses), are shown. In all three cases, the nuisance signal corresponded to an energy deposition of E^0_{dep} = 100 MeV.

12.2.1 Resolution and Pulse-Detection Efficiency

To study the effect Δt has on the energy and time resolution, pile-up events corresponding to different Δt values have been modelled and used as input to the VHDL simulation. For each Δt, distributions such as the ones in Figs. 12.6 and 12.7 were obtained, and their means $\langle A\rangle$, $\langle T\rangle$ and standard deviations σ_A, σ_T were determined. In Fig. 12.8, these are compared with the corresponding values for the case of isolated signals of interest. The comparisons are shown as functions of Δt for E_γ = 100 MeV at three different E^0_{dep} cases. Note that in these analyses the distributions were not fitted but the means and standard deviations were determined directly from the data. The four variables shown here will, along with the pulse-detection efficiency, be referred to as the *performance metrics* of the method.

The fifth performance metric, the pulse-detection efficiency *relative to the one when no nuisance signal is present*, was also determined for different pile-up scenarios. Fig. 12.9 shows the pulse-detection efficiency as function of Δt for E_γ = 100 MeV at three different E^0_{dep} cases.

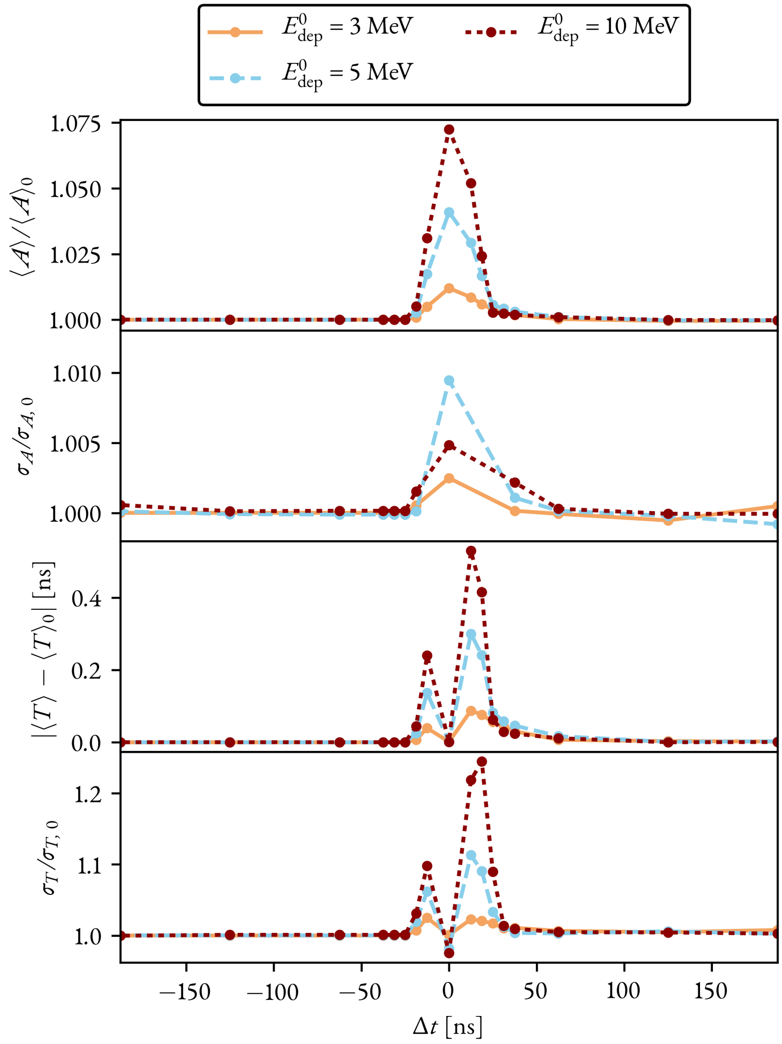

Figure 12.8: Means and standard deviations of the $E_\gamma = 100$ MeV pulse-height and timing distributions in the presence of a nuisance signal corresponding to an energy deposition of E^0_{dep}, plotted as a function of the time Δt between the two signals. Here, the $E_\gamma = 100$ MeV signal of interest arrives at a time Δt relative to the nuisance signal, so that $\Delta t < 0$ corresponds to a situation where the signal of interest arrives first. The means and standard deviations are compared to the cases where no nuisance signal is present. The relative shift $\langle A\rangle/\langle A\rangle_0$ of the pulse-height mean, the relative shift $\sigma_A/\sigma_{A,\,0}$ of the pulse-height standard deviation, the absolute shift $|\langle T\rangle - \langle T\rangle_0|$ of the timing mean and the relative shift $\sigma_T/\sigma_{T,\,0}$ are shown as functions of Δt. Three E^0_{dep} cases are shown. It is clear that a large E^0_{dep} and a small Δt causes the highest performance degradation, but that the method is able to reconstruct pulses separated by as little as $\sim$ 30 ns.

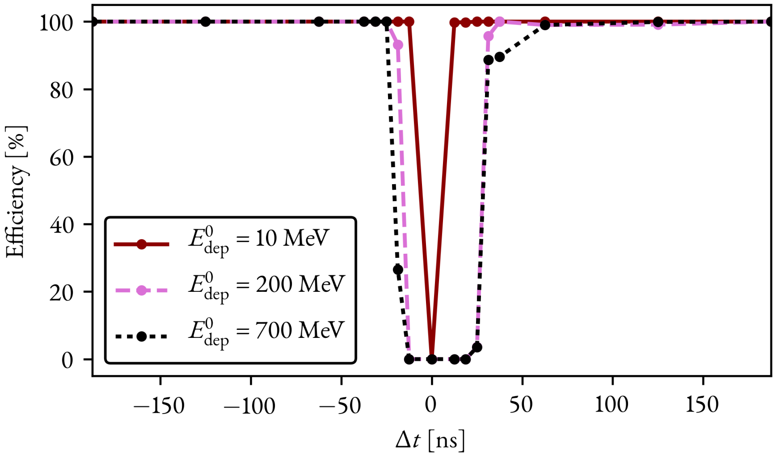

Figure 12.9: Pulse-detection efficiency for identifying a pulse corresponding to E_γ = 100 MeV in the presence of a nuisance signal corresponding to an energy deposition of E^0_{dep}, plotted as a function of the time Δt between the two signals. Here, the E_γ = 100 MeV signal of interest arrives at a time Δt relative to the nuisance signal, so that $\Delta t < 0$ corresponds to a situation where the signal of interest arrives first. As was the case for the pulse-height and timing determination shown in Fig. 12.8, it is clear that a large E^0_{dep} and a small Δt causes the highest performance degradation.

12.3 Feature Extraction Under PANDA Conditions

In the previous section the concept of a “nuisance signal”, with which the signal of interest may overlap up, was introduced. While the signal of interest always corresponds to a primary photon of a specific energy E_γ hitting the detector, the nuisance signal is defined by the amount of energy E^0_{dep} deposited in the cell. The reason for this will now be explained. During operation of PANDA, each cell will be subjected to a certain particle hit rate R. The highest per-cell rate is expected in the cells closest to the beam pipe, which corresponds to the most forward-directed region from the PANDA IP. The particles hitting each cell will have a certain energy distribution, leading to a distribution of energy deposits E^0_{dep} per cell. The distribution of E^0_{dep} in each shashlyk cell was obtained by using the PandaRoot framework (introduced in Sec. 8.2) to simulate $3 \cdot 10^6$ $\mathrm{p}\bar{\mathrm{p}}$ interactions at beam momenta of 1.5 and 15 GeV/c. The E^0_{dep} distribution per cell, averaged over the whole calorimeter, is shown in Fig. 12.10. Under the assumption that the *shape* of this distribution is fairly constant over the entire calorimeter, the two distributions shown here will be used through all further discussions in this chapter.

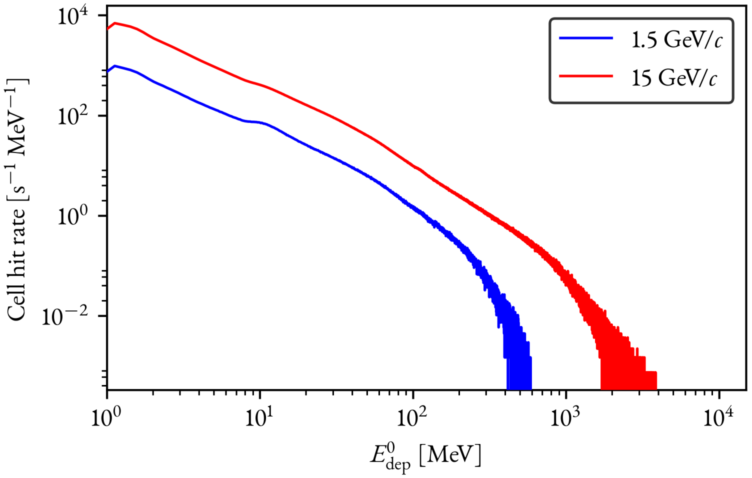

Figure 12.10: Expected distributions of E^0_{dep}, the energy deposition per cell in the shashlyk calorimeter, at two different antiproton-beam momenta and at a luminosity of $\mathcal{L} = 1 \cdot 10^{31}$ cm^{-2} s^{-1}. The lower limit of the distributions is at 1 MeV.

The expected hit rate per cell was also obtained from the PandaRoot simulation, and as expected, the highest hit rates are predicted in the cells closest to the beam pipe. The predicted hit rate in one of these cells under various luminosity and $\overline{\mathrm{p}}$-momentum conditions is shown in Tab. 12.1. In these cases, the lowest E^0_{dep} included in the rate determination was 1 MeV. If even smaller energy depositions are included, the rate increases due to combination from low-energy background events.

Table 12.1: Rate of hits giving an energy deposition of at least 1 MeV in one of shashlyk cells closest to the beam pipe, as simulated in PandaRoot. Hit rates for two different beam luminosities are shown.

Beam momentum [GeV/c]	Hit rate R [kHz]	
	$\mathcal{L} = 1 \cdot 10^{31}$ cm^{-2} s^{-1}	$\mathcal{L} = 1 \cdot 10^{32}$ cm^{-2} s^{-1}
1.5	2.3	23
15.0	61.6	616

By averaging the results obtained in the previous section over the E^0_{dep} and rate distributions in PANDA, the performance of the method under various conditions in the experiment may be estimated. Since the performance of the VHDL implementation was evaluated for E^0_{dep} values ranging from 1 MeV to 7000 GeV, the entire range of the distributions in Fig. 12.10 was covered. A parameter f (this could be any of the five performance metrics studied above), the value of which depends on E_γ, E^0_{dep} and Δt, may be averaged over the simulated E^0_{dep} distributions $p(E^0_{\text{dep}})$:

$$\langle f\rangle(E_\gamma, \Delta T_0) = \int_{E^0_{\text{dep, min}}}^{E^0_{\text{dep, max}}} p\left(E^0_{\text{dep}}\right) f\left(E^0_{\text{dep}}, E_\gamma, \Delta T_0\right) \mathrm{d}E^0_{\text{dep}}. \tag{12.4}$$

This procedure was repeated for two different $\overline{\mathrm{p}}$ momenta. The results are shown in Figs. 12.11 and 12.12 for three different signal-of-interest E_γ values. In Fig. 12.12, a comparison is also made with the efficiencies estimated for a situation where a more basic method for pulse height and timing is used. In this case, it was assumed that the signal of interest can be reconstructed only if it arrives before the risetime of the nuisance signal (in case of $\Delta t < 0$) or after the decay of the nuisance signal (in case of $\Delta t > 0$). If the two pulses arrive closer to each other, the event is assumed to be classified as a pile-up and rejected.

12.3.1 Hit-Rate Distribution

After averaging over the simulated E^0_{dep} distributions in PANDA, each performance metric is a function of E_γ and Δt only. To evaluate the performance of the method under different (average) hit rates R in the cell, each metric may be averaged over the probability distribution $p(\Delta t)$ corresponding to a particular R:

$$\langle f\rangle(E_\gamma) = \int_{-\infty}^{\infty} p\left(\Delta t\right) \langle f\rangle \left(E_\gamma, \Delta T_0\right) \mathrm{d}\Delta t. \tag{12.5}$$

As hits in a cell are assumed to follow Poisson statistics, the distribution of time differences between two consecutive hits is given by an exponential distribution. However, since we consider the two cases where the signal of interest can come either before or after the nuisance signal, the two-sided exponential distribution [192] (also known as the Laplace distribution) is used:

$$p(\Delta t) = \frac{R}{2} \exp(-R|\Delta t|), \tag{12.6}$$

where R is the average hit rate per cell. The rate dependence of the five performance metrics was determined from Eq. 12.5. The results are shown in Figs. 12.13 and 12.14. In Fig. 12.14, a comparison is also made with the efficiencies estimated for the pile-up rejection method described above.

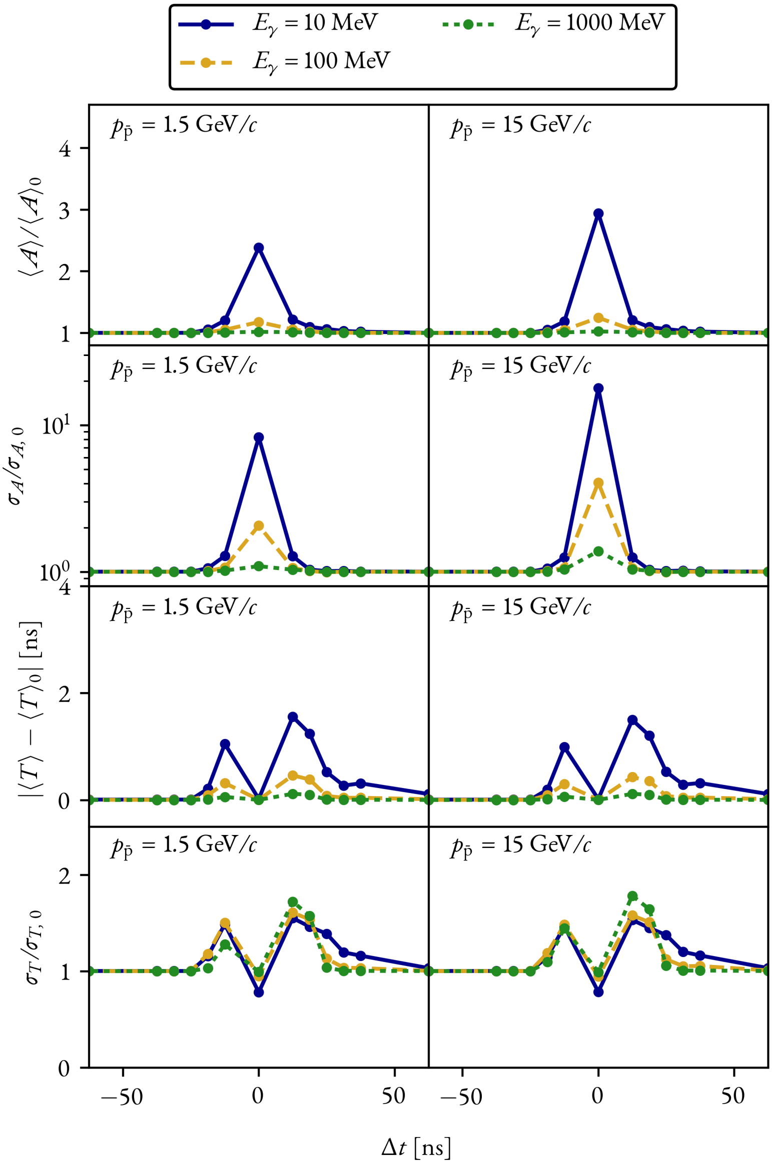

Figure 12.11: Means and standard deviations of the pulse-height and timing distributions for photons of three different energies E_γ, in the presence of a nuisance signal. The nuisance-signal E^0_{dep} has been obtained as an average of the simulated E^0_{dep} distributions in a shashlyk cell during operation of PANDA at beam momenta of 1.5 and 15 GeV/c. The four performance metrics are plotted as functions of the time Δt between the two signals. Here, the E_γ signal of interest arrives at a time Δt relative to the nuisance signal, so that $\Delta t < 0$ corresponds to a situation where the signal of interest arrives first.

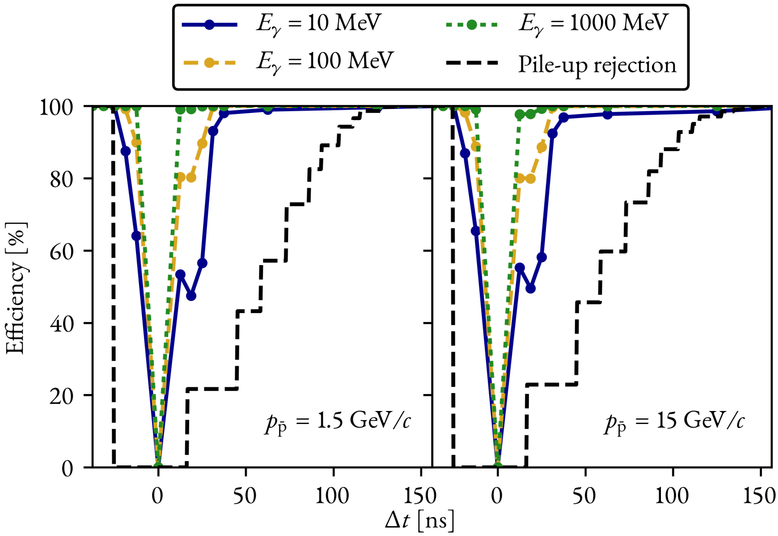

Figure 12.12: Pulse-detection efficiency for photons of three different energies E_γ, in the presence of a nuisance signal. The nuisance-signal E^0_{dep} has been obtained as an average of the simulated E^0_{dep} distributions in a shashlyk cell during operation of PANDA at beam momenta of 1.5 and 15 GeV/c. The efficiency is plotted as a function of the time Δt between the two signals. Here, the E_γ signal of interest arrives at a time Δt relative to the nuisance signal, so that $\Delta t < 0$ corresponds to a situation where the signal of interest arrives first. The efficiency when rejecting pile-up pulses was estimated as described in Sec. 12.3.

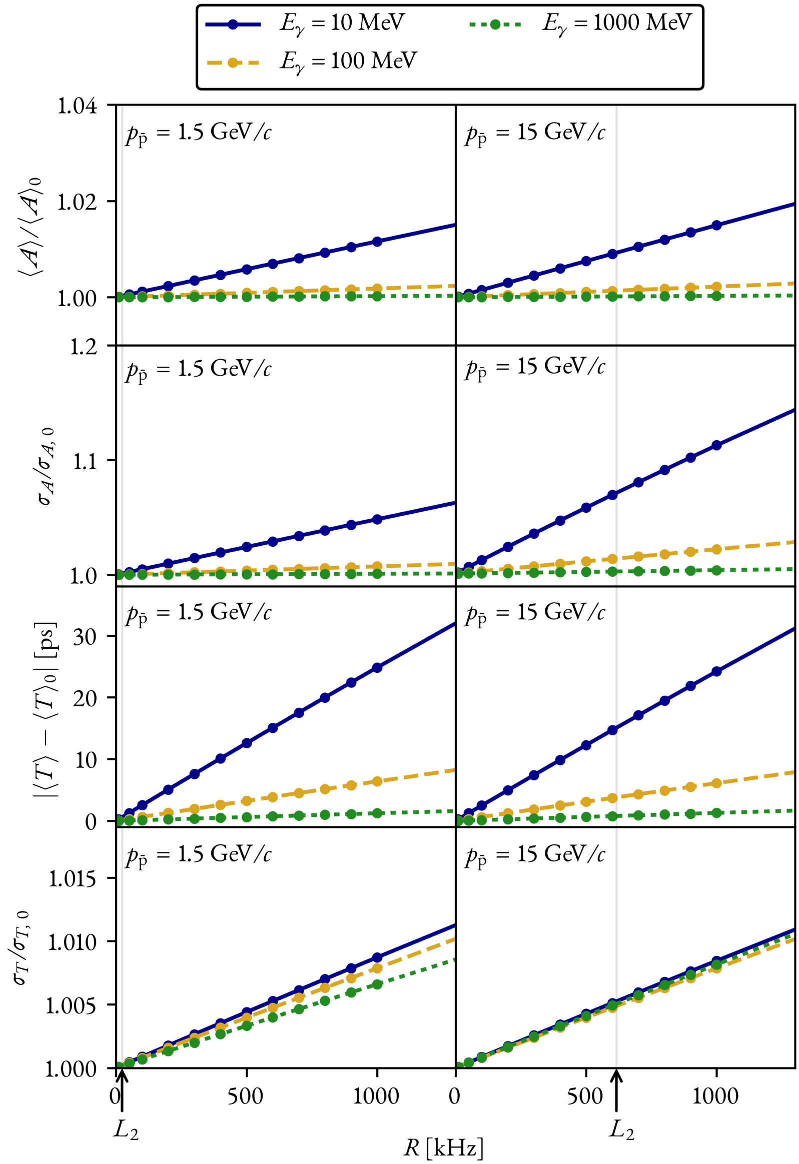

Figure 12.13: Means and standard deviations of the pulse-height and timing distributions for photons of three different energies E_γ, in the presence of nuisance signals matching the E^0_{dep} distribution in a shashlyk cell during operation of PANDA at beam momenta of 1.5 and 15 GeV/c, plotted as a function of the hit rate R. The expected hit rate at the highest average luminosity, $L_2 = 1 \cdot 10^{32}$ cm^{-2} s^{-1}, is indicated. The average luminosity during initial operation of PANDA will be a factor 10 lower.

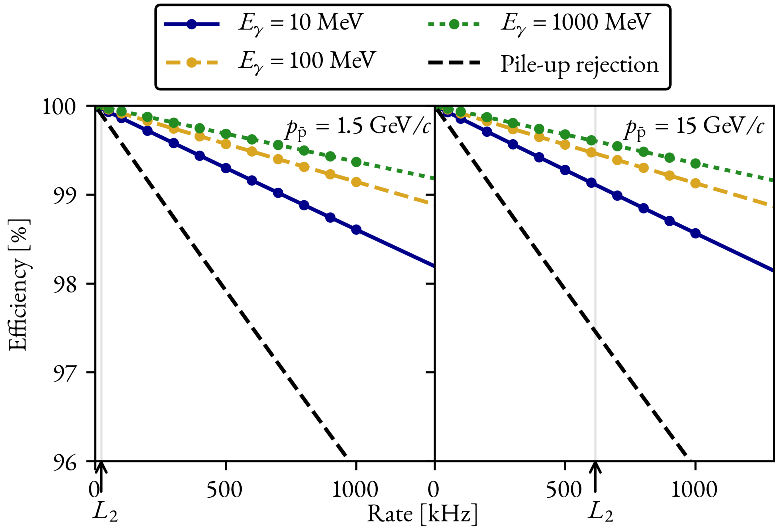

Figure 12.14: Pulse-detection efficiency for photons of three different energies E_γ, in the presence of nuisance signals matching the E^0_{dep} distribution in a shashlyk cell during operation of PANDA at beam momenta of 1.5 and 15 GeV/c, plotted as a function of the hit rate R. The expected hit rate at the highest average luminosity, $L_2 = 1 \cdot 10^{32}$ cm^{-2} s^{-1}, is indicated. The average luminosity during initial operation of PANDA will be a factor 10 lower. The efficiency when rejecting pile-up pulses was estimated as described in Sec. 12.3, and here this was weighted with the $p(\Delta t)$ distribution.

12.4 Discussion

The developed feature-extraction algorithm has been benchmarked using the Monte Carlo model of the shashlyk calorimeter described in Ch. 10. One of the key features of the described method is the major improvement in time resolution it provides compared to the linear CFD method. This is due to the fact that a linear CFD relies on a linear interpolation of the rising edge of the signal. The assumption that the signal shape has a linear behaviour in this region is not usually true, an this will lead to a loss in time resolution. The OF-based method described here takes more prior information about the detector pulse shape into account, and does not rely on a strict linear interpolation between two adjacent samples. The pulse height resolution of the method developed here is similar to that of simpler methods, but could be improved by optimising the pulse-shape template used to configure the OF. In general, the method should be re-optimised once the exact parameters of the shashlyk readout (such as possible shaping time and sampling frequency) have been fixed.

It has been shown that the method provides considerably better pulse-detection efficiencies under pile-up conditions than the more basic methods already evaluated for the PANDA EMC. For comparison with these, it was assumed that a more basic method would simply reject pile-up events if the constituent signals are close enough in time. The method described here allows separation and reconstruction of pile-up events separated by as little as $\sim$ 30 ns without considerable degradation in the energy or time resolution.

Based on a PandaRoot simulation of the hit rates in the shashlyk calorimeter, rates above 100 kHz are not expected during the first phase of PANDA (see Tab. 12.1). At such rates, a method where pile-up events are *not* reconstructed would probably suffice to keep within the limit of less than 1% of events lost due to pile-up. However, as luminosity is increased, pile-up will become more of an issue, and in such a high-rate situation the method developed here would outperform a method based on pile-up rejection. Note that the capabilities of a pile-up rejection algorithm were estimated based on the pulse shapes used in the model, and that the validity of the results should be verified against experimental data of pile-up events. Such an experimental validation of the method is needed in any case, and requires optimisation of the VHDL code (for instance with regards to timing and resource usage).

The hit rate in the detector was estimated from the PandaRoot simulation, where a low-energy threshold of 1 MeV was placed on the energy deposition in the cell. If one would include contributions at even lower energies, the hit rate would increase — at high luminosity the resulting rate could exceed 1 MHz. A more thorough study of the effect of such low-energy pileup would have to be performed, but also here the OF-based method described here could prove useful, since it is possible to tread such low-energy pile-up events as noise in the OF by incorporating information about their probability in the covariance matrix used in the filter construction.

The method used to evaluate the performance of the method in PANDA (Sec. 12.3) should be seen as a first approximation. In order to fully evaluate the method, and compare it with other feature-extraction methods, it should be incorporated into a time-based simulation of the PANDA experiment [79]. Among the effects that are not included in the present study is the probability for multiple pile-ups, i. e. when more than two pulses arrive so close to each others that they form a single pile-up event.

The method proposed here could be of more general interest to the radiation-detection community — especially for applications using a free-running trigger system similar to the one in PANDA. Since it has been developed both to run in real time and to enable fitting a known pulse shape to the incoming data, it provides a middle way between basic digital algorithms and analysis methods requiring offline analysis of acquired waveforms. The method does not rely on a specific detector pulse shape (such as one having a simple exponential decay), and so may be applied to shaped signals of different types as well.

Sammanfattning på svenska

Sedan mitten av 1950-talet har den så kallade standardmodellen inom partikelfysik vuxit fram som en väl testad modell för hur materiens minsta beståndsdelar fungerar och växelverkar med varandra. Denna utveckling har varit möjlig genom en kombination av experimentella mätningar och utveckling av mer och mer förfinade teoretiska modeller. Denna forskning är till sin natur grundforskning och drivs framåt av en nyfikenhet över hur världen fungerar, men samtidigt kräver de allt mer detaljerade experimenten och modellerna ofta utveckling av metoder och verktyg som ligger i teknologins framkant.

Denna avhandling är ett resultat av forskning gjord inom ramen för PANDA, ett acceleratorbaserat experiment som håller på att utvecklas som en del av FAIR (Facility for Antiproton and Ion Research) i Darmstadt, Tyskland. PANDA kommer att möjliggöra detaljerade studier av en av de grundläggande växelverkningarna i standardmodellen: den starka växelverkan. Denna verkar på längdskalor av storleksordningen femtometer (10^{-15} eller 0.000000000000001 meter) och binder samman kvarkar, som är bland de minsta partiklarna i standardmodellen. Partiklar bestående av sammanbundna kvarkar kallas för hadroner, en kategori av partiklar som inkluderar protonen och neutronen vilka utgör atomkärnor. Genom att studera den starka växelverkan kan man således öka vår förståelse för hur protoner, neutroner och atomkärnor fungerar.

På grund av speciella egenskaper hos den starka växelverkan är det väldigt svårt att teoretiskt beskriva hur den fungerar i en hadron. De modeller som nu utvecklas behöver valideras med hjälp av experimentella mätningar av dessa partiklar. Den gren av fysiken som rör dessa studier — både teoretiska och experimentella — kallas för hadronfysik och befinner sig i gränslandet mellan partikelfysik och kärnfysik.

För att studera partiklar på femtometerskalan krävs höga energier — så höga att man kan slå sönder partiklarna och studera resultatet. I PANDA kommer en accelererad stråle av antiprotoner med en rörelsemängd mellan 1.5 och 15 GeV/c att interagera i ett fast mål. Då antiprotonerna interagerar med protonerna eller atomkärnorna i detta mål kan olika typer av partiklar skapas. Flera av de möjliga reaktionsprodukterna kan ge viktig information om hur den starka växelverkan fungerar, och för att studera dessa behövs ett avancerat system av partikeldetektorer placerade runt interaktionspunkten. Detta system består av flera olika detektorer som är specialiserade på olika uppgifter: vissa kan spåra partiklars bana från interaktionspunkten, vissa kan mäta tiden det tar för en partikel att röra sig genom detektorsystemet och vissa kan mäta partiklars energi.

En detektor som är konstruerad för att noggrant mäta en partikels energi kallas för en kalorimeter, och den är konstruerad för att så effektivt som möjligt bromsa upp den inkommande partikeln så att denna helst lämnar all sin energi i detektorns volym. När en partikel med hög energi träffar ett material skapas en skur av partiklar, som illustrerat på omslaget till denna avhandling. Med en kalorimeter vill man alltså "fånga" så mycket som möjligt av denna skur. I PANDA kommer elektromagnetiska kalorimetrar (*electromagnetic calorimeters*, EMCs) att installeras, vilka syftar till att mäta energin hos fotoner (γ), elektroner (e^-) och positroner (e^+). Två typer av EMC:er kommer att användas: en bestående av drygt 16 000 $PbWO_4$-kristaller och en så kallad shashlyk-EMC bestående av drygt 1 500 detektorelement. Denna avhandling handlar om utveckling för elektroniken som ska användas för att läsa ut signalerna från dessa detektorer.

En av de stora utmaningarna inom acceleratorbaserade experiment idag är de stora datamängderna från detektorsystemen. I PANDA kommer antiprotoner att interagera i målet upp till 20 miljoner gånger per sekund, och om alla resulterande detektorsignaler skulle läsas ut direkt skulle 200 GB data per sekund behöva behandlas. Detta är inte rimligt, och för att minska datamängden utan att förlora händelser som kan vittna om intressant fysik behöver elektroniken som kopplas till detektorerna kunna bedöma vilka signaler som verkar intressanta och ska sparas. För kalorimetrarna utgörs det första steget i denna kedja av *front-end digitisers* — elektroniska moduler placerade nära detektorn som både digitaliserar och analyserar detektorsignalerna i realtid. Denna signalbehandling kommer att utföras av FPGA:er (*field-programmable gate array*), vilka är integrerade kretsar optimerade för att utföra parallella beräkningar i hög hastighet. Dessa FPGA:er kommer på grund av placeringen i experimentet att utsättas för höga doser av joniserande strålning (till exempel bestående av protoner och neutroner) vilken kan orsaka fel i FPGA:erna. Dessutom kommer signalerna som behöver analyseras komma med väldigt hög frekvens (flera hundra tusen signaler per sekund).

I kapitel 5–8 av avhandlingen beskrivs en undersökning av risken för *single event upsets* (SEUs) — förändringar i FPGA:ns minne orsakade av joniserande strålning. Detta har studerats genom experiment där FPGA:n har bestrålats med protoner och neutroner med olika energier, och för att ge ökad insikt i hur SEU-risken beror på den inkommande partikelns energi har teoretiska modeller för SEU:er utvecklats. Dessa modeller har kombinerats med data från de experimentella mätningarna för att göra det möjligt att förutsäga hur ofta SEU:er kan inträffa i PANDA. Resultaten, som presenteras i kapitel 8, visar att man i värsta fall kan förvänta sig ett SEU var sjuttonde minut i den del av EMC:n som undersökts.

I kapitel 9–12 av avhandlingen beskrivs utvecklingen av en FPGA-baserad algoritm för behandling av signalerna från shashlyk-kalorimetern i PANDA. Som ett första steg i detta arbete har en detaljerad modell av kalorimeterns respons då den träffas av fotoner utvecklats. Denna modell gör det möjligt att simulera realistiska detektorsignaler, vilka kan användas för att testa prestandan hos algoritmer för signalbehandling. En algoritm som kan köras av en FPGA har utvecklats, och denna gör det dels möjligt att noggrant bestämma signalers höjd och ankomsttid, men också att rekonstruera dessa parametrar för överlappande signaler (så kallade *pile-ups*). Pile-up är en direkt följd av den höga interaktionsfrekvensen i PANDA, och den metod som beskrivs här gör det möjligt för detektorn att fungera under dessa förhållanden utan avsevärd minskning i effektivitet. Resultaten från denna del av avhandlingen presenteras i kapitel 12.

References

[1] PANDA Collaboration, "Physics Performance Report for PANDA: Strong Interaction Studies with Antiprotons," 2009, arXiv:0903.3905 [hep-ex].

[2] GSI, "An international accelerator facility for beams of ions and antiprotons," conceptual design report, Darmstadt, Nov. 2001.

[3] M. Tanabashi *et al.* (Particle Data Group), "The Review of Particle Physics," *Phys. Rev. D*, vol. 98, p. 030001, 2018 and 2019 update, https://doi.org/10.1103/PhysRevD.98.030001.

[4] K. G. Wilson, "Confinement of quarks," *Phys. Rev. D*, vol. 10, no. 8, pp. 2445–2459, Oct. 1974, https://doi.org/10.1103/PhysRevD.10.2445.

[5] D. J. Gross and F. Wilczek, "Ultraviolet Behavior of Non-Abelian Gauge Theories," *Phys. Rev. Lett.*, vol. 30, no. 26, pp. 1343–1346, June 1973, https://doi.org/10.1103/PhysRevLett.30.1343.

[6] H. D. Politzer, "Reliable Perturbative Results for Strong Interactions?" *Phys. Rev. Lett.*, vol. 30, no. 26, pp. 1346–1349, June 1973, https://doi.org/10.1103/PhysRevLett.30.1346.

[7] C. Gignoux, B. Silvestre-Brac, and J. M. Richard, "Possibility of stable multiquark baryons," *Phys. Lett. B*, vol. 193, no. 2–3, pp. 323–326, July 1987, https://doi.org/10.1016/0370-2693(87)91244-5.

[8] H. J. Lipkin, "New possibilities for exotic hadrons — anticharmed strange baryons," *Phys. Lett. B*, vol. 195, no. 3, pp. 484–488, Sept. 1987, https://doi.org/10.1016/0370-2693(87)90055-4.

[9] H. Fritzsch and P. Minkowski, "Ψ-resonances, gluons and the Zweig rule," *Nuov. Cim. A*, vol. 30, no. 3, pp. 393–429, 1975, https://doi.org/10.1007/BF02730295.

[10] C. Gattringer and C. B. Lang, *Quantum Chromodynamics on the Lattice*, ser. Lect. Notes Phys. 788. Springer, Berlin Heidelberg, Germany, 2010, https://doi.org/10.1007/978-3-642-01850-3.

[11] P. F. Bedaque and U. van Kolck, "Effective Field Theory for Few-Nucleon Systems," *Ann. Rev. Nucl. Part. Sci.*, vol. 52, pp. 339–396, Dec. 2002, https://doi.org/10.1146/annurev.nucl.52.050102.090637.

[12] B. Aubert *et al.* (BABAR Collaboration), "The BABAR detector," *Nucl. Instrum. Methods Phys. Res. A*, vol. 479, no. 1, pp. 1–116, Feb. 2002, https://doi.org/10.1016/S0168-9002(01)02012-5.

[13] T. Abe *et al.* (Belle II Collaboration), "Belle II Technical Design Report," 2010, arXiv:1011.0352 [physics.ins-det].

[14] D. M. Asner *et al.* (BES-III Collaboration), "Physics at BES-III," 2008, arXiv:0809.1869 [hep-ex].

[15] J.-E. Augustin *et al.*, "Discovery of a Narrow Resonance in e^+e^- Annihilation," *Phys. Rev. Lett.*, vol. 33, no. 23, pp. 1406–1408, Dec. 1974, https://doi.org/10.1103/PhysRevLett.33.1406.

[16] J. J. Aubert *et al.*, "Experimental Observation of a Heavy Particle J," *Phys. Rev. Lett.*, vol. 33, no. 23, pp. 1405–1406, Dec. 1974, https://doi.org/10.1103/PhysRevLett.33.1404.

[17] T. Barnes, S. Godfrey, and E. S. Swanson, "Higher charmonia," *Phys. Rev. D*, vol. 72, no. 5, p. 054026, Sept. 2005, https://doi.org/10.1103/PhysRevD.72.054026.

[18] S.-K. Choi *et al.* (Belle Collaboration), "Observation of a Narrow Charmoniumlike State in Exclusive $B^{\pm} \rightarrow K^{\pm}\pi^{+}\pi^{-}J/\psi$ Decays," *Phys. Rev. Lett.*, vol. 91, no. 26, p. 262001, Dec. 2003, https://doi.org/10.1103/PhysRevLett.91.262001.

[19] T. Barnes and S. Godfrey, "Charmonium options for the X(3872)," *Phys. Rev. D*, vol. 69, no. 5, p. 054008, Mar. 2004, https://doi.org/10.1103/PhysRevD.69.054008.

[20] Y.-R. Liu, H.-X. Chen, W. Chen, X. Liu, and S.-L. Zhu, "Pentaquark and Tetraquark States," *Prog. Part. Nucl. Phys.*, vol. 107, pp. 237–320, July 2019, https://doi.org/10.1016/j.ppnp.2019.04.003.

[21] K. K. Seth, "The quintessential exotic X(3872)," *Prog. Part. Nucl. Phys.*, vol. 67, no. 2, pp. 390–394, Apr. 2012, https://doi.org/10.1016/j.ppnp.2011.12.049.

[22] G. Barucca *et al.* (PANDA Collaboration), "Precision resonance energy scans with the PANDA experiment at FAIR," *Eur. Phys. J. A*, vol. 55, no. 42, 2019, https://doi.org/10.1140/epja/i2019-12718-2.

[23] PANDA Collaboration, "Technical Design Report for PANDA Electromagnetic Calorimeter (EMC)," 2008, arXiv:0810.1216 [physics.ins-det].

[24] FAIR — Facility for Antiproton and Ion Research, "Official Website," 2020, [Online] Available: https://fair-center.eu/ [2 March 2020].

[25] A. Dolinskii *et al.*, "Antiproton complex at the FAIR project," *Nucl. Instrum. Methods Phys. Res. A*, vol. 629, no. 1, pp. 16–24, Feb. 2011, https://doi.org/10.1016/j.nima.2010.11.037.

[26] O. Kester *et al.*, "The Accelerator Facility of the Facility for Antiproton and Ion Research," in *6th International Particle Accelerator Conference (IPAC2015)*, 2015, pp. 1343–1345, https://doi.org/10.18429/JACoW-IPAC2015-TUBB2.

[27] C. Böhme *et al.*, "Status Overview of the HESR Beam Instrumentation," in *7th International Beam Instrumentation Conference*, 2018, pp. 26–28, https://doi.org/10.18429/JACoW-IBIC2018-MOPA01.

[28] Q. Hu *et al.*, "A recoil detector for the measurement of antiproton-proton elastic scattering at angles close to 90°," *Eur. Phys. J. A*, vol. 50, no. 156, 2014, https://doi.org/10.1140/epja/i2014-14156-0.

[29] T. Stöhlker *et al.*, "SPARC: The Stored Particle Atomic Research Collaboration At FAIR," *AIP Conf. Proc.*, vol. 1336, pp. 132–137, 2011, https://doi.org/10.1063/1.3586073.

[30] PANDA Collaboration, "Internal website (RN-DET-2017-001)," 2017.

[31] H. Stockhorst, D. Prasuhn, R. Maier, and B. Lorentz, "Cooling Scenario for the HESR Complex," *AIP Conf. Proc.*, vol. 821, pp. 190–195, 2006, https://doi.org/10.1063/1.2190110.

[32] A. Lehrach *et al.*, "Beam Dynamics Studies for the High-Energy Storage Ring," *Int. J. Mod. Phys. E*, vol. 18, pp. 420–429, 2009, https://doi.org/10.1142/S021830130901246X.

[33] PANDA Collaboration, "Technical Design Report for the PANDA Solenoid and Dipole Spectrometer Magnets," 2009, arXiv:0907.0169 [physics.ins-det].

[34] PANDA Collaboration, "Technical Design Report for the PANDA Internal Targets," 2012, [Online] Available: https://fair-center.eu/fileadmin/fair/publications_exp/PANDA_Targets_TDR.pdf [27 April 2018].

[35] A. Khoukaz, "Internal targets for the PANDA experiment," in *8th International Conference on Nuclear Physics at Storage Rings*, 2011, https://doi.org/10.22323/1.150.0036.

[36] T. H. Randriamalala, "Conceptual Design of the PANDA Luminosity Monitor and Reconstruction Strategy to Measure the Width of the X(3872) State," Ph.D. dissertation, Ruhr-Universität Bochum, Bochum, Germany, 2011.

[37] PANDA Collaboration, "Technical Design Report for the: PANDA Micro Vertex Detector," 2012, arXiv:1207.6581 [physics.ins-det].

[38] PANDA Collaboration, "Technical Design Report for the: PANDA Straw Tube Tracker," 2012, arXiv:1205.5441 [physics.ins-det].

[39] D. Melnychuk, B. Voss, and B. Zwieglinski, "Study of resolution of the PANDA GEM detector with Garfield," *Hyperfine Interact.*, vol. 229, pp. 165–168, 2014, https://doi.org/10.1007/s10751-014-1066-z.

[40] PANDA Collaboration, "Technical Design Report for the PANDA Barrel DIRC Detector," 2017, arXiv:1710.00684 [physics.ins-det].

[41] M. Düren *et al.*, "The Endcap Disc DIRC of PANDA," *Nucl. Instrum. Methods Phys. Res. A*, vol. 876, pp. 198–201, Dec. 2017, https://doi.org/10.1016/j.nima.2017.02.077.

[42] L. Gruber, S. E. Brunner, J. Marton, H. Orth, and K. Suzuki, "Barrel time-of-flight detector for the PANDA experiment at FAIR," *Nucl. Instrum. Methods Phys. Res. A*, vol. 824, pp. 104–105, July 2016, https://doi.org/10.1016/j.nima.2015.10.108.

[43] PANDA Collaboration, "Technical Design Report for the: PANDA Muon System," 2012, [Online] Available: https://fair-center.eu/fileadmin/fair/publications_exp/Muon_TDR.pdf [27 April 2018].

[44] A. Gal, E. V. Hungerford, and D. J. Millener, "Strangeness in nuclear physics," *Rev. Mod. Phys.*, vol. 88, no. 3, p. 035004, Jul.–Sept. 2016, https://doi.org/10.1103/RevModPhys.88.035004.

[45] A. Sanchez Lorente, "Hypernuclear physics studies of the PANDA experiment at FAIR," *Hyperfine Interact.*, vol. 229, pp. 45–51, 2014, https://doi.org/10.1007/s10751-014-1076-x.

[46] J. Smyrski *et al.*, "Design of the forward straw tube tracker for the PANDA experiment," *J. Instrum.*, vol. 12, p. C06032, June 2017, https://doi.org/10.1088/1748-0221/12/06/C06032.

[47] J. Smyrski, "Overview of the PANDA Experiment," *Phys. Procedia*, vol. 37, pp. 85–95, 2012, https://doi.org/10.1016/j.phpro.2012.02.359.

[48] PANDA Collaboration, "Technical Design Report for the Panda Forward Spectrometer Calorimeter," 2017, arXiv:1704.02713 [physics.ins-det].

[49] M. Tiemens, "A Triggerless readout system for the PANDA electromagnetic calorimeter," *J. Phys.: Conf. Ser.*, vol. 587, p. 012025, 2015, https://doi.org/10.1088/1742-6596/587/1/012025.

[50] J. Zhao *et al.*, "New version of high performance Compute Node for PANDA Streaming DAQ system," 2018, arXiv:1806.09128 [physics.ins-det].

[51] PANDA Collaboration, "Technical Progress Report for PANDA," 2005, [Online] Available: https://panda.gsi.de/oldwww/html/reports.php [22 January 2020].

[52] I. Konorov, H. Angerer, A. Mann, and S. Paul, "SODA: Time distribution system for the PANDA experiment," *2009 IEEE Nuclear Science Symposium Conference Record (NSS/MIC)*, pp. 1863–1865, 2009, https://doi.org/10.1109/NSSMIC.2009.5402172.

[53] K. Korcyl, I. Konorov, W. Kühn, and L. Schmitt, "Modeling event building architecture for the triggerless data acquisition system for PANDA experiment at the HESR facility at FAIR/GSI," *International Conference on Computing in High Energy and Nuclear Physics 2012 (CHEP2012)*, p. 012027, 2012, https://doi.org/10.1088/1742-6596/396/1/012027.

[54] W. Kühn *et al.*, "FPGA based Compute Nodes for High Level Triggering in PANDA," *International Conference on Computing in High Energy and Nuclear Physics (CHEP'07)*, p. 022027, 2007, https://doi.org/10.1088/1742-6596/119/2/022027.

[55] R. Wigmans, *Calorimetry: Energy Measurement in Particle Physics*, 2nd ed. Oxford University Press, Oxford, UK, 2017, p. 1.

[56] D. M. Storm, "Silicon Luminosity Monitors," in *Calorimetry in High Energy Physics — Proceedings of the Third International Conference*, P. Hale and J. Siegrist, Eds., 1992, https://doi.org/10.1142/1944.

[57] C. M. C. Calame, C. Lunardini, G. Montagna, O. Nicrosini, and F. Piccinini, "Large-angle Bhabha scattering and luminosity at flavour factories," *Nucl. Phys. B*, vol. 584, no. 1–2, pp. 459–479, Sept. 2000, https://doi.org/10.1016/S0550-3213(00)00356-4.

[58] C. Grupen and B. A. Schwartz, *Particle Detectors*, 2nd ed. Cambridge University Press, Cambridge, UK, 2008, pp. 19–22, https://doi.org/10.1017/CBO9780511534966.

[59] M. J. Berger, J. S. Coursey, M. A. Zucker, and J. Chang, "ESTAR, PSTAR, and ASTAR: Computer Programs for Calculating Stopping-Power and Range Tables for Electrons, Protons, and Helium Ions (version 1.2.3)," 2005, [Online] Available: http://physics.nist.gov/Star [30 April 2018]. National Institute of Standards and Technology, Gaithersburg, MD, USA.

[60] M. J. Berger *et al.*, "XCOM: Photon Cross Section Database (version 1.5)," 2010, [Online] Available: http://physics.nist.gov/xcom [30 April 2018]. National Institute of Standards and Technology, Gaithersburg, MD, USA.

[61] C. Schaerf, "Polarized Gamma-Ray Beams," *Phys. Today*, vol. 58, no. 8, pp. 44–50, Aug. 2005, https://doi.org/10.1063/1.2062918.

[62] H. Paetz gen. Schieck, *Nuclear Reactions: An Introduction*, ser. Lecture Notes in Physics. Springer-Verlag, Berlin, Germany, 2014, vol. 882, https://doi.org/10.1007/978-3-642-53986-2.

[63] K. S. Krane, *Introductory Nuclear Physics*. John Wiley & Sons, Inc., New York, USA, 1988, p. 419.

[64] S. K. L. Sjue, "Two-Body Kinematics Calculator and Plotter," 2010, [Online] Available: http://skisickness.com/2010/04/relativistic-kinematics-calculator/ [30 April 2018].

[65] C. W. Fabjan and T. Ludlam, "Calorimetry in High-Energy Physics," *Ann. Rev. Nucl. Part. Sci.*, vol. 32, pp. 335–389, Dec. 1982, https://doi.org/10.1146/annurev.ns.32.120182.002003.

[66] C. Grupen and B. A. Schwartz, *Particle Detectors*, 2nd ed. Cambridge University Press, Cambridge, UK, 2008, p. 237, https://doi.org/10.1017/CBO9780511534966.

[67] PANDA Collaboration, "The PANDA Detector — Integration," [Online] Available: https://panda.gsi.de/oldwww/framework/det_iframe.php?section=Integration [22 January 2020].

[68] C. Biino, "The CMS Electromagnetic Calorimeter: overview, lessons learned during Run 1 and future projections," *J. Phys.: Conf. Ser.*, vol. 587, p. 012001, 2014, https://doi.org/10.1088/1742-6596/587/1/012001.

[69] P. Wieczorek and H. Flemming, "Low noise preamplifier ASIC for the PANDA EMC," in *IEEE Nuclear Science Symposium & Medical Imaging Conference*, 2010, https://doi.org/10.1109/NSSMIC.2010.5873982.

[70] I. Keshelashvili, W. Erni, F. Müller, M. Steinacher, and B. Krusche, "Development of Low-Noise / Low-Power Preamplifier for the Readout of Inorganic Scintillators and their Mass Production Test System," *J. Phys.: Conf. Ser.*, vol. 587, p. 012024, 2015, https://doi.org/10.1088/1742-6596/587/1/012024.

[71] G. S. Atoyan *et al.*, "Lead-scintillator electromagnetic calorimeter with wavelength shifting fiber readout," *Nucl. Instrum. Methods Phys. Res. A*, vol. 320, no. 1–3, pp. 144–154, Aug. 1992, https://doi.org/10.1016/0168-9002(92)90773-W.

[72] G. David *et al.*, "Performance of the PHENIX EM Calorimeter," *IEEE Trans. Nucl. Sci.*, vol. 43, no. 3, pp. 1491–1495, June 1996, https://doi.org/10.1109/23.507090.

[73] G. Avoni *et al.* (HERA-B ECAL Collaboration), "The electromagnetic calorimeter of the HERA-B experiment," *Nucl. Instrum. Methods Phys. Res. A*, vol. 461, no. 1–3, pp. 332–336, Apr. 2001, https://doi.org/10.1016/S0168-9002(00)01237-7.

[74] I. Machikhiliyan (LHCb Calorimeter Group), "The LHCb electromagnetic calorimeter," *J. Phys.: Conf. Ser.*, vol. 160, p. 012047, 2009, https://doi.org/10.1088/1742-6596/1162/1/012026.

[75] N. Anfimov *et al.*, "Shashlyk EM calorimeter prototype readout by MAPD with superhigh pixel density for COMPASS II," *Nucl. Instrum. Methods Phys. Res. A*, vol. 718, pp. 75–77, Aug. 2013, https://doi.org/10.1016/j.nima.2012.11.104.

[76] G. S. Atoian, V. V. Issakov, O. V. Karavichev, T. L. Karavicheva, A. A. Poblaguev, and M. E. Zeller, "Development of Shashlyk calorimeter for KOPIO," *Nucl. Instrum. Methods Phys. Res. A*, vol. 531, no. 3, pp. 467–480, Oct. 2004, https://doi.org/10.1016/j.nima.2004.05.094.

[77] DuPont de Nemours, Inc., "Tyvek — Product Website," 2020, [Online] Available: https://www.dupont.com/brands/tyvek.html [26 February 2020].

[78] Hamamatsu, "Photomultiplier tube R7899," [Online] Available: https://www.hamamatsu.com/us/en/product/type/R7899/index.html [23 January 2020].

[79] M. Tiemens, "Online cluster-finding algorithms for the PANDA electromagnetic calorimeter," Ph.D. dissertation, Rijksuniversiteit Groningen, Groningen, the Netherlands, 2017.

[80] P. Marciniewski, "private communication," 2017.

[81] Analog Devices, Inc., "LTM9009-14 Datasheet and Product Info," 2020, [Online] Available: https://www.analog.com/en/products/ltm9009-14.html [5 March 2020].

[82] Xilinx, "7 Series FPGAs Data Sheet: Overview, DS180 (v2.6)," p. 1, 2018, [Online] Available: https://www.xilinx.com/support/documentation/data_sheets/ds180_7Series_Overview.pdf [30 April 2018].

[83] M. Kavatsyuk *et al.*, "Trigger-less readout system with pulse pile-up recovery for the PANDA electromagnetic calorimeter," *Nucl. Instrum. Methods Phys. Res. A*, vol. 718, pp. 217–219, Aug. 2013, https://doi.org/10.1016/j.nima.2012.10.007.

[84] Xilinx, "7 Series FPGAs Data Sheet: Overview, DS180 (v2.6)," p. 13, 2018, [Online] Available: https://www.xilinx.com/support/documentation/data_sheets/ds180_7Series_Overview.pdf [30 April 2018].

[85] T. S. Nidhin, A. Bhattacharyya, R. P. Behera, and T. Jayanthi, "A Review on SEU Mitigation Techniques for FPGA Configuration Memory," *IETE Tech. Rev.*, vol. 35, no. 2, pp. 1–12, 2017, https://doi.org/10.1080/02564602.2016.1265905.

[86] P. Hofmann, *Solid State Physics*, 2nd ed. Wiley-VCH, Weinheim, Germany, 2015, p. 148.

[87] Xilinx, "7 Series FPGAs Configuration User Guide, UG470 (v1.13)," p. 107, 2018, [Online] Available: https://www.xilinx.com/support/documentation/user_guides/ug470_7Series_Config.pdf [30 April 2018].

[88] R. Giordano, S. Perrella, V. Izzo, G. Milluzzo, and A. Aloisio, "Redundant-Configuration Scrubbing of SRAM-Based FPGAs," *IEEE Trans. Nucl. Sci.*, vol. 64, no. 9, pp. 2497–2504, Sept. 2017, https://doi.org/10.1109/TNS.2017.2730960.

[89] H. Hughes, "Historical Perspective," in *Ionizing Radiation Effects in MOS Devices and Circuits*, T. P. Ma and P. V. Dressendorfer, Eds. John Wiley & Sons, Inc., New York, USA, 1989, pp. 47–48.

[90] J. F. Ziegler, "Stopping and Range of Ions in Matter," 2008, [Online] Available: http://www.srim.org/ [30 April 2018].

[91] E. Petersen, *Single Event Effects in Aerospace*. John Wiley & Sons, Inc., Hoboken, New Jersey, USA, 2011, p. 307.

[92] P. E. Dodd and L. W. Massengill, "Basic Mechanisms and Modeling of Single-Event Upset in Digital Microelectronics," *IEEE Trans. Nucl. Sci.*, vol. 50, no. 3, pp. 583–602, June 2003, https://doi.org/10.1109/TNS.2003.813129.

[93] R. Baumann, "Soft Errors in Advanced Computer Systems," *IEEE Des. Test. Comput*, vol. 22, no. 3, pp. 258–266, May–June 2005, https://doi.org/10.1109/MDT.2005.69.

[94] S. Selberherr, *Analysis and Simulation of Semiconductor Devices*. Springer-Verlag, Vienna, Austria, 1984, p. 16, https://doi.org/10.1007/978-3-7091-8752-4.

[95] L. W. Massengill, B. L. Bhuva, W. T. Holman, M. L. Alles, and T. D. Loveless, "Technology scaling and soft error reliability," in *IEEE International Reliability Physics Symposium*, 2012, https://doi.org/10.1109/IRPS.2012.6241810.

[96] B. D. Sierawski *et al.*, "Effects of scaling on muon-induced soft errors," in *IEEE International Reliability Physics Symposium*, 2011, https://doi.org/10.1109/IRPS.2011.5784484.

[97] E. Petersen, *Single Event Effects in Aerospace*. John Wiley & Sons, Inc., Hoboken, New Jersey, USA, 2011, pp. 226–227.

[98] M. J. Wirthlin, H. Takai, and A. Harding, "Soft error rate estimations of the Kintex-7 FPGA within the ATLAS Liquid Argon (LAr) Calorimeter," *J. Instrum.*, vol. 9, p. C01025, 2014, https://doi.org/10.1088/1748-0221/9/01/C01025.

[99] JEDEC Solid State Technology Association, "Measurement and Reporting of Alpha Particle and Terrestrial Cosmic Ray-Induced Soft Errors in Semiconductor Devices (JESD89)," p. 33, 2012, [Online] Available: https://www.jedec.org [30 April 2018].

[100] P. E. Dodd, M. R. Shaneyfelt, and F. W. Sexton, "Charge Collection and SEU from Angled Ion Strikes," *IEEE Trans. Nucl. Sci.*, vol. 44, no. 6, pp. 2256–2265, Dec. 1997, https://doi.org/10.1109/23.659044.

[101] Xilinx, "Soft Error Mitigation Controller v4.1, PG036," 2018, [Online] Available: https://www.xilinx.com/support/documentation/ip_documentation/sem/v4_1/pg036_sem.pdf [30 April 2018].

[102] E. R. van der Graaf *et al.*, "AGORFIRM, the AGOR facility for irradiations of materials," in *European Conference on Radiation and Its Effects on Components and Systems*, 2009, https://doi.org/10.1109/RADECS.2009.5994694.

[103] KVI — Center for Advanced Radiation Technology, "AGORFIRM specifications," 2018, [Online] Available: https://www.rug.nl/kvi-cart/research/facilities/agor/agorfirm/agor-specifications [30 April 2018].

[104] A. V. Prokofiev, "Characterization of the ANITA Neutron Source for Accelerated SEE Testing at the Svedberg Laboratory," in *IEEE Radiation Effects Data Workshop*, 2009, https://doi.org/10.1109/REDW.2009.5336295.

[105] JEDEC Solid State Technology Association, "Measurement and Reporting of Alpha Particle and Terrestrial Cosmic Ray-Induced Soft Errors in Semiconductor Devices (JESD89)," p. 42, 2012, [Online] Available: https://www.jedec.org [30 April 2018].

[106] K. W. Geiger and L. van der Zwan, "Radioactive neutron source spectra from ^{9}Be(α, n) cross section data," *Nucl. Instrum. Methods*, vol. 131, no. 2, pp. 315–321, Dec. 1975, https://doi.org/10.1016/0029-554X(75)90336-5.

[107] B. Lindell and P. Reizenstein, "A Swedish building material for low-radioactivity laboratories," *Arkiv för Fysik*, vol. 26, no. 5, pp. 65–74, 1964.

[108] International Atomic Energy Agency, "Evaluated Nuclear Data File," [Online] Available: https://www-nds.iaea.org/exfor/endf.htm [30 April 2018].

[109] M. J. Gadlage, A. H. Roach, A. R. Duncan, M. W. Savage, and M. J. Kay, "Electron-Induced Single-Event Upsets in 45-nm and 28-nm Bulk CMOS SRAM-Based FPGAs Operating at Nominal Voltage," *IEEE Trans. Nucl. Sci.*, vol. 62, no. 6, pp. 2717–2724, Dec. 2015, https://doi.org/10.1109/TNS.2015.2491220.

[110] P. Caron *et al.*, "Physical mechanisms inducing electron Single Event Upset," *IEEE Trans. Nucl. Sci.*, vol. 65, no. 8, pp. 1759–1767, Aug. 2018, https://doi.org/10.1109/TNS.2018.2819421.

[111] Joint Committee for Guides in Metrology, "Evaluation of measurement data — Supplement 1 to the "Guide to the expression of uncertainty in measurement" — Propagation of distributions using a Monte Carlo method," 2008, [Online] Available: https://www.bipm.org/en/publications/guides/gum.html [30 April 2018].

[112] V. M. Placinta and L. N. Cojocariu, "Radiation Hardness Studies and Evaluation of SRAM-Based FPGAs for High Energy Physics Experiments," in *Topical Workshop on Electronics for Particle Physics*, 2017, https://doi.org/10.22323/1.313.0085.

[113] P. Maillard, M. Hart, J. Barton, P. Jain, and J. Karp, "Neutron, 64 MeV Proton, Thermal Neutron and Alpha Single-Event Upset Characterization of Xilinx 20nm UltraScale Kintex FPGA," in *IEEE Radiation Effects Data Workshop*, 2015, https://doi.org/10.1109/REDW.2015.7336723.

[114] D. M. Hiemstra and V. Kirischian, "Single Event Upset Characterization of the Kintex-7 Field Programmable Gate Array Using Proton Irradiation," in *IEEE Radiation Effects Data Workshop*, 2014, https://doi.org/10.1109/REDW.2014.7004593.

[115] K. M. Sielewicz *et al.*, "Experimental Methods and Results for the Evaluation of Triple Modular Redundancy SEU Mitigation Techniques with the Xilinx Kintex-7 FPGA," in *IEEE Radiation Effects Data Workshop*, 2017, https://doi.org/10.1109/NSREC.2017.8115451.

[116] R. A. Weller *et al.*, "Monte Carlo Simulation of Single Event Effects," *IEEE Trans. Nucl. Sci.*, vol. 57, no. 4, pp. 1726–1746, Aug. 2010, https://doi.org/10.1109/TNS.2010.2044807.

[117] R. A. Reed *et al.*, "Anthology of the Development of Radiation Transport Tools as Applied to Single Event Effects," *IEEE Trans. Nucl. Sci.*, vol. 60, no. 3, pp. 1876–1911, June 2013, https://doi.org/10.1109/TNS.2013.2262101.

[118] R. A. Reed *et al.*, "Physical Processes and Applications of the Monte Carlo Radiative Energy Deposition (MRED) Code," *IEEE Trans. Nucl. Sci.*, vol. 62, no. 4, pp. 1441–1461, Aug. 2015, https://doi.org/10.1109/TNS.2015.2454446.

[119] R. L. Woodruff and P. J. Rudeck, "Three-dimensional numerical simulation of single event upset of an SRAM cell," *IEEE Trans. Nucl. Sci.*, vol. 40, no. 6, pp. 1795–1803, Dec. 1993, https://doi.org/10.1109/23.273477.

[120] Y. Boulghassoul *et al.*, "Circuit modeling of the LM124 operational amplifier for analog single-event transient analysis," *IEEE Trans. Nucl. Sci.*, vol. 49, no. 6, pp. 3090–3096, Dec. 2002, https://doi.org/10.1109/TNS.2002.805400.

[121] G. Hubert, S. Duzellier, C. Inguimbert, C. Boatella-Polo, F. Bezerra, and R. Ecoffet, "Operational SER Calculations on the SAC-C Orbit Using the Multi-Scales Single Event Phenomena Predictive Platform (MUSCA SEP^3)," *IEEE Trans. Nucl. Sci.*, vol. 56, no. 6, pp. 3032–3042, Dec. 2009, https://doi.org/10.1109/TNS.2009.2034148.

[122] P. Roche, G. Gasiot, J.-L. Autran, D. Munteanu, R. A. Reed, and R. A. Weller, "Application of the TIARA Radiation Transport Tool to Single Event Effects Simulation," *IEEE Trans. Nucl. Sci.*, vol. 61, no. 3, pp. 1498–1500, June 2014, https://doi.org/10.1109/TNS.2014.2318778.

[123] E. Petersen, *Single Event Effects in Aerospace*. John Wiley & Sons, Inc., Hoboken, New Jersey, USA, 2011, p. 61.

[124] K. M. Warren, "Sensitive Volume models for Single Event upset analysis and rate prediction for space, atmospheric, and terrestrial radiation environments," Ph.D. dissertation, Faculty of the Graduate School, Vanderbilt University, Nashville, USA, 2010.

[125] J. N. Bradford, "Geometric analysis of soft errors and oxide damage produced by heavy cosmic rays and alpha particles," *IEEE Trans. Nucl. Sci.*, vol. NS-27, no. 1, pp. 941–947, Feb. 1980, https://doi.org/10.1109/TNS.1980.4330955.

[126] J. C. Pickel and J. T. Blandford, "Cosmic-Ray-Induced Errors in MOS Devices," *IEEE Trans. Nucl. Sci.*, vol. NS-27, no. 2, pp. 1006–1015, Apr. 1980, https://doi.org/10.1109/TNS.1980.4330967.

[127] E. L. Petersen and J. B. Langworthy, "Suggested single event upset figure of merit," *IEEE Trans. Nucl. Sci.*, vol. NS-30, no. 6, pp. 4533–4539, Dec. 1983, https://doi.org/10.1109/TNS.1983.4333166.

[128] E. L. Petersen, J. C. Pickel, E. C. Smith, P. J. Rudeck, and J. R. Letaw, "Geometrical Factors in SEE Rate Calculations," *IEEE Trans. Nucl. Sci.*, vol. 40, no. 6, pp. 1888–1909, Dec. 1993, https://doi.org/10.1109/23.273465.

[129] A. Tylka *et al.*, "CREME96: A revision of the cosmic ray effects on micro-electronics code," *IEEE Trans. Nucl. Sci.*, vol. 44, no. 6, pp. 2150–2160, Dec. 1997, https://doi.org/10.1109/23.659030.

[130] W. Tianqi *et al.*, "Single-Event Upset Prediction in SRAMs Account for On-Transistor Sensitive Volume," *IEEE Trans. Nucl. Sci.*, vol. 62, no. 6, pp. 3207–3215, Dec. 2015, https://doi.org/10.1109/TNS.2015.2480880.

[131] F. Wrobel, G. Hubert, and P. Iacconi, "A Semi-empirical Approach for Heavy Ion SEU Cross Section Calculations," *IEEE Trans. Nucl. Sci.*, vol. 53, no. 6, pp. 3271–3276, Dec. 2006, https://doi.org/10.1109/TNS.2006.886200.

[132] K. M. Warren *et al.*, "Predicting Thermal Neutron-Induced Soft Errors in Static Memories Using TCAD and Physics-Based Monte Carlo Simulation Tools," *IEEE Electr. Device. L.*, vol. 28, no. 2, pp. 180–182, Feb. 2007, https://doi.org/10.1109/LED.2006.889632.

[133] A. V. Sogoyan, A. I. Chumakov, and A. A. Smolin, "SEE rate estimation based on diffusion approximation of charge collection," *Nucl. Instrum. Methods Phys. Res. B*, vol. 418, pp. 87–93, Mar. 2018, https://doi.org/10.1016/j.nimb.2018.01.001.

[134] S. Agostinelli *et al.*, "GEANT4 — a simulation toolkit," *Nucl. Instrum. Methods Phys. Res. A*, vol. 506, no. 3, pp. 250–303, July 2003, https://doi.org/10.1016/S0168-9002(03)01368-8.

[135] J. Allison *et al.*, "Geant4 developments and applications," *IEEE Trans. Nucl. Sci.*, vol. 53, no. 1, pp. 270–278, Feb. 2006, https://doi.org/10.1109/TNS.2006.869826.

[136] N. H. E. Weste and D. M. Harris, *CMOS VLSI Design — A Circuits and Systems Perspective*, 4th ed. Addison-Wesley, Boston, USA, 2010, p. 520.

[137] N. H. E. Weste and D. M. Harris, *CMOS VLSI Design — A Circuits and Systems Perspective*, 4th ed. Addison-Wesley, Boston, USA, 2010, p. 505.

[138] S. Natarajan *et al.*, "A 32nm Logic Technology Featuring 2nd-Generation High-k + Metal-Gate Transistors, Enhanced Channel Strain and 0.171μm2 SRAM Cell Size in a 291Mb Array," in *IEEE International Electron Devices Meeting*, 2008, https://doi.org/10.1109/IEDM.2008.4796777.

[139] J. Allison *et al.*, "Recent developments in GEANT4," *Nucl. Instrum. Methods Phys. Res. A*, vol. 835, pp. 186–225, Nov. 2016, https://doi.org/10.1016/j.nima.2016.06.125.

[140] Geant4, "Physics Lists EM constructors in Geant4 10.4," 2020, [Online] Available: https://geant4.web.cern.ch/node/1731 [26 February 2020].

[141] D. Green, *The Physics of Particle Detectors*, 1st ed. Cambridge University Press, Cambridge, United Kingdom, 2000, p. 182.

[142] F. Paxton, "Solid Angle Calculation for a Circular Disk," *Rev. Sci. Instrum.*, vol. 30, no. 4, pp. 254–258, Apr. 1959, https://doi.org/10.1063/1.1716590.

[143] A. Gelman, J. B. Carlin, H. S. Stern, D. B. Dunson, A. Vehtari, and D. B. Rubin, *Bayesian Data Analysis*, 3rd ed. Chapman & Hall / CRC Press, 2013, p. 145.

[144] S. Spataro, "The PandaRoot framework for simulation, reconstruction and analysis," *J. Phys.: Conf. Ser.*, vol. 331, p. 032031, 2011, https://doi.org/10.1088/1742-6596/331/3/032031.

[145] A. Capella, U. Sukhatme, C.-I. Tan, and J. Tran Thanh Van, "Dual parton model," *Phys. Rep.*, vol. 236, no. 4–5, pp. 225–329, Jan. 1994, https://doi.org/10.1016/0370-1573(94)90064-7.

[146] S. Diehl, "Optimization of the Influence of Longitudinal and Lateral Non-Uniformity on the Performance of an Electromagnetic Calorimeter," Ph.D. dissertation, Justus-Liebig-Universität Gießen, Gießen, Germany, 2016.

[147] M. Nakhostin, *Signal Processing for Radiation Detectors*. John Wiley & Sons, Hoboken, NJ, USA, 2018, ch. 4.

[148] A. Georgiev and W. Gast, "Digital pulse processing in high resolution, high throughput, gamma-ray spectroscopy," *IEEE Trans. Nucl. Sci.*, vol. 40, no. 4, pp. 770–779, Aug. 1993, https://doi.org/10.1109/23.256659.

[149] V. T. Jordanov and G. F. Knoll, "Digital synthesis of pulse shapes in real time for high resolution radiation spectroscopy," *Nucl. Instrum. Methods Phys. Res. A*, vol. 345, no. 2, pp. 337–345, June 1994, https://doi.org/10.1016/0168-9002(94)91011-1.

[150] V. T. Jordanov, G. F. Knoll, A. C. Huber, and J. A. Pantazis, "Digital techniques for real-time pulse shaping in radiation measurements," *Nucl. Instrum. Methods Phys. Res. A*, vol. 353, no. 1–3, pp. 261–264, Dec. 1994, https://doi.org/10.1016/0168-9002(94)91652-7.

[151] M. Nakhostin, "Recursive Algorithms for Real-Time Digital CR-(RC)^n Pulse Shaping," *IEEE Trans. Nucl. Sci.*, vol. 58, no. 5, pp. 2378–2381, Oct. 2011, https://doi.org/10.1109/TNS.2011.2164556.

[152] G. Gerardi and L. Abbene, "A digital approach for real time high-rate high resolution radiation measurements," *Nucl. Instrum. Methods Phys. Res. A*, vol. 768, pp. 46–54, Dec. 2014, https://doi.org/10.1016/j.nima.2014.09.047.

[153] A. Di Fulvio, T. H. Shin, M. C. Hamel, and S. A. Pozzi, "Digital pulse processing for NaI(Tl) detectors," *Nucl. Instrum. Methods Phys. Res. A*, vol. 806, pp. 169–174, Jan. 2016, https://doi.org/10.1016/j.nima.2015.09.080.

[154] Y.-F. Liang, C.-W. Yang, J.-Y. Xu, and M.-M. Kang, "Applications in energy spectrum measurement based on pulse fitting," *Radiation Detection Technology and Methods*, vol. 3, p. 24, 2019, https://doi.org/10.1007/s41605-019-0096-0.

[155] W. E. Cleland and E. G. Stern, "Signal processing considerations for liquid ionization calorimeters in a high rate environment," *Nucl. Instrum. Methods Phys. Res. A*, vol. 338, no. 2–3, pp. 467–497, Jan. 1993, https://doi.org/10.1016/0168-9002(94)91332-3.

[156] E. Fullana *et al.*, "Digital Signal Reconstruction in the ATLAS Hadronic Tile Calorimeter," *IEEE Trans. Nucl. Sci.*, vol. 53, no. 4, pp. 2139–2143, Aug. 2006, https://doi.org/10.1109/TNS.2006.877267.

[157] L. Aperio Bella, "Status of the ATLAS Liquid Argon calorimeter and its performance after two years of LHC operation," *Nucl. Instrum. Methods Phys. Res. A*, vol. 718, pp. 60–62, Aug. 2013, https://doi.org/10.1016/j.nima.2012.11.077.

[158] E. Meoni, "Performances of the signal reconstruction in the ATLAS Hadronic Tile Calorimeter," *Nucl. Instrum. Methods Phys. Res. A*, vol. 718, pp. 97–98, Aug. 2013, https://doi.org/10.1016/j.nima.2013.01.021.

[159] M. Nakhostin, *Signal Processing for Radiation Detectors*. John Wiley & Sons, Hoboken, NJ, USA, 2018, ch. 6.

[160] D. A. Gedcke and W. J. McDonald, "A constant fraction of pulse height trigger for optimum time resolution," *Nucl. Instrum. Methods*, vol. 55, pp. 377–380, 1967, https://doi.org/10.1016/0029-554X(67)90145-0.

[161] S. V. Paulauskas, M. Madurga, R. Grzywacz, D. Miller, S. Padgett, and H. Tan, "A digital data acquisition framework for the Versatile Array of Neutron Detectors at Low Energy (VANDLE)," *Nucl. Instrum. Methods Phys. Res. A*, vol. 737, pp. 22–28, Feb. 2014, https://doi.org/10.1016/j.nima.2013.11.028.

[162] M. A. Nelson, B. D. Rooney, D. R. Dinwiddie, and G. S. Brunson, "Analysis of digital timing methods with BaF_2 scintillators," *Nucl. Instrum. Methods Phys. Res. A*, vol. 505, no. 1–2, pp. 324–327, June 2003, https://doi.org/10.1016/S0168-9002(03)01078-7.

[163] W. K. Warburton and W. Hennig, "New Algorithms for Improved Digital Pulse Arrival Timing With Sub-GSps ADCs," *IEEE Trans. Nucl. Sci.*, vol. 64, no. 12, pp. 2938–2050, Dec. 2017, https://doi.org/10.1109/TNS.2017.2766074.

[164] V. Drndarevic, P. Ryge, and T. Gozani, " Amplifier with time-invariant trapezoidal shaping and shape-sensitive pileup rejector for high-rate spectroscopy," *IEEE Trans. Nucl. Sci.*, vol. 36, no. 1, pp. 1326–1329, Feb. 1989, https://doi.org/10.1109/TNS.1989.574132.

[165] A. Chalupka and S. Tagesen, "A digital high precision pileup inspection unit," *Nucl. Instrum. Methods Phys. Res. A*, vol. 245, no. 1, pp. 159–161, 1986, https://doi.org/10.1016/0168-9002(86)90270-6.

[166] M. Moszyński, J. Jastrzebski, and B. Bengtson, "Reduction of pile-up effects in time and energy measurements," *Nucl. Instrum. Methods*, vol. 47, no. 1, pp. 61–70, Jan. 1967, https://doi.org/10.1016/0029-554X(67)90162-0.

[167] M. Nakhostin, *Signal Processing for Radiation Detectors*. John Wiley & Sons, Hoboken, NJ, USA, 2018, ch. 10.

[168] A. Georgiev, W. Gast, and R. M. Lieder, "An analog-to-digital conversion based on a moving window deconvolution," *IEEE Trans. Nucl. Sci.*, vol. 41, no. 4, pp. 1116–1124, Aug. 1994, https://doi.org/10.1109/23.322868.

[169] P. A. B. Scoullar and R. J. Evans, "Maximum likelihood estimation techniques for high rate, high throughput digital pulse processing," in *IEEE Nuclear Science Symposium & Medical Imaging Conference*, 2008, https://doi.org/10.1109/NSSMIC.2008.4774724.

[170] G. Blaj *et al.*, "Optimal Pulse Processing, Pile-Up Decomposition, and Applications of Silicon Drift Detectors at LCLS," *IEEE Trans. Nucl. Sci.*, vol. 64, no. 11, pp. 2854–2868, Nov. 2017, https://doi.org/10.1109/TNS.2017.2762281.

[171] X. L. Luo *et al.*, "Pulse pile-up identification and reconstruction for liquid scintillator based neutron detectors," *Nucl. Instrum. Methods Phys. Res. A*, vol. 897, pp. 59–65, July 2018, https://doi.org/10.1016/j.nima.2018.03.078.

[172] M. D. Haselman, J. Pasko, S. Hauck, T. K. Lewellen, and R. S. Miyaoka, "FPGA-Based Pulse Pile-Up Correction With Energy and Timing Recovery," *IEEE Trans. Nucl. Sci.*, vol. 59, no. 5, pp. 1823–1830, Oct. 2012, https://doi.org/10.1109/TNS.2012.2207403.

[173] P. Marciniewski, “private communication,” 2016.

[174] P. Marciniewski, “A compact size, 64-channel, 80 MSPS, 14-bit dynamic range ADC module for the PANDA Electromagnetic Calorimeter,” presented at the International Conference on Technology and Instrumentation in Particle Physics, Beijing, China, 2017.

[175] M. Jäger and T. Butz, “FPGA implementation of digital constant fraction algorithm with fractional delay for optimal time resolution,” *Nucl. Instrum. Methods Phys. Res. A*, vol. 674, pp. 24–27, May 2012, https://doi.org/10.1016/j.nima.2012.01.022.

[176] B. Mulgrew, P. Grant, and J. Thompson, *Digital Signal Processing: Concepts and Applications*. Macmillan Press Inc., London, UK, 1999, ch. 6.

[177] G. Usai (ATLAS Tile Calorimeter group), “Signal Reconstruction of the ATLAS Hadronic Tile Calorimeter: implementation and performance,” *J. Phys.: Conf. Ser.*, vol. 293, p. 012056, 2011, https://doi.org/10.1088/1742-6596/293/1/012056.

[178] H. Xu, D. Gong, and Y. Chiu, “A linear optimal filtering approach for pileup noise removal in high-rate liquid ionization calorimeters,” in *IEEE Nuclear Science Symposium & Medical Imaging Conference*, 2013, https://doi.org/10.1109/NSSMIC.2013.6829737.

[179] R. W. Novotny *et al.*, “Response of the shashlyk forward spectrometer of PANDA to photons below 800 MeV energy,” in *IEEE Nuclear Science Symposium & Medical Imaging Conference*, 2014, https://doi.org/10.1109/NSSMIC.2014.7431117.

[180] Wiener Power Electronics, GmbH, “AVM16 - 16 channel VME 12 bit x 160 MHz ADC,” 2020, [Online] Available: http://www.wiener-d.com/sc/modules/vme--modules/avm16.html [4 February 2020].

[181] A. Artikov *et al.*, “Properties of the Ukraine polystyrene-based plastic scintillator UPS 923A,” *Nucl. Instrum. Methods Phys. Res. A*, vol. 555, no. 1–2, pp. 125–131, Dec. 2005, https://doi.org/10.1016/j.nima.2005.09.021.

[182] Kuraray Co., Ltd., “Plastic Scintillating Fibers,” 2014, product catalogue [Online] Available: https://www.kuraray.com/uploads/5a717515df6f5/PR0150_psf01.pdf [10 February 2020].

[183] B. Bolen *et al.*, “Study of the performance of scintillating tiles with WLS fiber readout,” in *IEEE Nuclear Science Symposium*, 1994, https://doi.org/10.1109/NSSMIC.1994.474545.

[184] G. S. Atoian *et al.*, “An improved Shashlyk calorimeter,” *Nucl. Instrum. Methods Phys. Res. A*, vol. 584, no. 2–3, pp. 291–303, Jan. 2008, https://doi.org/10.1016/j.nima.2007.10.022.

[185] S.-O. Flyckt and C. Marmonier, “Photomultiplier tubes — Principles and applications,” Photonis, Tech. Rep., 2002.

[186] G. F. Knoll, *Radiation Detection and Measurement*, 3rd ed. John Wiley & Sons, Hoboken, NJ, USA, 2000, p. 293.

[187] H. Ikeda *et al.*, “A detailed test of the CsI(Tl) calorimeter for BELLE with photon beams of energy between 20 MeV and 5.4 GeV,” *Nucl. Instrum. Methods Phys. Res. A*, vol. 441, no. 3, pp. 401–426, Mar. 2000, https://doi.org/10.1016/S0168-9002(99)00992-4.

[188] A. Bevan and F. Wilson, “AFit User Guide,” 2010, [Online] Available: http://pprc.qmul.ac.uk/~bevan/afit/afit.pdf [10 February 2020].

[189] Xilinx, “Vivado Design Suite User Guide: Logic Simulation, UG900 (v2019.2),” 2019, [Online] Available: https://www.xilinx.com/content/dam/xilinx/support/documentation/sw_manuals/xilinx2019_2/ug900-vivado-logic-simulation.pdf [10 February 2020].

[190] M. Moszyński, “Prospects for new fast photomultipliers,” *Nucl. Instrum. Methods Phys. Res. A*, vol. 337, no. 1, pp. 154–164, Dec. 1993, https://doi.org/10.1016/0168-9002(93)91149-H.

[191] A. G. Wright, *The Photomultiplier Handbook*. Oxford University Press, Oxford, UK, 2017, p. 374.

[192] Springer Verlag GmbH, European Mathematical Society, “Encyclopedia of Mathematics — Laplace distribution,” [Online] Available: https://www.encyclopediaofmath.org/index.php/Laplace_distribution. [9 February 2020].